Structural Investigations of Organic Functional Materials using NMR Crystallography

Tommy-Lee Whewell

This thesis is submitted for the degree of Doctor of Philosophy

January 2024

Department of Chemistry, Lancaster University

I – Declaration

This thesis of approximately 52,500 words, fewer than the maximum 80,000, has not been submitted in support of an application for another degree at this or any other university. It is the result of my own work and includes nothing that is the outcome of collaboration, except where expressly stated. Many ideas in this thesis are the result of discussions with my supervisor Professor John M. Griffin.

The bulk of the work covered in Chapter 3 has been published in *Magnetic Resonance in Chemistry* as 'A Structural Investigation of Organic Battery Anode Materials by NMR Crystallography'. The work not included in the above publication is the work using density functional theory geometry optimisation Methods E, F and G which are detailed and discussed in Section 3.6.1.

Whewell, T., Seymour, V. R., Griffiths, K., Halcovitch, N. R., Desai, A. V., Morris, R. E., Armstrong, A. R., Griffin, J. M., *Magn Reson Chem* 2022, **60**(5), 489.

https://doi.org/10.1002/mrc.5249

The author contributions are as follows: Whewell, T. was responsible for the synthesis and characterisation of the reported organic anode materials. Griffiths, K. performed a Le Bail fit. Halcovitch, N.R. performed single-crystal XRD data collection. Desai, A.V. and Armstrong, A.R. synthesised a new phase of Na_2NDC. Armstong, A.R., Morris, R.E., and Griffin, J.M. provided supervision. Whewell, T., Seymour, V.R., and Griffin, J.M. were collectively responsible for the initial conception of the research. Whewell, T. and Griffin, J.M. were responsible for original draft preparation. All authors reviewed and provided edits.

II – Abstract

Structural Investigations of Organic Functional Materials using NMR Crystallography

Tommy-Lee Whewell - January 2024

In Chapter 1, an introduction to organic functional materials within the scope of lithium-ion batteries and ferroelectricity is given. The importance of structural characterisation aiding future molecular design is discussed. The role of the lithium-ion battery in context of electric vehicles, and society as a whole, is further explored using futures thinking methods.

In Chapter 2, a detailed summary of the key theory pertaining to NMR spectroscopy is presented alongside discussion of key experimental methods. Furthermore, the theory underpinning X-ray diffraction (XRD) and density functional theory (DFT) is given, along with discussion of the NMR crystallography method which encompasses the three techniques.

In Chapter 3, the structures of organic anode materials in their pristine phase are characterised using NMR crystallography. A systematic study of DFT geometry optimisation methods finds that very good agreement can be achieved between experimental and calculated NMR observables when all atomic positions are optimised in conjunction with the use of a semi-empirical dispersion correction scheme.

In Chapter 4, the reduced phases of organic anode materials are studied using a modified chemical lithiation methodology, found here to produce high purity samples. Through multinuclear NMR studies and random structure searching DFT methods, insights are gained into the structure of reduced organic anode materials where existing data from XRD is absent.

In Chapter 5, the structural changes that occur in a model organic ferroelectric material, phenazine chloranilic acid, are characterised by NMR crystallography. Use of isotopic enrichment and variable temperature NMR methods enable information to be gained on low temperature ferroelectric phases, with DFT calculations on three dimensional superstructures shedding light on structures that exist outside of the temperature range of experimental methods.

In Chapter 6, the conclusions from Chapters 3, 4 and 5 are presented aside suggestions for future work relating to these materials and methods.

III – Acknowledgements

Firstly, I would like to thank my supervisor John Griffin for allowing me the opportunity to complete this work and for whose support and guidance throughout this project has been invaluable. I would also like to thank the entire Griffin Research group, both past and present, K.G., A.H., R.B., C.C. and V.S. I would like to extend particular thanks to Valerie Seymour for always being available with great suggestions, technical help and supportive conversations. Thanks also to everyone who has helped with training or instrumentation; Nathan Halcovitch for his help with XRD; Geoff Akien for help with NMR; Chris Cook for help with EPR.

I'd like to extend my gratitude to the Material Social Futures Research Centre for offering an incredibly valuable and unique dynamic in which to complete PhD research, and to the Leverhulme Trust for financial support. Richard Harper and Rob Short, thank you for your endless support and tutelage. Finally, to my cohort, B.M., P.C., C.H., M.P., P.T., J.L., and A.D.-Z., thank you for all being tremendously open minded and engaging colleagues, for your discussions over the years and your friendship.

Thanks to the many friends who have offered support, counsel, and friendship not just during the last four years but always, particularly L.R., B.W., P.T., B.M., and P.C.

The last four years would not have been possible without the support of my family, Mom, Dad, Kirsty, Alfie, Darcie – thank you. Rita, Trevor, David, Holly, June and Sue – family in all but name, thank you. Most importantly, Sarah and Pogo, your patience, love, sacrifice, understanding, motivation, support, warmth, encouragement and faith is endlessly appreciated.

Nan Fodge and Granddad Geoff, forever my biggest fans and my biggest inspiration, this is for you, dedicated to you, and a partial repayment of the insurmountable debt I owe you both. Thank you.

IV – Contents

V – List of Acronyms

Acronym	Expansion
A	Acceptor
AIRSS	*ab-initio* Random Structure Searching
AlPO	aluminophosphate
BDC	benzenedicarboxylate
BPDC	biphenyldicarboxylate
BTO	barium titanate
CA	chloranilic acid
CASTEP	Cambridge Serial Total Energy Package
CCD	Charge-Coupled Device
CCDC	Cambridge Crystallographic Data Centre
CL	Chemical Lithiation
CP	Cross Polarisation
CPMAS	Cross Polarisation Magic Angle Spinning
CSA	Chemical Shift Anisotropy
CT (Chapter 2)	Central Transition
CT (Chapter 5)	Charge Transfer
CW	Continuous Wave
D	Donor
DABCO	diazabicyclo[2.2.2]octane
DCA	dichloroisocyanuric acid
DFT	Density Functional Theory
DNP	Dynamic Nuclear Polarisation
d-P-CA	Deuterated phenazine chloranilic acid
DUMBO	Decoupling Using Mind Boggling Optimisation
EE	Embodied Energy
EFG	Electric Field Gradient
EPR	Electron Paramagnetic Resonance
EQM	Electric Quadrupole Moment
EROI	Energy Return on Investment
EV	Electric Vehicle
FE	Ferroelectric
FeRAM	Ferroelectric Random Access Memory
FID	Free Induction Decay
FT	Fourier Transform
FWHM	Full Width at Half Maximum
GGA	Generalized Gradient Approximation
GIPAW	Gauge Induced Projector-Augmented Wave
HA	haloanilic acid
HETCOR	Heteronuclear Correlation
HMQC	Heteronuclear Multiple Quantum Correlation
I	Ionic

IC	Incommensurate
INADEQUATE	Incredible Natural Abundance Double Quantum Transfer Experiment
INEPT	Insensitive Nuclei Enhancement by Polarisation Transfer
IR	Infrared
KDP	potassium dihydrogen phosphate
LCO	lithium cobalt oxide
LDA	Local Density Approximation
LIB	Lithium-Ion Battery
LMO	lithium magnesium oxide
MAS	Magic Angle Spinning
MOF	Metal Organic Framework
MPL	Mauri, Pfommer and Louie
MQ	Multiple Quantum
MQMAS	Multiple Quantum Magic Angle Spinning
MSF	Material Social Futures
MW	Molecular Weight
N	Neutral
ND	Neutron Diffraction
NDC	naphthalenedicarboxylate
NIB	Sodium-Ion Battery
NMC	nickel magnesium cobalt oxide
NMR	Nuclear Magnetic Resonance
NQR	Nuclear Quadrupole Resonance
PAS	Principal Axis System
PAW	Projector-Augmented Wave
P-BA	phenazine bromanilic acid
PBE	Perdew, Burke and Ernzerhof
P-CA	phenazine chloranilic acid
PE	Paraelectric
PET	polyethyleneterephthalate
ppm	Parts per Million
PTFE	polytetrafluoroethylene
PVDF	polyvinylidene difluoride
PXRD	Powder X-ray Diffraction
PZT	lead zirconate titanate
RAM	Random Access Memory
rf	Radiofrequency
rPBE	revised Perdew, Burke and Ernzerhof
rSCAN	regularized Strongly Constrained and Appropriately Normed
S/N	Signal to Noise
SCAN	Strongly Constrained and Appropriately Normed
SCF	Self-Consistent Field
SCXRD	Single Crystal X-ray Diffraction
SDC	stilbene dicarboxylate
SEDC	Semi-Empirical Dispersion Correction
SEI	Solid-Electrolyte Interphase
SHE	Standard Hydrogen Electrode

SP	Super P
SPE	Single-Point Energy
SPINAL-64	Small Phase Incremental Alternation with 64 steps
SSB	Spinning Side Band
ST	Satellite Transition
sXRD	Synchrotron X-ray Diffraction
TGA	Thermogravimetric Analysis
THF	Tetrahydrofuran
THP	Tetrahydropyran
TMS	tetramethylsilane
TPPM	Two Phase Pulse Modulation
TS	Tkatchenko-Sheffler
TTF-CA	tetrathiafulvalene-chloroanil
TTF-HA	tetrathiafulvalene-haloanil
UV	Ultraviolet
VT	Variable Temperature
XC	Exchange-Correlation
XRD	X-ray Diffraction

Chapter 1

Introduction

Sustainability throughout science has never been more important than it is today, with the far-reaching effects of the climate crisis theorised for decades now being realised across the globe.[1] With the highest human population in history and an increasingly connected and technologically advanced society, the demand for portable technologies is set to continue rising. Many of these technologies require rapid shifts towards alternatives made from more sustainable materials if we are to avoid further acceleration of climate change through emissions and use of fossil fuels. While positive steps have been taken, like with the blossoming electric vehicle (EV) industry, significant challenges remain before many technologies can make the switch to sustainable materials. While the EV alleviates the dependence of personal travel on fossil fuels, the lithium-ion battery (LIB) used for power in EVs is not short of environmental impacts itself. Battery electrode materials often contain transition metals that have high associated energetic or environmental costs, however sustainable alternatives exist in the form of organic battery electrode materials, such as lithium benzenedicarboxylate ($Li_2C_8H_4O_4$, Li_2BDC). Organic materials offer sustainable alternative to many technologies, not just battery materials but also in portable electronics, such as organic ferroelectric materials. These two independent technologies feature large similarities in the benefits they can offer and the current drawbacks impeding their application. As relatively new materials, one of the key challenges that remains is to fully characterise and understand structure on a molecular level to aid future molecular design efforts and create better materials more suited to the intended application. The work in this thesis attempts to gain information about molecular structure and structural changes in both organic battery electrode materials and organic ferroelectric materials through the combined use of Solid-state nuclear magnetic resonance (NMR) spectroscopy, X-ray diffraction (XRD) and density functional theory (DFT).

1.1 Lithium-Ion Batteries

1.1.1 Battery Chemistry

In an increasingly connected and mobile society, the battery is more than ever before an essential component of modern life. By allowing *ad-hoc* usage of electricity by the storage and transformation of chemical energy, the battery circumvents the requirement of tethered

electrical connections. With increasing focus on renewable energy sources that are inherently intermittent, the battery provides a solution where energy can be stored at the point of production, and used later when the renewable energy source is not sufficient alone to meet demand. In its most simple form, a battery cell is comprised of two electrodes separated by an electrolyte, with an external connection between the electrodes through which the electric current flows (Figure 1.1). Alongside these components are current collectors, on which the electrodes are mounted to provide greater electric conductivity, and a separator to prevent the two electrodes from physically touching. The two electrodes are the negative anode and positive cathode with each possessing a different electric potential, this allows a spontaneous chemical reaction to proceed when connected. The electrolyte is an ionic conductor but electric insulator; this allows ions to move through the cell while ensuring no electric charge can pass through, which would cause a short circuit. When the electrodes are connected, electrons flow through the external circuit from the anode to the cathode, meanwhile a simultaneous migration of cations towards the cathode through the electrolyte occurs. During charging these processes are driven in the opposite direction, resulting in the cell returning to its charged state.

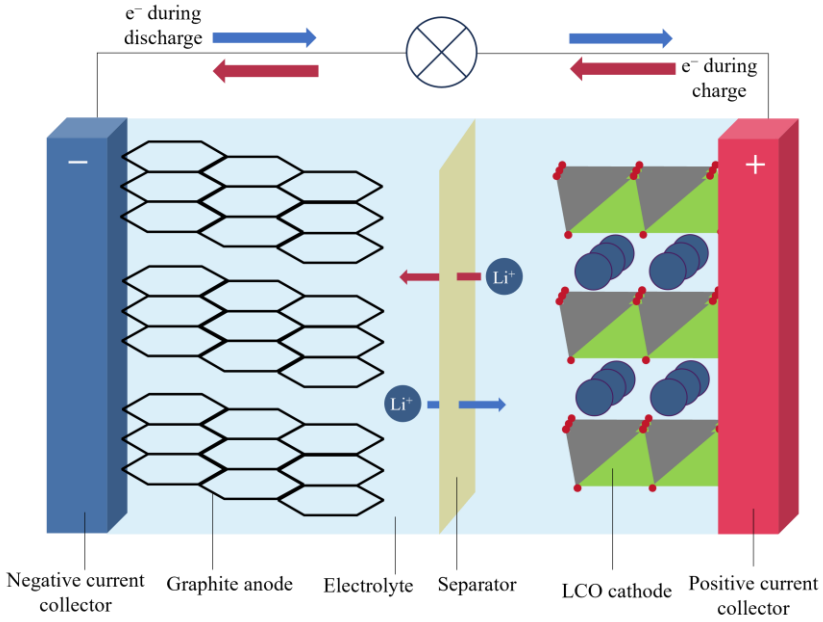

Figure 1.1 Simplified schematic of a lithium-ion battery. Diagram not to scale.

The properties of batteries are assessed using a number of different metrics, with one of the most important being the difference in electric potential between the two electrodes. This is reported as standard cell potential, $V_{\text{cell}}^{\ominus}$, and is defined as

$$V_{\text{cell}}^{\ominus} = V_{\text{cathode}}^{\ominus} - V_{\text{anode}}^{\ominus}\,, \tag{1.1}$$

where $V_{\text{cathode}}^{\ominus}$ and $V_{\text{anode}}^{\ominus}$ are standard electrode potentials. The standard electrode potentials are themselves defined by convention relative to the Standard Hydrogen Electrode (SHE),

defined as 0 V. Despite this, the cell potential, or voltage, is seldom reported against the SHE in the literature, with many researchers opting to report directly against Li^+/Li^0, which itself has a voltage of −3.04 V *vs.* SHE. To maximise the cell voltage, anodes are often selected for their low voltages, while cathodes are selected for their high voltage. For many applications, consideration is also given to the gravimetric capacity of an electrode. Gravimetric, or specific, capacity (Q_{cell}) is the amount of charge a cell can store relative to its mass and is usually given in mA h g^{-1}. Thus, a material with a lower molecular weight that has an identical stoichiometric lithium capacity will have a larger specific capacity and be a more attractive option for certain applications, particularly where portability is important. When designing batteries for portable applications, the energy density, E_{cell}, is also a key consideration and is given by

$$E_{\text{cell}} = V_{\text{cell}} \times Q_{\text{cell}} . \tag{1.2}$$

A portable device should have a battery that is able to draw the maximum power from the lowest possible mass, though in stationary storage applications more consideration may be given to volume rather than mass. Volumetric capacity is analogous to specific capacity but is the amount of charge stored per unit volume and given in mA h cm^{-3}. Volumetric capacity is rarely reported, as meaningful volumetric space saving is made difficult by the many components of a cell that cannot be reduced in size equally. In other words, even when the volume of the active materials can be minimised, the other components in the cell often cannot and as such it is usually not possible to make the cell smaller. Increasingly, good rate performance and high cycling stabilities are important properties that a battery should possess. Rate performance refers to the power delivered by a battery at different discharge rates, while cycling stability refers to the longevity of a battery over many charge and discharge cycles. These two parameters are closely related, as often charging and discharging a battery at high 'C-rates' can lead to a reduced cycling stability. This is particularly important for applications where a short charging time is beneficial, such as EVs and portable devices. It is often the case that a short charging time infers a fast rate of charging. Fast cycling rates can lead to degradation of the electrodes and electrolyte in the cell, reducing the performance over time.

1.1.2 Battery History

The origins of the battery rest with Alessandro Volta's voltaic pile in the 1800s, but practical and commercial usage of batteries did not occur until the early 1900s with the advent of nickel-cadmium alkaline batteries. Gilbert Lewis began experimenting with lithium batteries shortly after, but it would be another half a century before the increasing interest led to significant developments. These early works on lithium-ion batteries (LIB) were limited to primary cells such as the lithium dichloroisocyanuric acid (DCA) cells reported by Williams *et al*.[2] The next major development came in 1974 from M. Stanley Whittingham, who was investigating ion intercalation in transition metal disulfides. The work led to a battery with

a layered Li_xTiS_2 cathode and a lithium metal anode, with the cathode having a voltage of 2.0 V *vs*. Li^+/Li^0.[3] In the following years, John Goodenough and coworkers replaced the Li_xTiS_2 cathode with a lithium cobalt oxide (Li_xCoO_2, LCO) cathode.[4] The LCO cathode is another layered structure allowing lithium ion intercalation, while cobalt redox maintains neutrality of the cathode during charging and discharging cycles. The LCO cathode has a voltage in excess of 3.5 V *vs*. Li^+/Li^0, however upon repeat cycles, lithium ions did not return to the lithium metal anode surface homogenously, instead creating spindle-like structures called dendrites. Dendrites present a significant safety risk when allowed to form by protruding across the cell and causing short circuits and electrical fires, resulting in a major hurdle for commercialisation of the new LIB technology. Shortly after, Akira Yoshino filed a patent for an LCO cell where the problematic lithium anode had been replaced by a carbonaceous anode.[5] The graphite anode used featured a layered structure, similar to the LCO cathode, and allowed reversible intercalation of lithium ions while the strong π-bonding interactions between layers prevented dendrite formation.[6] Furthermore, graphite is an electronic conductor, allowing effective electron mobility and has a very similar electrode potential to lithium metal at just 0.1 V *vs*. Li^+/Li^0. This version of the LIB was the first to be commercialised by the SONY corporation and used in a portable telephone. This incredibly important work was recognised with the joint award of the Nobel Prize in Chemistry in 2019.[7]

1.1.3 Lithium-Ion Battery Materials

The surge of interest in LIBs was kickstarted by the energy crisis of the 1950s and 1960s, though key studies and eventually commercialisation occurred through the 1970s and 1980s. While the LCO cathode is one of the most well-known cathodes today, many other LIB electrode materials exist, and many of those are transition metal-based inorganic compounds featuring cobalt, manganese, nickel or iron. These materials rely on oxidation and reduction of the metal atom to store charge, though the inclusion of heavier metal atoms can lead to limitations in specific capacity to around 150 mA h g^{-1}.[8] Lithium magnesium oxide (LMO) cathodes are commonly found in power tool batteries, while lithium nickel magnesium cobalt oxide (NMC, $LiNi_xMn_yCo_zO_2$) cathodes are the modern cathode of choice in the EV market. Cobalt usage in cathode materials presents a significant hurdle which researchers are working to overcome. Much of the global reservoir of cobalt is located within the Democratic Republic of the Congo, where reports of dangerous work environments, worker exploitation and environmental and social concerns dominate discourse.[9] As such, low-cobalt or cobalt-free cathodes have become the subject of much interest, with NMC811 ($LiNi_{0.8}Mn_{0.1}Co_{0.1}O_2$) a leading low-cobalt cathode.

Research into battery materials has not been exclusive to the cathode, with the graphite anode another source of scientific interest. Similarly to cobalt, deposits of graphite are few and

are localised in equally few countries around the globe.[10] The environmental impact of graphite mining can be significant, with a lengthy and energetically costly refinement processes as well as significant pollution. Reports of graphitic dust covering entire villages, impeding crop growth and polluting natural water courses provide a superficial look at the larger issue.[11] While synthetic graphite presents a cleaner alternative, the synthetic process still requires enormous energetic costs including temperatures in excess of 2500 K.[12] Silicon anodes gained interest as a graphite replacement stemming from high theoretical charge capacities and their abundant feedstocks.[13] Silicon is already a widely used semiconducting material due to its high electronic conductivity. However, the practicality of silicon anodes is significantly limited by a volume expansion of approximately 400% during cycling. This expansion leads to significant electrode degradation, reduced performance and safety concerns.

1.1.4 Organic Battery Electrode Materials

A possible solution to the issues with graphite and silicon anodes is to use organic anode materials. Anode materials made from organic feedstocks can present an opportunity to use highly versatile, adaptable and sustainable materials. Research into organic electrode materials first occurred prior to the commercialisation of the LIB, but research over the past two decades has demonstrated the promise of these materials. One of the first classes of organic electrode materials studied was conductive polymers on account of their redox activity, but were limited by low energy densities.[14-16] The large molecular weights of the polymers, in conjunction with large portions of the molecule not involved with the redox behaviour, was the cause of the low energy density. In 2008, Armand and coworkers studied an oxocarbon, lithium rhodizonate, aiming to replicate the redox activity of conductive polymers through the carbonyl groups.[17] Results showed promising capacity but were limited by poor cycle stability. A year later, more promising results were reported by the same group, this time replacing the rhodizonate with a weakly electron withdrawing redox active carboxylate containing species.[18] The two molecules of interest, lithium muconate ($Li_2C_6H_4O_4$) and Li_2BDC, have low voltages *vs.* Li^+/Li^0 and thus are more suitable as anode materials. A reversible incorporation of two lithium ions per formula unit was reported, alongside a suggested mechanism for the rearrangement of the π-electron conjugation. This rearrangement leads to a capacity of 150 mA h g^{-1} and 300 mA h g^{-1}, respectively, at voltages of 1.4 V *vs.* Li^+/Li^0 and 0.8 V *vs.* Li^+/Li^0, respectively. Discharge of both systems at 1/C (one Li^+ per stoichiometric unit per 10 hours) results in a capacity loss of less than 30%. The slow cycling rate is due to the low electronic conductivity of these materials, a property shared by the majority of organic materials. A capacity fade was observed and was attributed to electrode material dissolving in the electrolyte $LiPF_6$. Li_2BDC would go on to be the subject of much interest over the following years, due to its superior electrode potential, capacity and cycling stability compared to lithium

muconate. Li_2BDC also shares structural similarities with the LCO cathode, with a layered structure allowing for reversible lithium-ion intercalation, though with no metal site for redox, the π-conjugated organic backbone is the source of redox activity. Furthermore, the synthesis of Li_2BDC is a relatively simple and safe procedure combining benzenedicarboxylic acid and lithium hydroxide at low temperatures.[19, 20] Benzenedicarboxylic acid, more commonly known as terephthalic acid, is commonly found copolymerised with ethylene glycol as the functional polymer polyethylene terephthalate (PET), which is a widely used single-use plastic found in water bottles, plastic straws and food containers. Single-use plastics have presented a significant environmental issue in recent years, in part due to a tendency of modern societies towards busy lifestyles, where on-the-go consumption and use-discard mindsets have been prevalent. Despite this, terephthalic acid can be obtained from waste PET *via* multiple routes. The first is a thermal digestion bomb approach, where PET chips are heated to just over 100 °C with water in a sealed digestion bomb, utilising the high pressures created to digest the PET and yield terephthalic acid.[21] Raja *et al*. used this method to create terephthalate ligands for a paddlewheel metal-organic framework (MOF) from waste PET. Another method is to use enzymatic depolymerisation as shown recently by Lu *et al*. In that work, machine learning was used to engineer a PET hydrolase that can completely degrade many different thermoformed products within one week.[22] One final alternative method was demonstrated by Ghosh *et al*., where PET flakes were up-cycled using an ultrafast microwave irradiation process to yield ready-made organic anode materials.[23] These methods highlight an opportunity for a cradle-to-cradle approach where waste plastics can be recycled into a product with greater benefit, such as a LIB.

The terephthalate ligand has been the subject of widespread interest, with the effects of functionalisation and substitutions to the aromatic ring highlighting new design routes and fine-tuning possibilities. The ability to fine-tune material properties could allow the lithiation mechanism to be controlled, for example by creating or closing ion migration channels that may exist within the structure. Lakraychi *et al*. functionalised the terephthalate system with methyl groups, reducing the voltage by 0.1 V to 0.65 V *vs*. Li^+/Li^0.[24] Similarly, Renault *et al*. substituted amino groups onto the terephthalate backbone, increasing the voltage by 0.1 V.[25] Neither substitution had a large impact on the voltage or specific capacity; however, both studies showed that functionalisation could prove useful in future attempts to improve the properties of organic anode materials. The interest in terephthalate anode materials has extended to studies applying the material into sodium-ion batteries (NIB).[26, 27] NIBs present a cheaper and more sustainable long-term solution for the battery market on account of the relative abundance of sodium as compared to lithium. While sodium is one of the most abundant elements in the Earth's crust, there are concerns about the long-term availability of lithium deposits which is

already leading to higher costs. Unfortunately, however, the increased atomic mass of sodium means the specific capacity of a like-for-like NIB would be reduced compared to the analogous LIB. Park *et al*. showed that the sodium terephthalate analogue has a voltage of 0.4 V *vs*. Na^+/Na^0, slightly improving on the 0.8 V *vs*. Li^+/Li^0 of the lithium analogue reported by Armand *et al*.[18, 26] Wang *et al*. then showed that cycling stability could be improved by extending the length of the conjugation in the organic ligand, attributed to the increased electronic conductivity.[28] In the study, a conjugated dimer of terephthalates, 4,4-stilbene dicarboxylate (SDC) was used. However, due to the increased molecular weight, the specific capacity is reduced. Another example of elongated conjugation that also mitigates the impact of increased molecular weight on the specific capacity is to use directly adjacent ring systems such as a naphthalene backbone. Ogihara and coworkers used 2,6-naphthalenedicarboxylic acid to create lithium naphthalenedicarboxylate, Li_2NDC, giving an operating cell voltage of 0.88 V *vs*. Li^+/Li^0, with a capacity of just under 200 mA h g^{-1}.[29-31] Similar results were reported by Tarascon and coworkers, with additional insights gained by ^{13}C cross polarisation (CP) magic angle spinning (MAS) NMR experiments.[32] The CPMAS NMR experiments confirmed the formation of the Li_2NDC with a decrease in intensity of the carboxylate resonance. The authors hypothesised that the extended aromaticity was in part the reason for the slightly improved voltage *c*. *f*. Li_2BDC, thus suggesting that extended π-conjugation can increase both voltage and cycling stability.

Extension of the π-conjugation system can lead to large improvements in cycling capabilities due to high electronic conductivity.[28, 33-36] Fédèle *et al*. showed that improvements to cyclic stability is proportional to the distance between the redox active carboxylate groups.[36] Increasing conjugation further, molecules derived from perylene units have a large delocalised electronic structure, and with anhydride functionalisation allows lithium redox.[33-35] A low voltage of 0.5 V *vs*. Li^+/Li^0 is an improvement upon small organic anode materials such as Li_2BDC, but the large molecular structure significantly limits the gravimetric capacity to 80 mA h g^{-1}. A biphenyldicarboxylate (BPDC) backbone is another route to extended conjugation, with less of the molecular weight uninvolved in electrochemical activity than the previously mentioned SDC and perylene backbones. Fédèle *et al*. showed that Li_2BPDC maintains a capacity of 180 mA h g^{-1}, with improved cycling performance to Li_2BDC.[36]

Despite the wealth of research that has focused on the improvement of cycling stability, voltage or capacity of organic anode materials, relatively little is still understood about the structural changes that occur on the molecular level within these materials. An understanding of these structural changes can shed light on the lithiation or sodiation mechanism and aid future molecular design efforts. Due to the standard electrochemical methodologies used to study properties of battery materials, it can be difficult to retrieve and isolate different components of

a battery following cycling. Due to this, crystallography is often limited in the information that can be gained of the structure of cycled materials due to these additional components such as binding agents, conductive additives, liquid electrolytes. Furthermore, cycled materials are usually unstable within ambient atmosphere and must be studied under inert conditions.

1.2 Ferroelectricity and Data Storage

In some cases where rapid electrical power is required, a capacitor may be more suitable than a battery as a source of stored electrical energy, with one key application being in random access memory (RAM). With increasing electrification and transportable technologies in modern society, capacitors present a technology where improved material and energetic sustainability could prove hugely beneficial. A capacitor is comprised of two conductive plates separated by a dielectric material, such that an electric field can be generated within the capacitor. A wide variety of materials are used in different components of capacitors, such as polymers and ceramics which often contain transition metals. Ferroelectric materials have also been used in place of the dielectric in capacitors, where the non-linear capacitance of ferroelectric materials allows for tuneable applications such as tuneable filters for microwave applications or non-volatile memory in ferroelectric RAM (FeRAM).

Ferroelectricity is the property of a material to exhibit spontaneous electric polarisation, which can then be reversed with the application of an external electric field. While ferroelectricity was first observed in 1920, it is an analogous phenomenon to ferromagnetism which has been known for centuries prior. The first observations of ferroelectricity were made by Joseph Valasek who noted that the polarisation of Rochelle salt (potassium sodium tartrate tetrahydrate) remained high after exposure to an applied electric field. The discovery stemmed from previous work centuries earlier where the piezoelectric effect was noted after mechanical stress upon a quartz crystal generated an electrical charge. Pyroelectricity is a similar phenomenon by which electrical charge is generated by change in temperature. All ferroelectric materials are also piezoelectric and pyroelectric. Once electrically polarised, ferroelectric materials can then have the polarisation flipped by application of a coercive field, which makes the ferroelectric effect attractive for application in FeRAM. Each ferroelectric material is unique in that the temperature at which the phase transition occurs, the Curie Temperature (T_C), is an intrinsic property of the material. Above T_C, the materials are paraelectric, in that no polarisation is retained following application of an external electric field. However, as temperature approaches T_C, the dielectric constant (κ) of the material increases in obeyance of the Curie-Weiss law. The Curie-Weiss law describes the electric susceptibility (χ) of a ferroelectric material in the paraelectric phase above T_C, and is given by

$$\chi = \frac{C}{T - T_C}, \tag{1.3}$$

where C is a material specific Curie constant. These high-κ states can be exploited in applications such as condensers, transducers and capacitors.

1.2.1 Ferroelectric Materials

Since the discovery of ferroelectricity in 1920, vast numbers of ferroelectric materials have been identified, with the majority being perovskite oxide materials with the formula ABO_3.[37] Barium titanate ($BaTiO_3$, BTO) is one of the key examples that has been studied extensively, while lead zirconate titanate ($PbZr_{1-x}Ti_xO_3$, PZT) has reached large scale application in ultrasonic transducers.[38] Inorganic ferroelectric materials have been more widespread, and three key structural mechanisms have been identified that accompany the phase transition as shown in Figure 1.2.[39] The first is a dipolar reorganisation observed in permanently dipolar molecules such as $NaNO_2$. The polar molecules become more ordered creating an overall polarisation, with the reversibility of the order and disordered states the source of ferroelectricity. The second mechanism is an ionic displacive mechanism, where an ion in the unit cell is reversibly displaced creating a spontaneous polarisation. This mechanism is most notably observed in BTO and PZT. The final mechanism observed in inorganic ferroelectric materials is proton transfer, most notably observed in potassium dihydrogen phosphate (KH_2PO_4, KDP). In this mechanism, dynamic protons on hydrogen bonds reversibly switch between donor (D) and acceptor (A) sites, giving rise to electric polarisation through ionically charged molecules.

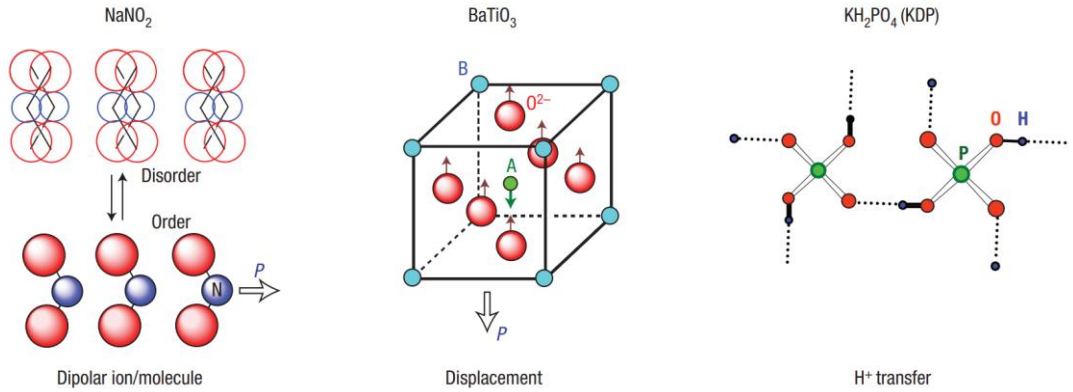

Figure 1.2 Three key structural mechanisms of inorganic ferroelectric materials. Figure adapted from Horiuchi and Tokura, 2008, Reference no. 38.

Organic ferroelectric materials, while not widespread, have been of increasing interest over recent decades. In the 1950s, glycine salts were shown to exhibit room temperature ferroelectric behaviour and became the first commercialised usage of an organic ferroelectric. However, low molecular weight organic ferroelectric materials have been even fewer in number. Thiourea (CH_4N_2S) has been studied extensively since the discovery of its ferroelectric

behaviour in 1956, with its low molecular weight (76.12 g mol^{-3}) a source of great potential for application in portable all organic electronics. Thiourea is an example of a single component ferroelectric, and along with polymer ferroelectrics such as polyvinylidene difluoride (PVDF), exhibits a mechanism analogous to the dipolar reorganisation observed in $NaNO_2$. Thiourea garnered significant interest due to the complex structural changes that occurred with decreasing temperature, including commensurate and incommensurate superstructures. Organic ferroelectrics that exhibit structural changes analogous to inorganic ferroelectrics are not limited to the dipolar reorganisation mechanism, however. Multicomponent charge transfer complexes exhibit structural change analogous to the displacive mechanism. Here, π-π stacks of donor and acceptor molecules arranged in D-A-D-A stacks undergo a change in symmetry and dimerise into stacked pairs of D^+-A^-. Ferroelectricity in materials of this type was first noted in tetrathiafulvalene-haloanil (TTF-HA) complexes such as TTF-chloranil (TTF-CA). Similarly, charge transfer can be achieved with a proton instead of an electron, with this exhibited in hydrogen bonded organic ferroelectrics. An early example of this is in diazabicyclo[2.2.2]octane (DABCO) where a chain of hydrogen bonded H–$DABCO^+$ cation units can undergo collective proton transfer. Recently, Horiuchi and coworkers reignited research interest in the area with studies of phenazine haloanilic acid complexes (*i.e.*, phenazine chloranilic acid, P-CA). These low molecular weight, room temperature ferroelectric materials exhibit ferroelectricity through a mechanism as yet not fully understood consisting of proton transfer through multiple commensurate and incommensurate phases.

1.2.2 Phase Transitions

In some materials, such as P-CA, structural changes that occur as a result of changing temperature unlock ferroelectricity through the formation of new phases *via* a phase transition as shown in Figure 1.3. In this thesis, the structural changes of P-CA are studied using Solid-state NMR spectroscopy and DFT calculations. At room temperature, P-CA is paraelectric and has $P2_{1/n}$ symmetry.[40, 41] The unit cell consists of two phenazine molecules and two chloranilic acid molecules related by symmetry in alternating stacks. At the first Curie temperature, $T_{C,I}$ = 253 K and below, P-CA is ferroelectric with a reduction in symmetry to $P2_1$.[41, 42] The molecules in the unit cell are no longer related by symmetry, on account of the chloranilic acid hydroxyl group proton now occupying a more diffuse location towards the nitrogen atom of the phenazine molecule. The first ferroelectric phase, FE-I, is then stable for a wide temperature range, where at the second Curie temperature, $T_{C,IC}$ = 147 K, another phase transition occurs. Here, P-CA becomes a twofold incommensurate superstructure with superspace group $P2_1$ (½ σ_2 ½)0 where σ_2 = 0.5139, where the modulation of the position of the proton in the O–H···N hydrogen bond cannot be described in a rational number of unit cell lengths.[42, 43] This incommensurate phase, FE-IC, is only stable in a small temperature window,

where below a lock-in temperature, $T_{C,II}$ = 137 K, P-CA is described as a twofold commensurately modulated superstructure with supercell symmetry $P2_1(½\ \sigma_2\ ½)0$ where σ_2 = ½.[42, 44] Replacement of the chloranilic acid protons with deuterons has a significant effect on the phase transition temperatures. The deuteration effect raises phase transition temperatures by 51 K, such that $T_{C,I}$ = 304 K, moving the ferroelectric behaviour well into the room temperature regime.[40] While this may not be ideal in application due to the high costs of isotopically-enriched synthesis, the higher temperatures of phase transition enable study of a greater thermal range with temperature-limited analytical techniques.

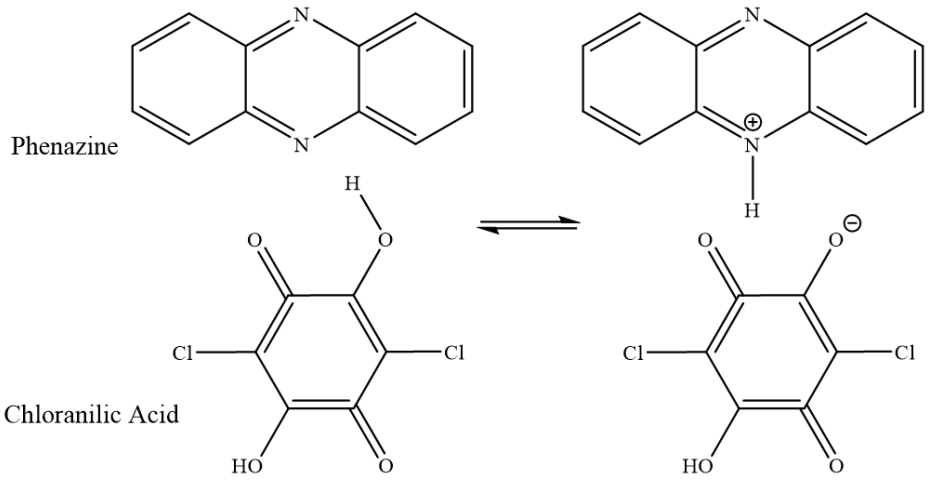

Figure 1.3 Simplified schematic of the chemical structure of P-CA showing complete proton transfer at low temperature.

1.3 The Importance of Structural Insights into Organic Functional Materials

With both organic anode materials and organic ferroelectric materials, one of the key issues remaining with these materials is poor suitability when compared to the market leading alternatives. The benefits of organic materials being low cost, sustainable and highly tuneable is likely to be outweighed by performance until a comparable or superior performance is achieved. Significant research efforts are ongoing to improve performance, but a surprisingly small fraction of this is focused on chemical structure. A deep understanding of chemical structure, structural changes and the impact on chemical properties can improve decision-making in molecular design and chemical engineering in the search for higher-performance materials. To truly understand chemical structure, a variety of complimentary analytical techniques are required. One of the key techniques in the chemists' toolkit is NMR spectroscopy, which is a non-destructive, element specific and highly informative local chemical structure probe. Solution-state NMR is the more common variant with its rapid experiments and high resolution, but Solid-state NMR can give additional chemical information on account of the different

sensitivity to certain magnetic interactions. XRD is another widely used technique to study the structure of crystalline solids giving more information about long-range structure and disorder complimentary to NMR. These techniques along with DFT, which calculates a wide variety of properties based on the electronic structure, form the basis of NMR crystallography – a chemical structure analysis method that has been applied to organic functional materials throughout this thesis.

1.4 A Material Social Futures Outlook

The work presented in this thesis has been carried out as part of the Material Social Futures (MSF) doctoral training programme at Lancaster University. The MSF programme brings together researchers from a wide array of materials science and social science disciplines with the aim of enabling all involved to benefit from interdisciplinary communication and collaboration, allowing researchers the freedom to consider 'big picture' issues outside of their respective fields. Whether that be enabling social scientists with the scientific knowledge to understand the technicalities of their research, or arming material scientists with the skills to think outside of the laboratory and interact with the wide-ranging actors upon their field. These actors, or drivers of research, are collectively grouped under the acronym PESTLE which includes the political, economic, sociological, technological, legal, and environmental. Additionally, the ever-expanding horizons of scientific knowledge has led researchers to become experts in increasingly small areas, and in response new discoveries and scientific advancements are often increasingly incremental. As the idiom goes: "an expert knows more and more, about less and less, until they know everything about nothing". This is not a fault of the individual researchers themselves, but for truly holistic approaches to answering real-world issues through meaningful science, interdisciplinary communication with experts from wide ranging disciplines becomes a necessity. In this section, the lithium-ion battery technology that is the subject of Chapters 3 and 4 is used as a case study to demonstrate some of these foundational ideas, with particular consideration given to the importance of the LIB in EV technology, enabled through participation with the MSF programme.

1.4.1 Energy in Society

When considering a technology such as the LIB, one must recognise the deep entanglement with energy. The LIB, in its most simple terms, is a repository of energy. While humanity has managed to harness and manipulate energy, it is a ubiquity to all life on Earth. From the earliest instances of human history, energy was harnessed within the technological limitations of the time, from the burning of wood for heat, or using wind for transport on sailboats. With advancements in technology over centuries past, a turning point was reached where mining for coal or drilling for oil and gas became feasible sources of energy. More

recently renewables are of increasingly vital importance in light of the climate crisis. In the UK, nuclear power provides a base load to the national grid, supplemented by renewable energy with demand usually met through *ad-hoc* burning of natural gas. Intermittent renewable energy sources such as solar and wind harnessed using solar panels and wind turbines are too infrequent to be relied upon to meet demand, and so this energy must be stored ready to meet demand. The battery itself was a technological advancement in order to store energy and allow for a more on-demand usage. The LIB in particular has enabled significant changes to the way we use energy. The LIB, in tandem with mobile devices and internet access, has created an ever-connected society with an endemic on-the-go mindset. This lifestyle that has become commonplace, particularly in the Global North, is interlinked with a use-then-dispose throw-away culture sometimes known as 'cradle-to-grave'. Products are regularly and swiftly disposed of in the fastest and most convenient way for the user, sparing little thought for the energy embodied in that product, or how and where it will be recycled, if at all. Throw-away culture is partially a result of the disconnection of the modern citizen to the roots of energy, where energy is seen as an unlimited resource that is ever-present through connection to an electrical outlet. Of course, this is not true in all industries, *e.g.*, agriculture, where there is still a deep-rooted connection with energy in terms of the effort required to plough a field and the growing of crops for food. While modern machinery has made this process more efficient, historically fields were ploughed with the aid of horses, or purely human resources. In absolute terms, the energy required to plough a field has not changed, but instead a modern machine could achieve in one hour, what a workforce of many people could achieve in an entire day. This quotient of energy has previously been termed somewhat distastefully, 'slave energy', relating to the work that could be done by a human workforce.

In large parts of the World, the ever-present availability of electricity is still not the norm. In the Global South, where energy inequality is particularly vast, this disconnection to energy is not so pronounced. To illustrate, according to the Energy Institute, in 2022 the energy usage per capita varied from as low as 217 kWh in Somalia, to in excess of 100,000 kWh in Kuwait, UAE, Qatar and Canada.[45] It is worthy of note that these figures are state-wide energy consumption, where the aforementioned high-usage states all feature large scale oil and natural gas production with relatively small populations. Still, the majority of western European nations including the UK, Germany, France and Spain have energy usage of approximately 30,000 kWh to 40,000 kWh per capita. Perhaps from these figures, it is easy to imagine how the modern person has lost sight of the energetic costs of everyday objects and think not of the embodied energy (EE) of their possessions.

EE is a conceptual descriptor of how much energy is embodied within an object, including the energetic costs of the collection of the raw materials, and the energy consumed

during the manufacturing process. EE can be an incredibly difficult parameter to calculate accurately, as defining where to draw the borders of what is or is not embodied can be subjective. For example, in some cases a portion of the energetic costs of transport and shipping might be included, but then it could be argued a portion of the manufacture of the transport vehicles also be included with this process then repeated *ad infinitum*. Despite this, with appropriate boundaries drawn, EE calculations are possible and can reveal surprising results. To take the EV as an example of a technology designed to be environmentally friendly. In terms of emissions during usage, the EV far outperforms the petrol vehicle, that is assuming the electricity used comes from a renewable source. Charging an EV with electricity generated through the combustion of natural gas seems superficially inane, but is likely more common than one might realise. However, with consideration given to the EE of the vehicle itself, the EV does not perform as well. EVs are incredibly energy intensive to manufacture, more so than the petrol vehicle, thus having a higher EE. A large contributing factor is the manufacturing of the large LIB packs, which as mentioned above have intensive mineral production processes among other high energetic costs during manufacture.

In Chapters 3 and 4, the structures of organic anode materials have been studied. Organic anode materials are of particular interest for the possibility that these materials present a more sustainable alternative to graphite in LIBs. Some of the issues with graphite have been presented previously, such as the pollution locally to graphite mines and high energetic costs. The decision to switch from graphite to a more environmentally friendly anode material may seem trivial, but defining what is truly more sustainable can be difficult. Organic anode materials, like many organic compounds usually come from a petrochemical feedstock, often the result of a byproduct. In this case it is probable that organic anode materials are in fact a more sustainable alternative, however not inherently sustainable themselves. This could present an example of where one scientific problem is solved, and in so doing creates another problem that future work will set out to solve, or within the MSF lexicon, to ‘kick the can down the road’. Some research efforts have sought to find ways of recycling waste petrochemical-based products, such as waste plastics into something of greater value. More specifically, waste polyethylene terephthalate (PET) can be recycled into terephthalic acid, one of the starting materials for an organic anode material. This can be achieved by several methods, utilising either a high temperature (and thus a high energetic cost) or with enzymes.[21-23] Utilising waste in this way is a central to the idea of ‘cradle-to-cradle’ manufacturing, a concept popularised by William McDonough. A key difference is noted that in future iterations of the idea, the products should in the first instance be designed to be recycled at their end-of-life, rather than recaptured from waste. Should interlinked cradle-to-cradle processes be interwoven across all industries, an almost utopian ideal of a truly circular economy can be imagined. In this utopic picture, nothing

is ever truly waste and products are repeatedly recycled and reused. This harnesses as much of the EE as is possible before returning the product back to the Earth to help with agriculture and leaving no EE locked in a persistent waste product in landfill. Of course, this ideal has two significant energetic flaws. The first, relates to the energetic losses that are inevitable with any conversion, whether that be energetic or material. Energy losses are certain when converting energy between forms, much like energetic losses are certain when recycling or converting objects or products between different uses. While savings to the quantity of energy lost during conversions through increased energy efficiency is preferable, resulting in cheaper products, this does not result in less energy being used. This is linked to Jevons Paradox, which states that when more efficient processes are in place, the usage of energy increases instead of decreases. More succinctly, if cheaper energy is available, the user will use what they can afford, even if that is more than what they need. The second flaw is much more fundamental, in that a truly idealist circular economy is forbidden under the laws of thermodynamics. The entropy of the universe is always increasing, with that, some energy is lost to the surroundings of any system. Of course, the first law of thermodynamics states that this energy is not destroyed. Therefore, this energy could be reharnessed once more, however the energy involved in reharnessing the lost energy would be greater than what could be regained, and thus a further increase in entropy. In acceptance of an imperfect circular economy, a measure exists which quantifies the energetic savings that can be made through conversion or manufacturing processes. This measure is the Energy Return on Investment (EROI), or more simply is the amount of energy that can be used as a ratio of the energy invested in creation. This is particularly pertinent to the global LIB or EV discussion, where a LIB that could deliver more energy with less energetic investment would surely be an attractive option compared to an alternative with a lower EROI.

1.4.2 Futures Thinking

When considering a technology such as the LIB, it is perhaps easy to appreciate some of the real-world impacts that research advancements can have. This advantage is due to the deep entanglement of the LIB with modern society, where the impacts of other chemical or material technologies may be somewhat more difficult to define. With such an important and widely used technology such as the LIB, any significant alteration in the technology toward any goal, is sure to cause wide-reaching effects throughout society and the environment. With the use of futures thinking methods, one can imagine some of the societal outcomes that may arise from these seemingly small and innocuous technological changes.

Futures thinking exercises surrounding the use of LIBs in EVs can reveal some interesting possible future scenarios. If organic anode materials became widely used in their current form inside of EV LIBs, the societal usage of the EV would be forced to change. Currently, LIBs with organic anode materials do not perform as well as current commercial

options using graphite. While the more sustainable choice, the way society interacts with a technology and the far-reaching effects this can have on society as a whole dictate the success of a technology. Or in other words, society would vote with their wallets as to which technology was preferable, the one with better performance, or the one with less environmental impacts. A lower performance battery in an EV would cause more frequent or longer-term charging. It would also require more frequent replacement of the battery, which comes with significant cost. Charge times and vehicle range are a still a barrier to large-scale uptake with the current commercialised batteries. Thus, for the lower performance battery to be successful, it may require a large scale infrastructural change. A greater abundance of charging opportunities would be required, this could come in the form of more chargers in parking bays, or one of the solutions that is already on trial such as converting existing street lighting into ubiquitous EV chargers. While more charging points enables more EVs to charge simultaneously, it does not solve the problem of range. It could be expected that the range limitation of EVs begins to limit the frequency of longer journeys undertaken. This may cause an affected population to begin relocating closer to city centres where there is proximity to employment opportunities, instead of moving away from cities into commuter suburbs. An alternative solution might involve the end of private ownership of EVs. In this scenario, a large fleet of EVs would need to be available for short-term or unidirectional rental. This is of course somewhat akin to the model of electric personal mobility vehicles such as scooters that have become a common occurrence in cities throughout the Global North in the last decade. From this illustration it is possible to envision how the seemingly small change of an anode material in a LIB could manifest in deciding where people choose to live and impact on the level of ownership of private vehicles.

Uncertainty axes are an alternative futures thinking tool that can shed light on some unforeseen scenarios. To use this tool, a matrix of two axes is created from two critical uncertainties related to the topic of choice. Prior to creating such axes, one should attempt to identify any potential biases by consideration of their own epistemology, that is the unique positionality of that person in the world made up of their unique lived experiences. To illustrate with the example of the LIB within the EV, the first axis is the uncertainty of whether LIB technology progresses to a level where cheap, abundant, and sustainable batteries are created. The second axis relates to how the price of oil and natural gas would change over time with efforts to lower fossil fuel consumption. The uncertainty axes are plotted below in Figure 1.4. Each segment of the grid then presents a future scenario pertaining to the conditions of the relative axes. To elaborate on scenario **B**, where fuel prices have increased alongside the failure of LIB technology to provide an affordable alternative. In this scenario, one could imagine that personal travel becomes somewhat more of a luxury, with private vehicle ownership impacted as the average person is unable to afford an EV or fuel for their petrol vehicles. Public

transportation would become essential in the interim, with a more large-scale population shift towards short distance travel for things such as entertainment, employment and essentials. Meanwhile, the scenario **A** is likely to be reminiscent of modern society, and with low fuel costs increasing usage as described by Jevons Paradox, accelerated greenhouse gas emissions and climate change could be expected. Alternatively, the opposite scenario, **D**, with higher fuel costs and affordable EVs, society is likely to rapidly uptake EVs, which overtime should reduce the impact of travel on the environment. However, in scenario **C**, with cheap fuel and cheap EVs, society is likely to choose the technology that most suits individual needs with both technologies widespread.

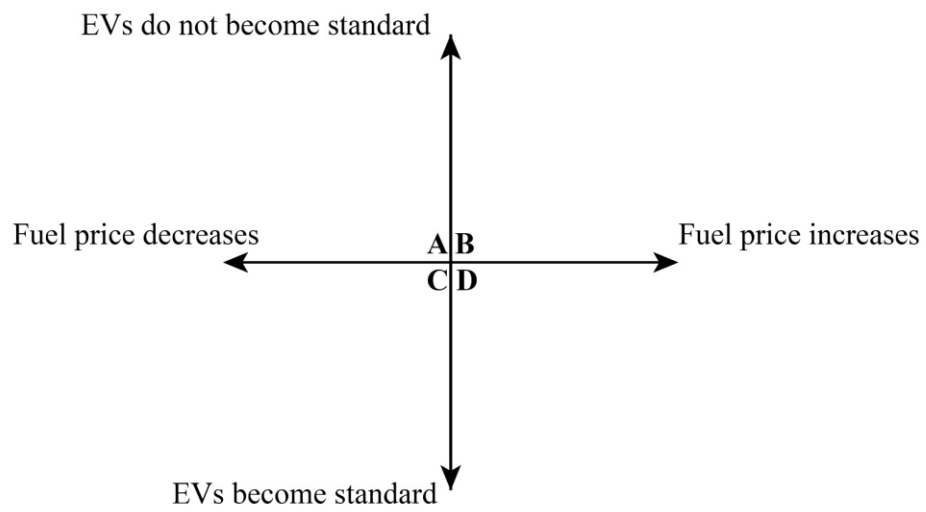

Figure 1.4 Uncertainty axes for future scenarios thinking, plotting uncertainty in the future price of vehicle fuel against the uncertainty in the success of LIB technology in the EV industry.

1.5 Thesis Summary

This thesis focuses on the use of Solid-state NMR spectroscopy to probe structure in a number of small organic functional molecules, specifically organic battery anode materials and organic ferroelectric materials. An introduction to these materials was given above along with a brief discussion of the applicability of NMR as a tool for their study. Chapter 2 features theoretical background to NMR spectroscopy including both the basic principles and relevant experimental methods. Furthermore, discussion of the basis and methods of X-ray Crystallography and DFT are also given in Chapter 2, due to the prevalence of these techniques within this work.

Results and discussion of the various materials studied within this thesis are presented in the chapters following. In Chapter 3, results are presented from the study of the pristine phases of six organic anode materials, along with investigation into hydration behaviours and

polymorphism in two of these materials. A detailed study of the applicability of NMR and DFT to the study of small organic materials is also presented. Chapter 4 is a progression onto the study of the reduced phases of two of the organic anode materials stemming from the use of chemical prelithiation as a non-electrochemical synthetic route. Discussion of the optimisation of this synthetic procedure is given along with a detailed study of predicted structures using *ab-initio* random structure searching to provide additional insights into structural changes within reduced organic anode materials. Chapter 5 presents the work studying the structural changes that accompany temperature driven phase transitions in a promising organic ferroelectric material, phenazine chloranilic acid. Alongside NMR studies, a systematic DFT study of supercell structure is presented in attempt to gain clarification on the hydrogen bond geometries within the structure which are important in defining phase and are the origin of ferroelectric behaviour.

1.6 References

1. A. Rawat, D. Kumar and B. S. Khati, *Journal of Water and Climate Change*, 2024, **15**, 104-126.
2. D. L. Williams, J. J. Byrne and J. S. Driscoll, *J. Electrochem. Soc*, 1969, **116**, 1-4.
3. M. S. Whittingham, *J. Chem. Soc. Chem. Commun.*, 1974, 328-329.
4. K. Mizushima, P. C. Jones, P. J. Wiseman and J. B. Goodenough, *Mater. Res. Bull.*, 1980, **15**, 783-789.
5. *United States Pat.*, 4,668,595A, 1986.
6. V. Petkov, A. Timmons, J. Camardese and Y. Ren, *J Phys Condens Matter*, 2011, **23**, 435003.
7. J. B. Goodenough and K. S. Park, *J Am Chem Soc*, 2013, **135**, 1167-1176.
8. Y. Liang, Z. Tao and J. Chen, *Advanced Energy Materials*, 2012, **2**, 742-769.
9. T. C. Frankel, Cobalt mining for lithium ion batteries has a high human cost - Washington Post, https://www.washingtonpost.com/graphics/business/batteries/congo-cobalt-mining-for-lithium-ion-battery/ (Accessed 9 January 2020).
10. A. D. Jara, A. Betemariam, G. Woldetinsae and J. Y. Kim, *International Journal of Mining Science and Technology*, 2019, **29**, 671-689.
11. P. Whoriskey, China pollution caused by graphite mining for smartphone battery - Washington Post, https://www.washingtonpost.com/graphics/business/batteries/graphite-mining-pollution-in-china/, (accessed 15 January 2020).
12. H. Marsh and F. Rodriguez-Reinoso, *Activated Carbon*, Elsevier Science Ltd, 2006.
13. C. K. Chan, H. Peng, G. Liu, K. McIlwrath, X. F. Zhang, R. A. Huggins and Y. Cui, *Nat Nanotechnol*, 2008, **3**, 31-35.
14. T. Le Gall, K. H. Reiman, M. C. Grossel and J. R. Owen, *Journal of Power Sources*, 2003, **119-121**, 316-320.

15. W. Walker, S. Grugeon, H. Vezin, S. Laruelle, M. Armand, J. M. Tarascon and F. Wudl, *Electrochemistry Communications*, 2010, **12**, 1348-1351.

16. H. Numazawa, K. Sato, H. Imai and Y. Oaki, *NPG Asia Materials*, 2018, **10**, 397-405.

17. H. Chen, M. Armand, G. Demailly, F. Dolhem, P. Poizot and J. M. Tarascon, *ChemSusChem*, 2008, **1**, 348-355.

18. M. Armand, S. Grugeon, H. Vezin, S. Laruelle, P. Ribiere, P. Poizot and J. M. Tarascon, *Nat Mater*, 2009, **8**, 120-125.

19. J. A. Kaduk, *Acta Crystallogr. Sect. B Struct. Sci.*, 2000, **56**, 474-485.

20. Y.-Y. Liu, J. Zhang, L.-X. Sun, F. Xu, W.-S. You and Y. Zhao, *Inorganic Chemistry Communications*, 2008, **11**, 396-399.

21. D. Senthil Raja, C.-C. Pan, C.-W. Chen, Y.-H. Kang, J.-J. Chen and C.-H. Lin, *Microporous and Mesoporous Materials*, 2016, **231**, 186-191.

22. H. Lu, D. J. Diaz, N. J. Czarnecki, C. Zhu, W. Kim, R. Shroff, D. J. Acosta, B. R. Alexander, H. O. Cole, Y. Zhang, N. A. Lynd, A. D. Ellington and H. S. Alper, *Nature*, 2022, **604**, 662-667.

23. S. Ghosh, M. A. Makeev, Z. Qi, H. Wang, N. N. Rajput, S. K. Martha and V. G. Pol, *ACS Sustainable Chemistry & Engineering*, 2020, **8**, 6252-6262.

24. A. E. Lakraychi, F. Dolhem, F. Djedaïni-Pilard, A. Thiam, C. Frayret and M. Becuwe, *Journal of Power Sources*, 2017, **359**, 198-204.

25. S. Renault, V. A. Oltean, M. Ebadi, K. Edström and D. Brandell, *Solid State Ionics*, 2017, **307**, 1-5.

26. Y. Park, D. S. Shin, S. H. Woo, N. S. Choi, K. H. Shin, S. M. Oh, K. T. Lee and S. Y. Hong, *Adv Mater*, 2012, **24**, 3562-3567.

27. L. Zhao, J. Zhao, Y.-S. Hu, H. Li, Z. Zhou, M. Armand and L. Chen, *Advanced Energy Materials*, 2012, **2**, 962-965.

28. C. Wang, Y. Xu, Y. Fang, M. Zhou, L. Liang, S. Singh, H. Zhao, A. Schober and Y. Lei, *J. Am. Chem. Soc.*, 2015, **137**, 3124-3130.

29. N. Ogihara, T. Yasuda, Y. Kishida, T. Ohsuna, K. Miyamoto and N. Ohba, *Angew Chem Int Ed Engl*, 2014, **53**, 11467-11472.

30. T. Yasuda and N. Ogihara, *Chem Commun (Camb)*, 2014, **50**, 11565-11567.

31. N. Ogihara, N. Ohba and Y. Kishida, *Sci. Adv.*, 2017, **3**, 1-10.

32. L. Fédèle, F. Sauvage, J. Bois, J.-M. Tarascon and M. Bécuwe, *Journal of The Electrochemical Society*, 2013, **161**, A46-A52.

33. X. Han, C. Chang, L. Yuan, T. Sun and J. Sun, *Advanced Materials*, 2007, **19**, 1616-1621.

34. X. Han, G. Qing, J. Sun and T. Sun, *Angew Chem Int Ed Engl*, 2012, **51**, 5147-5151.

35. L. Fédèle, F. Sauvage and M. Bécuwe, *J. Mater. Chem. A*, 2014, **2**, 18225-18228.

36. L. Fédèle, F. Sauvage, S. Gottis, C. Davoisne, E. Salager, J.-N. Chotard and M. Becuwe, *Chemistry of Materials*, 2017, **29**, 546-554.

37. W. X. Zhou and A. Ariando, *Japanese Journal of Applied Physics*, 2020, **59**.

38. S. I. Shkuratov and C. S. Lynch, *Journal of Materiomics*, 2022, **8**, 739-752.

39. S. Horiuchi and Y. Tokura, *Nature Materials*, 2008, **7**, 357-366.

40. S. Horiuchi, R. Kumai and Y. Tokura, *J Am Chem Soc*, 2005, **127**, 5010-5011.

41. R. Kumai, S. Horiuchi, H. Sagayama, T. Arima, M. Watanabe, Y. Noda and Y. Tokura, *J Am Chem Soc*, 2007, **129**, 12920-12921.

42. K. Gotoh, T. Asaji and H. Ishida, *Acta Crystallogr C*, 2007, **63**, o17-20.

43. L. Noohinejad, S. Mondal, S. I. Ali, S. Dey, S. van Smaalen and A. Schonleber, *Acta Crystallogr B Struct Sci Cryst Eng Mater*, 2015, **71**, 228-234.

44. L. Noohinejad, S. Mondal, A. Wölfel, S. I. Ali, A. Schönleber and S. van Smaalen, *Journal of Chemical Crystallography*, 2014, **44**, 387-393.

45. Statistical Review of World Energy, energyinst.org/statistical-review, (accessed 31st October 2023).

Chapter 2

Background & Experimental Methods

2.1 Theory of Nuclear Magnetic Resonance (NMR)

2.1.1 Nuclear Spin

Nuclei have an intrinsic property known as spin, which is a form of angular momentum. Spin can be represented as a vector, $\boldsymbol{I}$, with magnitude

$$|\boldsymbol{I}| = \hbar\sqrt{I(I+1)}\ , \tag{2.1}$$

where I is the corresponding spin quantum number and can take the form of zero, half-integer or integer (I = 0, 1/2, 1, 3/2, 2…), and $\hbar$ is the reduced Planck constant. For a nucleus to be NMR active it must have $I > 0$. The projection of the angular momentum vector on to an arbitrarily chosen z-axis corresponds to the magnetic quantum number, m_I, which has $2I + 1$ values, or spin states, ranging from $+I$ to $-I$ (*e.g.*, if I = 2, then $m_\mathrm{I} = -2, -1, 0, 1, 2$). The angular momentum along the z-axis is given by

$$I_\mathrm{z} = m_\mathrm{I}\hbar\ . \tag{2.2}$$

The magnetic moment, $\boldsymbol{\mu}$, of a nucleus relates the spin angular momentum with the gyromagnetic ratio, γ, according to

$$\boldsymbol{\mu} = \gamma\boldsymbol{I}\ . \tag{2.3}$$

When no external magnetic field is applied, the $2I + 1$ spin states are degenerate in energy. When a magnetic field, B_0, is applied, the degeneracy of the spin states is lifted by the Zeeman interaction. Figure 2.1 shows the Zeeman splitting of spin states for spin I = 1/2, 1 and 3/2 nuclei. Application of the field along the z-axis results in energies of the spin states given by

$$E_{|m_\mathrm{I}\rangle} = -\mu_\mathrm{Z}B_0 = -m_\mathrm{I}\hbar\gamma B_0\ . \tag{2.4}$$

Observable transitions are limited by the quantum selection rule

$$\Delta m_\mathrm{I} = \pm 1\ , \tag{2.5}$$

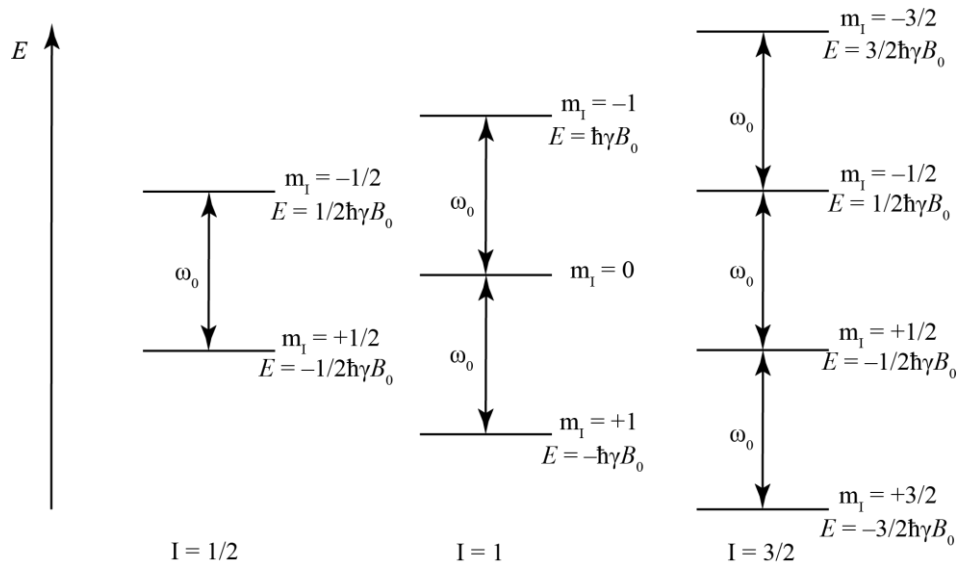

Figure 2.1 Effect of Zeeman interaction on energy levels for spin $I = 1/2$, $I = 1$ and $I = 3/2$ nuclei. Diagram is based on a nucleus with a positive gyromagnetic ratio, where a nucleus with a negative gyromagnetic ratio would invert the sign of the spin state energy.

which results in transitions with frequency given by

$$\omega_0 = \frac{\Delta E}{\hbar} = -\gamma B_0 \,, \tag{2.6}$$

where ω_0 is the Larmor frequency in rad s^{-1}. In an NMR experiment, electromagnetic radiation is used to induce transitions between the Zeeman energy levels. The required frequency of the radiation depends on the γ of the nuclei of interest and the magnetic field strength, B_0. For the field strengths typically used in NMR experiments (several Tesla), the resulting Larmor frequency of most nuclei is usually in the radiofrequency (rf) regime, therefore rf pulses are typically used in order to be on resonance with the spins in the sample.

In a bulk sample, the magnetic moments of all the nuclei will average in the absence of an external magnetic field, resulting in zero net magnetization. Application of an external field will cause spins to occupy the available Zeeman energy levels. Individual spins however do not align with the field, instead they freely precess around the applied field. For an $I = 1/2$ nucleus there are two Zeeman energy levels with energies given by Equation 2.4, where the α energy level relates to the spin with quantum number −1/2, and the β energy level relates to the spin with quantum number +1/2. The α energy level has energy equal to $-1/2\ \hbar\ \gamma\ B_0$ while the β energy level has energy equal to $+1/2\ \hbar\ \gamma\ B_0$. The population of these energy levels is given by the Boltzmann distribution

$$\frac{N_\alpha}{N_\beta} = e^{\frac{-\Delta E}{k_B T}} \,, \tag{2.7}$$

where N_α and N_β are the populations of nuclei in the α and β energy states, ΔE is the energy difference between the spin states and k_B is the Boltzmann constant. For example, a ^{1}H atom in a magnetic field of 9.4 T will have an energy difference between Zeeman energy levels of

$$\Delta E = -\gamma B_0 \hbar \,, \tag{2.8}$$

$$-2.675 \times 10^8 \text{ rad T}^{-1}\text{s}^{-1} \times 9.4 \text{ T} \times \frac{6.626\times10^{-34} \text{ Js}}{2\pi} = -2.62 \times 10^{-24} \text{ J} \,, \tag{2.9}$$

which can be used to calculate the population difference at 298 K,

$$\frac{N_\alpha}{N_\beta} = \text{e}^{\frac{-\Delta E}{k_B T}} = \text{e}^{\frac{-2.62\times10^{-24}\text{ J}}{1.38\times10^{-23}\text{JK}^{-1}\times 298\text{ K}}} = 0.9993631053 \,. \tag{2.10}$$

This difference in population is around 64 spins per 200,000 spins, where for every 100,000 in the α state, there are 99,936 in the β state. The small population difference means NMR has relatively low sensitivity compared with other spectroscopic techniques such as infrared or UV-vis where the ratio of states approaches 0:1 at ambient temperature. The population difference of NMR results in a net difference in the number of spins with a +*z* or −*z* component, where *z* is defined by the applied field, B_0. There is therefore a bulk magnetization, represented by a vector, $\mathbf{M_0}$, aligned with the field, however there is no coherence between spins in the *x*- or *y*- dimensions at thermal equilibrium. At constant magnetic field, the population difference and therefore the magnitude of $\mathbf{M_0}$ is larger for high-γ nuclei (*e.g.*, ^{1}H), conversely for a given nucleus, the magnitude of $\mathbf{M_0}$ will increase with increased field strength. The population difference also depends on temperature, Figure 2.2 shows the effect of temperature on the population difference for a ^{1}H atom in a 9.4 T magnetic field. At room temperature the

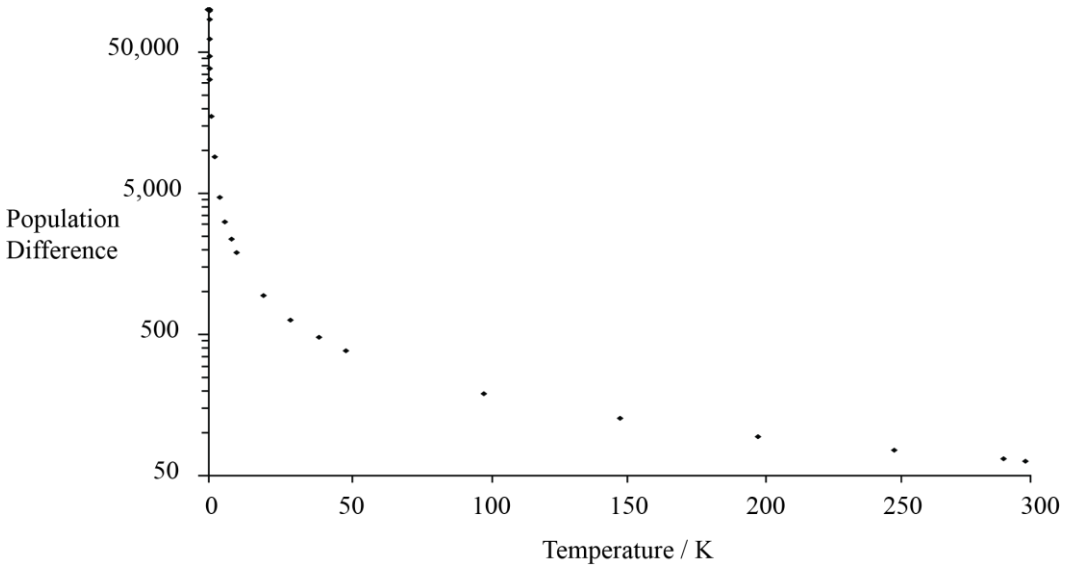

Figure 2.2 Effect of temperature on the population difference between Zeeman energy levels a ^{1}H nucleus in a 9.4 T magnetic field. Population difference plotted as $N_\beta - N_\alpha$.

population difference is small and only increases slowly until the temperature is reduced below approximately 20 K, with only large population differences achieved in the region of < 1 K.

2.1.2 The Vector Model

During NMR experiments nuclear spins can be described by the vector model. In an external magnetic field, the bulk magnetization caused by the Zeeman interaction will align with the field. The direction of the magnetic field is by convention considered the *z*-axis of the laboratory frame. However, it is more convenient to use the rotating frame as an alternative reference frame where the bulk magnetization precesses at a frequency, ω_{rf}, around B_0, shown in Figure 2.3. The rf coil applies a pulse with frequency ω_{rf} in the transverse plane, where the oscillating magnetic component of the electromagnetic wave can be considered as a rotating magnetic field and thus appears as the static field B_1. The bulk magnetization will then precess around B_1 at the nutation frequency, ω_1, given by

$$\omega_1 = -\gamma B_1. \tag{2.11}$$

The pulse, with magnetic field strength B_1, interacts with the spins in the sample and causes the bulk magnetization to nutate through a flip angle, β, away from the *z*-axis which is given by

$$\beta = \gamma B_1 \tau_p\,, \tag{2.12}$$

where τ_P is the pulse duration. At this point, if the pulse is on resonance, that is when

$$\omega_0 = \omega_{rf}\,, \tag{2.13}$$

then the bulk magnetization will appear static in the rotating frame. However, if the pulse is not exactly on resonance, then the frequency offset, Ω, describes the slow precession of the magnetization in the rotating frame and is the difference between the rotation frequency of the rotating frame and the Larmor frequency, where

$$\Omega = \omega_0 - \omega_{rf}\,. \tag{2.14}$$

The same rf coil that delivers the rf pulse then detects an induced current as the magnetization relaxes back to alignment with the external field, B_0.

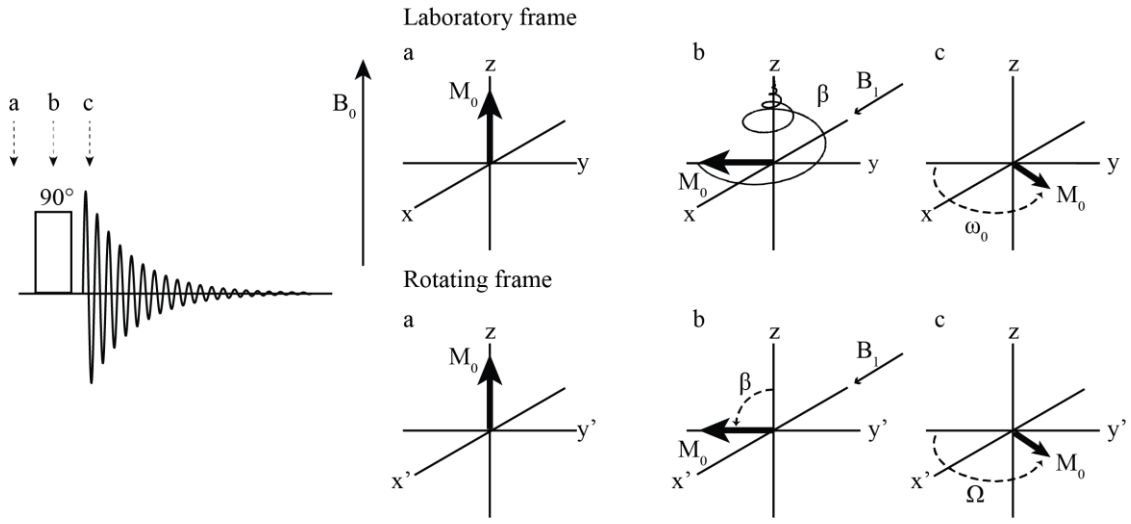

Figure 2.3 Schematic depiction of the result of an rf pulse on bulk magnetization in the laboratory and rotating frames at different points in time. x' and y' are the axes of the rotating frame such that the axis system rotates about the *z*-axis at the Larmor frequency. Diagram not to scale.

2.1.3 Relaxation

During an NMR experiment, relaxation processes occur in the time following an rf pulse. There are two mechanisms of relaxation which occur simultaneously and pertain to different components of the magnetization. The first is longitudinal relaxation, which is the relaxation of *z*-component of the magnetization following an rf pulse, back to thermal equilibrium where the bulk magnetization, $\mathbf{M_0}$, is aligned with the applied field, B_0. Longitudinal relaxation is characterised by an exponential time constant T_1,

$$M_z(t) - \mathbf{M_0} = [M_z(0) - \mathbf{M_0}]e^{\frac{-t}{T_1}}, \tag{2.15}$$

where $M_z(0)$ is the *z*-component of magnetization following an rf pulse.

The other relaxation mechanism is transverse relaxation, which is the evolving decoherence of spins precessing in the *xy*-plane, as shown in Figure 2.4. A given spin will experience a unique local magnetic field which will uniquely perturb its Larmor frequency, and in turn drives decoherence within the spin system as different spins will precess at slightly different frequencies. Transverse relaxation occurs over a time period T_2, during which the magnitude of $\mathbf{M_0}$ in the *xy*-plane decays resulting from the loss of coherence as the spins precess. Loss of signal via T_2 relaxation can be described by an exponential decay,

$$M_{xy} = \mathbf{M_0} e^{\left(\frac{-t}{T_2}\right)}, \tag{2.16}$$

where M_{xy} is the magnitude of the magnetization in the *xy*-plane.

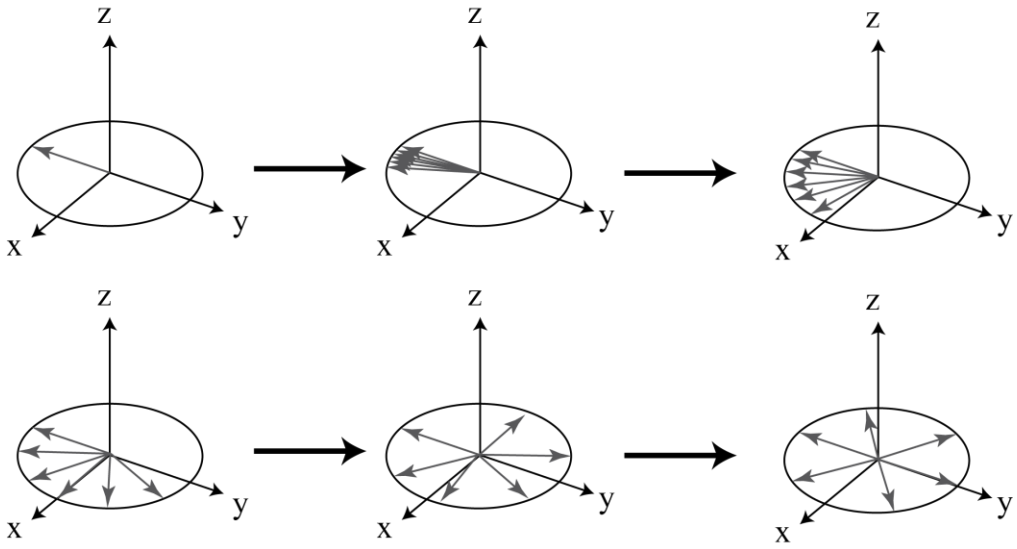

Figure 2.4 Progression of magnetization decoherence in the *xy*-plane.

As the magnetization precesses and undergoes transverse relaxation in the *xy*-plane, a single detector would not be able to distinguish if precession was occurring clockwise or anti-clockwise. To overcome this, quadrature detection is used.[1] This is analogous to using two detectors that are separated by 90° in the rotating frame, but is actually achieved by phase shifting the receiver reference frequency. Detection of the two orthogonal signals affords the ability to elucidate phase and results in a precise spectrum. The decaying signal detected in the rf coil is termed the free induction decay (FID). Detection of the decaying transverse magnetization as a function of time is mathematically transformed into the frequency domain using a Fourier Transform (FT) as shown in Figure 2.5.[2] The time domain signal is complex and is comprised of a real and imaginary component corresponding to the *x*- and *y*- components. In the frequency domain, the signal still has both a real and imaginary component, where the real part is absorptive and the imaginary is dispersive. The real part of a spectrum has an absorptive line with a Lorentzian character. The lineshape has a full width at half maximum (FWHM) of

$$FWHM = \frac{1}{\pi T_2}, \tag{2.17}$$

which means broader lineshapes are a result of faster decay of the FID.

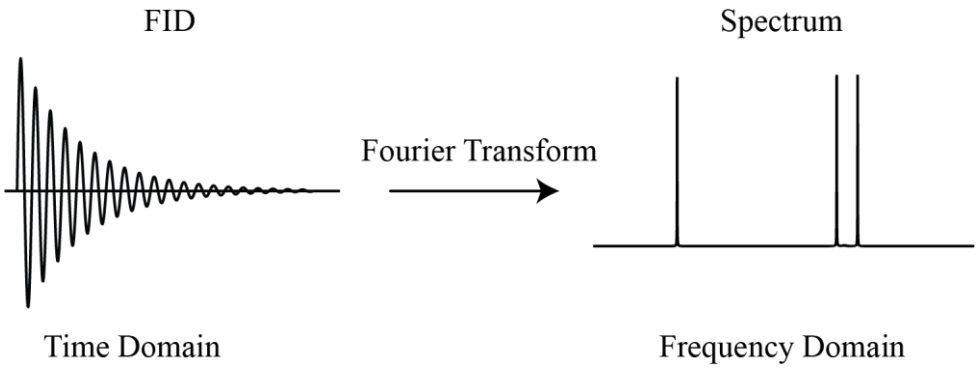

Figure 2.5 A Fourier transform of an FID in the time domain giving an NMR spectrum in the frequency domain. FID is for illustration only.

While it is T_2 that is measured in the form of FID, in solids T_1 dictates the frequency at which NMR experiments can be repeated as $T_1 > T_2$. In an optimised experiment where the length of the acquisition time is roughly equal to T_2, the FID will decay to zero before the magnetization has returned to equilibrium. Therefore, it is necessary to wait until this relaxation process is completed before applying further pulses, with this delay period known as the *recycle interval*. Repetition of experiments is necessary to improve sensitivity, where each collected FID is added to the sum of all the previous FIDs. The magnitude of the signal is then proportional to the number of scans, or transients, completed. Conversely, the random noise only increases equal to the square root of the number of transients, and so with more repetitions of the experiment, a higher signal-to-noise (S/N) ratio can be achieved. In some cases, S/N ratio is not the only consideration, for example when an experiment is to be quantitative. If the recycle delay chosen in this experiment is too short, *i.e.*, the subsequent pulse is applied before M_z recovers to M_0, the amount of signal the pulse generates will be reduced. Alternatively, an excessive recycle delay can lead to wasted spectrometer time. The required recycle interval for a quantitative experiment is equal to five periods of T_1, which recovers 99.3% of signal, while for optimal S/N ratio with respect to spectrometer time is equal to 1.25 periods of T_1. Cross Polarisation (CP) experiments (discussed later in Section 2.2.2) are common non-quantitative experiments, where the main consideration is the S/N ratio, and not ensuring complete T_1 relaxation occurs.

2.1.4 Two-Dimensional NMR

Two-dimensional (2D) experiments can give additional information on through-bond or through-space proximities than is possible with one-dimensional experiments. 2D experiments generally follow a procedure of a preparation, evolution, mixing and acquisition steps. Magnetization is created during the preparation step and is allowed to evolve for a time, t_1, before the mixing step transfers magnetization between spins. Acquisition of the FID then occurs during t_2, with the amplitude modulating according to the evolution of t_1. Subsequent

incremental increase of the t_1 time period and acquisition is completed before FT in both dimensions, as follows

$$S(t_1 t_2) \xrightarrow{\text{FT along } t_2} S(t_1 \omega_2) \xrightarrow{\text{FT along } t_1} S(\omega_1 \omega_2)\,. \tag{2.18}$$

Due to this, 2D experiments can take a long time to acquire (sometimes multiple days) as the experiment repeats with incremental increases to t_1, and so are relatively expensive experiments to complete.

2.1.5 NMR Interactions

The Zeeman interaction is generally the dominant interaction in NMR experiments, but a number of smaller interactions can exist between spins and other spins, and between spins and their environments. The arrangement of atoms and nuclei within a sample leads nuclei to experience other magnetic and electric fields which provide information about local structure. The interactions experienced by a given nucleus can be described by its Hamiltonian, $\hat{H}$, which is a combination of Hamiltonians,

$$\hat{H} = \hat{H}_{\mathrm{Z}} + \hat{H}_{\mathrm{RF}} + \hat{H}_{\mathrm{CS}} + \hat{H}_{\mathrm{D}} + \hat{H}_{\mathrm{Q}} + \hat{H}_{\mathrm{J}}\,. \tag{2.19}$$

Here $\hat{H}_{\mathrm{Z}}$ is the Hamiltonian describing the Zeeman interaction, $\hat{H}_{\mathrm{RF}}$ is the Hamiltonian describing the interaction of spins with the applied rf pulse, $\hat{H}_{\mathrm{CS}}$ is the chemical shielding Hamiltonian, $\hat{H}_{\mathrm{D}}$ is the dipolar Hamiltonian, $\hat{H}_{\mathrm{Q}}$ is the quadrupolar Hamiltonian and $\hat{H}_{\mathrm{J}}$ is the Hamiltonian describing scalar coupling (J-coupling). While the magnitudes of NMR interactions can vary significantly depending on the system and local structure, the typical magnitudes of these NMR interactions are compared to the Zeeman interaction in Table 2.1.

Table 2.1 Typical magnitudes of some key NMR interactions compared to the Zeeman interaction. Magnitudes given in Hz.

NMR Interaction	Typical magnitude (Hz)
Zeeman interaction	10^7 - 10^8
Quadrupolar coupling	10^5 – 10^7
Chemical shift	10^3 – 10^5
Dipolar coupling	10^2 – 10^4
Scalar coupling	1 – 10^2

In general, each of the NMR interactions mentioned above can be described by a second-rank tensors with both a magnitude and orientation relative to the magnetic field. Interactions can be described within either the laboratory frame or the principal axis system (PAS), which are two frames related by rotation (Figure 2.6). In the laboratory frame, the *z*-axis is aligned with the applied magnetic field with the interaction tensor external to the defined axes. In contrast, the PAS *z*-axis is aligned with the largest component of the interaction tensor. It is convenient to use the PAS to define interaction parameters and the laboratory frame to understand angular dependence with respect to the external magnetic field for a given crystallite.

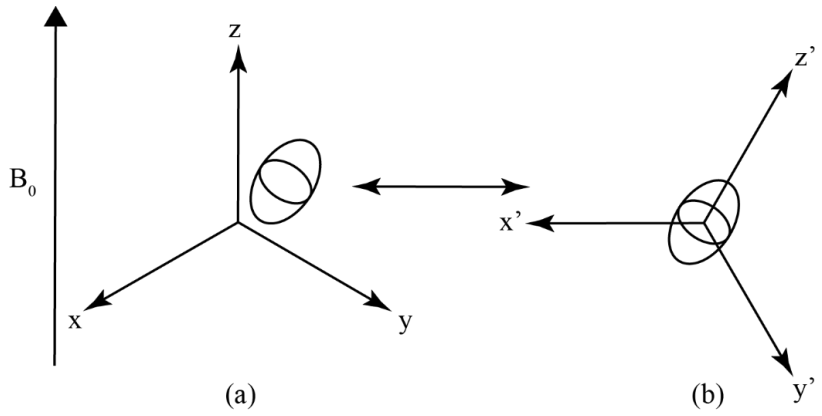

Figure 2.6 Schematic of the laboratory frame (a) and the principal axis system (PAS) (b). The interaction tensor is represented as an ellipsoid where the interactions principal axes are synonymous with the principal axes.

Chemical Shift

The chemical shift, δ, is the difference between resonance frequencies of the nucleus (ω) and a reference frequency (ω_{ref})[3] and can be defined as

$$\delta = 10^6 \frac{(\omega_0 - \omega_{ref})}{\omega_{ref}}. \quad (2.20)$$

The reference frequency is that of a known reference sample selected for each nucleus (*e.g.*, tetramethylsilane (TMS) for ^{13}C). Chemical shift is a dimensionless deshielding parameter usually expressed in parts per million (ppm) due to its typically low nominal value. Deshielding is the result of nuclei experiencing a slightly augmented applied magnetic field due to local magnetic fields of nearby nuclei. The inverse is also true, where shielding is the result of a slightly diminished magnetic field experienced by nuclei. The augmented or diminished magnetic field experienced by the nucleus is called the effective field, B_{eff}, and is given by

$$B_{eff} = (1 - \sigma) B_0 , \quad (2.21)$$

where σ is the absolute chemical shielding parameter. Shielding and deshielding are perturbations to the Zeeman energy levels and therefore perturbations of the Larmor frequency. The perturbed Larmor frequency, ω_0', is given by

$$\omega_0' = -\gamma B_0(1-\sigma)\,. \tag{2.22}$$

Assuming $\sigma << 1$, then δ and σ can be approximated by

$$\delta = 10^6 \frac{(\sigma_{\mathrm{ref}} - \sigma)}{(1-\sigma_{\mathrm{ref}})} \approx 10^6(\sigma_{\mathrm{ref}} - \sigma)\,. \tag{2.23}$$

Absolute chemical shielding is dependent on field strength and as such it is convention to consider chemical shift. By convention, NMR spectra are plotted such that δ increases from right to left, where more shielded nuclei appear on the right.

Chemical Shielding Anisotropy

The local electronic environment of a given nucleus is rarely spherical, and as such gives rise to chemical shielding anisotropy (CSA). Chemical shielding is orientation dependent and varies with respect to the orientation of the applied magnetic field, B_0. The chemical shift tensor is described by three principal components, which are given by the Standard convention as

$$\delta_{11} \geq \delta_{22} \geq \delta_{33}\,, \tag{2.24}$$

where δ_{iso} is the average isotropic chemical shift

$$\delta_{\mathrm{iso}} = \frac{\delta_{11} + \delta_{22} + \delta_{33}}{3}, \tag{2.25}$$

and is the centre of gravity of the lineshape. The shielding tensor in the PAS, σ^{PAS}, can be described by a diagonal matrix:

$$\sigma^{\mathrm{PAS}} = \begin{pmatrix} \sigma_{11} & 0 & 0 \\ 0 & \sigma_{22} & 0 \\ 0 & 0 & \sigma_{33} \end{pmatrix}, \tag{2.26}$$

where σ_{11}, σ_{22} and σ_{33} are the three principal components of the tensor as shown by Figure 2.7.

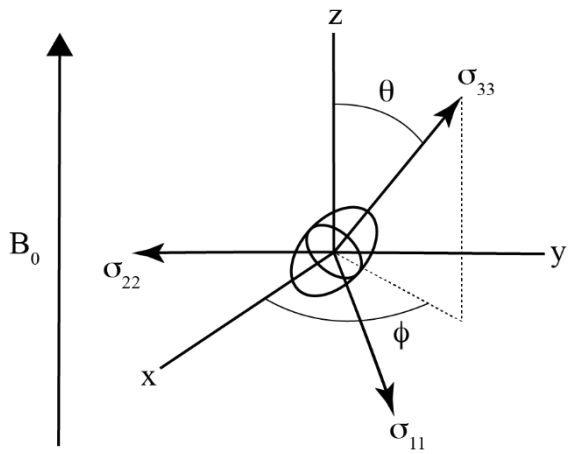

Figure 2.7 Schematic of the chemical shielding tensor, with the three principal components of the principal axis system defined as σ_{11}, σ_{22} and σ_{33}. θ and Φ are angles defining the orientation of the tensor with respect to B_0.

The shielding parameter can then be described by the isotropic chemical shift, δ_{iso}, the chemical shielding anisotropy, $\Delta\delta_{CS}$, and the asymmetry parameter, η_{CS}.

$$\Delta\delta_{CS} = (\delta_{33} - \delta_{iso}) \tag{2.27}$$

$$\eta_{CS} = \frac{(\delta_{22} - \delta_{11})}{(\delta_{33} - \delta_{iso})} \tag{2.28}$$

For simplicity, the observed chemical shift for a particular tensor orientation is given using spherical coordinates by

$$\delta = \delta_{iso} + \left(\frac{\Delta\sigma_{CS}}{2}\right)[(3\cos^2\theta - 1) + \eta_{CS} \times (\sin^2\theta \times \cos 2\Phi)], \tag{2.29}$$

where θ and Φ are angles that define the relative orientation of the tensor to the external magnetic field. This means that each possible orientation of the tensor will result in a different observed chemical shift. In powdered samples that comprise many crystals each with a random orientation relative to the external magnetic field, a continuum of chemical shifts is observed. The spectrum would then feature a broad powder pattern lineshape that is characteristic of $\Delta\delta_{CS}$ and η_{CS} as shown in Figure 2.8 by simulated lineshapes created using the SIMPSON program.[4]

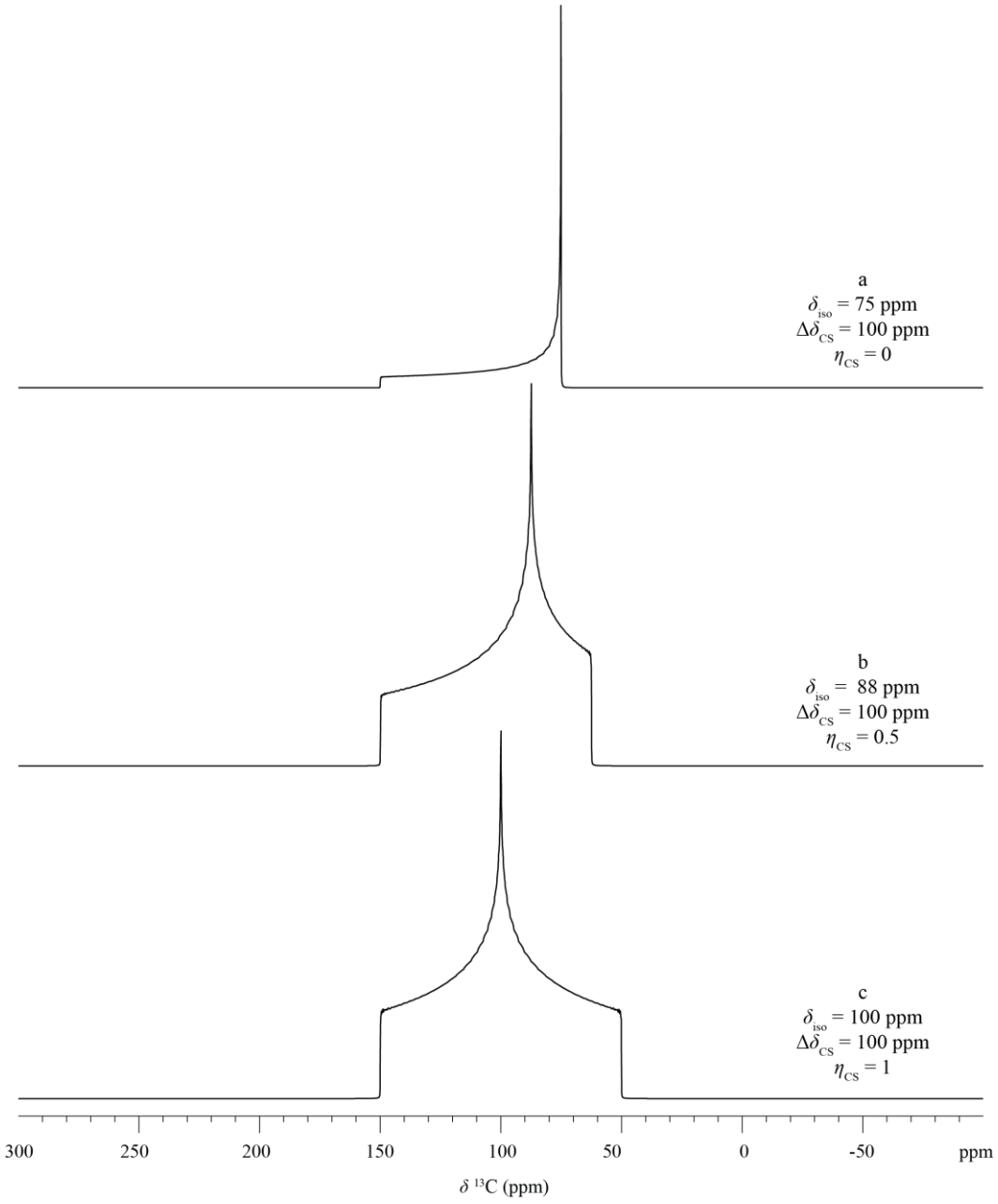

Figure 2.8 Simulated ^{13}C powder patterns for a spin I = 1/2 nucleus at varying asymmetry parameter, η_{CS}, values (a = 0, b = 0.5 and c = 1).

Dipolar Coupling

Dipolar coupling is a through space interaction where the magnetic moments of nearby nuclei interact. In solids, dipolar coupling is a major source of broadening which has a dipolar splitting parameter ω_D,[5]

$$\omega_D = \omega_D^{PAS} \frac{1}{2}(3\cos^2\theta - 1), \quad (2.30)$$

where θ is the angle between the applied magnetic field and the internuclear interaction and ω_D^{PAS} is the dipolar coupling constant in the PAS,

$$\omega_{\mathrm{D}}^{\mathrm{PAS}} = -\hbar\left(\frac{\mu_0}{4\pi}\right)\frac{1}{r^3}\gamma_{\mathrm{I}}\gamma_{\mathrm{S}}\,. \tag{2.31}$$

where r is the internuclear distance, μ_0 is the permeability of a vacuum and γ_I and γ_S are the gyromagnetic ratios of the two individual spins labelled I and S, as shown in Figure 2.9.

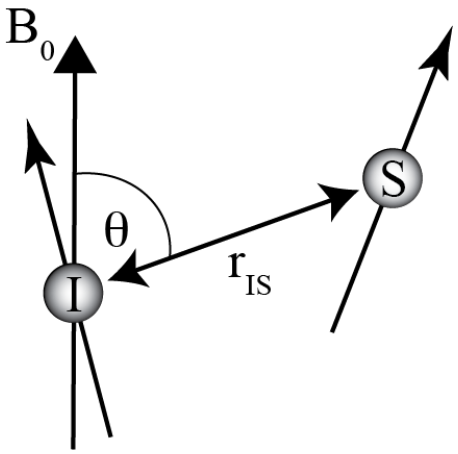

Figure 2.9 Schematic showing the dependencies of dipolar coupling, where θ is the angle of the internuclear interaction, r_{IS}, relative to B_0. Diagram not to scale.

Dipolar coupling manifests in an NMR spectrum in the form of splitting. For a spin I = 1/2 nucleus, each resonance is split into a doublet separated by $2\omega_D$ in heteronuclear dipolar coupling (where I ≠ S), and $3\omega_D$ in homonuclear dipolar coupling (where I = S). Due to the orientation dependence, the dipolar splitting also depends on the angle between the magnetic field and the internuclear interaction. In an isolated spin-pair, variation of this angle in powdered crystalline samples gives a "Pake-doublet" lineshape, as shown in Figure 2.10a. However, this is not commonly observed as generally there are many spins exhibiting dipolar coupling, which results in Gaussian broadening, as shown in Figure 2.10b, making the extraction of relevant structural information challenging.

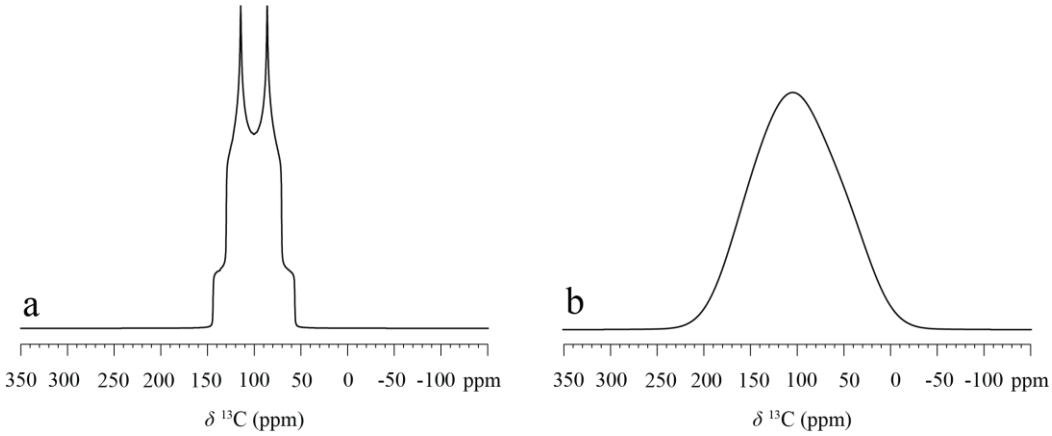

Figure 2.10 Simulated ^{13}C powder lineshapes of an isolated spin pair (a) and many spin pairs (b) illustrating the effects of dipolar broadening.

Quadrupolar Coupling

Any nucleus with $I > 1/2$ (*e.g.*, ^{2}H, ^{7}Li, ^{23}Na) has an electric quadrupole moment (EQM). The EQM arises from non-spherical charge distribution at the nucleus and interacts with the electric field gradient (EFG) at the nucleus. The EFG is generated by nearby electron density and the magnitude of the EFG along with the magnitude of the EQM dictate the strength of the quadrupolar interaction. The EFG is described as a tensor with three principal values V_{XX}, V_{YY} and V_{ZZ}, which by convention are described $|V_{ZZ}| \geq |V_{YY}| \geq |V_{XX}|$. The quadrupolar coupling constant, C_Q, and the asymmetry parameter, η_Q, values specify the EFG of a given nucleus. The largest principal value of the EFG, V_{ZZ}, is equal to the electric quadrupole moment,

$$V_{ZZ} = eq. \tag{2.32}$$

which is a constant for each nucleus. The value of η_Q is limited to

$$1 \geq \eta_Q \geq 0\,, \tag{2.33}$$

and is given by

$$\eta_Q = \frac{V_{XX} - V_{YY}}{V_{ZZ}}\,. \tag{2.34}$$

The magnitude of the quadrupolar interaction is given by C_Q, and is given by

$$C_Q = \frac{eqeQ}{h} = \frac{e^2qQ}{h} = \frac{eQV_{ZZ}}{h}, \tag{2.35}$$

where eQ is the EFG at the nucleus and Q is the nuclear quadrupole moment.

The quadrupolar interaction perturbs the Zeeman energy levels such that the transitions are no longer degenerate (Figure 2.11). To a first-order approximation, the central transition (CT) is unaffected, while the energy levels associated with satellite transitions (ST) are shifted. This results in $2I$ transitions that are equally perturbed by $2\omega_Q$, where ω_Q is the quadrupolar splitting parameter in rad s^{-1}. In the laboratory frame the first-order quadrupolar interaction, $\omega_Q^{(1)}$, is given by

$$\omega_Q^{(1)} = \omega_Q^{PAS} \times \frac{1}{2}\left(3\cos^2\theta - 1 + \eta_Q \sin^2\theta \times \cos^2\Phi\right), \tag{2.36}$$

where θ and Φ are angles relating B_0 to the PAS and ω_Q^{PAS} is the quadrupolar splitting parameter in the PAS, given by

$$\omega_Q^{PAS} = \frac{3\pi C_Q}{2I(2I-1)}, \tag{2.37}$$

C_Q is the quadrupolar coupling constant and η_Q is the quadrupolar asymmetry parameter. While for half-integer nuclei the CT is unaffected, for nuclei with integer spin no CT exists, and as such the only resonances are ST and are dependent on ω_Q.

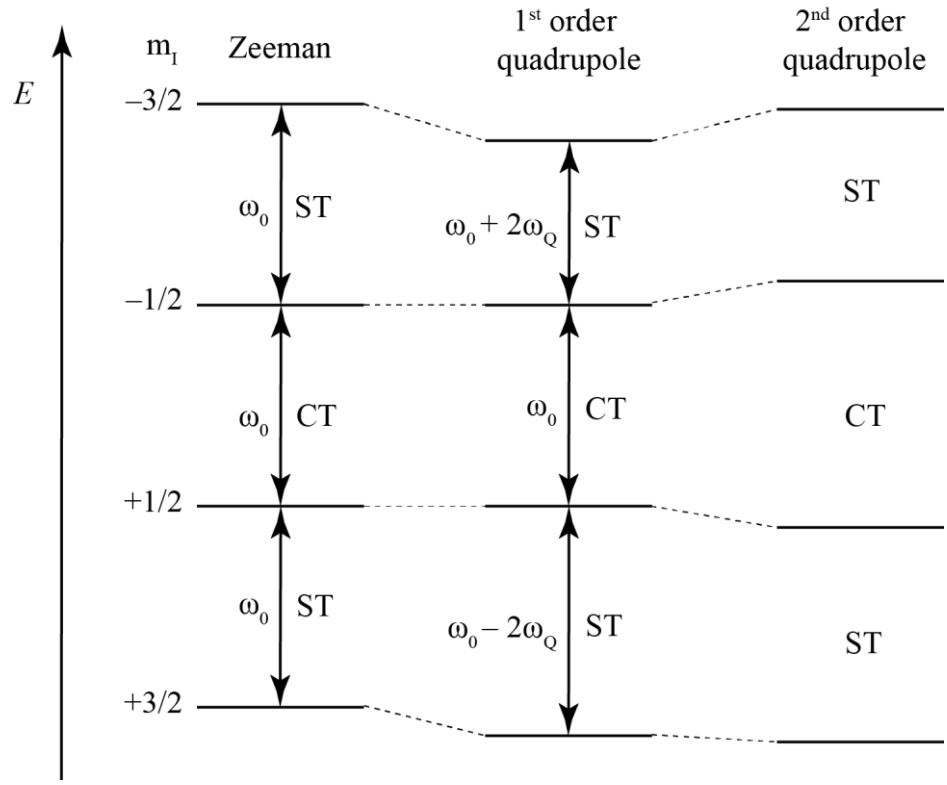

Figure 2.11 Energy levels of an I = 3/2 nucleus. To a first approximation of the quadrupolar interaction, only the CT is affected. Both CT and STs are affected to a second-order approximation. Diagram is based on a nucleus with a positive gyromagnetic ratio. Diagram not to scale.

For powdered samples which comprise many tiny crystallites each with random orientation, a broadened lineshape, or powder pattern, is observed. The width of the lineshape is dictated by C_Q, while the shape is dictated by η_Q. As such, the lineshape contains information on the local environment of the nucleus. An orientation dependence exists which is the result of the $3\cos^2\theta - 1$ term in Equation 2.35. Magic angle spinning (MAS) experiments are routinely used to average first-order quadrupolar broadening, as with dipolar and CSA interactions. A detailed explanation of MAS is discussed later in this chapter in Section 2.2.1.

For many solids, the quadrupolar interaction is so large that a first-order approximation is not sufficient and the second-order quadrupolar interaction must also be considered. This can be described a further perturbation to Zeeman energy levels, but now affecting the CT as well as the STs. The effect on the central transition is that of anisotropic broadening of the lineshape. The second-order quadrupolar splitting parameter, $\omega_Q^{(2)}$, is much smaller than first-order quadrupolar splitting, with its magnitude proportional to

$$\omega_Q^{(2)} \propto \frac{\left(\omega_Q^{PAS}\right)^2}{\omega_0}. \tag{2.38}$$

As such, the second-order quadrupolar coupling is inversely proportional to magnetic field strength. $\omega_Q^{(2)}$ has a complex orientation dependence which can be described, for a transition of m_I to $-m_I$ (for an $I = 3/2$ nucleus with $\eta_Q = 0$) by

$$\omega_Q^{(2)} \propto \frac{(\omega_Q^{PAS})^2}{\omega_0}\left[A + B\frac{1}{2}(3\cos^2\theta - 1) + C\frac{1}{8}(35\cos^4\theta - \cos^2\theta + 3)\right]. \quad (2.39)$$

For the CT, A, B and C are spin-dependant coefficients where $A = -2/5$, $B = -8/7$ and $C = 54/35$. The A term is isotropic, while the second term (B) has the $3\cos^2\theta - 1$ angular dependence, and can therefore be averaged using MAS. The third term (C) has the most complex angular dependence and cannot be averaged using standard MAS experiments. It is possible to remove the effects of second-order quadrupolar broadening with highly specialised experimental set ups such as using double angle rotation experiments, however this requires expensive equipment and as such is non-routine. Multiple quantum (MQ) MAS experiments are often used to reduce the effects of second-order quadrupolar broadening which is discussed in more detail in Section 2.2.6.

Scalar Coupling

Scalar coupling, often referred to as J-coupling, is an electron-mediated through-bond magnetic interaction between nuclei. The coupling is a result of the hyperfine interaction of an electron with the nucleus. A scalar coupling constant, J_{IS}, between two spins, I and S, gives the magnitude of the interaction. It is possible for the interaction to occur across multiple bonds, where the bond angles become important, although the magnitude of the interaction typically decreases with increasing number of bonds. In Solid-state NMR, splittings due to scalar couplings are usually not observed in spectra due to the low magnitude compared with the other NMR interactions and line broadening arising from disorder. However, scalar couplings can be used in through-bond correlation experiments such as refocused INADEQUATE, refocused INEPT and HMQC variants.[6-8] Furthermore, the calculation of scalar couplings using DFT has gained interest over the past decade driven by improvements to experimental technique such as increased spinning speeds and the accurate setting of the magic angle.[9-15]

2.2 Solid-State NMR Methods

2.2.1 Magic Angle Spinning

The NMR interactions discussed in Section 2.1.3 provide information on material structure, but can also make Solid-state NMR spectra more challenging to interpret. Powdered samples are comprised of many crystallites with random orientations and as such causes anisotropic broadening which reduces the resolution in spectra. Magic-angle spinning (MAS) is a common

practical method that can be employed to remove anisotropic interactions, resulting in increased resolution and sensitivity.[16-18]

The experimental set up of an MAS experiment is illustrated in Figure 2.12, where θ_R is the angle between B_0 and the MAS rotation axis. θ is the angle between B_0 and the principal *z*-axis of the interaction tensor while β is the angle between the MAS rotation axis and the principal *z*-axis of the interaction tensor.

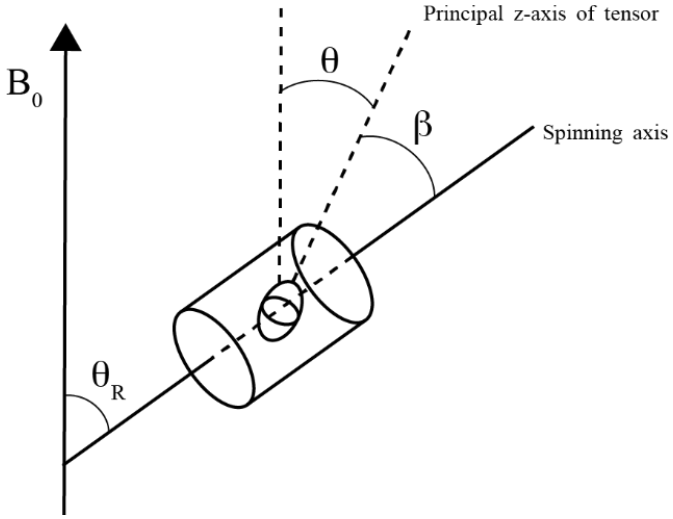

Figure 2.12 Schematic representation of a magic angle spinning experimental set up. Diagram not to scale.

The main aim of MAS experiments is to remove the effects of CSA, but MAS also helps to remove dipolar and first-order quadrupolar contributions. CSA, dipolar coupling and first-order quadrupolar coupling have a $3\cos^2\theta - 1$ orientation dependence. Rotation of the sample at θ_R to B_0 causes θ to vary as the sample rotates. The orientation dependence can be averaged by spinning the NMR rotor at the 'magic' angle of $\theta = 54.736°$ from the external field B_0.

$$\langle 3\cos^2\theta - 1\rangle = \frac{1}{2}(3\cos^2\theta_R - 1)(3\cos^2\beta - 1) \quad (2.40)$$

$$if\ \theta_R = 54.736° \quad (2.41)$$

$$then\ (3\cos^2\theta_R - 1) = 0 \quad (2.42)$$

$$and\ \langle 3\cos^2\theta - 1\rangle = 0 \quad (2.43)$$

Provided that the MAS rate is sufficient to completely average θ, then the anisotropic interaction will be averaged to zero. When MAS rate is not sufficient, spinning sidebands (SSBs) will be present in the spectrum, which are extra resonances centred around the isotropic resonance and separated by the spinning frequency. MAS rate is one of the key practical considerations of Solid-state NMR experiments as the fastest spinning rates are only accessible

using the smallest rotor sizes. Possible MAS rates now exceed 100 kHz using NMR rotors with an external diameter of 0.7 mm.[19] Rotors of this size have limited volume for sample, and as such the signal intensity observed will be reduced.

MAS can only partially reduce the quadrupolar interaction of quadrupolar nuclei, as MAS averages the quadrupolar interaction to a first-order approximation. However, owing to the more complex orientation dependence discussed in Section 2.1.4, to second-order approximation MAS cannot completed average the quadrupolar interaction. The second-order quadrupolar interaction results in a broadening of spectra which is narrowed by MAS shown in Figure 2.13.

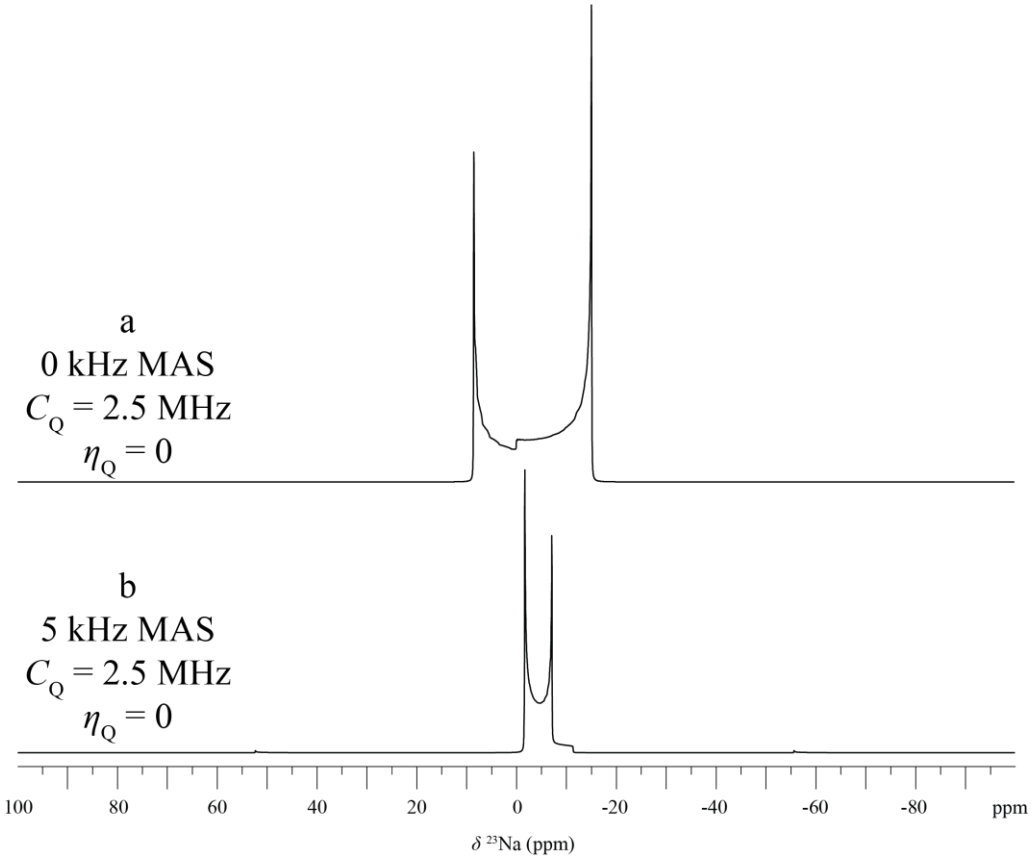

Figure 2.13 Simulated ^{23}Na spectra at two MAS rates (a = 0 kHz, b = 5 kHz).

2.2.2 Cross Polarisation

Cross polarisation (CP) experiments are commonly used as a method to boost sensitivity when studying low-γ nuclei.[20, 21] Magnetization is transferred through space from an abundant high-γ nucleus such as ^{1}H to the low-γ nucleus such as ^{13}C. The signal enhancement is equal to the ratio of γ of the two nuclei, which for a ^{1}H-^{13}C CP experiment is around four-times enhancement compared with a direct observation ^{13}C experiment (^{1}H γ = 42.58 MHz/T; ^{13}C γ = 10.71 MHz/T). Additionally, T_1 relaxation times are often shorter for high-γ nuclei, meaning that experimental scans can be repeated more rapidly than in a direct observation of the

low-γ nuclei, this means that the overall signal enhancement in a given time is usually greater still.

A standard CP experiment pulse sequence is shown in Figure 2.14. An initial 90° pulse to the high-γ nuclei, *I* (*e.g.*, ^{1}H), along the *x*-axis nutates the magnetization onto the *y*-axis. A second phase shifted 90° pulse locks the magnetization, and as such is called the spin-lock pulse. During the spin-locking period, a 'contact' pulse is applied to the low-γ nuclei, *S* (*e.g.*, ^{13}C). During this time magnetization is transferred from the I nuclei to the S nuclei, but only if the nutation frequencies, ω, of the nuclei are equal,

$$\omega_{1\mathrm{I}} = \omega_{1\mathrm{S}}, \tag{2.44}$$

which is the case when the Hartman-Hahn matching condition is met,

$$\gamma_{\mathrm{I}} B_{1\mathrm{I}} = \gamma_{\mathrm{S}} B_{1\mathrm{S}}. \tag{2.45}$$

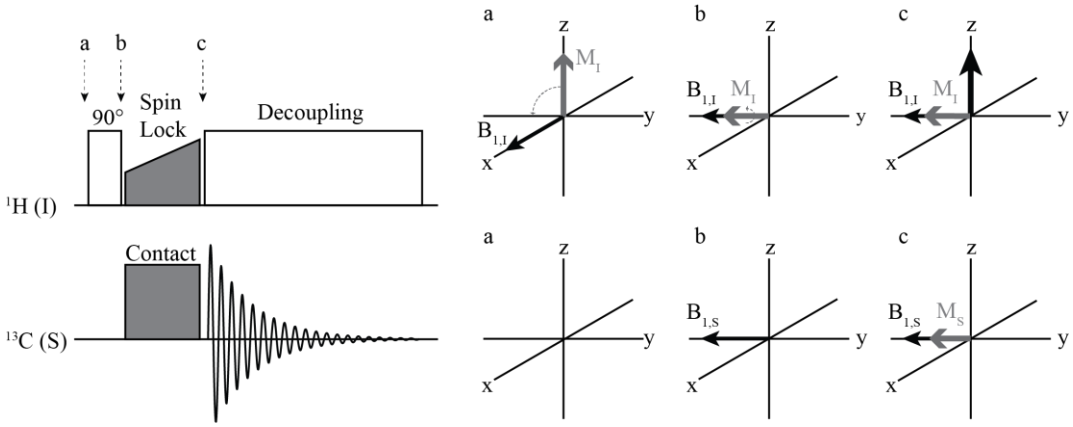

Figure 2.14 Schematic of the pulse sequence of a cross polarisation experiment along with illustration of the spin precession at various point throughout shown in the rotating frame. White and grey pulses represent different phases. Diagram not to scale.

2.2.3 Decoupling

MAS alone is often not sufficient to reduce the effects of dipolar coupling, especially in cases where this interaction is strong, in particular during ^{13}C experiments of organic systems. In these systems, the heteronuclear dipolar interaction is strong owing to the close proximity of high-γ ^{1}H atoms. Removing the dipolar coupling interaction involves averaging the magnetic field perturbation on a spin generated by all of its neighbouring spins. Different methods have been reported to achieve this, with the simplest being the continuous wave (CW) approach. In this approach a continuous high power rf pulse is applied at the Larmor frequency of the nuclei that is not being detected *e.g.*, in routine ^{13}C experiments a decoupling pulse is applied at the ^{1}H Larmor frequency during the acquisition of the ^{13}C FID. There are many decoupling sequences, such as SPINAL-64, XiX and Two-Pulse Phase Modulation (TPPM).[22-24] A common feature that links most decoupling sequences is they consist of blocks of pulses that vary in duration

and/or phase which are optimised theoretically or experimentally for the greatest possible resolution. The method used in all decoupling experiments discussed in this thesis is the TPPM approach. This method was developed to address the reduction in effectiveness of decoupling at fast MAS rates. TPPM involves continuous irradiation of nuclei, but with a sequence of repeating pulses with slightly different phase as shown by Figure 2.15.

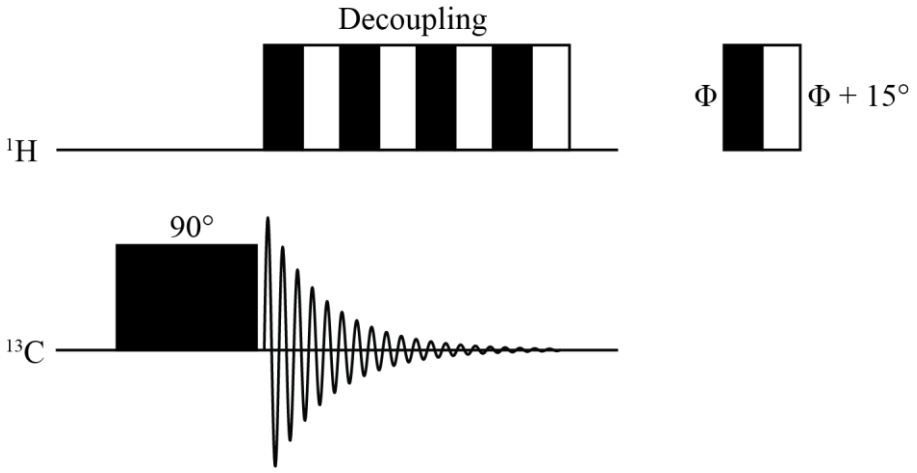

Figure 2.15 Schematic representation of a decoupling pulse sequence showing the two pulse phase modulation during the acquisition of the nuclei of interest. *Φ* is the phase of a decoupling pulse. Diagram not to scale.

2.2.4 Spin Echo

Simple pulse-acquire NMR experiments can suffer from background signals arising from the probe and from a dead-time between the pulse and acquisition, during which the rf coil responsible for both pulse and acquisition continues to resonate. A spin-echo experiment can incorporate this dead-time and suppress probe background signals by 'refocusing' magnetization after a short delay, as shown by Figure 2.16. First a 90° pulse is applied to generate transverse magnetization which can freely precess during a first delay period, *τ*. Then a 180° pulse is applied to flip the phase of the spins and following another delay period the magnetization is refocused and signal can be acquired. An advanced version of a spin-echo experiment, the 'depth' experiment, uses two back-to-back spin echo sequences to further reduce the probe background signals.[25]

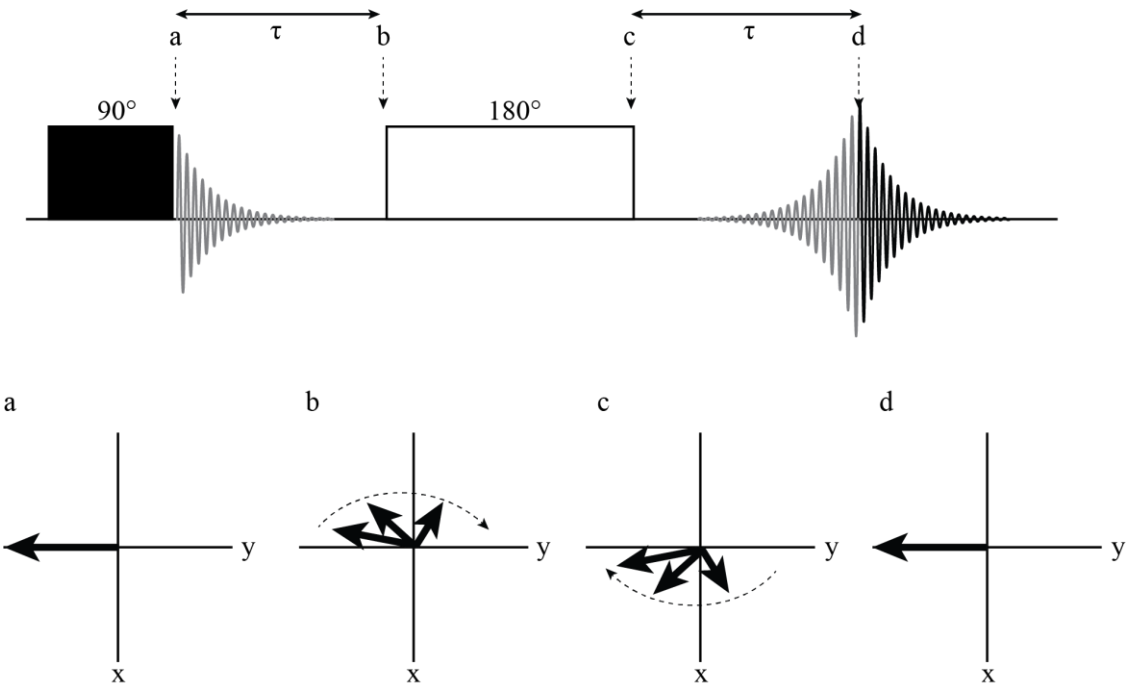

Figure 2.16 Schematic of the pulse sequence of a spin echo experiment. Solid and blank pulses represent phases, where solid is a pulse of phase 'x' and blank is a pulse of phase 'y'. Schematic of the positions of magnetization in the rotating frame at various times during the pulse sequence to illustrate the manipulation of magnetization by the rf pulses. Diagram not to scale.

2.2.5 Measurement of T_1 Relaxation Time

The inversion recovery and saturation recovery experiments are two methods of measuring the longitudinal relaxation time, T_1. The inversion recovery method can result in a potentially large signal range but suffers from the requirement of a recycle interval of at least $5T_1$ to allow full relaxation between acquisitions. Particularly with slow relaxing species, this can make the inversion recovery experiment unfavourably long. The saturation recovery method is a more commonly used approach. It utilises a "saturation train", where a series of 90° pulses separated by millisecond delays, removes the bulk magnetization completely as shown in Figure 2.17. As the magnetization recovers during the delay time, τ, a 90° pulse creates transverse magnetization which is then measured. A series of these experiments are carried out with variation of τ, the resulting signal, $I(\tau)$, is plotted to elucidate the T_1 time, given by

$$I(\tau) = I_0 \left[1 - e^{\left(\frac{-\tau}{T_1}\right)}\right], \tag{2.46}$$

where I_0 is the signal obtained prior to the return to magnetic equilibrium.

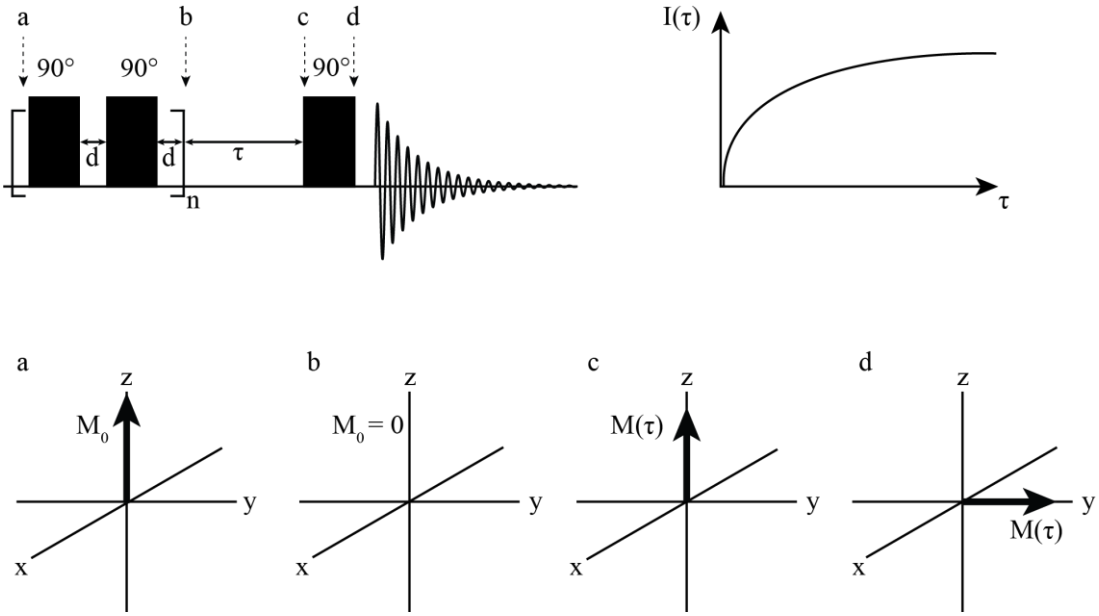

Figure 2.17 Schematic of a saturation recovery pulse sequence along with diagram showing the response of magnetization at various points throughout and graphical mapping of the longitudinal relaxation. Diagram not to scale.

2.2.6 Multiple-Quantum Magic Angle Spinning

MQMAS experiments are 2D experiments that can give high-resolution spectra for quadrupolar nuclei (I = >1/2) with half-integer spin by removing second-order quadrupolar broadening, which cannot be removed by MAS alone.[26] The MQMAS experiment does not require additional specialist equipment and can be completed at standard field strengths, making it an accessible and affordable experimental option.

The basic 1D MAS experiment of a quadrupolar nucleus gives a spectrum featuring broad peaks from which extraction of quadrupolar parameters (C_Q and η_Q) is not always possible. MQMAS experiments can be used to elucidate the number of crystallographically distinct sites and extract quadrupolar parameters. The MQMAS experiment correlates the anisotropic powder pattern in the δ_2 dimension with the isotropic spectrum free of quadrupolar broadening in the δ_1 dimension. The most basic MQMAS pulse sequence features two pulses separated by a delay, with the first pulse exciting the MQ transition and the second pulse converting the evolved magnetization into a detectable form. A slightly more complicated z-filtered pulse sequence is typically preferred to obtain better lineshapes. In this experiment, the second pulse temporarily stores the magnetization along the z-axis before a final 90° pulse is applied (Figure 2.18a).[27] During the 2D experiment, the t_1 delay time is incrementally varied which allows the acquisition of 'slices' which make up the indirect dimension following a 2D FT.

The 2D spectrum obtained shows the indirectly detected signal in the δ_1 dimension and the associated powder pattern of the CT in the δ_2 dimension. The signals appear tilted at an angle dependent on the MQMAS ratio, which for an $I = 3/2$ nucleus is −7/9. To correct this, the spectrum is sheared following the FT to align the ridge-like features parallel to δ_2 (Figure 2.18b). This allows the isotropic projections to be obtained in the δ_1 dimension. The split-t_1 experiment introduced by Brown and Wimperis reduces the need for additional processing following the FT (Figure 2.18c).[28] The t_1 delay is split into separate single-quantum and triple-quantum evolution periods so that shearing is not required.

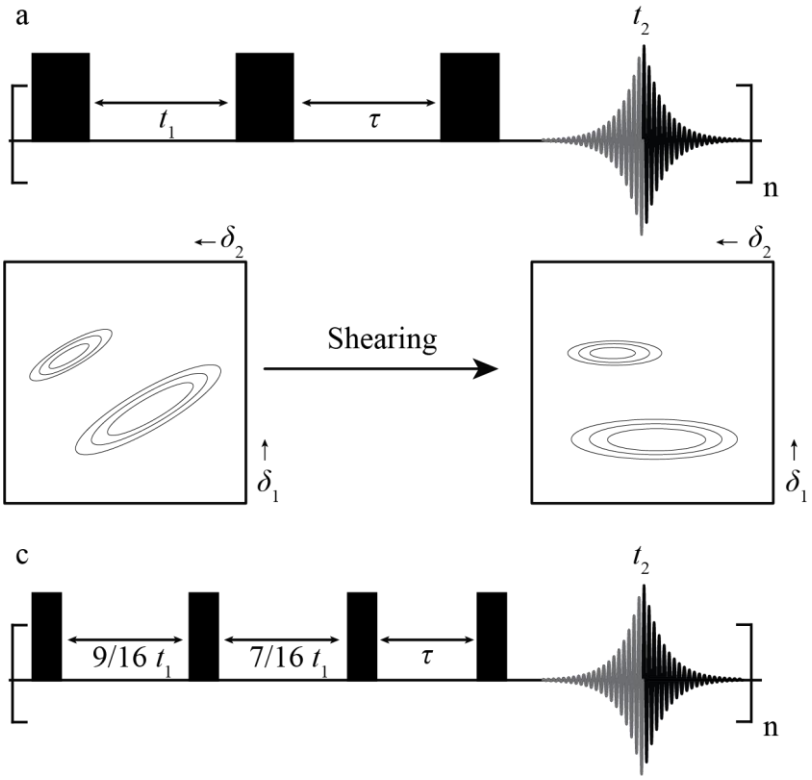

Figure 2.18 Schematic representations of a z-filter MQMAS experiment pulse sequence (a), the shearing transformation and a split-t_1 z-filtered MQMAS experiment pulse sequence for a spin 3/2 nucleus (c). Diagram not to scale.

Provided there is sufficient resolution in the MQMAS spectrum, information such as the number of crystallographically distinct sites can be determined by assessing the number of ridges that appear. Each ridge can then be isolated such that a lineshape is obtained corresponding to that individual site. Fitting of the lineshape obtains NMR parameters such as δ_{iso}, C_Q and η_Q, which give insight into the local geometry of that particular site.

2.2.7 Variable Temperature (VT) NMR

In some cases it may be of interest to study a system at some temperature other than ambient temperature, particularly to study dynamics or in the characterisation of thermally-driven phase transitions. Both high temperature and low temperature experiments are

available, combined under the moniker of variable temperature (VT) NMR, with higher temperatures reached with the assistance of an external heater connected *ad hoc* to the probe, blowing warmer gas around the rotor. Low temperature experiments are accessed with cryogens, such as liquid nitrogen, where a heat exchanger is placed in a cryogenic dewar where the external gas is passed through to lower the temperature of the gas before being blown over the rotor. The temperature of the gas can be carefully controlled by connecting a heater and cryogenic dewar in sequence, and with two independent temperature sensors inside the probe which provide real time *in situ* temperature measurements. However, the temperature of the sample may still differ when using MAS. The high spinning speeds of modern experiments cause frictional heating. The true temperature of a sample at a given spinning rate can be found using lead nitrate, $Pb(NO_3)_2$, as described by Bielecki and Burum in 1995.[29] The isotropic resonance in the $Pb(NO_3)_2$ spectrum was shown to shift to higher chemical shift with increasing temperature, with the relationship 0.753 ppm / K. As such, this relationship can be used to calculate the true temperature of a sample by first calibrating the temperature sensors, and then calculating the degree of frictional heating at various MAS rates. Details of the temperature calibration carried out in this work can be found in Appendix 2.1.

A limitation of VT experiments is the temperature range available, where the thermal stability of the plastic rotor caps is limited to around 240 – 350 K. Users may wish to push these boundaries but typical operating temperature ranges of NMR probes is around 220 – 370 K. More specialised equipment is available that can expand the range of temperatures that are accessible. Further limitations for low temperature experiments include the use of nitrogen as the bearing and drive gas instead of compressed air to prevent the formation of ice crystals inside the probe, which would cause spinning instability and potentially probe damage. Additionally, the stability of the temperature in VT experiment can sometimes present additional challenges, particularly at the extremes of the thermal range, which can limit the length of experiments that can be completed with stable temperature.

2.3 X-ray Crystallography

All of the materials studied in this thesis are crystalline, which is defined as having a three-dimensional repeating structure. Due to this, a single repeating unit called a unit cell can describe the entire structure. The unit cell has lattice parameters where *a*, *b*, and *c* are the lengths of the edges and α, β and γ are angles between them. The smallest possible unit cell does not always describe the symmetry of the structure at large, so larger higher symmetry unit cells are often required. All crystal types can be described by one of the 14 Bravais lattices, *e.g.*, body-centred (I) or face-centred (F). Furthermore, based on the symmetry within the cell, a structure can be categorised into one of 32 point groups. However, crystalline structures also

possess some symmetry through space, where symmetry is described by one of 230 space groups. Space groups contain additional translational symmetry operations such as glide planes or screw axes, which are a combination of some translational transformation in addition to a transformative symmetry operation such as a rotational axis or mirror plane. Lattice planes are imaginary parallel planes in the unit cell and are described using their Miller indices (*hkl*). The fractional coordinates of where the lattice plane intersects the edge of the unit cell are noted, then represented as their reciprocals (*i.e.*, a lattice plane that intersects at a = 1, b = 0.5, c = 0.25 will have the Miller indices (124)).

X-ray diffraction (XRD) is a useful tool for structural determination of crystalline solids as it is sensitive to long-range ordering. In laboratory XRD experiments, monochromatic X-rays are generated by a high-vacuum X-ray tube in sequence with a monochromator. An electron beam from a hot tungsten filament is focused onto a copper metal anode in the X-ray tube, which causes the emission of X-ray radiation (though other metals can be used to achieve X-rays with different wavelengths). The emission is triggered when an electron is knocked out of a Cu core shell (K-shell) and a higher energy electron relaxes (usually from the L-shell) to fill the electron hole, emitting radiation. Copper Kα radiation (λ = 1.54 Å) is commonly used in XRD experiments and is used in all XRD experiments throughout this thesis.

During the XRD experiment, X-rays interact with electrons in the sample where photons are scattered, with those scattered without loss of energy or change in wavelength elastically scattered. Diffracted radiation is then detected when the diffracted radiation is in phase and constructively interferes (known as a Bragg reflection). Bragg reflections occurs when the path difference between the radiation waves ($2d\sin\theta$) is an integer multiple of the wavelength of the radiation, which can be expressed by Braggs Law:

$$n\lambda = 2d\sin\theta, \tag{2.47}$$

where λ is the wavelength of radiation, n is an integer, θ is the angle of the incident radiation and d is the distance between lattice planes, as shown by Figure 2.19.

In some instances, powder XRD (PXRD) is preferred, such as when obtaining single crystals proves too difficult or when the material is intrinsically powdered like in the study of battery electrodes. Powdered samples are polycrystalline, meaning they have many tiny crystals each with a random orientation. Incident radiation is diffracted by the crystal lattice in all directions creating a sphere of diffracted radiation known as an Ewald's Sphere. However, constructive interference occurs in a series of concentric cones, where each cone is angled at 2θ from the incident radiation, known as Debye cones. The Debye cones intersect the detector in a Debye ring, where the detector will scan along an arc that intersects the Debye cone at a single point. This allows all possible reflections to be observed simultaneously, with the detector

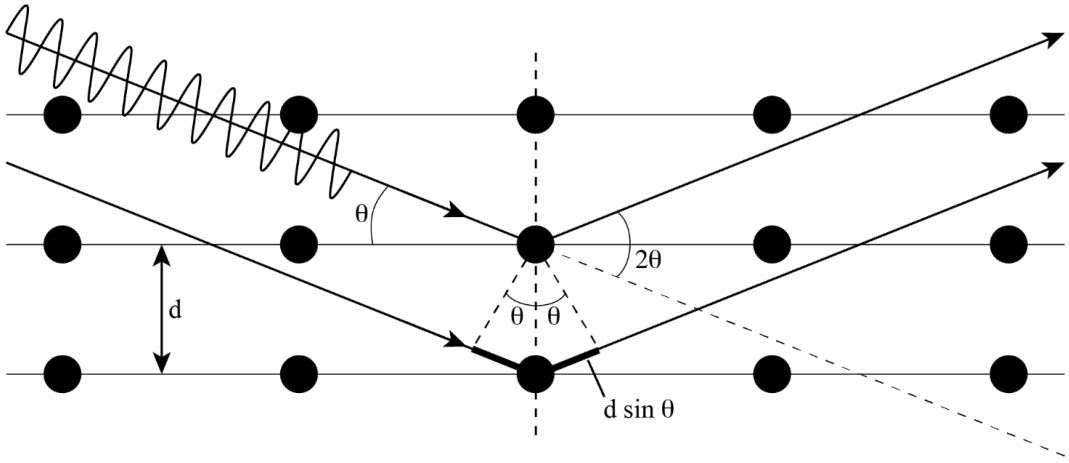

Figure 2.19 Schematic showing the Bragg diffraction of incident radiation by lattice planes.

measuring intensity in counts, which is plotted as a function of 2θ. In PXRD experiments the sample is kept still while the X-ray source slowly moves changing the θ angle, meanwhile the detector also moves, with which its position is recorded as 2θ. Samples are often packed onto a flat glass plate, though in some cases when air-sensitivity is an issue, samples can be packed into borosilicate capillary tubes and capped to maintain an inert atmosphere.

Solving the complete crystal structure is not possible directly from PXRD experiments, however, some refinement techniques such as Rietveld refinements or Le Bail fits allow solutions to be gained from a suitable starting model. The Rietveld method is a structural prediction tool where a theoretical structure is refined until a reasonable agreement is obtained. When it is possible to obtain a single crystal, single crystal XRD experiments can give detailed structural information. Here the crystal is mounted and adhered to a loop which then rotates the crystal to all desired orientation with respect to the static X-ray source. Diffracted radiation produces bright spots on the detector which can be used to solve the crystal structure. However, there remains some positional ambiguity for hydrogen atoms due to the small scattering factor. The scattering factor of an atom increases with the number of electrons and decreases with increase in 2θ, therefore hydrogen atoms do not scatter X-rays very well. Other higher resolution crystallography experiments can be used to more accurately locate hydrogen atoms, such as neutron diffraction, where an incident beam of neutrons is scattered instead of an X-ray beam. An alternative source of X-rays is a Synchrotron light source, where a beam of electrons are controlled with bending magnets, with X-ray radiation emitted with change to the electrons velocity. Synchrotron facilities offer increased X-ray flux, but as experimental time is valuable there exists competition for experimental time, as such these experiments are not routine.

While XRD is more suited to give information on long-range structures, it can give some information on disorder. Positional disorder, where the location of an atom in one unit cell differs from the next unit cell, and compositional disorder, where the element in a site may

change from one unit cell to the next, can both be observed in XRD experiments. However, investigation of defects, disorder and dynamics with XRD can be challenging, hence when used in tandem with a local probe such as NMR becomes a powerful structural analysis method.

2.4 Density Functional Theory

Density functional theory (DFT) can be used in order to relate long-range structural information from XRD experiments to the local structure information from NMR experiments. Experimental NMR can often be a challenge to assign without information from DFT in part due to the presence of multiple resonances which are difficult to directly link to specific chemical sites. Computational calculations can provide a wealth of information on the electronic structure of a system and are able to use this to calculate NMR observables, such as chemical shielding and quadrupolar parameters. There are two approaches of DFT calculations that are often employed. The first is to use a cluster-based code such as Gaussian, which is used to study isolated molecules; the other method is that which is used throughout this work, and is to use a periodic code such as CASTEP,[30-32] which is preferable for studying periodic materials such as crystalline solids.

2.4.1 Fundamentals of Density Functional Theory

In order to calculate NMR parameters using DFT, the electronic structure and energy of a system must first be calculated. The time-dependent Schrödinger equation is difficult to solve and can be simplified by the Born-Oppenheimer Approximation, which states that electrons respond instantaneously to nuclear motion due to the large difference in mass between the nucleus and electron, such that nuclear motion can be ignored. With this we can consider the time-independent Schrödinger equation which takes the form,

$$\hat{H}\psi = E\psi \,, \tag{2.48}$$

where $\hat{H}$ is the Hamiltonian operator, E is the energy and ψ is the wavefunction describing the electron. The Hamiltonian contains terms relating to the kinetic and potential energies of nuclei and electrons in a system and the interactions between them, but is simplified by fixing nuclear positions under Born-Oppenheimer Approximation. This enables calculation of the Schrödinger equation for simple systems, but in more complicated systems it can be impossible to solve directly. One solution is to use self-consistent field (SCF) calculations which approximate the wavefunction, more specifically the average potential, of one electron. The potential depends on the positions of other electrons, so the initial estimates for electron potential are then used to find new wavefunctions. The process repeats until the wavefunctions become ‘self-consistent’.

An alternative is to assume that the electronic energy of a system can be described by its electron density, ρ(r). The Hohenberg and Kohn theorem states that ground state electron

density defines the ground state energy *via* a single functional.[33] In the Kohn-Sham scheme we write

$$E_{\mathrm{e}} = T_{\mathrm{e}} + V_{\mathrm{n-e}} + V_{\mathrm{e-e}} + E_{\mathrm{XC}}[\rho] , \tag{2.49}$$

where E_{e} is energy of an electron, T_{e} is the kinetic energy of the electrons, $V_{\mathrm{n\text{-}e}}$ is the potential energy of the interaction between nuclei and the electron, $V_{\mathrm{e\text{-}e}}$ is the potential energy of electronic repulsion, and E_{XC} is the exchange-correlation (XC) functional.[34] A nuclear kinetic energy term can be ignored due to the Born-Oppenheimer Approximation, similarly, a nuclear interaction term can be treated as constant. The XC functional term exists to cover all of the information we do not know about the system, as we can calculate discrete values for all other terms, and can be deconstructed as

$$E_{\mathrm{XC}}[\rho] = E_{\mathrm{X}}[\rho] + E_{\mathrm{C}}[\rho] , \tag{2.50}$$

where E_{X} is the interaction of electrons with like-spin, and E_{C} is the interaction of electrons with opposite spin. The XC functional cannot be calculated exactly and accounts for around 10% of the total energy. It is possible to make approximations of the XC functional, *e.g.*, the Local Density Approximation (LDA) is the simplest approximation and assumes that electrons are evenly spread in space. More advanced approximations exist that use the gradient of ρ, known as Generalized Gradient Approximations (GGA), of which the most widely used is that proposed by Perdew, Burke and Ernzerhof (PBE).[35] Furthermore, some functionals include the kinetic energy density which is related to the curvature of ρ, these are known as *meta*-GGAs, such as the recent regularized SCAN (rSCAN) functional.[36]

In periodic materials, planewave basis sets are chosen as known sets of functionals in order to calculate ρ.[37] Larger basis sets will increase the accuracy of calculations, but quickly increase computational cost; as such, a cut off energy, E_{cut}, is applied to define an upper limit. It is not possible to know this value in advance and as such optimisations to find a value that gives sufficiently accurate results without using an excess of computational power are completed. This process involves completing convergence checking calculations with variation of the cut off energy. A suitable value is found when the value is such that results would not be significantly improved by using larger basis sets.

Explicit descriptions of all electrons in a system can be computationally expensive. An approach to limit this is to describe the core electrons using a pseudopotential and therefore limiting the number of planewaves required to describe the nature of valence wavefunctions near to the nucleus. For NMR calculations which depend on the electron density near to the nucleus, the all-electron wavefunction can be reconstructed using Blöchl's projector-augmented wave (PAW) method.[38, 39] Mauri, Pfommer and Louie (MPL) then calculated NMR chemical

shifts using the all-electron Hamiltonian in simple crystalline materials.[40] However, the MPL method is computationally expensive except when studying systems with few electrons. In 2001, Mauri and Pickard introduced a gauge correction to the PAW method, allowing calculation of NMR parameters in a magnetic field with the gauge induced PAW (GIPAW) formalism.[41] GIPAW was subsequently incorporated into several *ab-initio* codes including Quantum Espresso, CASTEP and WIEN2K.

CASTEP has been used extensively throughout this thesis using the GIPAW formalism, ultrasoft pseudopotentials and periodic boundary conditions.[30-32] Periodic boundary conditions provide an improved description of a crystal rather than a cluster based code which would introduce edge effects at termini, while simultaneously reducing computational costs. Consideration must be given to the E_{cut} and the number of *k*-points sampled before completing any work. *k*-points are locations in the first Brillouin zone in the reciprocal space lattice, where a greater number will result in a smaller spacing and thus a higher degree of sampling, more accurate results and more computationally expensive calculations. Calculations using a higher E_{cut} and greater number of *k*-points would give improved accuracy, although the improvements become negligible at a certain point despite continued increases to the computational cost. Therefore, standard practice is to use the minimum values that achieve sufficiently accurate results while not using excessive computational time. The process of finding these optimum values is known as convergence testing, where the user attempts to find the point where the calculated observables converge to a particular value and insufficient improvements can be made with increased computational cost. Convergence testing is carried out on a test structure that has key properties, such as being a simple, well studied system that is free from disorder or dynamics which can cause complications. Furthermore, the test structure needs to be chemically similar to the materials of interest so that the assumptions of converged E_{cut} and number of *k*-points can be transferred. Finally, consideration must be given to the band gap of the system, as conductors or semi-conductors (small band gaps) require a high number of *k*-points whereas insulators (large band gap) do not. While it would be preferable to conduct convergence tests on every structure of interest, this is time-consuming and as such the assumption that the test system is a suitable replacement chemically and structurally is made to mitigate this.

For this work, convergence testing has been completed using *L*-alanine as a small organic polycrystalline material which shares similarities with the organic battery anode materials discussed in Chapters 3 and 4, as well as the organic ferroelectric materials discussed in Chapter 5. A set of NMR calculations on the *L*-alanine structure with systematic variation of each of the two parameters was completed. The *k*-point spacing was varied to cover the range of 0.01 $Å^{-1}$ – 0.07 $Å^{-1}$ equating to a range of 4 – 405 *k*-points (while using an E_{cut} of 50 Ry). The E_{cut} was varied to cover the range of 20 − 70 Ry (while using a *k*-point spacing of 0.05 $Å^{-1}$,

n = 18 *k*-points). From the NMR calculations the single point energies (SPE), calculated isotropic chemical shieldings, $\sigma^{iso,\ calc.}$, of ^{1}H and ^{13}C, and arbitrarily selected symmetrised force parameters (H_x, C_y, N_z, O_x) were extracted. For energy minimisation, or geometry optimisation, calculations, SPE and symmetrised force parameters are important in assessing convergence, while for NMR parameter prediction calculations the $\sigma^{iso,\ calc.}$ is more important. The extracted parameters were plotted against both the E_{cut} and the number of *k*-points and is shown in Figure 2.20.[42] In Figure 2.20a, as E_{cut} is increased the calculated SPE converges at around 50 Ry. A similar trend is observed in each of Figure 2.20b-d, where convergence is reached by 50 Ry for both ^{1}H and ^{13}C $\sigma^{iso,\ calc}$ as well as a symmetrised force component from each atom type. When considering the *k*-point spacing, in Figure 2.20e only small variations are observed in the calculated SPE (<0.01 eV) with increased *k*-point sampling. The calculated SPE is approximately equal to the converged value observed in Figure 2.20a, with the small variations expected for a wide band gap solid such as *L*-alanine. Additionally, Figure 2.20f-h show that only very small variation in $\sigma^{iso,\ calc.}$ or symmetrised force components are observed with varying numbers of *k*-points across this range. Based on these results, an E_{cut} of 50 Ry was chosen for all work in this thesis. Similarly, a *k*-point spacing of 0.05 $Å^{-1}$ was chosen as a compromise between computational time and calculation accuracy due to the limited impact that additional *k*-point sampling has on the calculated parameters.

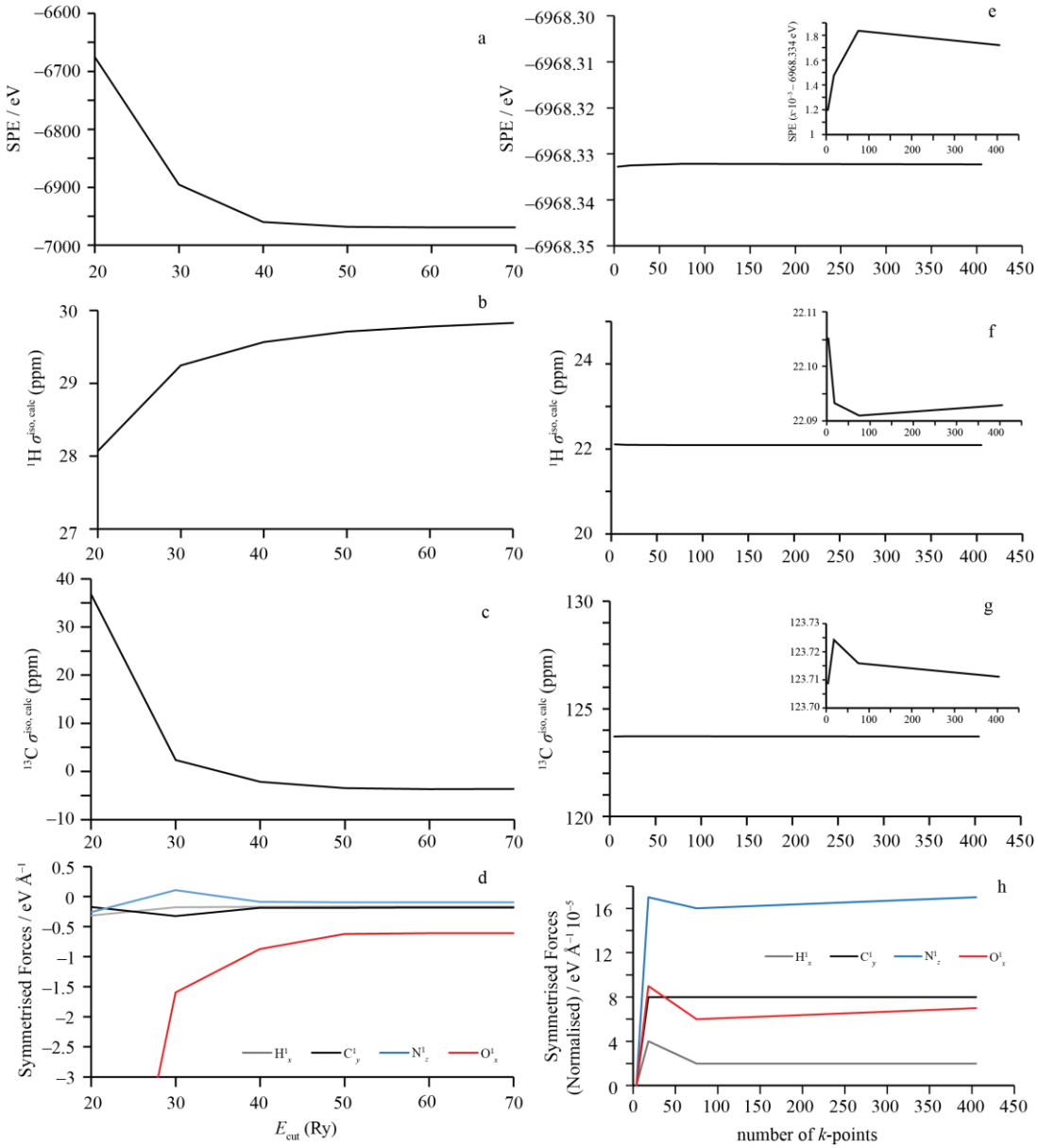

Figure 2.20 Convergence graphs of E_{cut} plotted against SPE (a), ^{1}H $\sigma^{iso, calc.}$ (b), ^{13}C $\sigma^{iso, calc.}$ (c) and symmetrised force components (H^1_x = grey, C^1_y = black, N^1_z = blue, O^1_x = red) (d). Convergence of the number of k-points plotted against SPE (e), ^{1}H $\sigma^{iso, calc.}$ (f), ^{13}C $\sigma^{iso, calc.}$ (g) and symmetrised force components (H^1_x, C^1_y, N^1_z, O^1_x) (h). Insets included for (e-g) with smaller ppm range on the y-axis to show scale of change. Force components are normalised in (h) to aid visualisation and are defined as the difference of the force component to the value obtained for the lowest number of k-points (4). Calculations completed in CASTEP on alanine (CCDC Deposition number: 278464).

2.5 NMR Crystallography

NMR crystallography is a field that emerged from the combination of NMR, DFT and XRD for the characterisation of atomic-level structure and disorder in the solid state.[43-47] Solid-state NMR does not require long-range order and as such can give information about the local structure or disorder of a material, while XRD is a useful and complimentary technique for

studying long-range order in crystalline solids while equally being able to give some information on disorder. Neither XRD nor NMR can give a complete picture of complex materials and so DFT calculations are crucial to link between the two techniques and the opposite regimes in which they excel. Limitations to diffraction include the weak scattering of X-rays by the single electron of the hydrogen atoms, which leads to ambiguity over the exact position of the proton in the structure. Secondly, any disorder within the structure, such as thermal motion can distort the bond lengths as defined by diffraction. Finally, XRD also struggles to differentiate between species with equal numbers of electrons, such as between a methyl group, hydroxyl group or a fluorine atom (all nine electron species). Neutron diffraction presents a solution to some of these issues but the technique is far from routine on account of the large facilities required to conduct such experiments and large amount of sample required.

In order to use electronic structure calculations to determine NMR parameters, the calculation must have an inputted crystal structure. Usually this structure comes from diffraction. XRD is particularly poor at accurately locating protons due to its low scattering factor, and since NMR parameters are highly sensitive to local electronic structure, accurately locating protons is important. The geometry optimisation calculation iteratively computes the forces and strains on the input structure, adjusting bond lengths and angles until convergence on a structure with lower energy. Due to the high sensitivity of NMR parameters to the local electronic environment, choices such as whether to apply unit cell constraints or include a semi-empirical dispersion correction (SEDC) scheme as part of the geometry optimisation can have a significant impact. As such, additional consideration must be given to certain aspects of the geometry optimisation procedure. Unit cell constraints, such as fixing the unit cell dimensions or the position of any particular atom, can be applied to reduce or stop the structure from undergoing an unrealistic unit cell change. Furthermore, SEDC schemes are a recent advancement in the calculation of NMR parameters. SEDC schemes account for weak intermolecular non-bonding interactions such as van der Waals forces that are not well described by standard DFT codes. This can lead to poor descriptions of structures where these forces are important, such as between the layers of graphite, where the delocalised electron structure is an important facet of the electronic and structural properties as a whole. Some popular SEDC schemes include those created by Grimme and co-workers (DFT-D, -D2, -D3 and -D4) and Tkatchenko-Sheffler (TS).[48-51] Further discussion of SEDC schemes can be found in Chapter 3, along with a thorough investigation of the optimal geometry optimisation procedure for organic functional materials. The second calculation in the prediction of NMR parameters is the NMR calculation. During which, the ground state electronic structure is calculated, and subsequently the NMR observables are calculated. As the calculation does not

directly output chemical shift, instead outputting chemical shielding, σ_{iso}, it is necessary to relate σ_{iso}, to experimental shifts, δ_{iso}, with the shielding of a reference compound, σ_{ref}, according to

$$\delta_{iso} = \sigma_{ref} - \sigma_{iso} . \quad (2.51)$$

In some situations, a structural model solved with diffraction is not available. In these cases, chemical structure prediction techniques such as *ab-initio* random structure searching (AIRSS) offer an alternative route by generating a candidate structure.[52, 53] The AIRSS approach creates many different structures and uses energetics to estimate which structures are the most reasonable starting structures. Geometry optimisation of AIRSS structures is equally as important as with diffraction structures as the AIRSS method starts with a manipulated and computationally generated guess structure input. Despite this, the use of AIRSS where no solved structure exists gives the NMR crystallographer the ability to study unknown or uncharacterised structures.

The increasingly popular and maturing field of NMR crystallography is therefore a powerful tool for study and characterisation of crystalline materials owing to its varied and wide reaching analytical tool kit; particularly for cases where XRD struggles or in situations where no initial model structure is known. NMR crystallography has been used throughout this thesis to investigate the structures of a range of crystalline organic functional materials in cases where the initial model structures are both known and unknown.

2.6 References

1. A. E. Derome, *Modern NMR Techniques for Chemistry Research*, Pergamon Press, Oxford, 1991.
2. R. R. Ernst and W. A. Anderson, *Review of Scientific Instruments*, 1966, **37**, 93-102.
3. P. J. Hore, J. A. Jones and S. Wimperis, *NMR: The Toolkit*, Oxford University Press, Oxford, 2006.
4. M. Bak, J. T. Rasmussen and N. C. Nielsen, *J Magn Reson*, 2000, **147**, 296-330.
5. R. R. Ernst, G. Bodenhausen and A. Wokaun, *Principles of Nuclear Magnetic Resonance in One and Two Dimensions*, 1987.
6. G. A. Morris and R. Freeman, *J Am Chem Soc*, 1979, **101**, 760-762.
7. G. A. Morris, *J Am Chem Soc*, 1980, **102**, 428-429.
8. J. P. Amoureux, J. Trebosc, J. Wiench and M. Pruski, *J Magn Reson*, 2007, **184**, 1-14.
9. S. A. Joyce, J. R. Yates, C. J. Pickard and F. Mauri, *J Chem Phys*, 2007, **127**, 204107.
10. C. Bonhomme, C. Gervais, C. Coelho, F. Pourpoint, T. Azais, L. Bonhomme-Coury, F. Babonneau, G. Jacob, M. Ferrari, D. Canet, J. R. Yates, C. J. Pickard, S. A. Joyce, F. Mauri and D. Massiot, *Magn Reson Chem*, 2010, **48 Suppl 1**, S86-102.
11. J. R. Yates, *Magn Reson Chem*, 2010, **48 Suppl 1**, S23-31.
12. J. P. Amoureux, J. Trebosc, J. W. Wiench, D. Massiot and M. Pruski, *Solid State Nucl Magn Reson*, 2005, **27**, 228-232.
13. D. L. Bryce, *Magn Reson Chem*, 2010, **48 Suppl 1**, S69-75.
14. D. Massiot, F. Fayon, B. Alonso, J. Trebosc and J. P. Amoureux, *J Magn Reson*, 2003, **164**, 160-164.
15. X. Xue, *Solid State Nucl Magn Reson*, 2010, **38**, 62-73.
16. E. R. Andrew, A. Bradbury and R. G. Eades, *Nature*, 1958, 1659.
17. E. R. Andrew, A. Bradbury and R. G. Eades, *Nature*, 1959, **183**, 1802-1803.
18. I. J. Lowe, *Physical Review Letters*, 1959, **2**, 285-287.

19. J. Struppe, C. M. Quinn, S. Sarkar, A. M. Gronenborn and T. Polenova, *Mol Pharm*, 2020, **17**, 674-682.

20. S. R. Hartmann and E. L. Hahn, *Physical Review*, 1962, **128**, 2042-2053.

21. G. Metz, X. Wu and S. O. Smith, *J Magn Reson*, 1994, **110**, 219-227.

22. A. E. Bennett, C. M. Rienstra and M. Auger, *J. Chem. Phys.*, 1995, **103**, 6951.

23. B. M. Fung, A. K. Khitrin and K. Ermolaev, *J Magn Reson*, 2000, **142**, 97-101.

24. M. Ernst, A. Samoson and B. H. Meier, *J Magn Reson*, 2003, **163**, 332-339.

25. S. Odedra and S. Wimperis, *J Magn Reson*, 2012, **221**, 41-50.

26. L. Frydman and J. S. Harwood, *J Am Chem Soc*, 1995, **117**, 5367-5368.

27. J. P. Amoureux, C. Fernandez and S. Steuernagel, *J Magn Reson*, 1996, **123**, 116-118.

28. S. P. Brown and S. Wimperis, *J Magn Reson*, 1997, **124**, 279-285.

29. A. Bielecki and D. P. Burum, *J Magn Reson*, 1995, **116**, 215-220.

30. S. J. Clark, M. D. Segall, C. J. Pickard, P. J. Hasnip, M. J. Probert, K. Refson and M. C. Payne, *Z Kristallogr*, 2005, **220**, 567-570.

31. J. R. Yates, C. J. Pickard and F. Mauri, *Physical Review B*, 2007, **76**.

32. M. D. Segall, P. J. D. Lindan, M. J. Probert, C. J. Pickard, P. J. Hasnip, S. J. Clark and M. C. Payne, *J Phys Condens Matter*, 2002, **14**, 2717-2744.

33. P. Hohenberg and W. Kohn, *Physical Review*, 1964, **136**, B864-B871.

34. W. Kohn and L. J. Sham, *Physical Review*, 1965, **140**, A1133-A1138.

35. J. P. Perdew, K. Burke and M. Ernzerhof, *Phys Rev Lett*, 1996, **77**, 3865-3868.

36. A. P. Bartok and J. R. Yates, *J Chem Phys*, 2019, **150**, 161101.

37. J. R. Yates and C. J. Pickard, in *Encyclopedia of Magnetic Resonance*, 2008, DOI: 10.1002/9780470034590.emrstm1009.

38. C. G. Van de Walle and P. E. Blochl, *Phys Rev B*, 1993, **47**, 4244-4255.

39. P. E. Blochl, *Phys Rev B Condens Matter*, 1994, **50**, 17953-17979.

40. F. Mauri, B. G. Pfrommer and S. G. Louie, *Phys Rev Lett*, 1996, **77**, 5300-5303.

41. C. J. Pickard and F. Mauri, *Physical Review B*, 2001, **63**.

42. C. C. Wilson, D. Myles, M. Ghosh, L. N. Johnson and W. Wang, *New J Chem*, 2005, **29**, 1318-1322.

43. P. Hodgkinson, *Prog Nucl Magn Reson Spectrosc*, 2020, **118-119**, 10-53.

44. S. E. Ashbrook and D. McKay, *Chem Commun (Camb)*, 2016, **52**, 7186-7204.

45. A. Lesage, *Phys Chem Chem Phys*, 2009, **11**, 6876-6891.

46. B. Reif, S. E. Ashbrook, L. Emsley and M. Hong, *Nat Rev Methods Primers*, 2021, **1**.

47. C. Bonhomme, C. Gervais, F. Babonneau, C. Coelho, F. Pourpoint, T. Azais, S. E. Ashbrook, J. M. Griffin, J. R. Yates, F. Mauri and C. J. Pickard, *Chem Rev*, 2012, **112**, 5733-5779.

48. E. Caldeweyher, S. Ehlert, A. Hansen, H. Neugebauer, S. Spicher, C. Bannwarth and S. Grimme, *J Chem Phys*, 2019, **150**, 154122.

49. S. Grimme, *J Comput Chem*, 2006, **27**, 1787-1799.

50. S. Grimme, J. Antony, S. Ehrlich and H. Krieg, *J Chem Phys*, 2010, **132**, 154104.

51. A. Tkatchenko and M. Scheffler, *Phys Rev Lett*, 2009, **102**, 073005.

52. C. J. Pickard and R. J. Needs, *Phys Rev Lett*, 2006, **97**, 045504.

53. C. J. Pickard and R. J. Needs, *J Phys Condens Matter*, 2011, **23**, 053201.

Appendix 2.1 – Temperature Calibration

A.2.1.1 Calibration Details

A temperature calibration was carried out to determine the degree of frictional heating and the true response of temperature sensors for increased accuracy in the reporting of temperature in VT NMR data sets. The calibration was carried out using a rotor with 3.2 mm external diameter in a Bruker Avance III HD spectrometer operating at a field strength of 16.4 T. The probe in use has two temperature sensors which can be independently calibrated to gain the true temperature of the sample. To assess the degree of rotational heating, lead nitrate $Pb(NO_3)_2$, was spun at incremental MAS rates, with the response of the isotropic resonance recorded as a function of MAS rate. The assumption is made that an MAS rate of 1 kHz provides a negligible amount of frictional heating, and thus is taken to mean the sample is at ambient temperature of the laboratory (293 K). Before acquisition, the sample was allowed to equilibrate for five minutes for every 1 kHz change in MAS rate, such that between 1 kHz and 2 kHz, five minutes were given, and between 5 kHz and 7 kHz, 10 minutes were given. Finally, FWHM is tabulated which is a measure of the temperature homogeneity of the sample. A full tabulation is given below in Table 2.A2. An MAS rate of 15 kHz leads to a heating of the sample of approximately 9 K, which can be factored into the temperature calibration of the temperature sensors.

To calibrate the temperature sensors, the sample is rotated at the desired MAS rate (15 kHz), the temperature is then systematically varied, with the response of the temperature detectors related to the sample temperature through the chemical shift response of $Pb(NO_3)_2$. The demanded temperature is the temperature the VT setup automatically regulates the temperature to based on the reading of one of the detectors. As temperature was systematically varied by using the temperature reading of this detector, the difference in temperature between experiments in reality is different to the demanded temperature difference. Experiments were completed across a detected temperature range of 330 K to 250 K, which after calibration relates to a true temperature range of 331 K to 252 K. Following a temperature change and prior to acquisition, the sample was allowed to equilibrate to the changed temperature. The period of time allowed for equilibration was one minute per K, such that for 10 K change, 10 minutes were allowed following the stabilisation of the temperature read from detector 1. Through correlation of the sample temperature from the chemical shift and the detected temperature, the true temperature can be elucidated from the read temperature. Full details can be found tabulated below in Table 2.A3, with correlation chart shown in Figure 2.A21.

Table 2.A2 Tabulation of the results of frictional heating temperature calibration of $Pb(NO_3)_2$. Carried out in a 3.2 mm rotor on a Bruker Avance III HD spectrometer.

MAS Rate (kHz)	δ (ppm)	$\Delta\ \delta$ (ppm)	Δ Temperature (K)	Detector 1 Read (K)	Detector 2 Read (K)	FWHM (ppm)	Sample Temperature (K)
1	−3503.614	0	0	295.7	296.0	0.27	293
2	−3503.659	−0.045	−0.03	295.6	295.9	0.27	292.97
3	−3503.354	0.26	0.20	295.5	295.9	0.27	293.2
4	−3503.103	0.511	0.38	295.5	295.8	0.25	293.38
5	−3502.707	0.907	0.68	295.6	295.8	0.28	293.68
7	−3501.416	2.198	1.66	295.8	295.7	0.46	294.66
9	−3499.585	4.029	3.03	296.2	295.7	0.58	296.03
11	−3497.209	6.405	4.82	296.8	295.9	0.79	297.82
13	−3494.417	9.197	6.93	297.4	296.1	1.02	299.93
15	−3490.993	12.621	9.50	298.3	296.4	1.23	302.50

Table 2.A3 Tabulation of the results of temperature detector calibration using $Pb(NO_3)_2$. Carried out in a 3.2 mm rotor on a Bruker Avance III HD spectrometer, with sample rotating at 15 kHz. *T* = Temperature

T **Detector 1 (K)**	***T*** **Detector 2 (K)**	***T*** **Sample (K)**	**FWHM (ppm)**	**Detector 1 Calculated *T* (K)**	**Detector 1 Deviation (K)**	**Detector 2 Calculated *T* (K)**	**Detector 2 Deviation (K)**
330	345.8	331.23	1.32	330.91	−0.32	331.05	−0.19
320	330.9	323.15	1.14	322.98	−0.17	323.31	0.16
310	316.6	315.00	1.05	315.06	0.06	315.89	0.89
300	300.4	306.96	0.99	307.13	0.17	307.49	−0.190.52
297	294.3	304.18	1.03	304.75	0.57	304.32	0.14
290	282.8	298.78	1.01	299.20	0.42	298.35	−0.43
280	271.7	292.92	1.30	291.28	−1.64	292.60	−0.32
270	250.6	282.65	1.03	283.35	0.70	281.65	−1.00
260	233.9	274.48	1.01	275.42	0.94	272.98	−1.50
250	223.3	267.43	1.18	267.50	0.07	267.48	0.05
240	207.9	259.70	1.17	259.57	−0.13	259.49	−0.21
230	197.4	252.17	1.31	251.64	−0.53	254.04	1.87

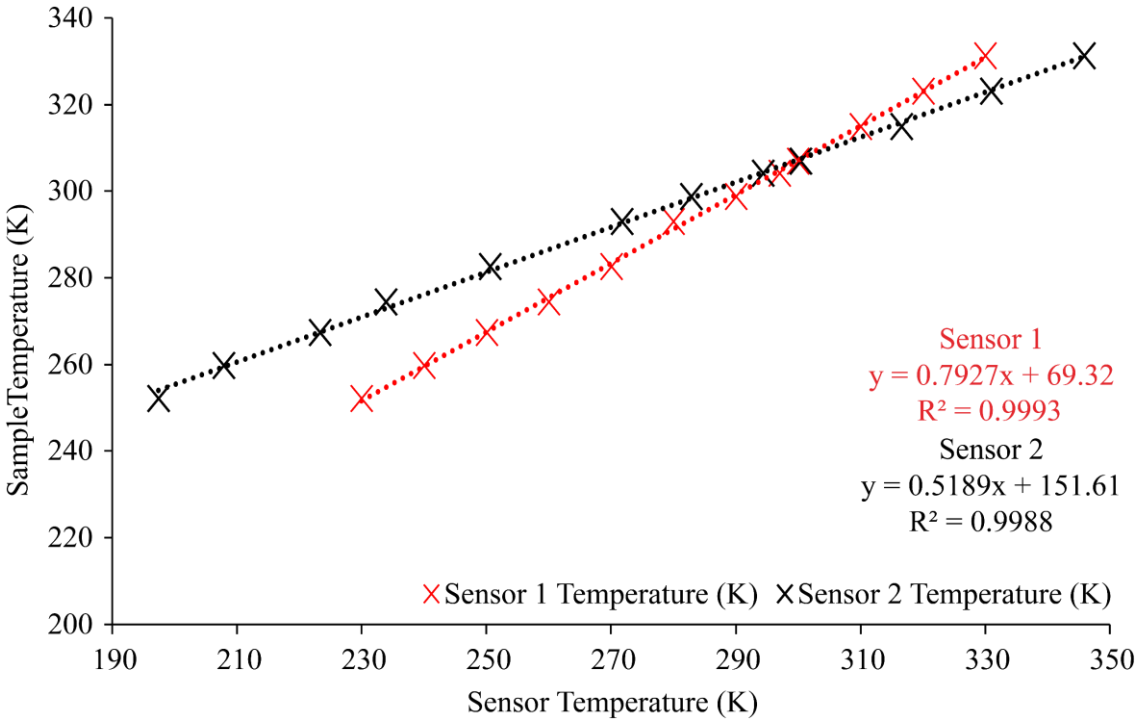

Figure 2.A21 Correlation plot of the temperature calibration of two temperature sensors using $Pb(NO_3)_2$.

Chapter 3

Understanding the Structure of Pristine Organic Battery Anode Materials

3.1 Introduction

3.1.1 Lithium- and Sodium-Ion Battery Materials

In recent decades, batteries have held an increasing importance in everyday life. Lithium-ion batteries (LIBs) are now well-established in society with a growing focus on green-tech applications, including electric vehicles, demand for LIBs is set to increase further. As their usage increases, there are concerns surrounding the ethics and sustainability of the raw materials used, which is driving development of new battery chemistries. One aspect concerns the development of new chemistries based on more sustainable charge carrying ions, such as sodium which is seen as a low-cost alternative to lithium due to its much higher natural abundance. Another goal is to increase the sustainability of other aspects of battery chemistry. In this respect, organic compounds based on layered conjugated carboxylate salts have gained interest in recent years as potential anode materials for lithium- and sodium-ion batteries. In principle these organic coordination polymers can be derived from green and sustainable sources or from recycled waste plastic.[1, 2]

Demonstrated in 2009 by Armand *et al*., one of the first candidate organic anode materials was lithium benzenedicarboxylate (Li_2BDC).[3] This lithium salt can undergo reversible lithiation by rearrangement of the π-electron conjugation system to incorporate two further Li^+ ions per formula unit, resulting in a formula of Li_4BDC. This reaction occurs at 0.8 V *vs*. Li^+/Li^0 and gives a specific capacity of 300 mA h g^{-1}. More recently, sodium dicarboxylates have also shown promising properties for sodium-ion batteries.[4] Armand and co-workers demonstrated that sodium benzenedicarboxylate (Na_2BDC) can also reversibly intercalate Na^+ ions with a capacity of 250 mA h g^{-1} at a voltage of 0.4 V *vs*. Na^+/Na^0.[4] Park *et al*. subsequently demonstrated that Na_2BDC can exhibit rate performance equivalent to commercial LIBs.[5]

As interest in organic anode materials has increased, a number of systematic studies have attempted to gain insight into their reduction mechanisms and structure-property relationships. It has been demonstrated that increasing the length of the conjugation system of the organic backbone can improve cycling stability as a result of increased electronic conductivity.[6-10] This effect can be seen when comparing benzenedicarboxylate (BDC) based molecules with biphenyldicarboxylate (BPDC) based molecules such as lithium BPDC (Li_2BPDC) and sodium BPDC (Na_2BPDC).[11] However the drawback to increasing the length and molecular weight of the organic backbone is that this reduces the specific capacity of the material. This can be partially mitigated by using directly adjacent ring systems, such as those found in naphthalene.[12-15] Lithium naphthalenedicarboxylate (Li_2NDC) and sodium naphthalenedicarboxylate (Na_2NDC) both feature two rings in the organic component of the structure, while possessing a lower molecular weight than the BPDC analogues.

Despite the progress that has been made in understanding structure-property relationships in organic anodes, there is still no clear consensus on the precise structural details of the reduction mechanisms. In order to understand these, it is necessary to have a detailed understanding of the crystal structure, and to have characterisation methods that are capable of probing both the long-range and local structure. The crystal structures of many organic anode materials are known from single-crystal X-ray diffraction (SCXRD) but NMR has not previously been widely used to characterise the local structures. For studying battery cells, it is also important to have techniques that are capable of providing atomic-level structural information for powder samples that are used in electrode formulations. Here, NMR crystallography (discussed previously in Chapter 2 section 2.5) can provide a wealth of information.[16-18] In particular, organic anode materials feature several NMR active nuclei enabling local probing of the structure at many different positions in the structure.

In this chapter, a systematic study of model organic anode materials for lithium- and sodium-ion batteries using NMR crystallography is presented. The purpose of this work is to evaluate the use of NMR crystallography for a set of materials which share common structural features and interactions, in order to progress onto the study of structural changes upon lithiation and sodiation discussed later in Chapter 4. A key consideration in organic conjugated carboxylates is the presence of weak non-bonding interactions between ligands, which are not well accounted for by standard density functional theory (DFT) approaches. Therefore, a range of different DFT structural optimisation methods are evaluated herein, including the use of semi-empirical dispersion correction (SEDC), with consideration given to the effect on the optimised crystal structure and calculated NMR parameters. It is shown that the choice of optimisation method can have a measurable effect on the unit cell parameters and atomic positions from the point of view of powder XRD (PXRD), but that in most cases the effect on

the local structure is small and calculated NMR parameters are relatively insensitive to the optimisation method used. The results also provide insight into the hydration behaviour of two salt forms which have as-yet uncharacterised structures.

3.2 Experimental Details

3.2.1 Synthetic Details

Li_2BDC was synthesised following a procedure adapted from that reported by Armand and co-workers.[3] An aqueous solution (20 mL) of LiOH (0.53 g, 22.20 mmol) was combined with a solution of terephthalic acid (1.03 g, 6.22 mmol) in ethanol (50 mL). The combined solution was stirred at reflux conditions for 12 hours. The resulting milky solution was washed with ethanol yielding a white powder, which was filtered and then dried for 24 hours at 120 °C *in vacuo*.

Li_2NDC was synthesised following a procedure adapted from that reported by Ogihara and co-workers.[14] Methanol (100 mL) was added to an aqueous solution (0.23 mL) of LiOH (0.33 g, 13.78 mmol). 2,6-naphthalenedicarboxylic acid (0.98 g, 4.53 mmol) was added rapidly under stirring. The solution was stirred at reflux conditions for 12 hours. The resulting white solid was filtered, washed with methanol and dried at 120 °C *in vacuo* for 24 hours.

Li_2BPDC was synthesised following a procedure adapted from that reported by Choi *et al.* for the synthesis of sodium biphenyldicarboxylate.[11] An aqueous solution (50 mL) of 4,4-biphenyldicarboxylic acid (4.80 g, 19.82 mmol) was combined with an aqueous solution (15 mL) of LiOH (1.40 g, 58.46 mmol) under stirring. This solution was stirred for 12 hours at ambient temperature. The resulting precipitate was filtered, washed with ethanol and dried for 24 hours at 120 °C *in vacuo*.

Na_2BDC was synthesised following a procedure adapted from that reported by Kaduk.[19] Terephthalic acid (1.73 g, 10.41 mmol) was added to a warm aqueous solution (5 mL) of NaOH (1.38 g, 34.50 mmol). Deionised water (40 mL) was added until the acid dissolved, at which point ethanol (30 mL) was added slowly to the clear solution at 80 °C until a precipitate formed. This mixture was then stirred at reflux conditions for two hours. The resultant suspension was filtered, washed with ethanol and dried at 120 °C *in vacuo*.

Na_2NDC was synthesised following a procedure adapted from that reported by Cabañero *et al.*[15] NaOH (0.25 g, 6.25 mmol) was dissolved in methanol (50 mL), to this solution 2,6-naphthalenedicarboxylic acid (0.50 g, 2.31 mmol) was added rapidly under stirring. The solution was stirred at reflux conditions for 24 hours. The resulting solution was filtered, washed with methanol and dried at 120 °C *in vacuo*.

Na_2NDC tetrahydrate ($Na_2NDC{\cdot}4H_2O$) was synthesised following a procedure adapted from that reported by Cabañero *et al*.[15] Full discussion of this sample can be found in Section 3.7.1. 2,6-naphthalene dicarboxylic acid (0.50 g, 2.31 mmol) was added to a warm aqueous solution of NaOH (0.2 g, 5.00 mmol). Methanol was added (5 mL) and the resulting solution stirred for 30 minutes. The mixture was then exposed to acetone vapour inside a refrigerator and single-crystals were extracted after two weeks.

Na_2BPDC was synthesised following a procedure adapted from that reported by Choi *et al.*[11] An aqueous solution (50 mL) of 4,4-biphenyldicarboxylic acid (2.40 g, 9.91 mmol) was combined with an aqueous solution (15 mL) of NaOH (1.20 g, 30.00 mmol) and stirred for 12 hours at ambient temperature. The resulting precipitate was filtered, washed with ethanol and dried for 24 hours at 120 °C *in vacuo*.

Na_2BPDC monohydrate ($Na_2BPDC{\cdot}H_2O$) was synthesised following a procedure adapted from that reported by Choi *et al.*[11] An aqueous solution (13 mL) of 4,4-biphenyldicarboxylic acid (1.02 g, 4.21 mmol) was added to an aqueous solution (9 mL) of NaOH (0.6 g, 15.00 mmol). The resulting solution was exposed to ethanol vapours inside a refrigerator. Crystals began to appear within three weeks and were extracted after four weeks before being dried in air.

3.2.2 Solid-State NMR Details

Unless otherwise stated, Solid-state NMR experiments were performed on Bruker Avance III HD spectrometers operating at magnetic field strengths of 9.4 and 16.4 T. ^{13}C NMR spectra are referenced relative to tetramethylsilane using the methyl resonance of *L*−alanine at 20.5 ppm as a secondary reference. ^{7}Li NMR spectra are referenced relative to 1 M $LiCl_{(aq)}$ using solid LiCl at –1.2 ppm as a secondary reference. ^{23}Na NMR spectra are referenced relative to 1 M $NaCl_{(aq)}$ using solid NaCl at 7.5 ppm as a secondary reference. Full NMR details are given in the relevant figure captions but are summarised below.

^{13}C NMR spectra were recorded at a magic-angle spinning (MAS) rate of between 15 and 16 kHz using cross polarisation (CP) to transfer magnetisation from ^{1}H with a contact time of between 1 and 5 ms. The CP pulse power was ramped linearly from 70% to 100%. ^{1}H heteronuclear decoupling using two-pulse phase modulation (TPPM)[20] with a pulse length of 4.8 μs and a radiofrequency field strength of 100 kHz was applied during acquisition. Spectra are the sum of between 64 and 960 transients separated by a recycle interval of between 60 and 120 s.

The ^{7}Li MAS NMR spectra were recorded at a MAS rate of 5 kHz. Static spectra were recorded using a solid-echo (90°–τ–90°–τ–acquire) pulse sequence with a 16-step phase cycle.

Spectra are the sum of between 64 and 16,384 transients separated by a recycle interval of between 3 and 10 s.

The ^{23}Na MAS NMR spectra were recorded at a MAS rate of 12.5 kHz. Spectra are the sum of between 16 and 800 transients separated by a recycle interval of between 1 and 3 s.

^{23}Na multiple-quantum (MQ) MAS spectra were recorded at a MAS rate of 12.5 kHz using a split-t_1 pulse sequence. A two-component fast amplitude modulation pulse[21] was used for conversion of triple-quantum to single-quantum coherence. Spectra are the sum of between 192 and 768 transients for each of between 70 and 180 t_1 rows separated by a recycle interval of between 1 and 3 s.

3.2.3 Computational Details

First-principles calculations of theoretical NMR parameters were carried out using the CASTEP[22] code including the gauge-including projector augmented wave (GIPAW) algorithm,[23] which allows the reconstruction of the all-electron wave function in the presence of a magnetic field. The CASTEP calculations employed the Perdew-Burke-Ernzerhof (PBE) generalised gradient approximation (GGA) exchange-correlation (XC) functional,[24] and core valence interactions were described by ultrasoft pseudopotentials.[25] Other XC functionals used include the *meta*-GGA XC functional, revised PBE (rPBE),[26] and the regularized SCAN (rSCAN) XC functional.[27] Prior to the calculation of NMR parameters, structural models from diffraction experiments were geometry optimised using a range of different strategies, including full relaxation and the use of both DFT-D2 and DFT-D3 SEDC schemes.[28, 29] Finally, the damping parameter, *d*, was varied from the default value of 20, to an optimised value (d = 3.25) to match with a methodology reported in the literature.[30]

Geometry optimisations and NMR calculations were carried out using a planewave energy cut off, E_{cut}, of 50 Ry and a *k*-point spacing of 0.05 2π Å^{-1}. The calculations generate the absolute shielding tensor (σ) in the crystal frame. Diagonalisation of the symmetric part of σ yields the three principal components, σ_{XX}, σ_{YY} and σ_{ZZ}. The isotropic shielding, σ_{iso}, is given by (1/3)Tr[σ]. The isotropic chemical shift, δ_{iso}, is given by $\sigma_{ref} - \sigma_{iso}$, where σ_{ref} is a reference shielding determined by comparison of experimental chemical shifts over the complete range of structures. The quadrupolar coupling constant, $C_Q = eQV_{ZZ}/h$ and asymmetry parameter, $\eta_Q = (V_{XX} - V_{YY})/V_{ZZ}$ are obtained directly from the principal components of the electric field gradient tensor, which are ordered such that $|V_{ZZ}| \geq |V_{YY}| \geq |V_{XX}|$. Q is the nuclear quadrupole moment, and values of –40.1 and 104 mb were used for ^{7}Li and ^{23}Na respectively.[31] In addition to the magnitude, the calculations also generate the sign of C_Q. However, the sign of C_Q cannot be determined from the experimental data presented in this work; therefore, when comparing

calculated and experimental quadrupolar couplings, only the magnitude of the calculated C_Q is considered.

3.2.4 Crystallography Details

Single crystals were mounted on a Mitegen loop using Paratone-N oil and were analysed using an Rigaku Oxford Diffraction SuperNova diffractometer equipped with an Atlas S2 charge-coupled device (CCD) detector using CuKα radiation (λ = 1.54184 Å). Crystals were kept at 100 K during data collection. Using Olex2,[32] crystal structures were solved with the ShelXT[33] structure solution programme using Intrinsic Phasing and refined with the SHELXL[34] package using least-squares minimisation; data collection and integration was performed using CrysAlisPro.

Polycrystalline materials were analysed using powder XRD. Samples were analysed with a Rigaku SmartLab diffractometer equipped with a D/teX-ULTRA 250 High-Speed Position-Sensitive Detector system and a Ge(220)x2 2-bounce monochromator using CuKα_1 radiation (λ = 1.54059 Å) within a 2θ range of 5°−70° (step size of 0.01°).

Results of single crystal X-ray diffraction experiments were obtained from the literature for all six dicarboxylate salts. Deposition details for all structures used in this work can be found in Table 3.1.[11, 15, 19, 35-38]

Table 3.1 CCDC codes for crystal structures used in this chapter.

Structure	CCDC Deposition Number
Li_2BDC	664607
Li_2NDC	722281
Li_2BPDC	757041
Na_2BDC	145817
Na_2NDC	N/A
$Na_2NDC{\cdot}4H_2O$	1558952
$Na_2BPDC{\cdot}H_2O$	2120033 (This Work) & 944127

3.3 Results

3.3.1 X-ray Crystallography

Crystal structures for the six dicarboxylate salts are shown in Figure 3.1.[15, 19, 35-37] The structures considered are Li_2BDC ($Li_2C_8H_4O_4$), Li_2NDC ($Li_2C_{12}H_6O_4$), Li_2BPDC ($Li_2C_{14}H_8O_4$), Na_2BDC ($Na_2C_8H_4O_4$), Na_2NDC ($Na_2C_{12}H_6O_4$), and $Na_2BPDC{\cdot}H_2O$ ($Na_2C_{14}H_{10}O_5$). All structures shown are from the literature with the exception of $Na_2BPDC{\cdot}H_2O$, which was solved by single-crystal XRD analysis in this work (CCDC Deposition Number: 2120033). $Na_2BPDC{\cdot}H_2O$ is considered here as no reported structure of anhydrous Na_2BPDC could be found at the time of these investigations, however, the anhydrous phase is discussed later in Section 3.7.2. Each structure features metal carboxylate layers separated by diagonally offset organic linkers. The diagonal offset results in a herringbone-like stacking of the organic linkers.

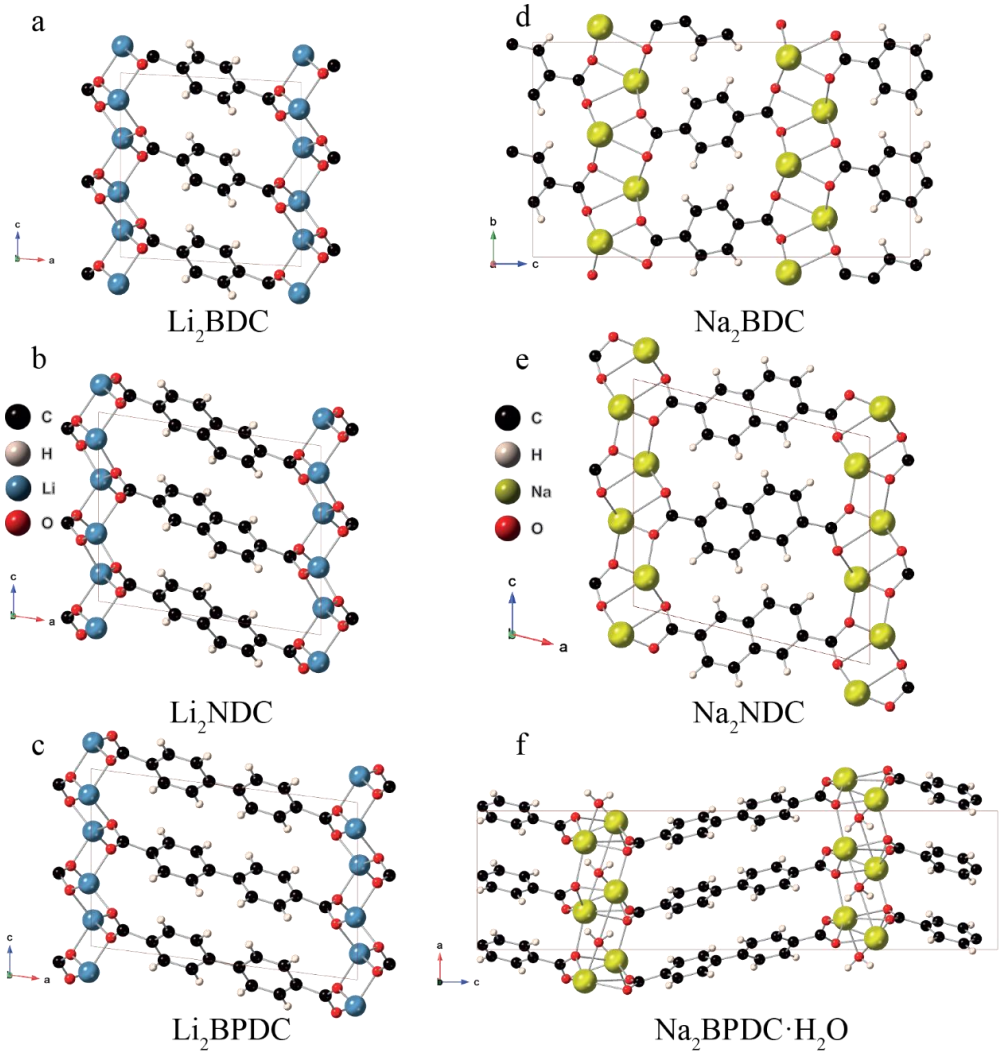

Figure 3.1 Crystal structures of (a) Li_2BDC, (b) Li_2NDC, (c) Li_2BPDC, (d) Na_2BDC, (e) Na_2NDC and (f) $Na_2BPDC{\cdot}H_2O$.

In the sodium salts, there is considerable further offset in both non-stacking dimensions, creating a double herringbone arrangement. In $Na_2BPDC{\cdot}H_2O$, a water molecule resides within the sodium carboxylate layer, increasing the inter-ionic distance between neighbouring sodium ions relative to the other sodium salts. Consequently, the inter-ring distance between the organic backbone units is also increased by ≈ 2 Å.

With respect to the metal ions, all lithium compounds have a single, crystallographically distinct lithium site, and the sodium compounds (Na_2BDC, Na_2NDC and $Na_2BPDC{\cdot}H_2O$) have two, one and two sodium sites, respectively. Li_2BDC possesses four carbon sites due to an inversion-type symmetry on the organic linker. This inversion-type symmetry is also found in Li_2NDC and Li_2BPDC, resulting in six and seven carbon sites, respectively. Although the sodium dicarboxylates feature a similar herringbone stacking arrangement observed in the lithium analogues, neither Na_2BDC nor $Na_2BPDC{\cdot}H_2O$ retain the inversion-type symmetry and as a result all carbon sites are crystallographically distinct. In contrast, Na_2NDC possesses six carbon sites, similar to its lithium analogue.

In general, the structures of the metal carboxylate layers are similar across all compounds, with one key difference between lithium and sodium compounds observed in the metal oxide layer. In the lithium compounds, lithium ions form almost planar layers, with each lithium ion coordinated to four oxygen atoms in a distorted tetrahedral geometry. In contrast, in the sodium compounds the metal ions are forced out of planarity by the increased ionic radius while also coordinating to between four and six oxygen atoms in more distorted geometries.

The six dicarboxylate salts were synthesised as powders according to the procedures described in Section 3.2.1. Experimental PXRD patterns are shown in Figure 3.2 together with simulated patterns based on the crystal structures. For the BDC and NDC salts, very good agreement is observed between the experimental and simulated patterns. For Li_2BPDC, small deviations in some of the peak positions and intensities are observed at high angles. It is noted that in the original structure solution, the sample was found to contain multiple components, suggesting that this material can crystallise in multiple polymorphs.[37] The simulated PXRD data is therefore based upon the structure determined for the major component as solved by Banerjee *et al*., but it is possible that other components with subtly different structures could also be present in the powder sample.[37] For $Na_2BPDC{\cdot}H_2O$, the experimental PXRD pattern for the powder sample shows some minor differences with a simulated pattern for the single-crystal structure determined in the current work. It is noted that a slightly different crystal structure was previously reported by Choi *et al*., which is characterised by a planar ring arrangement in contrast to the twisted ring arrangement in the structure from the current work (Figure 3.3).[11] A multi-phase Le Bail fit performed by Dr Kieran Griffiths shows that $Na_2BPDC{\cdot}H_2O$ crystallised

as a mixture (Figure 3.4). The mixture comprises a dominant orthorhombic phase, consistent with the structure solved by SCXRD in this work, and a further monoclinic phase consistent with the structure reported by Choi *et al*.[11]

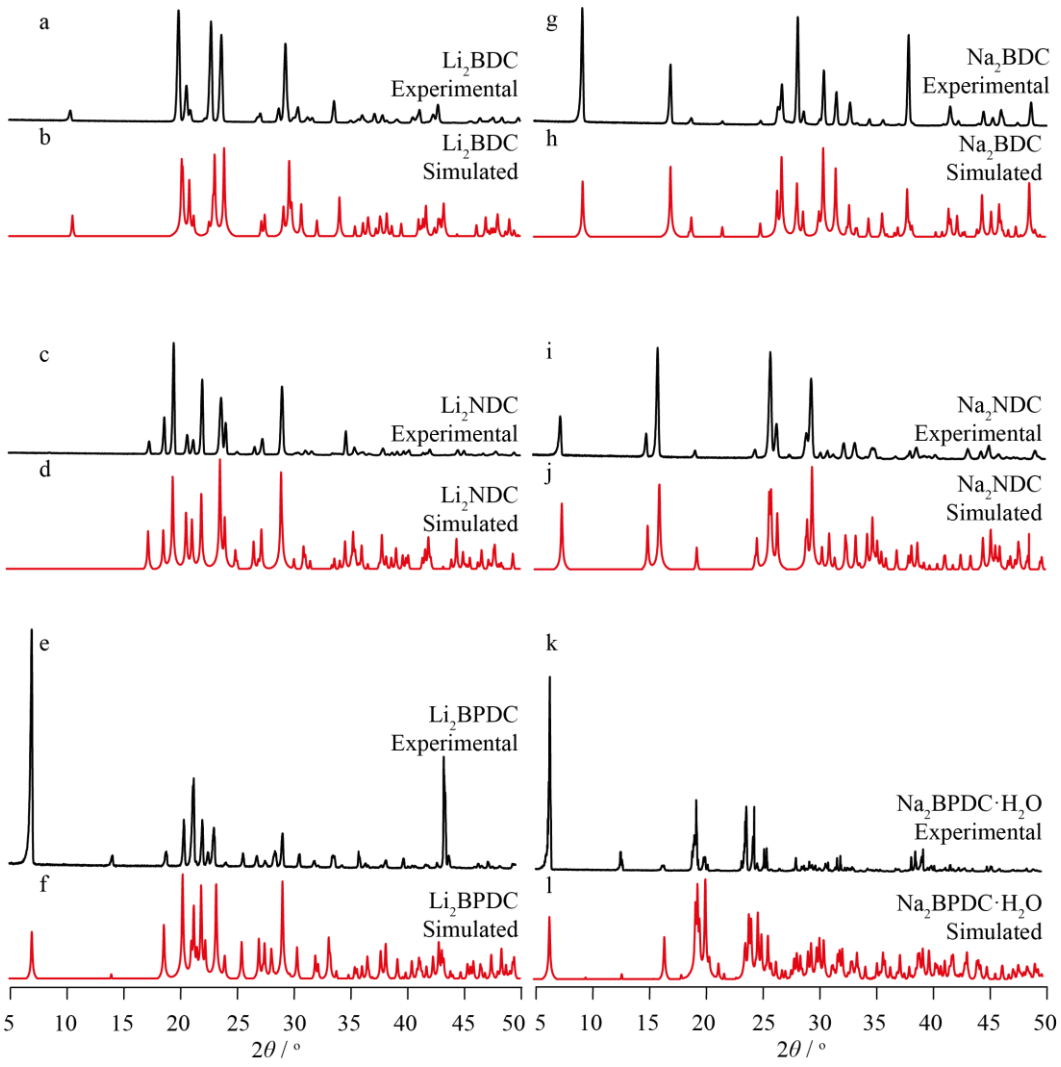

Figure 3.2 Experimental (black) and simulated (red) PXRD patterns for each of the six dicarboxylate salts.

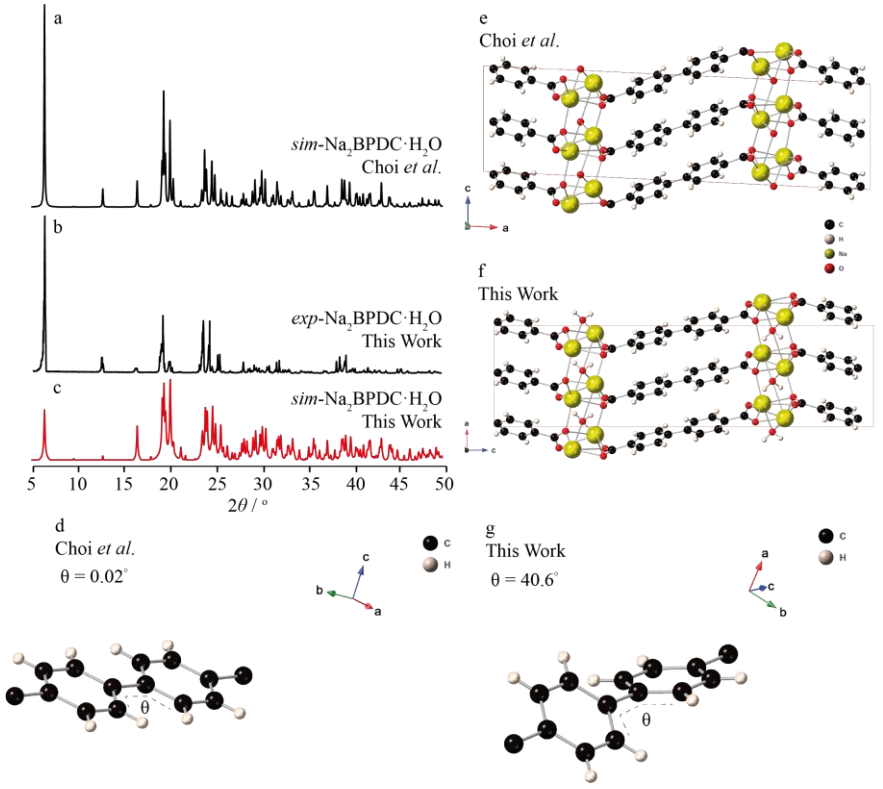

Figure 3.3 Experimental PXRD of $Na_2BPDC·H_2O$ (b) from This Work and simulated PXRD of $Na_2BPDC·H_2O$ from Choi *et al.* (a) and This Work (c). Crystal structures solved by single-crystal XRD from Choi *et al*. (e) and This Work (f). Comparison of torsional angle between the adjacent rings of the biphenyl backbone in the crystal structures from Choi *et al*. (d) and This Work (g).

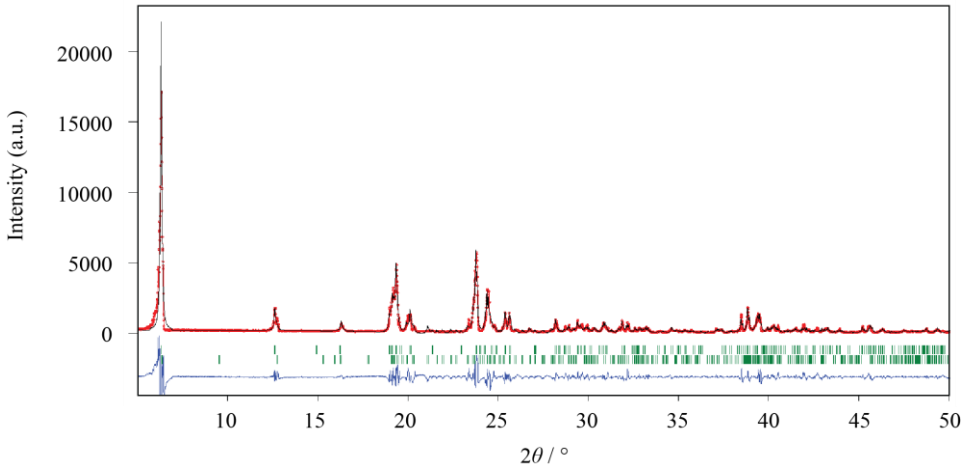

Figure 3.4 Le Bail fit of $Na_2BPDC·H_2O$. Two phases were identified. The crystal system of the dominant phase was found to be orthorhombic. The lattice parameters were refined to be a = 7.481(9) Å, b = 5.934(5) Å c = 28.057(4) Å, $\alpha = \beta = \gamma = 90°$. The space group was found to be $Pca2_1$. This is consistent with the structure solved in this work by SCXRD. The second crystal system was found to be monoclinic. The lattice parameters were refined to be a = 27.833(5) Å, b = 5.920(1) Å, c = 7.546(2) Å, $\alpha = \gamma = 90°$, $\beta = 92.71°$. The space group was found to be $P2_1/c$ which is consistent with the structure reported by Choi *et al.* The reliability (R) factor based on the powder profile *Rp* was 12.93%.

3.4 ^{13}C Solid-State NMR Spectroscopy

^{13}C cross polarisation (CP) MAS NMR spectra for each of the six organic salts are shown in Figure 3.5. Each spectrum shows characteristic resonances expected for the carboxylate and ring carbons present in the structures. For the lithium salts, the carboxylate resonances are shifted to higher chemical shift than those of the respective sodium salts; this can be attributed to the depletion of electron density at the carboxylate carbon due to the reduced electronegativity of the sodium ion, and the longer Na−O bond lengths in the sodium salts. For Li_2BDC, all of the crystallographically distinct carbon sites are resolved. For Li_2NDC, Li_2BPDC, Na_2BDC, and Na_2NDC, some of the crystallographically distinct ring carbons are unresolved. Despite chemical equivalence between some aromatic carbons, minor variations remain between their respective local bonding environments arising from crystallographic inequivalence, particularly relative position to adjacent rings. This produces small but notable differences in the respective chemical shifts.

For Na_2BPDC·H_2O, the two crystallographically inequivalent carboxylate sites at either end of the BPDC ligand are resolved. Figure 3.6 shows the torsional angles of the biphenyl backbone. Despite the chemical equivalence, the two carboxylate groups are crystallographically distinct, this distinction arises due to a difference in torsional angle relative to the adjacent rings. The plane of the O–C1–O bond is offset from the plane of the adjacent aromatic ring by approximately 2.5° – 4.8°, this is a considerably less distorted than the opposite carboxylate group where the O–C14–O plane is offset from the adjacent ring by approximately 11.3° – 12.7°. Thus, this results in the appearance of two carboxylate resonances in the ^{13}C CPMAS NMR spectrum.

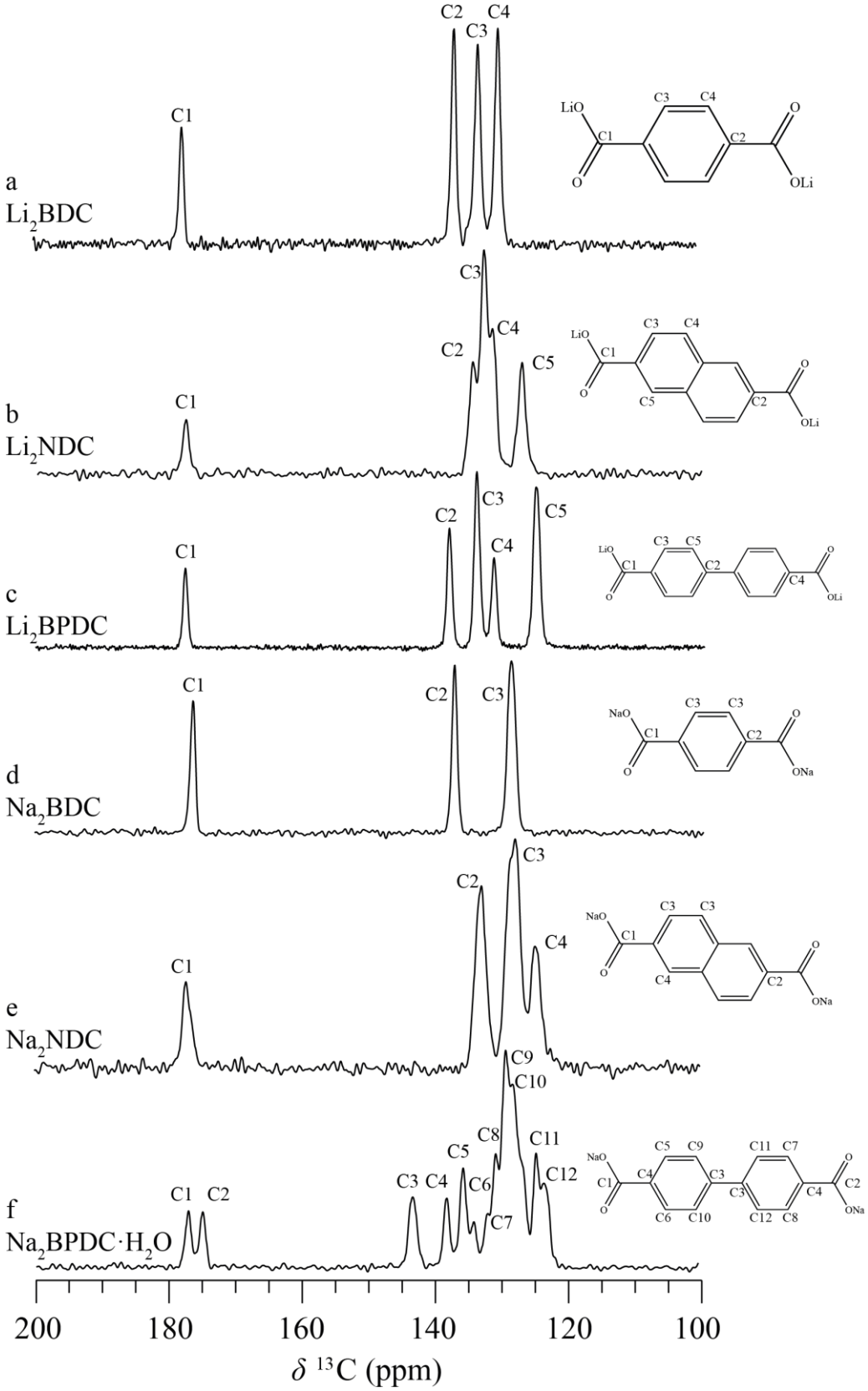

Figure 3.5 Assigned ^{13}C CPMAS NMR spectra of (a) Li_2BDC, (b) Li_2NDC, (c) Li_2BPDC, (d) Na_2BDC, (e) Na_2NDC and (f) $Na_2BPDC{\cdot}H_2O$. Spectra collected at 16.4 T. MAS rates: (a, b, e, f) collected at 15 kHz, (c, d) collected at 16 kHz. Recycle intervals: 60 s (a, b) or 120 s (c-f). Contact pulse length: 1 ms (a, b), 3 ms (d, f) or 5 ms (c, e). Number of transients collected: (a) 240; (b) 960; (c) 304; (d) 64; (e) 104; (f) 464.

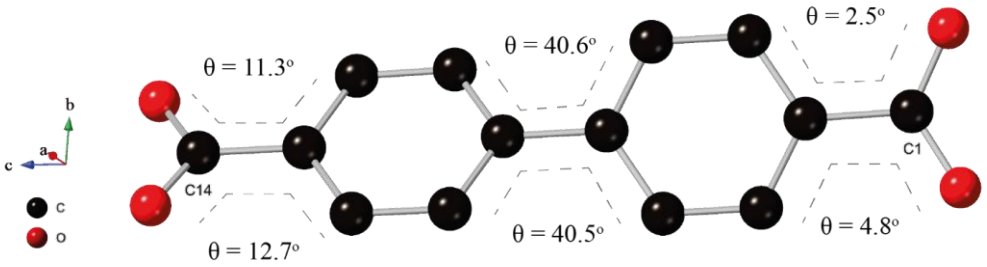

Figure 3.6 Torsional angles of carboxylate groups at either end of the $Na_2BPDC{\cdot}H_2O$ organic backbone in the SCXRD structure solved in this work. The carbonyl groups have slightly different orientations relative to their adjacent ring, which can explain the small chemical shift difference in the ^{13}C CPMAS NMR spectrum. Protons omitted for clarity.

3.5 Solid-State NMR Spectroscopy of Quadrupolar Nuclei

3.5.1 ^{7}Li Solid-State NMR Spectroscopy

Experimental ^{7}Li MAS and static NMR spectra for the three lithium salts are shown in Figure 3.7. Considering the MAS NMR data (Figure 3.7a, c and e), each spectrum comprises a central transition resonance surrounded by satellite transition spinning sideband manifolds. For both the static and MAS data, the lineshapes are broadened due to ^{7}Li–^{7}Li homonuclear dipolar coupling interactions; this also increases the intensity of the central pair of spinning sidebands

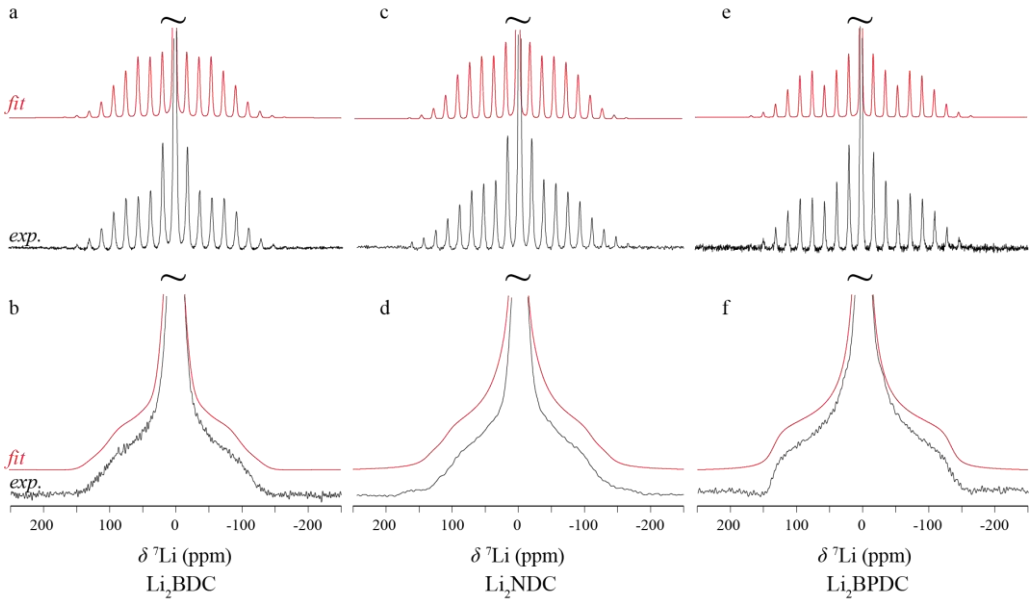

Figure 3.7 Experimental MAS (5 kHz, top) and static (bottom) ^{7}Li NMR of (a, b) Li_2BDC, (c, d) Li_2NDC and (e, f) Li_2BPDC. Fits to the experimental lineshapes are shown in red. Quadrupolar parameters are given in Table 3.2. Spectra were collected at 16.4 T. Recycle intervals: 3 s (a, b) or 10 s (c – f). Number of transients collected: (a) 64; (b) 512; (c) 128; (d) 16,384; (e) 128; (f) 16,384.

in the MAS data. Experimental chemical shift and quadrupolar parameters (summarised in Table 3.2) were determined by iteratively fitting the MAS and static spectra until consistent values were obtained. The measured chemical shifts of between −0.5 and 0.0 ppm are consistent with the small chemical shift range of ^{7}Li. The extracted C_Q values (71 – 75 kHz) and non-zero η_Q values between 0.5 – 0.9 are consistent with the distorted tetrahedral Li−O bonding geometry in the three salts.

Table 3.2 Summary of experimental ^{7}Li parameters for each lithium dicarboxylate salt.

Compound	δ (ppm)	$\lvert C_Q \rvert$ / kHz	η_Q
Li_2BDC	0.0 ± 0.3	71 ± 2	0.5 ± 0.1
Li_2NDC	−0.2 ± 0.1	74 ± 5	0.6 ± 0.1
Li_2BPDC	−0.5 ± 0.2	75 ± 5	0.9 ± 0.1

3.5.2 ^{23}Na Solid-State NMR Spectroscopy

^{23}Na MAS and MQMAS NMR spectra of the sodium salts are shown in Figure 3.8. ^{23}Na NMR parameters obtained by fitting to the sodium lineshapes are summarised in Table 3.3. The MAS spectrum of Na_2NDC shows a single second-order quadrupolar broadened resonance, which is consistent with the single crystallographic sodium site within the structure. MQMAS of Na_2NDC confirmed only one site is present in the sample (Figure 3.A26 of Appendix 3.1). The MAS NMR spectra of Na_2BDC and Na_2BPDC·H_2O both show second-order quadrupolar broadened lineshapes with features suggesting the presence of more than one unresolved resonance. In the corresponding MQMAS spectra, two sites are observed for both materials, in agreement with the crystal structures. Similar to the lithium salts, the high η_Q values measured for each site are consistent with the distorted non-axially symmetric Na−O bonding environments in each structure.

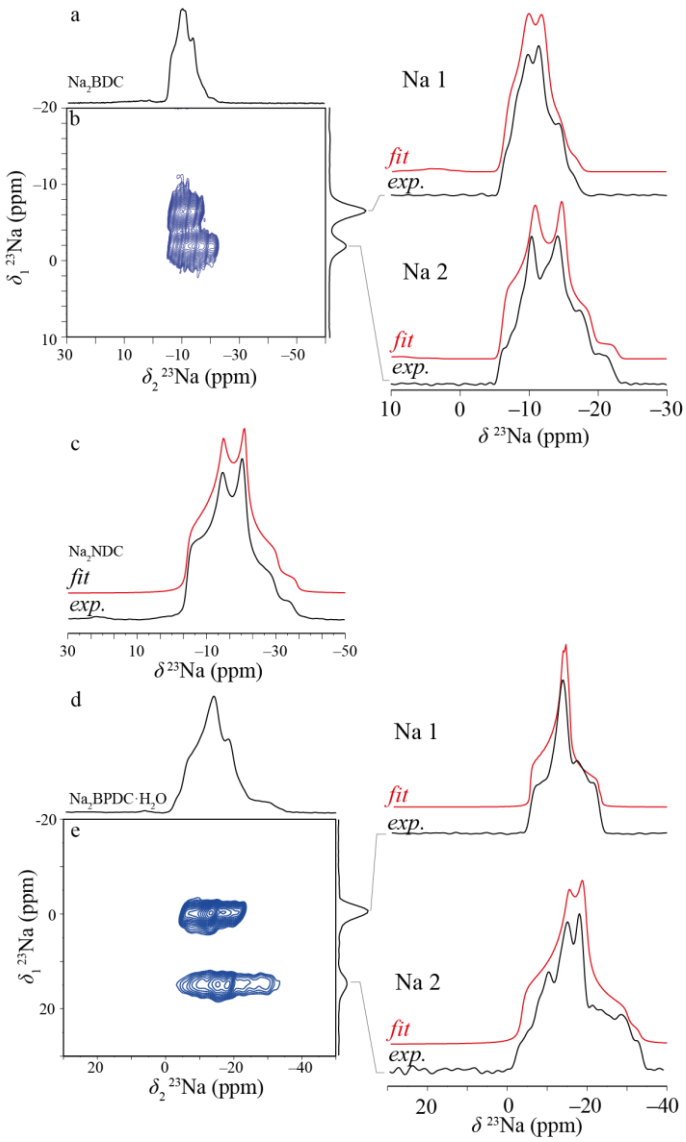

Figure 3.8 ^{23}Na MAS NMR spectra for (a) Na_2BDC, (c) Na_2NDC and (d) $Na_2BPDC{\cdot}H_2O$, and ^{23}Na MQMAS spectra of (b) Na_2BDC and (e) $Na_2BPDC{\cdot}H_2O$. Individual sodium lineshapes extracted from the MQMAS spectra are shown on the right together with fits (shown in red). All spectra recorded at 9.4 T with an MAS rate of 12.5 kHz. MAS spectra are the result of 800 (a), 408 (c) and 168 (d) transients separated by a recycle interval of 3 s. MQMAS spectra are the result of 384 (a) and 192 (e) transients for each of 70 (a) and 129 (e) t_1 rows separated by a recycle interval of 3 s.

Table 3.3 Summary of experimental ^{23}Na NMR parameters for the sodium dicarboxylate salts.

Compound	Site	δ (ppm)	$\lvert C_Q \rvert$ / MHz	η_Q
Na_2BDC	Na 1	−7.0 ± 0.8	1.3 ± 0.1	0.7 ± 0.1
	Na 2	−5.5 ± 0.6	1.6 ± 0.1	0.5 ± 0.1
Na_2NDC	Na 1	−4.0 ± 0.5	2.3 ± 0.1	0.6 ± 0.1
$Na_2BPDC{\cdot}H_2O$	Na 1	−4.8 ± 0.4	1.7 ± 0.1	0.9 ± 0.1
	Na 2	−2.8 ± 0.6	2.2 ± 0.1	0.8 ± 0.1

3.6 Density Functional Theory

3.6.1 Geometry Optimisation Procedures

DFT calculations are able to provide a link between experimental Solid-state NMR data and experimental crystallography data. Convergence testing was performed according to the procedure detailed in Chapter 2 Section 2.4.1 and using Li_2BDC and Na_2BDC as test systems for organic anode materials. Convergence of the basis set energy cut off, E_{cut}, and the number of *k*-points occurred in line with a previous test system, *L*-alanine, and so the assumption was made that the same values are appropriate for use in all calculations on organic anode materials discussed within this chapter. As such, E_{cut} = 50 Ry, and a 0.05 2π $Å^{-1}$ *k*-point spacing were used. Prior to the calculation of NMR parameters, crystal structures were geometry optimised. As discussed in Section 3.1, DFT often fails to describe long-range non-bonding interactions, such as van der Waals forces, adequately. This is because standard XC functionals only account for electron-electron interactions over a short distance, and in cases where the electron densities of two nearby atoms do not overlap, no interaction is observed. Since the electron density decays exponentially, atoms must be in relatively close proximity for an electron-electron interaction to be accounted for. This is particularly important for systems such as biomolecules and molecular crystals wherein long-range interactions can be particularly important. For the carboxylate salts considered in this work, much of the structure is defined by covalent bonds within the organic ligands and ionic bonds within the Li−O and Na−O layers, which should be well described by DFT. However, it is not clear to what extent weak interactions between adjacent ligands (e.g., π–π interactions between stacked or partially stacked rings) may influence the structure. The absence of electrostatic interactions can lead to unrealistic cell expansions during the geometry optimisation procedure. One way to address this is to constrain the unit cell parameters to the experimental values during the geometry optimisation; however, in recent years a number of semi-empirical dispersion correction (SEDC) schemes have been developed which modify the DFT-calculated energy using an empirically derived dispersion correction.[39] In this study, seven different geometry optimisation procedures (labelled A-G) were explored in order to assess how well different methods account for any dispersion interactions from the perspectives of both the optimised structure and the calculated NMR parameters. A summary of optimisation methods can be found in Table 3.4, but a detailed explanation can be found below.

In Method A, the unit cell parameters were constrained to experimental values and only proton positions were allowed to vary, such that the relative arrangement of the ligands and metal oxide layers were constrained to the experimental data. This method was designed to test the structures as determined by XRD but acknowledges the low scattering factor of the proton

Table 3.4 Labels used for different optimisation methods in this work.

Method	SEDC Scheme	Optimisation Parameters
A	None	Unit cell parameters and heavy atom positions fixed to experimental values. Proton positions allowed to vary
B	None	Unit cell parameters fixed to experimental values. All atom positions allowed to vary
C	None	Unit cell parameters and all atom positions allowed to vary
D	DFT-D2	Unit cell parameters and all atom positions allowed to vary
E	DFT-D3	Unit cell parameters and all atom positions allowed to vary
F	DFT-D2	Unit cell parameters fixed to experimental values. All atom positions allowed to vary. Damping parameter set to 3.25. Uses the rPBE XC functional.
G	None	Unit cell parameters and all atom positions allowed to vary. Uses the rSCAN XC functional.

and the ambiguity of the proton location by allowing optimisation of the proton position. In Method B, unit cell parameters were constrained to experimental values creating a fixed unit cell volume, while all atomic positions within were allowed to vary. In Method C, no geometric constraints are placed on the unit cell with all atom positions and unit cell parameters allowed to vary. In Method D, all atom positions and the unit cell parameters were allowed to vary with the inclusion of the commonly used DFT-D2 (sometimes referred to as Grimme 06) SEDC scheme.[28] The DFT-D2 method incorporates an additional energy term, E_{disp}, to describe the dispersion interaction. However, this early dispersion correction method suffers from two major drawbacks. Firstly, the coefficients used to describe the dispersion for each alkali metal (such as Li or Na herein) are not directly defined, instead are calculated from the average of the previous noble gas and group three element. Secondly, E_{disp} is scaled based on the choice of XC used, so is not constant but sensitive to the level of theory used. Method E again features the unconstrained unit cell but includes the use of the updated DFT-D3 SEDC scheme as reported in 2010 by Grimme and co-workers.[29] The updated D3 method implemented consideration for the effective volume of atoms, such that when an atom is surrounded tightly its electron density is less polarisable, and thus reduces the E_{disp}. An updated DFT-D4 SEDC scheme has recently been reported which introduces a charge dependence, although it had not been implemented into CASTEP during the course of these investigations.[40]

Method F is based on the recent work by Schurko and co-workers and features an alteration of the damping parameter, d, to 3.25 from the default value (d = 20).[30] d is an

additional parameter that corrects for inaccuracies caused by E_{disp} at short interatomic distances. To keep consistency with the reported method, Method F herein features fixed unit cell parameters with atom positions unrestricted, and the rPBE XC functional was used instead of the PBE XC functional. In that work, *d* was parameterised and refined using ^{15}N, ^{17}O and ^{35}Cl nuclei in a set of candidate structures consisting of neutral small organic molecules and HCl salts, with a value of 3.25 giving the strongest agreement. The final method, Method G, utilises the recent rSCAN *meta*-GGA XC functional reported in 2019 by Bartók-Pártay and Yates, with no constraints on the unit cell.[27] rSCAN (or regularized Strongly Constrained and Appropriately Normed) is an upgraded version of the SCAN functional[41] seeking to improve the method by increasing the numerical stability and creating a library of readily available ultrasoft pseudopotentials. The SCAN functional was the first *meta*-GGA to satisfy all known constraints that a semi-local functional can, which is particularly applicable for metal-oxides and semi-conductors. The rSCAN method unfortunately breaks some constraints in attempting to improve upon the SCAN method.[42] Many revisions of the SCAN functional have been reported in recent years, such as r^{2}SCAN, r^{4}SCAN and r++SCAN.[43, 44] No SEDC scheme is included as the rSCAN functional was incompatible with the use of SEDC schemes inside of the CASTEP program at the time calculations were completed. Although in recent years, the incorporation of dispersion correction into SCAN functionals has become an active research area.[42, 45, 46]

3.6.2 Unit Cell Dimensions

Figure 3.9 shows percentage changes in unit cell parameters and volumes for all optimisation methods where the unit cell was allowed to vary (Methods C, D, E and G). Method C resulted in significant increases of unit cell volume of between 6% − 20% for all structures (Figure 3.9a). For most structures, the expansion is anisotropic with a dominant contribution to the volume expansion along one particular dimension. In all cases, the dominant expansion dimension is parallel to the axis defining the herringbone stacking arrangement of the organic linkers. To illustrate, Figure 3.10 shows the distance between the centre of two stacked aromatic rings in Na_2NDC highlighted by orange '*Zz*' ghost atoms. Following optimisation *via* Method C, the distance between the stacked rings increased by 21.6% from 3.617 Å to 4.399 Å.

Figure 3.9b shows changes in unit cell parameters and volume for structures optimised *via* Method D. These results show a clear contrast to Method C, with slight contractions in unit cell volume observed for all compounds. It is notable that the magnitudes of the contractions in unit cell volume (2% − 6%) are significantly smaller than the expansions observed for Method C (6% − 20%), indicating smaller overall changes to the structure during the optimisation process. It is also notable that the same dimensions are responsible for the contraction of the unit cell volume that were responsible for the unit cell expansions in Method C. The distance between the aromatic ring systems in the Na_2NDC structure decreased by 2.8% from 3.617 Å to

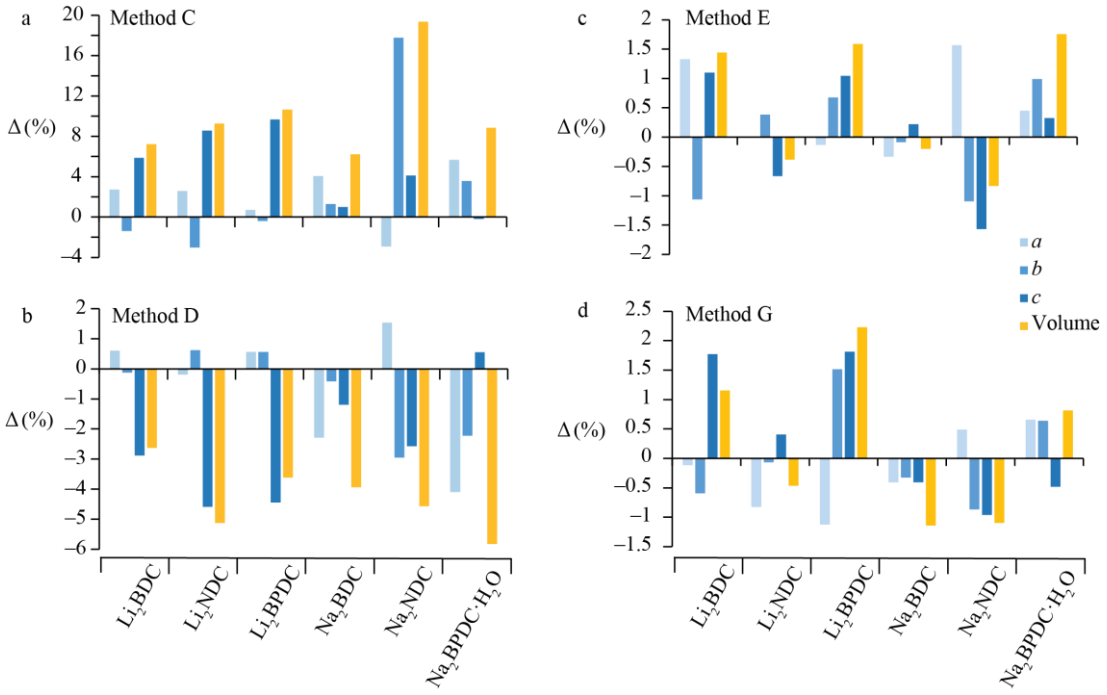

Figure 3.9 The percentage change in unit cell dimensions (*a*, *b*, *c*) and total unit cell volume between the unoptimised and optimised structures for optimisation Method C (a), Method D (b), Method E (c) and Method G (d) for each of the dicarboxylate salts (structures available in Figure 3.1). Full details of optimisation method can be found in Table 3.4.

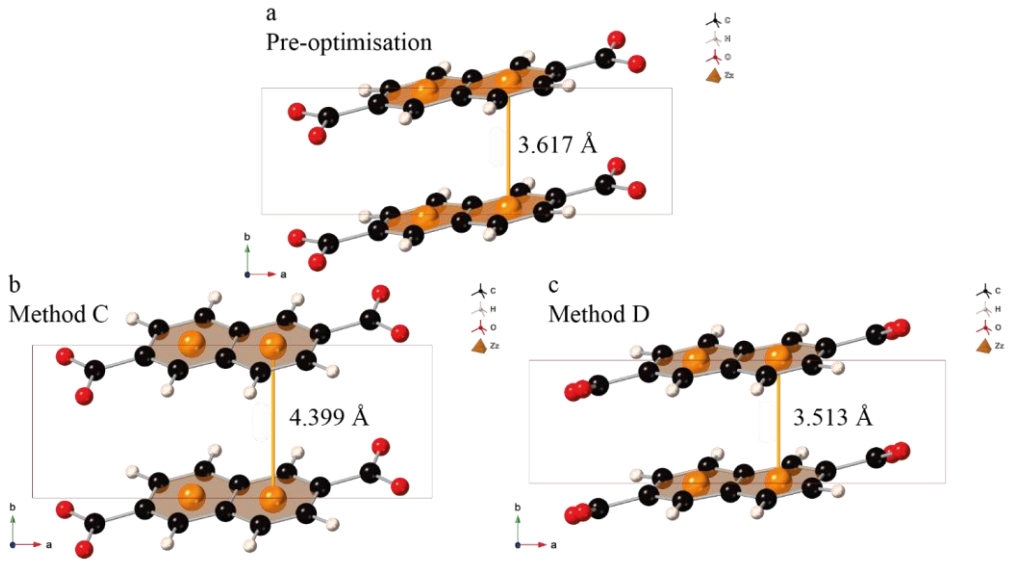

Figure 3.10 Inter-ring distance of Na_2NDC structures. Zz atoms (shown in orange) are artificially added centroid 'ghost' atoms to enable accurate measurement between the centre of two stacked aromatic rings. See Table 3.4 for full details of optimisation methods.

3.513 Å (Figure 3.10a and c). This shows that as the geometry optimisation causes unit cell changes, this also manifests in the form of changes to the relative geometries of the aromatic ring stacking structure, with contractions or expansions in similar magnitudes to the changes in unit cell volume.

Figure 3.9c shows the changes of unit cell parameters of structures when optimised by Method E. No overall trend is observed with both expansions and contractions observed across the structure set. Compared to Method C and D, the total unit cell volume undergoes much smaller changes with no expansions or contractions of >2% observed. Interestingly, a notable difference can be seen between the two SEDC methods D2 (Method D) and D3 (Method E), in which the D3 seems to give unit cell parameters much closer to those defined by XRD experiment. Furthermore, the anisotropic nature of expansions or contractions observed in Methods C and D is no longer present in Method E. Similar observations are made for Method G in Figure 3.9d, in which only small unit cell changes are observed, with no clear trend.

The expansions observed for Method C are consistent in magnitude to a study using a layered metal organic framework (MOF) which saw a ≈ 12% increase in unit cell volume using the equivalent geometry optimisation procedure.[47] This is notably larger than the expansion observed in a recent study (≈ 3%) that used the same geometry optimisation procedure on aluminophosphate (AlPO) compounds; however, AlPOs feature large 3D covalent bonding networks which are comparatively more rigid than the layered intramolecular bonding nature of metal carboxylate salts.[48] The contractions observed for Method D are consistent with the layered MOF and AlPO studies, where smaller magnitude contractions were seen (≈ 1%) with the inclusion of an SEDC scheme as part of the geometry optimisation.[48] A recent study of organoaluminium complexes observed large contractions of ≈ 8% using the same optimisation method; however, the structures considered were molecular complexes with an even greater structural dependence on weak intermolecular interactions.[49]

The clear differences in total unit cell volume change between the methods highlights the importance of weak π–π non-bonding interactions in defining the inter-ring stacking distance within the lithium and sodium carboxylate structure considered here. Furthermore, they show that the inclusion of an SEDC scheme in the optimisation procedure can effectively address the large expansions observed in the standard DFT approach. When an SEDC scheme is used, the unit cell changes are much smaller, but there is an overall tendency for structural contraction. One potential explanation for this could be thermal effects in the diffraction-derived structures which are typically obtained at temperatures between 90 – 150 K. In contrast, the DFT calculations do not account for temperature effects and therefore will not reproduce any thermal expansion that may be present in real structures under experimental conditions at finite temperatures.[48] However, since the main dimension of contraction is also the one that defines the organic linker stacking, the observed contractions could also suggest that the SEDC scheme slightly overestimates the strength of the π–π interactions between the linkers.

In addition to changing the unit cell size, it is important to consider how the atomic positions within the unit cell change during geometry optimisation. This can be explored through comparison of simulated PXRD patterns for the optimised structures (Figure 3.11 and Figure 3.12). The position of reflections can be solely determined from the unit cell dimensions, therefore in Methods A, B and F where the unit cell is fixed no changes in positions are observed; however the reflection intensities do vary. Unsurprisingly then, the largest deviations from the experimental PXRD data are observed for Method C accompanying the large unit cell changes. Here, in addition to a tendency for peaks to shift to lower 2θ (consistent with the unit cell expansion), the relative positions and intensities of peaks also changes significantly for some structures. This shows that the significant unit cell expansions observed for this method are also accompanied by changes in the relative arrangements of the ligands and metal carboxylate layers. It is also noteworthy that although the methods incorporating fixed unit cells and SEDC generally show closer agreement with the experimental data, there are still notable changes in relative peak positions with those methods where the heavy atom positions and unit cell dimensions are allowed to vary.

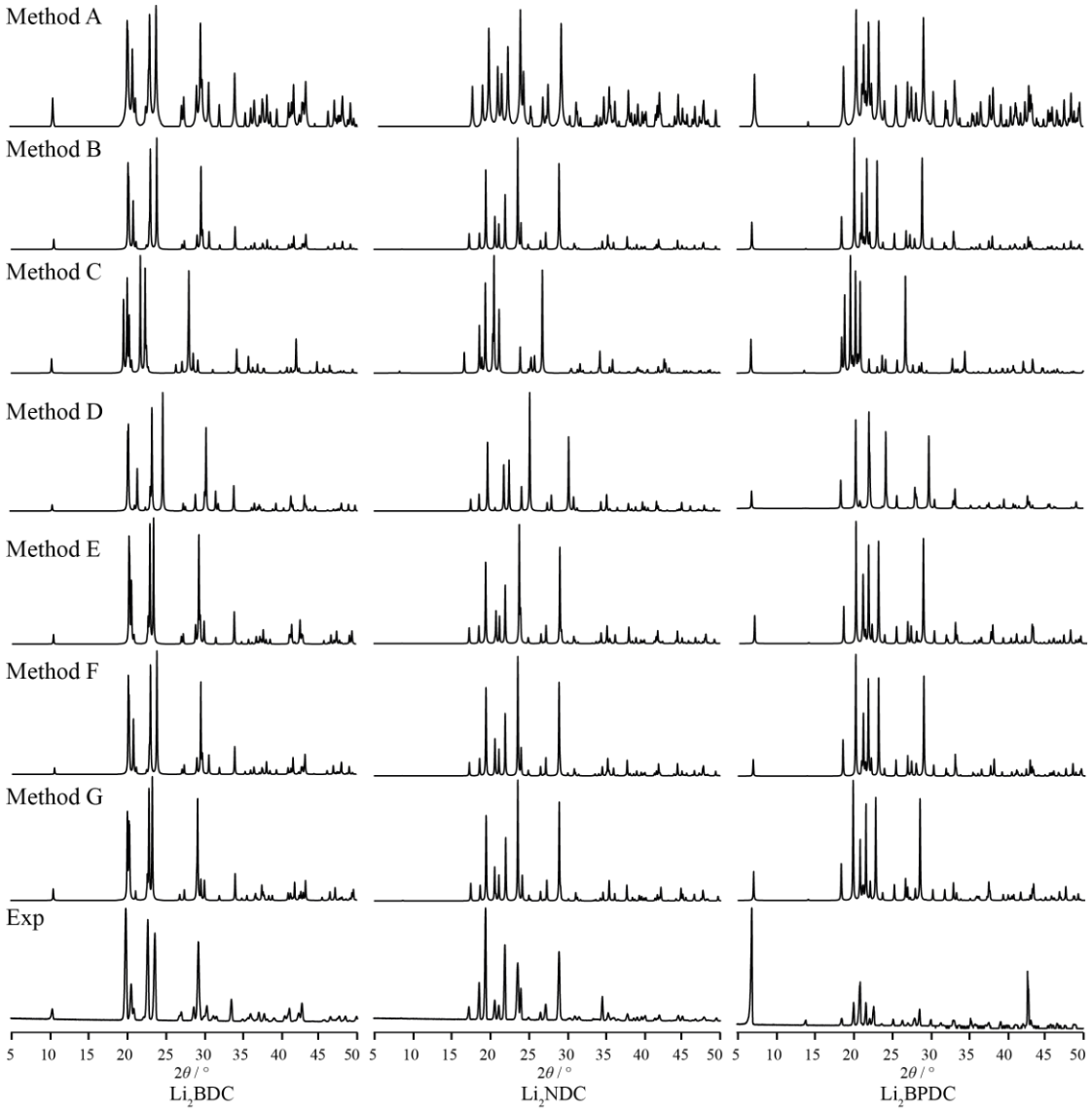

Figure 3.11 Comparison of experimental and post-geometry optimisation simulated PXRD of lithium dicarboxylate salts. See Table 3.4 for full details of optimisation methods.

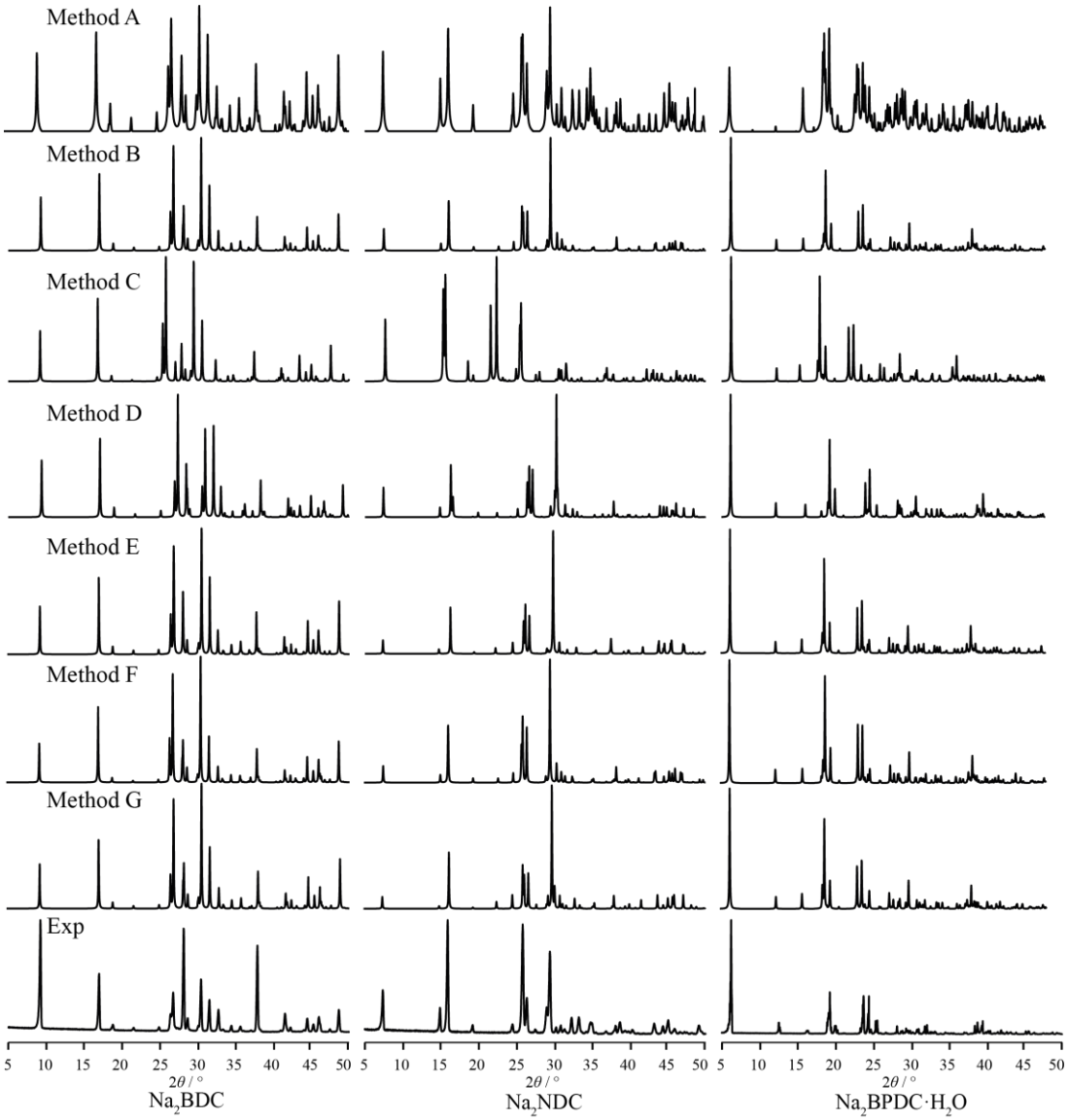

Figure 3.12 Comparison of experimental and post-geometry optimisation simulated PXRD of sodium dicarboxylate salts. See Table 3.4 for full details of optimisation methods.

3.6.3 Calculated ^{13}C NMR Parameters

Correlations of the experimental chemical shifts with the calculated chemical shieldings for each metal dicarboxylate salt from each of the optimisation methods are shown in Figure 3.13. All optimisation methods give linear correlations with gradients close to −1. Method A gives the weakest correlation ($R^2 = 0.9786$) compared with the other methods ($R^2 = 0.9955 – 0.9985$), which highlights that proton optimisation alone is not sufficient to give good agreement for ^{13}C NMR. In particular, Na_2NDC shows particularly poor agreement, with the data point corresponding to the carboxylate group ($\sigma^{iso,\,calc} = -18$ ppm) lying furthest from the line of best fit. Methods B – G show improved correlations with similar scatter, suggesting that the optimisation approach does not have a significant impact on the ^{13}C chemical shieldings,

providing that all atoms are optimised. For Methods A – E, the reference shielding based on the correlations are within ±1 ppm of each other, while Methods F and G have much higher reference values (+8 ppm and +16 ppm respectively), though the overall agreement is unaffected. Interestingly, the large unit cell expansion observed for Method C does not appear to significantly affect the overall correlation. Similarly, the small unit cell contractions observed for Method D also do not reduce the overall agreement. Overall, these results show that while different optimisation strategies alter the geometry of the structures, they do not appear to significantly affect the ^{13}C chemical shifts, provided that all atoms are optimised.

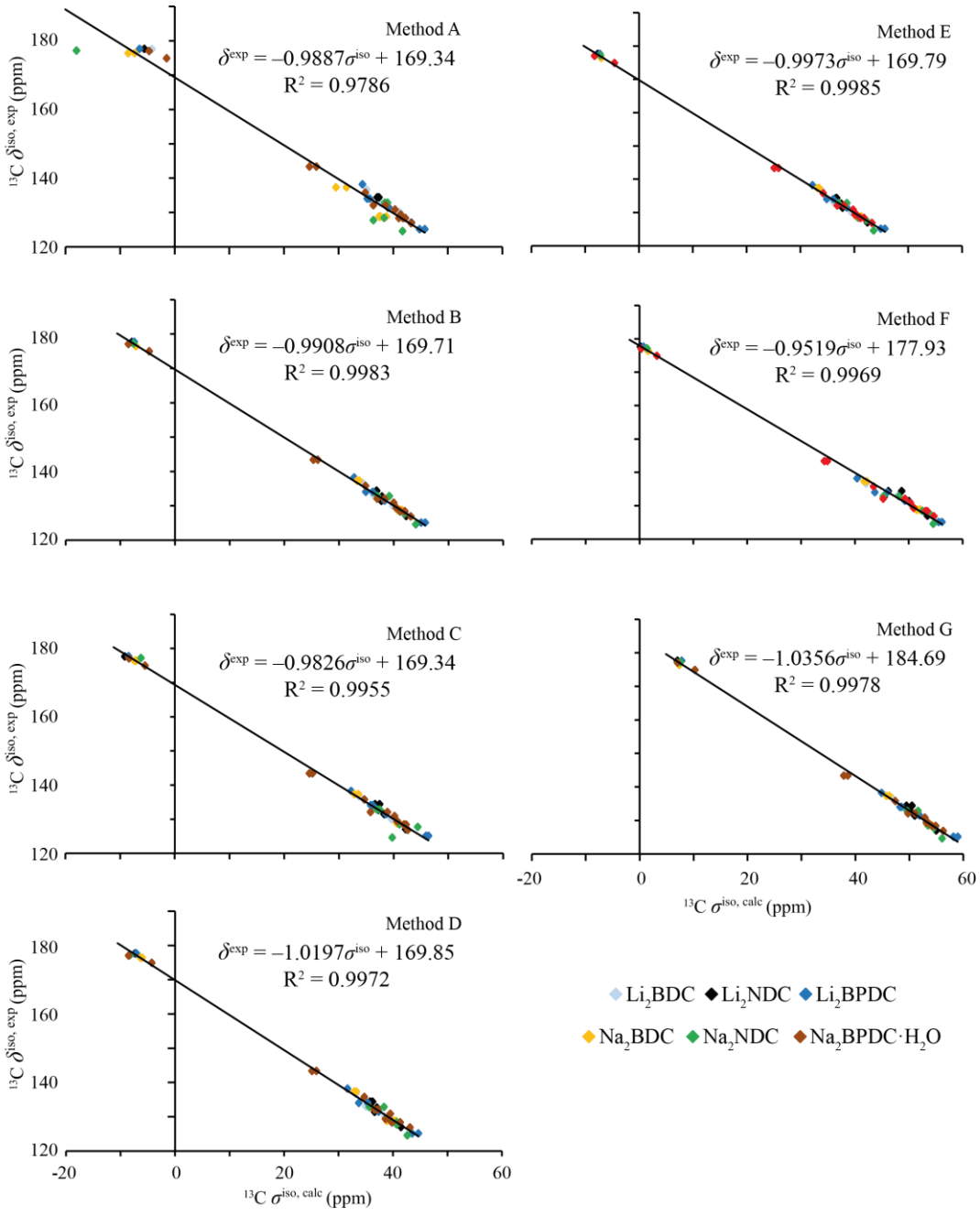

Figure 3.13 Plot of ^{13}C calculated chemical shielding and experimental isotropic chemical shift. Full details of optimisation methods can be found in Table 3.4.

3.6.4 Calculated ^{7}Li NMR Parameters

To aid comparison of the calculated parameters and experimental quadrupolar parameters, experimental C_Q and η_Q values were converted to the three individual components of the EFG tensor, V_{XX}, V_{YY} and V_{ZZ}. Magnitudes of the experimental and calculated tensor components are correlated in Figure 3.14. Full summaries of the calculated quadrupolar parameters together with simulated ^{7}Li spectra are shown in Table 3.5, Figure 3.15 and Figure 3.16.

Figure 3.14 shows that the calculated ^{7}Li quadrupolar NMR parameters give reasonable agreement with experiment for all methods with a tendency for calculated tensor components to be overestimated by between 21 − 35%. Reasonable scatter is observed in all cases with no method showing a notable differences in accuracy compared to the others.

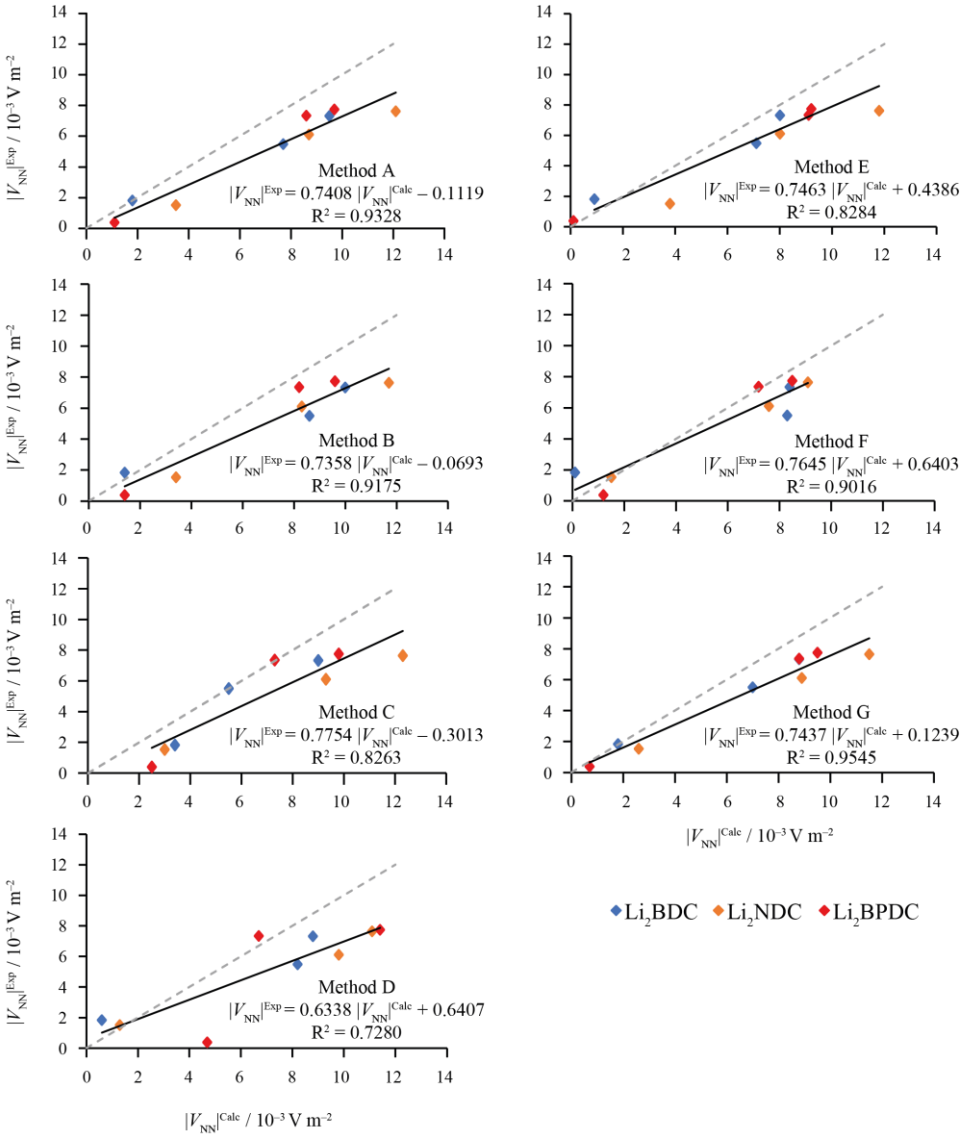

Figure 3.14 Plot of calculated and experimental ^{7}Li quadrupolar tensor components for lithium dicarboxylates. $|V_{NN}|$ = V_{XX}, V_{YY} and V_{ZZ}. Grey dashed line represents perfect agreement. Full details of optimisation method can be found in Table 3.4.

Table 3.5 Summary of calculated ^{7}Li NMR parameters from CASTEP for each lithium dicarboxylate salt. See Table 3.4 for full details of optimisation methods.

Compound	Optimisation Method	δ (ppm)	$\lvert C_Q \rvert$ / kHz	η_Q
Li_2BDC	A	−0.80	89	0.63
	B	−0.72	94	0.73
	C	−1.10	84	0.23
	D	−0.60	83	0.86
	E	−0.76	76	0.78
	F	−1.28	79	0.99
	G	−0.34	83	0.59
Li_2NDC	A	−0.77	114	0.43
	B	−0.72	110	0.41
	C	−1.22	115	0.52
	D	−0.55	105	0.77
	E	−0.68	111	0.36
	F	−1.31	85	0.67
	G	−0.31	118	0.55
Li_2BPDC	A	−0.62	91	0.77
	B	−0.65	91	0.70
	C	−1.23	93	0.49
	D	−0.51	107	0.17
	E	−0.69	86	0.98
	F	−1.18	80	0.71
	G	−0.28	90	0.86

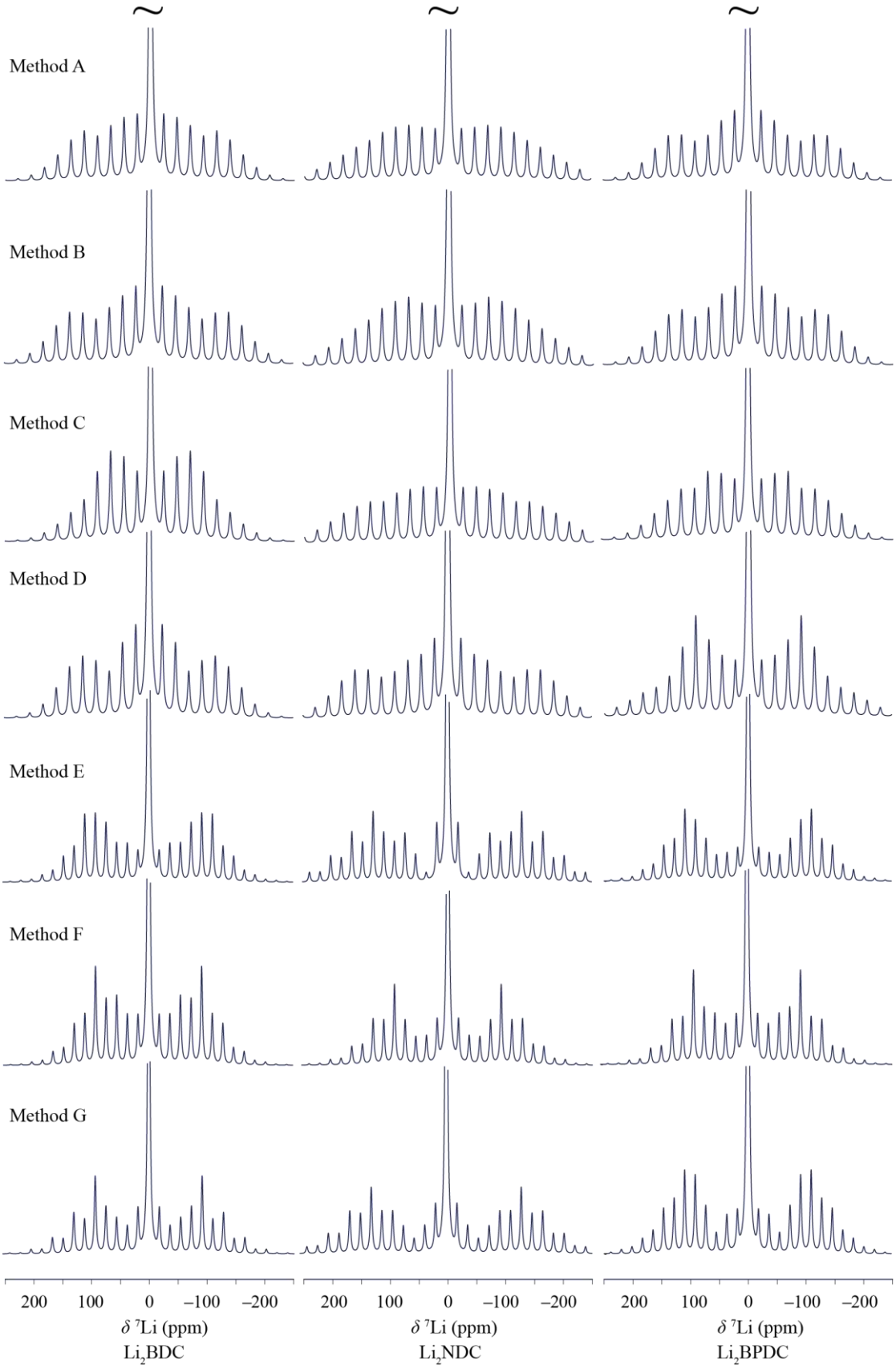

Figure 3.15 Simulated ^{7}Li MAS NMR spectra assuming a MAS rate of 5 kHz. Spectra have been cropped and scaled vertically to show the features of the quadrupolar lineshape. See Table 3.4 for full details of optimisation methods. Spectra generated using SIMPSON and visualised in GSim

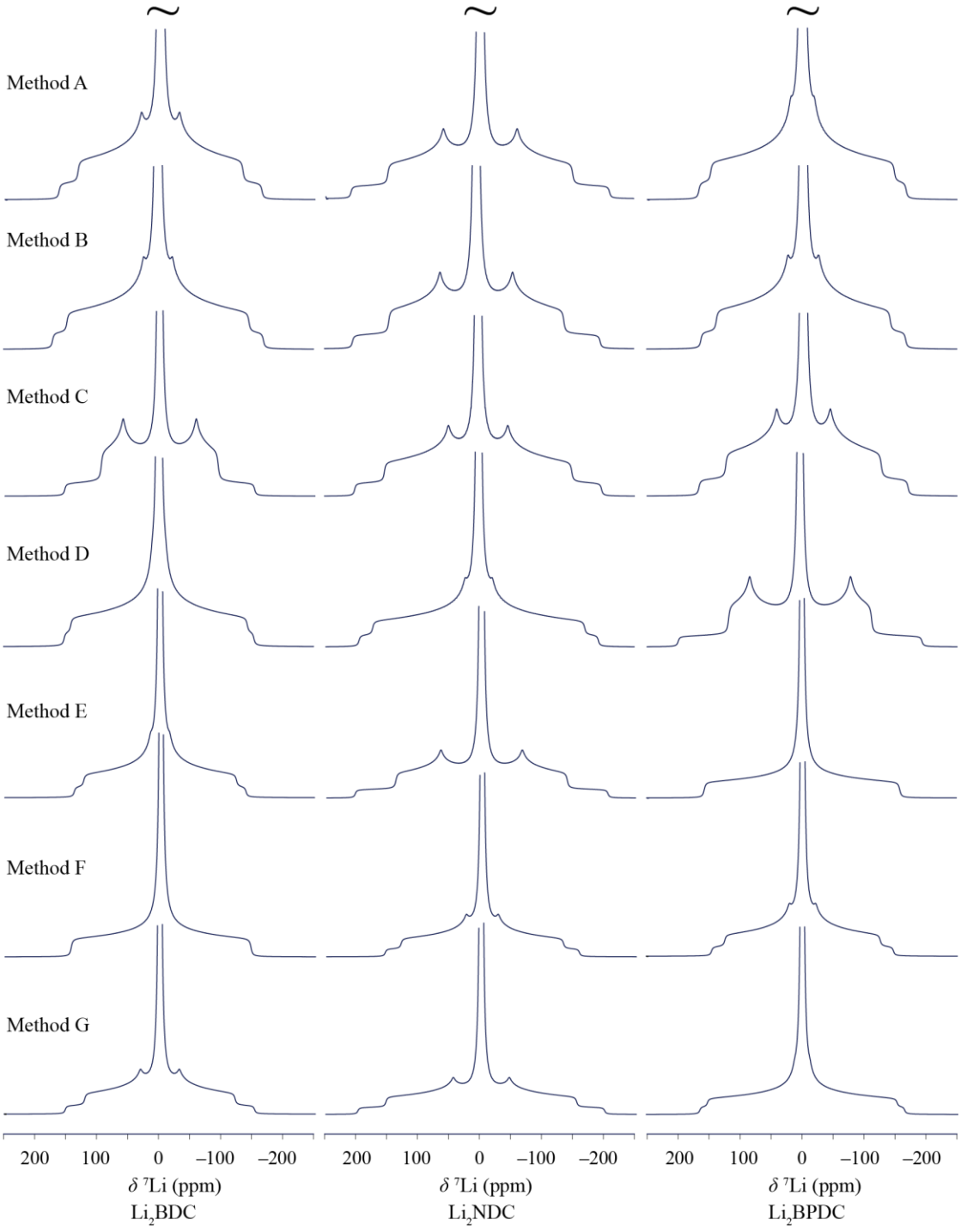

Figure 3.16 Simulated ^{7}Li static NMR spectra. Spectra have been cropped and scaled vertically to show the features of the quadrupolar lineshape. See Table 3.4 for full details of optimisation methods. Spectra generated using SIMPSON and visualised in GSim

3.6.5 Calculated ^{23}Na NMR Parameters

Similarly to calculated ^{7}Li NMR parameters, experimental C_Q and η_Q values were converted to the three individual components of the EFG tensor, V_{XX}, V_{YY} and V_{ZZ} with the magnitudes of the experimental and calculated tensor components correlated in Figure 3.17. A full summary of the calculated quadrupolar parameters are given in Table 3.6. Simulated ^{23}Na NMR spectra are shown in Figure 3.18.

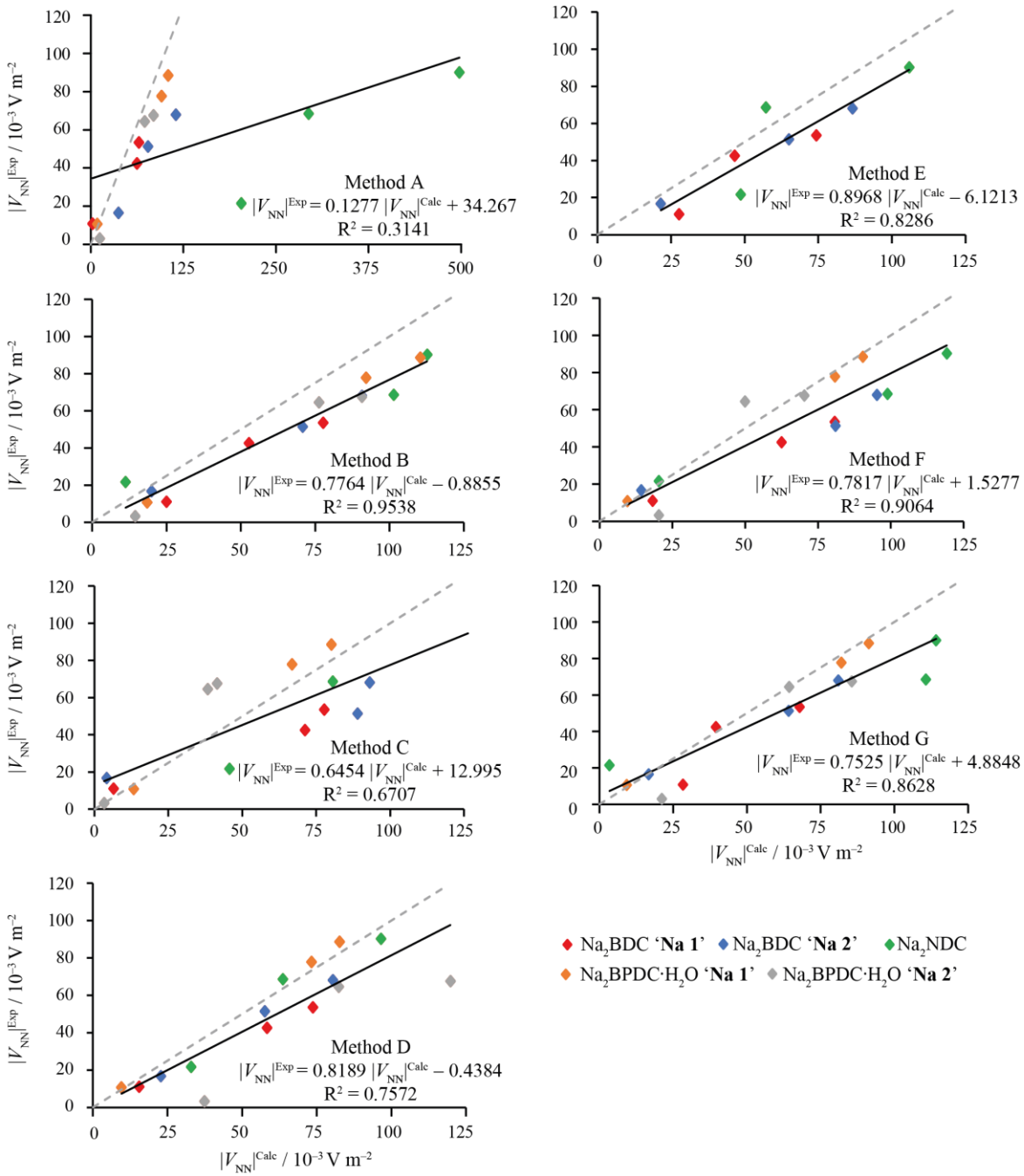

Figure 3.17 Plot of calculated and experimental ^{23}Na quadrupolar tensor components for sodium dicarboxylates. $|V_{NN}| = V_{XX}$, V_{YY} and V_{ZZ}. Grey dashed line represents perfect agreement. Full details of optimisation method can be found in Table 3.4.

Table 3.6 Summary of calculated ^{23}Na NMR parameters from CASTEP for each sodium dicarboxylate salt. See Table 3.4 for full details of optimisation methods.

Compound	Optimisation Method	δ (ppm)	$\lvert C_Q \rvert$ / MHz	η_Q
Na_2BDC 'Na 1'	A	6.54	1.59	0.92
	B	6.13	1.90	0.36
	C	0.47	1.90	0.83
	D	6.64	1.80	0.58
	E	5.39	1.82	0.25
	F	−0.24	1.97	0.55
	G	4.65	1.66	0.16
Na_2BDC 'Na 2'	A	4.63	2.81	0.35
	B	5.41	2.22	0.56
	C	1.84	2.27	0.91
	D	7.80	1.96	0.43
	E	5.98	2.12	0.50
	F	0.54	2.33	0.70
	G	5.74	1.98	0.59
Na_2NDC	A	34.47	12.16	0.18
	B	2.10	2.75	0.80
	C	6.78	3.09	0.28
	D	5.02	2.36	0.32
	E	2.55	2.59	0.08
	F	−2.61	2.91	0.66
	G	1.83	2.79	0.94
Na_2BPDC·H_2O 'Na 1'	A	18.10	2.08	0.72
	B	17.80	2.22	0.68
	C	9.54	1.01	0.84
	D	24.32	2.93	0.38
	E	17.13	2.04	0.75
	F	6.74	1.72	0.42
	G	5.63	2.10	0.50
Na_2BPDC·H_2O 'Na 2'	A	22.76	2.55	0.83
	B	22.83	2.70	0.67
	C	12.27	1.96	0.67
	D	27.17	2.02	0.77
	E	19.52	2.80	0.60
	F	10.11	2.21	0.79
	G	9.45	2.23	0.80

As observed for ^{7}Li, there is a tendency for overestimation of ^{23}Na predicted tensor components of a similar magnitude. This overestimation is consistent with a recent ^{25}Mg NMR study of magnesium acetate clusters where C_Q values were also overestimated. In that study, using a DFT approach equivalent to Method B resulted in overestimated C_Q values of approximately 30% on average, while η_Q parameters were predicted reasonably well.[50] In contrast, other works have observed underestimation of ^{27}Al C_Q values for organoaluminium complexes,[49] or very good agreement for aluminophosphate frameworks.[48] Despite the range of

results, overestimation is rather common, with a further study on organic hydrogen-bonded systems overestimating calculated ^{35}Cl C_Q values. In that work, better agreement was obtained by empirically optimising the damping parameter in the SEDC used. However, modification of the SEDC scheme had no effect on the reproduction of ^{14}N and ^{17}O C_Q values. The apparent overestimation of calculated EFG tensor components in the current study is therefore likely to originate from a number of factors. Firstly, the limited number and range of values means that it is difficult to draw strong conclusions. A wider study of a larger number of structures and wider range of C_Q values would enable a better statistical picture to be obtained. Secondly, as shown

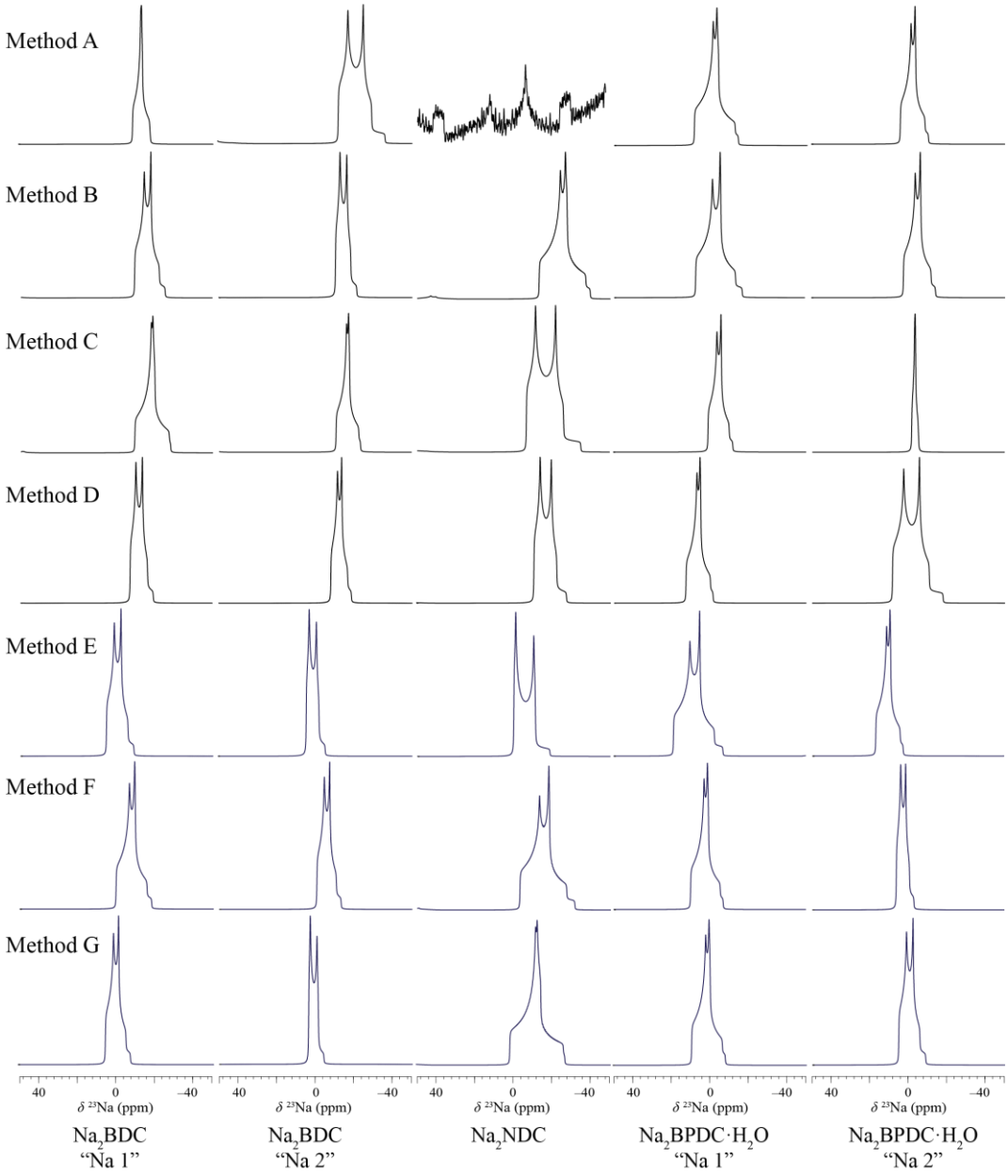

Figure 3.18 Simulated ^{23}Na MAS NMR spectra assuming an MAS rate of 12.5 kHz. See Table 3.4 for full details of optimisation methods. Simulated lineshape for Na_2NDC optimised by Method A is caused by bond anisotropy in the single crystal X-ray structure. Spectra generated using SIMPSON and visualised in GSim

by Holmes *et al.* the agreement between calculated and experimental quadrupolar parameters can be highly nucleus dependent, even within the same materials.[51] Empirical optimisation of the SEDC damping parameter can increase the overall accuracy of calculated C_Q values but the optimal parameter is likely to be dependent on both the nucleus and structure type under consideration. Overall, for the organic dicarboxylate salts studied herein, the results show that the choice of optimisation method does not significantly change the accuracy of calculated chemical shielding or quadrupolar parameters. It is noteworthy that the accuracy of calculated ^{13}C chemical shifts is slightly reduced for optimisations where only proton positions are varied, despite the fact that simulated PXRD patterns show best agreement with experimental PXRD. In contrast, optimisations where all atom positions are allowed to vary typically lead to measurable changes in the simulated PXRD patterns but closer overall agreement between calculated and experiment ^{13}C chemical shifts. This highlights the differences between PXRD and Solid-state NMR in terms of sensitivity to local *vs*. long-range structural effects.

3.6.6 Na_2NDC Structure

Method A gives a very poor agreement between experimental and calculated ^{23}Na NMR parameters, which is primarily due to the calculated Na_2NDC data significantly overestimating the magnitude of the quadrupolar coupling tensor components. Inspection of the sodium carboxylate layer in the optimised structure from Method A reveals significant asymmetry in the bond lengths around the sodium site (Figure 3.19), with considerable variation in Na−O bond lengths from 1.811 Å to 3.095 Å. As Method A only optimises proton positions, this suggests that the position of the sodium ion in the experimental diffraction structure is not accurately defined. The observation is consistent with the ^{13}C NMR data (Figure 3.13) where the shielding of the carboxylate carbon, which is situated closest to the sodium carboxylate layer, is also

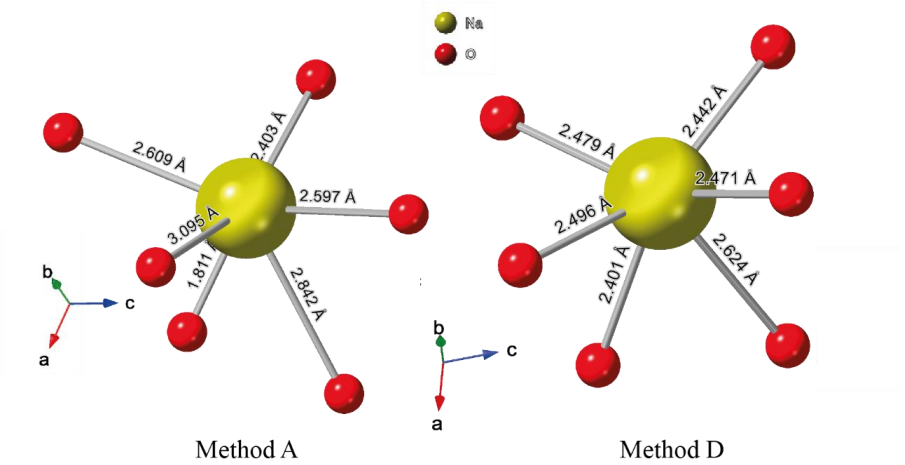

Figure 3.19 3.6 Å clusters set around sodium sites in Na_2NDC structures optimised by Method A (left) and Method D (right). The Na and O atomic positions in the structure optimised by 'Method A' are equivalent to the experimental atomic positions because in this optimisation method only proton positions were varied. See Table 3.4 for full details of optimisation methods.

poorly reproduced by the DFT calculations using Method A. In the other optimisation methods where the position of heavy atom positions are allowed to vary, a significant change in the Na−O bond lengths is observed, *e.g.*, in Method D, Na−O bond lengths are all of a similar length with a range of 2.401 Å to 2.624 Å (Figure 3.19). The calculated quadrupolar tensor components for these structures are in much better agreement with experiment, a further suggestion that the Na position in the diffraction structure is not accurately defined. Despite this, considering the simulated PXRD data (Figure 3.12), Method A gives reasonable agreement with experiment and is significantly better than Method C. This highlights the high sensitivity of NMR to the local structure and shows the benefits of NMR crystallography in considering both the local and long-range structure.

3.7 Hydration Behaviours

3.7.1 Na_2NDC Hydration Behaviour

While the anhydrous phase of Na_2NDC has been discussed in previous sections, a tetrahydrate form, $Na_2NDC{\cdot}4H_2O$, has also previously been reported.[38] In the current work, this phase was isolated as a single crystal from a slow crystallisation, though not enough sample was obtained for for Solid-state NMR analysis. However, during the course of experiments a new phase was identified as a powder. The sample was prepared by a similar method to anhydrous Na_2NDC except that after initial filtration, the filtrate was concentrated before being washed with methanol forming a milky suspension. The resulting suspension was then filtered again and the recovered powder was dried *in vacuo*. The PXRD pattern of this phase (Figure 3.20a) does not match either of the known anhydrous Na_2NDC or $Na_2NDC{\cdot}4H_2O$ phases and thus is labelled 'Phase III'. The ^{13}C CPMAS NMR spectrum (Figure 3.20b) shows two carboxylate resonances at 177.3 and 175.8 ppm, which suggests the structure has a different symmetry from the known anhydrous phase which has only one carboxylate resonance at 177.2 ppm. The resonances corresponding to the ring carbons show a similar overall form to those observed for the anhydrous phase (Figure 3.5e) appearing between 135 and 120 ppm. The ^{23}Na MAS spectrum (Figure 3.21a) shows a complex unresolved lineshape. The ^{23}Na MQMAS spectrum (Figure 3.21b) reveals this is made up of at least five separate resonances, with two relatively sharp resonances at δ_1 = 6.0 (Na 2) and 9.7 ppm (Na 3), and broader resonances at −13.9 (Na 1), 15.7 (Na 4) and 18.0 ppm (Na 5). In a high-field MQMAS spectrum, recorded at 23.5 T (Figure 3.22), the resolution of the sharp resonances in δ_1 increases but the broad resonances at 15.4 and 18.6 ppm remain unresolved. This could suggest the presence of more than one phase in the sample, with an ordered crystalline phase giving rise to the sharp resonances and a more disordered phase (possibly not observed in the PXRD pattern) giving rise to the broader resonances.

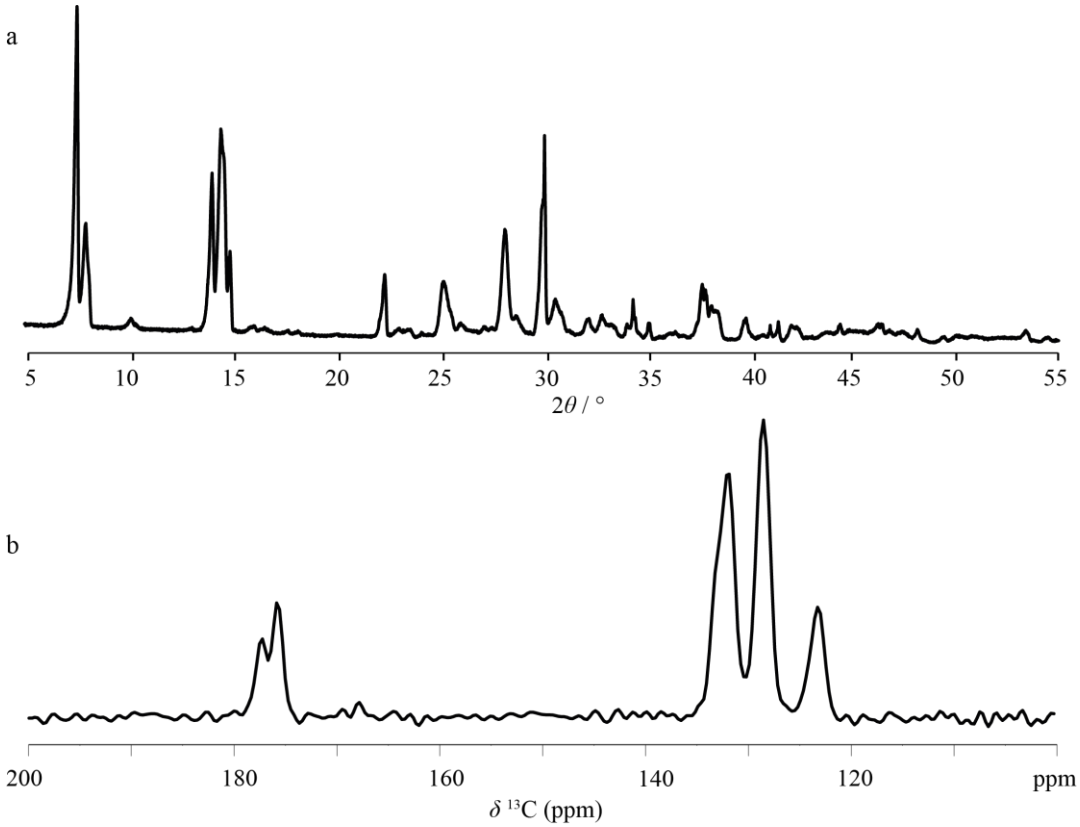

Figure 3.20 Experimental PXRD pattern (a) and ^{13}C CPMAS NMR spectrum (b) of Na_2NDC Phase III. ^{13}C spectrum collected at 16.4 T with an MAS rate of 15 kHz. Spectrum is the result of 512 transients separated by a recycle interval of 120 s, utilising a contact pulse length of 5 ms.

To assess the hydration level of Na_2NDC Phase III, thermogravimetric analysis (TGA) was completed. TGA shows a mass loss of around 10.6% between 100 – 200 °C (Figure 3.23). If Phase III featured a tetrahydrate stoichiometry ($Na_2NDC{\cdot}4H_2O$, MW = 332.21 g mol^{-1}), this would correspond to a mass loss of 34.05 g mol^{-1}. This mass loss is very close to that of two H_2O molecules (36.03 g mol^{-1}); however, it is unlikely that only two H_2O molecules would be lost with the other two remaining in the structure up to the decomposition temperature of 600 °C. Whereas, if Phase III had a dihydrate stoichiometry ($Na_2NDC{\cdot}2H_2O$, MW = 296.18 g mol^{-1}) this would correspond to a mass loss of 31.40 g mol^{-1}. Since this mass loss does not correspond to an integer multiple of H_2O molecules, a possible explanation could be that the sample corresponds to a mixture of a dihydrate Na_2NDC phase and a (possibly disordered) anhydrous Na_2NDC phase, which is not observed in the PXRD pattern. This would be consistent with the observation of the broad and sharp resonances in the MQMAS spectrum. Furthermore, if only a portion of the sample is a dihydrate stoichiometry, the remaining portion of the sample would not lose mass at high temperature and result in a reduced mass loss as observed by TGA, where H_2O molecules are only lost from the hydrated portion of the sample.

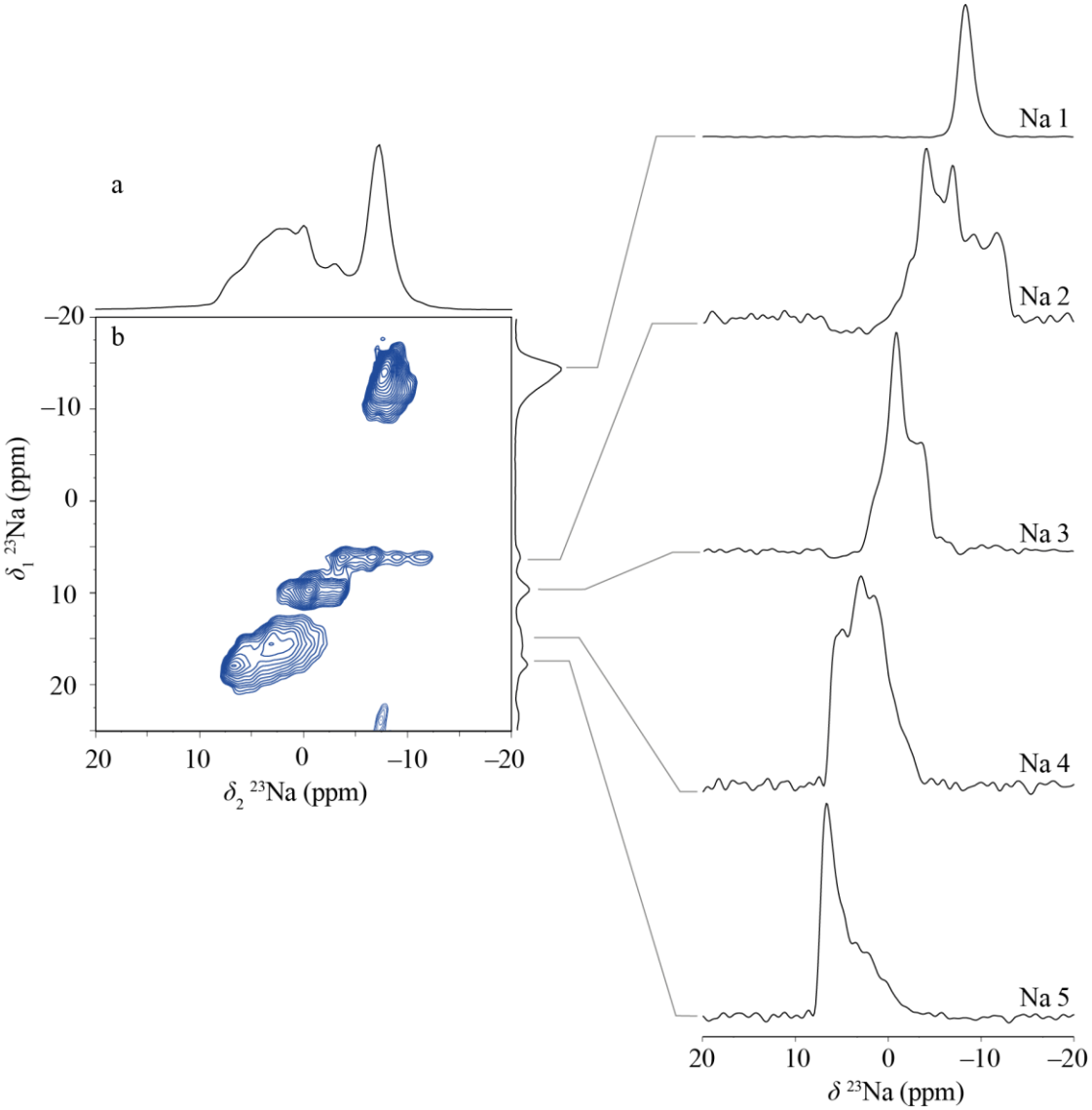

Figure 3.21 ^{23}Na MAS (a) and MQMAS (b) spectra of Na_2NDC Phase III. Individual sodium lineshapes extracted from the MQMAS spectrum are shown on the right. Spectra were recorded at 16.4 T with an MAS rate of 12.5 kHz. MAS spectrum is the result of 336 transients separated by a recycle interval of 3 s. MQMAS spectrum is the result of 768 transients for each of 96 t_1 rows separated by a recycle interval of 3 s.

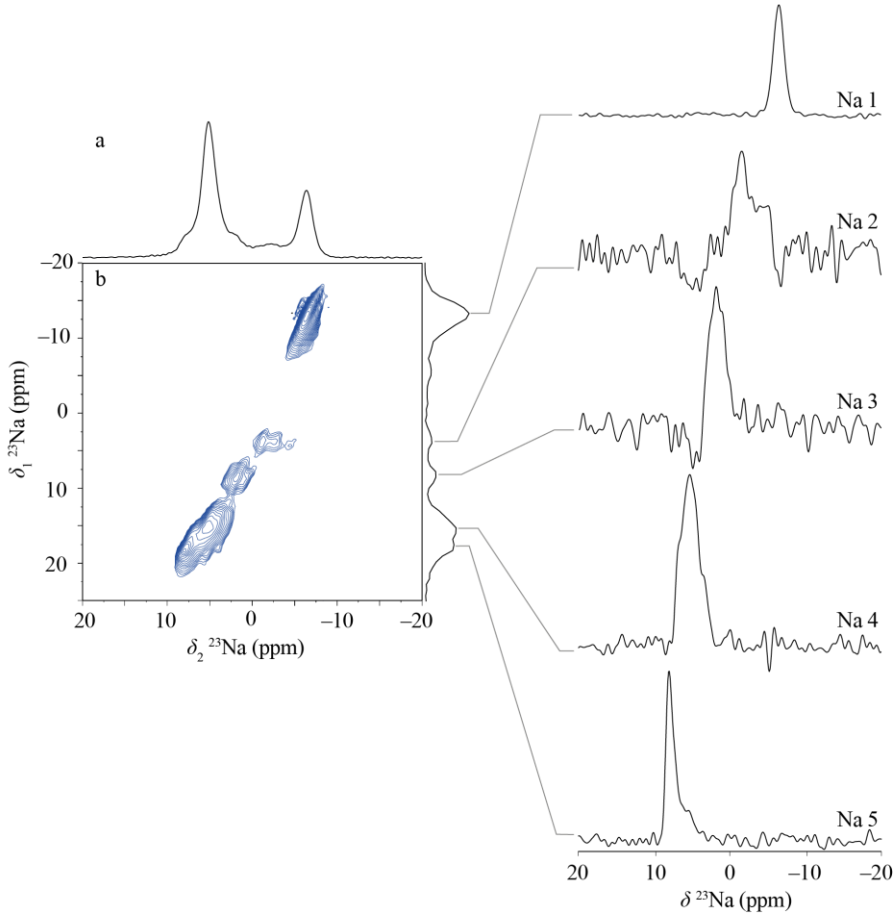

Figure 3.22 ^{23}Na MAS (a) and MQMAS (b) spectra of Na_2NDC Phase III. Individual sodium lineshapes extracted from the MQMAS spectrum are shown on the right. Spectra were recorded using a Bruker Avance Neo spectrometer operating at a magnetic field strength of 23.5 T corresponding to ^{1}H Larmor frequency of 1 GHz. Data collected by staff at the UK High-Field Solid-state NMR Facility, University of Warwick, UK in February 2021. The sample was packed into a rotor with 1.3 mm outer diameter and spun at an MAS rate of 20 kHz. The spectrum was recorded using a split-t_1 MQMAS pulse sequence. MAS spectrum is the result of 16 transients separated by a recycle interval of 1 s. MQMAS spectrum is the result of 384 transients for each of 144 t_1 rows separated by a recycle interval of 1 s.

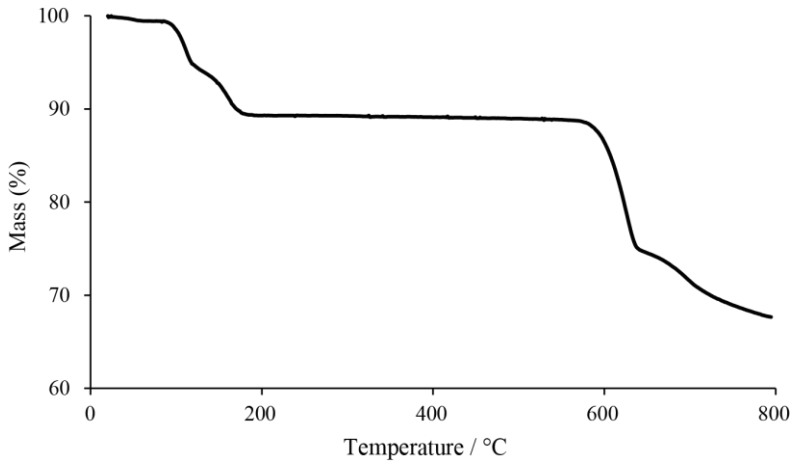

Figure 3.23 Thermogravimetric analysis of Na_2NDC Phase III.

3.7.2 Na_2BPDC Hydration Behaviour

As discussed earlier, the previously reported crystal structure of Na_2BPDC and the one determined in this work both correspond to monohydrate phases ($Na_2BPDC{\cdot}H_2O$) with small structural differences characterised by the twisting of the BPDC linker. Choi *et al.* prepared anhydrous Na_2BPDC through thermal treatment of $Na_2BPDC{\cdot}H_2O$ at 120 °C *in vacuo*, although a crystal structure was not reported.[11] To investigate the structure of anhydrous Na_2BPDC, a sample was prepared by a similar procedure to that reported by Choi *et al.* and different from that used in this work for $Na_2BPDC{\cdot}H_2O$, where instead of crystallisation the sample was filtered and heated *in vacuo* at 120 °C for 12 hours. The PXRD pattern (Figure 3.24a) confirms that this treatment changes the structure, and shows close agreement with that reported for anhydrous Na_2BPDC by Choi *et al.*[11] with significant differences noted compared to the PXRD pattern of $Na_2BPDC{\cdot}H_2O$. The ^{13}C CPMAS NMR spectrum (Figure 3.25a) shows one carboxylate and four ring carbon resonances which is consistent with the number of chemically distinct carbons in the structure, although the resonances are broad and as such there may be more crystallographically distinct carbons in the structure. The range at which aromatic resonances appear is slightly reduced in the anhydrous sample, with a range of 139 – 120 ppm. In contrast, the aromatic carbon resonances occupy a range of 144 – 120 ppm in the monohydrate phase. In view of the twisted configuration of the ligands in the monohydrate structure, this could suggest a difference in the relative orientations of rings in the ligands, or closer packing of the rings leading to increased ring current shielding. The ^{23}Na MAS NMR spectrum (Figure 3.25b) shows a featureless broad lineshape centred at −7.5 ppm, together with a low intensity resonance at −0.3 ppm, which is attributed to a minor impurity. The lineshape shows a broadened ‘tail’ to low frequency which is characteristic of a distribution of quadrupolar interactions, indicative of disorder. The ^{23}Na MQMAS NMR spectrum (Figure 3.25c) confirms this, as a single resonance is observed which is broadened in both dimensions indicating that the Na ions have a disordered local environment. Overall, these results indicate that dehydration of $Na_2BPDC{\cdot}H_2O$ leaves a structure characterised by some degree of long-range order (as evidenced from the PXRD pattern), but that the ordering of sodium ions in the sodium carboxylate layers is disrupted leaving local disorder. The closer packing of the ligands indicated by the reduction in chemical shift of the ring carbons suggests that the overall layered structure may be retained.

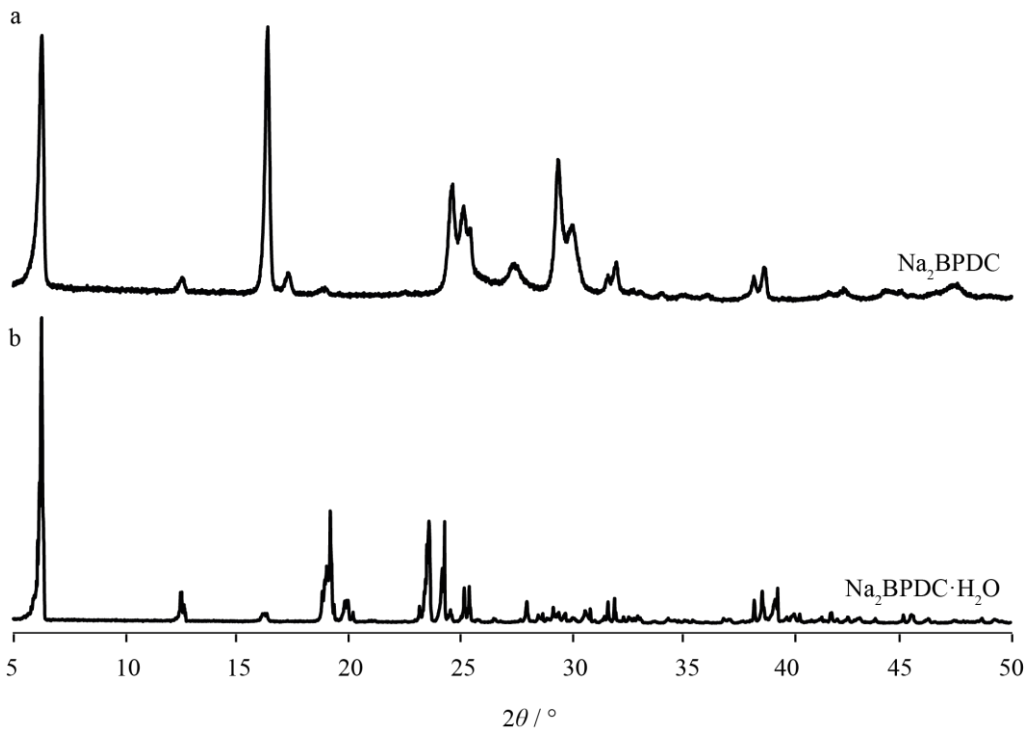

Figure 3.24 Experimental PXRD patterns of anhydrous Na_2BPDC (a) and $Na_2BPDC \cdot H_2O$ (b).

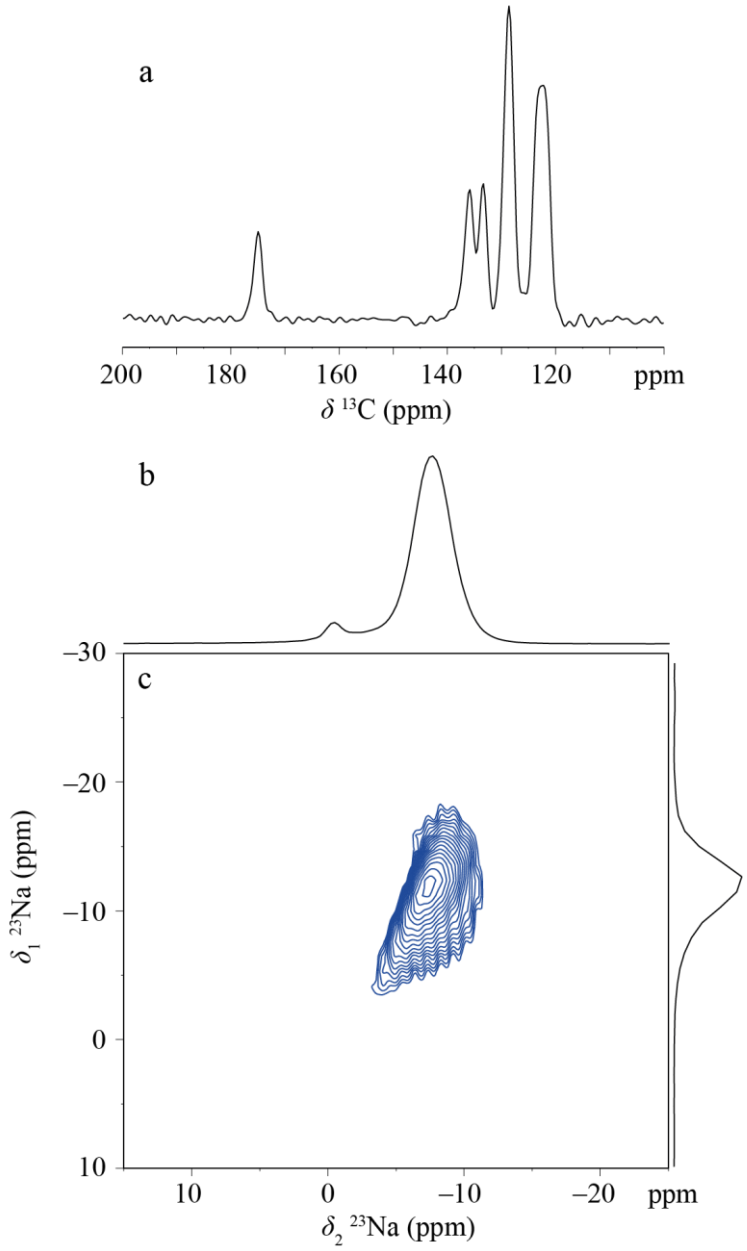

Figure 3.25 ^{13}C CPMAS (a), ^{23}Na MAS (b) and ^{23}Na MQMAS (c) NMR spectra of anhydrous Na_2BPDC. All spectra recorded at 16.4 T. ^{13}C spectrum collected at an MAS rate of 15 kHz, ^{23}Na spectra collected at an MAS rate of 12.5 kHz. ^{13}C spectrum is the result of 464 transients separated by a recycle interval of 120 s, utilising a contact time of 5 ms. MQMAS spectrum was recorded using a split-t_1 pulse sequence. MAS spectrum is the result of 400 transients separated by a recycle interval of 3 s. MQMAS spectrum is the result of 720 transients for each of 96 t_1 rows separated by a recycle interval of 3 s.

3.8 Conclusions

In this chapter, a systematic structural study of model lithium and sodium battery organic anode materials by NMR crystallography has been presented. For the six samples studied, the calculation of NMR parameters using diffraction structures enable distinct chemical and crystallographic environments to be assigned in ^{13}C, ^{7}Li and ^{23}Na Solid-state NMR spectra. Comparison of the DFT-calculated ^{13}C, ^{7}Li and ^{23}Na NMR parameters shows that the choice of optimisation method does not significantly affect the accuracy of the calculated NMR parameters, providing that all atoms are optimised. For proton-only optimisations, slightly poorer agreement between calculated and experimental ^{13}C chemical shifts is observed. Additionally, this optimisation method highlights the sensitivity of the ^{23}Na quadrupolar interaction to the local chemical environment, which is very poorly reproduced for Na_2NDC. Allowing all atom positions to vary changes the Na−O bond lengths resulting in much better agreement with experiment. The DFT geometry optimisations also show that despite the strong ionic bonds holding the layered structures together, weak non-bonding interactions between adjacent ligands are also important in defining the structure, and large unit cell expansions are observed if these are not accounted for. This problem can be mitigated by either fixing the unit cell parameters to experimental values during the structural optimisation, or by including a SEDC scheme. Both of these methods give comparable accuracy in terms of calculated ^{13}C, ^{7}Li and ^{23}Na NMR parameters.

This work suggests that it would be possible to extend the NMR crystallographic approach to the study of lithiation and sodiation mechanisms in organic anode materials, where the known structures of these pristine phases could serve as a starting point for investigating the currently unknown structures of the electrochemically reduced forms. However, in this case, the lithiation or sodiation process may result in changes to the unit cell parameters, even if the overall ordering of the ligands and metal carboxylate layers is retained. Therefore, fixing the unit cell parameters to experimental values for the parent phase may impose unrealistic constraints on the system; instead, the preferable optimisation method would be to allow the unit cell parameters to vary in conjunction with a SEDC scheme to account for ligand-ligand interactions. As the theory develops and accuracy of computational methods improves, a further systematic study of the effects of using different XC functionals and SEDC schemes could shed light on potential preferable geometry optimisation strategies to use with organic anode materials.

In addition, the hydration behaviour of Na_2NDC and Na_2BPDC has been investigated. For Na_2NDC, a new hydrated phase has been observed, which is likely to be a dihydrate, in contrast to the known tetrahydrate structure. It is also shown that the anhydorus phase of

Na_2BPDC exhibits disorder within the metal-dicarboxylate layer, which perhaps explains why the structure of this phase has so far not been solved by XRD. It seems that the sodium dicarboxylate salts have a greater propensity to form hydrated phases than lithium dicarboxylate salts which could be linked to the larger ionic radius of sodium providing more possibility for structural incorporation of H_2O molecules into the metal-carboxylate layers. The hydrated phases may be less desirable for battery applications since the presence of even small amounts of free water in battery cells typically leads to irreversible capacity loss. However, this may not be an issue if the H_2O molecules remain within the metal-dicarboxylate layers under electrochemical cycling. Therefore, to understand how the presence of structural H_2O impacts the anode performance, further investigations are required with systematic comparisons of the anhydrous and hydrated phases. Nevertheless, it is noted that the specific capacity of the hydrated phases should be reduced even if no chemical effects are seen, owing to the additional mass of the H_2O molecules.

3.9 References

1. D. Senthil Raja, C.-C. Pan, C.-W. Chen, Y.-H. Kang, J.-J. Chen and C.-H. Lin, *Microporous and Mesoporous Materials*, 2016, **231**, 186-191.
2. W. Walker, S. Grugeon, H. Vezin, S. Laruelle, M. Armand, J. M. Tarascon and F. Wudl, *Electrochemistry Communications*, 2010, **12**, 1348-1351.
3. M. Armand, S. Grugeon, H. Vezin, S. Laruelle, P. Ribiere, P. Poizot and J. M. Tarascon, *Nat Mater*, 2009, **8**, 120-125.
4. L. Zhao, J. Zhao, Y.-S. Hu, H. Li, Z. Zhou, M. Armand and L. Chen, *Advanced Energy Materials*, 2012, **2**, 962-965.
5. Y. Park, D. S. Shin, S. H. Woo, N. S. Choi, K. H. Shin, S. M. Oh, K. T. Lee and S. Y. Hong, *Adv Mater*, 2012, **24**, 3562-3567.
6. Y. Wang, Y. Deng, Q. Qu, X. Zheng, J. Zhang, G. Liu, V. S. Battaglia and H. Zheng, *ACS Energy Letters*, 2017, **2**, 2140-2148.
7. X. Han, C. Chang, L. Yuan, T. Sun and J. Sun, *Advanced Materials*, 2007, **19**, 1616-1621.
8. X. Han, G. Qing, J. Sun and T. Sun, *Angew Chem Int Ed Engl*, 2012, **51**, 5147-5151.
9. L. Fédèle, F. Sauvage and M. Bécuwe, *J. Mater. Chem. A*, 2014, **2**, 18225-18228.
10. L. Fédèle, F. Sauvage, S. Gottis, C. Davoisne, E. Salager, J.-N. Chotard and M. Becuwe, *Chemistry of Materials*, 2017, **29**, 546-554.
11. A. Choi, Y. K. Kim, T. K. Kim, M.-S. Kwon, K. T. Lee and H. R. Moon, *J. Mater. Chem. A*, 2014, **2**, 14986-14993.
12. L. Fédèle, F. Sauvage, J. Bois, J.-M. Tarascon and M. Bécuwe, *Journal of The Electrochemical Society*, 2013, **161**, A46-A52.
13. N. Ogihara, T. Yasuda, Y. Kishida, T. Ohsuna, K. Miyamoto and N. Ohba, *Angew Chem Int Ed Engl*, 2014, **53**, 11467-11472.
14. T. Yasuda and N. Ogihara, *Chem Commun (Camb)*, 2014, **50**, 11565-11567.

15. J. M. Cabanero, Jr., V. Pimenta, K. C. Cannon, R. E. Morris and A. R. Armstrong, *ChemSusChem*, 2019, **12**, 4522-4528.

16. S. E. Ashbrook and D. McKay, *Chem Commun (Camb)*, 2016, **52**, 7186-7204.

17. C. Bonhomme, C. Gervais, F. Babonneau, C. Coelho, F. Pourpoint, T. Azais, S. E. Ashbrook, J. M. Griffin, J. R. Yates, F. Mauri and C. J. Pickard, *Chem Rev*, 2012, **112**, 5733-5779.

18. P. Hodgkinson, *Prog Nucl Magn Reson Spectrosc*, 2020, **118-119**, 10-53.

19. J. A. Kaduk, *Acta Crystallogr. Sect. B Struct. Sci.*, 2000, **56**, 474-485.

20. A. E. Bennett, C. M. Rienstra and M. Auger, *J. Chem. Phys.*, 1995, **103**, 6951.

21. P. K. Madhu, A. Goldbourt, L. Frydman and S. Vega, *Chemical Physics Letters*, 1999, **307**, 41-47.

22. M. D. Segall, P. J. D. Lindan, M. J. Probert, C. J. Pickard, P. J. Hasnip, S. J. Clark and M. C. Payne, *J Phys Condens Matter*, 2002, **14**, 2717-2744.

23. C. J. Pickard and F. Mauri, *Physical Review B*, 2001, **63**.

24. J. P. Perdew, K. Burke and M. Ernzerhof, *Phys Rev Lett*, 1996, **77**, 3865-3868.

25. J. R. Yates, C. J. Pickard and F. Mauri, *Physical Review B*, 2007, **76**.

26. B. Hammer, L. B. Hansen and J. K. Nørskov, *Physical Review B*, 1999, **59**, 7413-7421.

27. A. P. Bartok and J. R. Yates, *J Chem Phys*, 2019, **150**, 161101.

28. S. Grimme, *J Comput Chem*, 2006, **27**, 1787-1799.

29. S. Grimme, J. Antony, S. Ehrlich and H. Krieg, *J Chem Phys*, 2010, **132**, 154104.

30. S. T. Holmes, C. S. Vojvodin and R. W. Schurko, *J Phys Chem A*, 2020, **124**, 10312-10323.

31. P. Pyykkö, *Molecular Physics*, 2008, **106**, 1965-1974.

32. O. V. Dolomanov, L. J. Bourhis, R. J. Gildea, J. A. K. Howard and H. Puschmann, *Journal of Applied Crystallography*, 2009, **42**, 339-341.

33. G. M. Sheldrick, *Acta Crystallogr Sect A*, 2014, **71**, 3-8.

34. G. M. Sheldrick, *Acta Crystallogr Sect C*, 2014, **71**, 3-8.

35. Y.-Y. Liu, J. Zhang, L.-X. Sun, F. Xu, W.-S. You and Y. Zhao, *Inorganic Chemistry Communications*, 2008, **11**, 396-399.

36. D. Banerjee, S. J. Kim and J. B. Parise, *Crystal Growth & Design*, 2009, **9**, 2500-2503.

37. D. Banerjee, L. A. Borkowski, S. J. Kim and J. B. Parise, *Crystal Growth & Design*, 2009, **9**, 4922-4926.

38. V. Medabalmi, K. Ramanujam and V. Ramkumar, *CSD Communications*, 2018, DOI: https://doi.org/10.5517/ccdc.csd.cc1pb6s0.

39. J. Klimes and A. Michaelides, *J Chem Phys*, 2012, **137**, 120901.

40. E. Caldeweyher, S. Ehlert, A. Hansen, H. Neugebauer, S. Spicher, C. Bannwarth and S. Grimme, *J Chem Phys*, 2019, **150**, 154122.

41. J. Sun, A. Ruzsinszky and J. P. Perdew, *Phys Rev Lett*, 2015, **115**, 036402.

42. G. Santra and J. M. L. Martin, *Molecules*, 2021, **27**.

43. J. W. Furness, A. D. Kaplan, J. Ning, J. P. Perdew and J. Sun, *J Phys Chem Lett*, 2020, **11**, 8208-8215.

44. J. W. Furness, A. D. Kaplan, J. Ning, J. P. Perdew and J. Sun, *J Chem Phys*, 2022, **156**, 034109.

45. M. Bursch, H. Neugebauer, S. Ehlert and S. Grimme, *J Chem Phys*, 2022, **156**, 134105.

46. S. Song, S. Vuckovic, Y. Kim, H. Yu, E. Sim and K. Burke, *Nat Commun*, 2023, **14**, 799.

47. B. K. Chang, N. C. Bristowe, P. D. Bristowe and A. K. Cheetham, *Phys Chem Chem Phys*, 2012, **14**, 7059-7064.

48. S. Sneddon, D. M. Dawson, C. J. Pickard and S. E. Ashbrook, *Phys Chem Chem Phys*, 2014, **16**, 2660-2673.

49. C. Cross, L. Cervini, N. R. Halcovitch and J. M. Griffin, *Magn Reson Chem*, 2021, **59**, 1024-1037.

50. V. R. Seymour, S. P. Day, G. Scholz, K. Scheurell, D. Iuga, J. M. Griffin, E. Kemnitz, J. V. Hanna and M. E. Smith, *Chemphyschem*, 2018, **19**, 1722-1732.

51. S. T. Holmes and R. W. Schurko, *The Journal of Physical Chemistry C*, 2018, **122**, 1809-1820.

Appendix 3.1 – Na_2NDC ^{23}Na MQMAS NMR

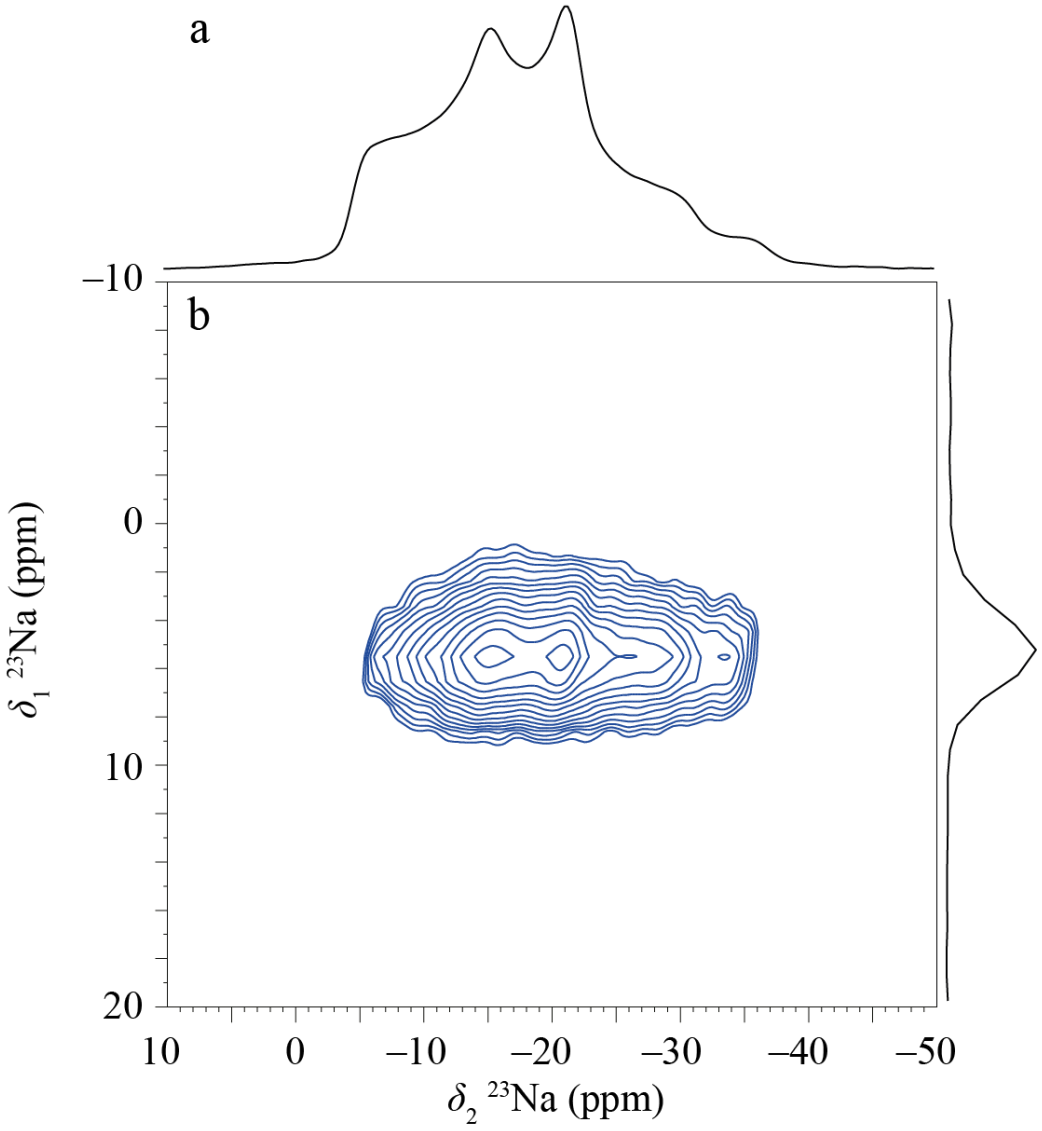

Figure 3.A26 ^{23}Na MAS (a – as shown previously in Figure 3.8c) and MQMAS (b) spectrum of Na_2NDC. MQMAS spectrum recorded at a field strength of 9.4 T and was collected at an MAS rate of 12.5 kHz. The spectrum was recorded using a split-t_1 MQMAS pulse sequence. Spectrum is the result of 192 transients for each of 180 t_1 rows separated by a recycle interval of 3 s.

Chapter 4

Investigating the Structure of Reduced Organic Battery Anode Materials

4.1 Introduction

As discussed in the previous chapter, conjugated metal dicarboxylates present a sustainable alternative to conventionally used graphite anodes. Various organic battery anode materials have been studied electrochemically over the last decade; however, the structural changes that accompany the charging process are still unclear. In the previous chapter the pristine, uncharged phases of a set of six model organic anode materials were fully characterised using a combination of analytical and computational techniques. With the pristine phases characterised, the next challenge is to characterise the charged phases.

Lithium terephthalate (lithium benzenedicarboxylate, Li_2BDC) was first investigated as an anode material alongside lithium muconate ($Li_2C_6H_4O_4$) by Armand *et al*. in 2009 with the hope of finding candidates for low-voltage redox activity.[1] Figure 4.1 shows the proposed chemical reaction scheme that describes the insertion of two lithium ions into the Li_2BDC structure.[1] In that work, Li_2BDC was electrochemically cycled in Swagelok-cells between 0.7 V and 3.0 V at a rate of 0.1 C (complete lithiation or delithiation in 10 hours) *vs*. Li^+/Li^0 using a 1M $LiPF_6$ electrolyte solution in ethylene carbonate-dimethyl carbonate. The working electrodes were powder electrodes with an active mass of between 8 and 10 mg cm^{-2} and

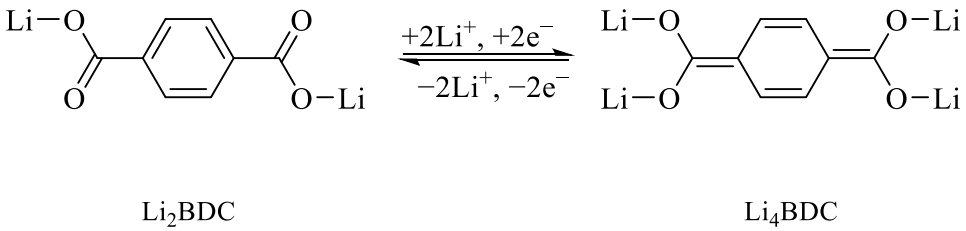

Li_2BDC Li_4BDC

Figure 4.1 Proposed chemical reaction scheme accompanying lithiation or delithiation of Li_2BDC and the changes in π-bonding that occur as a result.

approximately 30% w/w carbon super P (SP) additive. Carbon SP is a conductive additive with a high void volume which aids ion transport. They reported the insertion of two lithium ions per formula unit into the terephthalate material at a potential of 0.8 V, based on a reversible specific capacity of approximately 300 mA h g^{-1} which agrees with the theoretical specific capacity of 300 mA h g^{-1}. The irreversible specific capacity of the first cycle was much higher at approximately 360 mA h g^{-1}, where it sharply decreased to 300 mA h g^{-1} on the second cycle. The additional capacity on the first cycle was attributed to use of the conductive carbon additive, which has been shown to have an irreversible capacity, with the additional capacity fade ascribed to the formation of solid electrolyte interphase (SEI).[2] The reversible specific capacity then slowly decreased over 50 cycles to 234 mA h g^{-1}. When cycled at 1 C (one Li^+/h), 70% of the capacity was retained (240 mA h g^{-1}). This indicates Li_2BDC can reversibly accommodate approximately two additional lithium ions per formula unit, which decreases over multiple cycles to approximately 1.4 lithium ions per formula unit. Reversible capacity past the 50^{th} cycle was not reported, and thus could continue to decrease further. Nevertheless, Li_2BDC is a promising anode material, and with many development opportunities from the rich pool of conjugated organic molecules, improvements could be possible.

Lithium muconate was studied as a vinylic alternative to the aromatic lithium terephthalate. The lithium muconate had an uptake of 1.2 lithium ion per formula unit at a potential of 1.4 V, despite an expected uptake of two lithium ions per formula unit. This is based on a reversible specific capacity of approximately 150 mA h g^{-1} which is significantly lower than the theoretical capacity of 348 mA h g^{-1}. After 80 cycles, the specific capacity decreases to 125 mA h g^{-1} in a capacity fade of 16.6%. These results suggest that although both terephthalate and muconate systems exhibit conjugated organic units, the reduction mechanisms are different, resulting in a notable capacity difference between the terephthalate and muconate species. In a chemical structural model, the intercalation of lithium ions in the muconate was attributed to the carboxylate groups at the termini of the conjugated chain, which undergoes a π-electron rearrangement to maintain charge balance, though no structure for the charged phase is reported and as such the lithium ion positions and the nature of any accompanying structural changes remain unknown.

For both materials studied, various characterisation techniques were employed to probe the structural and chemical changes taking place during the lithium intercalation process, such as infrared spectroscopy (IR), X-ray diffraction (XRD) and electron paramagnetic resonance spectroscopy (EPR). IR showed that the discharged phases are identical to the pristine materials, while the charged phases ($Li_{2+x}BDC$ and $Li_{2+x}C_6H_4O_4$) are distinctly different, suggesting both the materials are able to reversibly undergo the lithium insertion-extraction process. For Li_2BDC, the *ex situ* XRD powder patterns corroborate this observation, with the charged phase

distinctly different to that of the pristine and discharged materials. Lithium muconate also has a different powder pattern for the pristine and charged phases, but in the discharged phase the reflections become much broader than the sharper reflections of the pristine phase. While the electrochemical reversibility of the muconate was proven, this observation suggests a loss of structural ordering and that the crystal structure does not respond reversibly to electrochemical charging. The authors suggest that the loss of structural reversibility of the muconate directly contrasting the terephthalate is attributed to the π-π stacking of the aromatic linkers of the terephthalate providing stronger 3D crystal packing, compared with the weak crystal packing of the linear vinylic muconate linker. EPR of the muconate had no response for both the pristine and discharged phases, which is expected due to the absence of unpaired electrons and therefore lithium ions. A strong resonance was observed for the charged phase of both the muconate and terephthalate. The insertion of two lithium ions as per the scheme shown in Figure 4.1 should lead to a closed shell electronic structure. Therefore, it would be expected that no EPR signal should be observed as the materials should be diamagnetic and thus, EPR silent. The observed EPR signals for the lithiated phases were presumed to be di-radical di-cation species first reported by Bechgaard in 1972.[3] However, the absence of dipolar coupling observed in the charged materials confirmed this not to be the case. Instead, the authors ascribe the EPR signal to electron-electron interactions through a spin-exchange mechanism.

Lithium muconate and lithium terephthalate have thus been demonstrated as promising anode materials with the ability to reversibly intercalate additional lithium ions. While the mechanism may appear to be broadly transferrable to all structures, it is demonstrably different between structures. EPR data demonstrates the structures behave unexpectedly in part due to the apparent formation of non-closed shell structures. Though both structures do feature similarly poor capacity fades which would need to be addressed for further development. In both cases, the structural information gained leaves much left to be learned.

More recently, Walker *et al*. showed that comparable electrochemical performance can be achieved in organic acyclic dicarboxylates with extended π-conjugation systems.[4] A significant portion of the recent work has focused on sodium containing analogues for sodium-ion batteries such as that of Na_2BDC,[5, 6] with some studies focusing on potassium-ion batteries,[7] or even alkaline earth analogues (Ca, Sr, Ba).[8] Further studies attempt to improve electrochemical performance with structural isomers or functionalisation of the aromatic ring with groups including but not limited to methyls, methoxys, amines, nitroxides and additional carboxylates.[9-12] Despite this wealth of work, studies that focus on structure are few in number. One such example is the recent work by Mikita *et al*., where in attempt to understand the mechanism of intercalation, two mechanisms are proposed using data from lithium diffusivity measurements.[13] Low lithium diffusivity is observed in some structures, such as lithium

naphthalene dicarboxylate, (Li_2NDC). Li_2NDC is analogous to Li_2BDC but has an elongated π-conjugated organic backbone between the Li–O layers utilising a naphthalene system instead of a single benzene ring. Extension of the conjugation system in organic anode materials has been studied with increases of cycling stability noted for structures with extended conjugation systems.[14-19] Adapting the mechanism proposed by Armand *et al*. (shown in Figure 4.2) shows that the organic backbone could undergo similar π-electron reorganisation to yield a closed shell structure, Li_4NDC. The low lithium diffusivity of structures such as Li_2NDC is due to a strong interaction between the framework and the lithium ion, causing a *meta*-stable intermediate phase with the process proceeding *via* a two-phase mechanism. By this mechanism, there is a reduced and pristine phase in the sample with an interface between them. As the level of lithium intercalation increases, the interface moves through the structure reducing the remaining fraction of pristine phase. Alternatively, in systems with a high lithium diffusivity, such as lithium biphenyldicarboxylate (Li_2BPDC), a solid-solution mechanism is proposed. Here, the weak interaction between lithium ions and the framework allows the entire sample to gradually fill randomly with lithium ions, with no intermediate *meta*-stable phase.

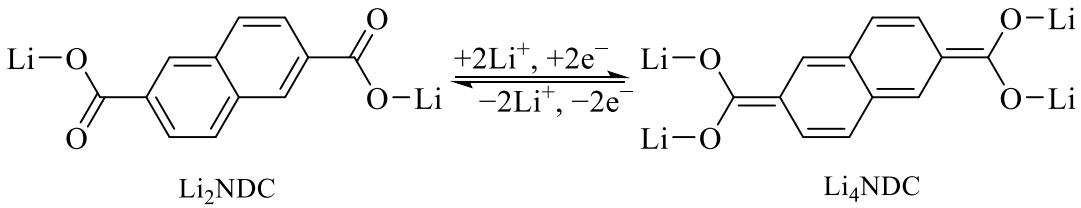

Figure 4.2 Adapted chemical reaction scheme accompanying lithiation or delithiation of Li_2NDC and the changes in π-bonding that occur as a result.

Despite these insights, much remains to be learned of the structural changes in these materials during charging and discharging cycles. As mentioned in Chapter 1, structural study of electrochemically cycled materials by NMR can prove challenging. Although much *ex-situ* NMR work has been completed, there are significant drawbacks to the method, particularly in the case of organic materials. The binder components used are polymers such as polyvinylidene fluoride (PVDF) or polytetrafluoroethylene (PTFE) and as such will appear in ^{1}H and ^{13}C experiments. The inherent disorder of polymers causes broad resonances which can overlap and obscure other signals from the active material. The conductive additives also present complications for the magic angle spinning (MAS) method. The rapid rotation induces a current alongside temperature increases from frictional heating and decoupling. Furthermore, the observation of lithium can be complicated due to residual electrolyte salts that may contaminate the active material after extraction.

An alternative approach that circumvents some of the issues of electrochemical cycling is to use chemical lithiation (CL), also known as chemical pre-lithiation. CL has been used in

studies of battery materials to insert lithium ions into anode materials prior to cell assembly in effort to minimise lithium loss during the formation of the SEI.[20, 21] The method utilises lithium ions in a solution in contact with the active material, together with a redox mediator. The requirement of the redox mediator is that it should have a lower potential than the active material, and will therefore drive electron transfer from the mediator to the active material. Lithium ion insertion into the active material occurs simultaneously to maintain charge balancing. In this work, naphthalene was chosen as the redox mediator for its reduction potential of −2.5 V *vs*. the Standard Hydrogen Electrode (SHE). By this convention, species with the higher of the two reduction potentials will be reduced (accepts electrons) while the other species is itself oxidised (donates electrons). Lithium metal has a reduction potential of −3.0 V *vs*. SHE, thus the reduction potential of naphthalene is +0.5 V *vs*. Li^+/Li^0. Based on the plateau observed by Armand *et al*. during electrochemical cycling of Li_2BDC, this material has a reduction potential of approximately +0.8 V *vs*. Li^+/Li^0. The reduction potential of naphthalene is between that of lithium metal and Li_2BDC. Therefore, in a suitable solvent, naphthalene should oxidise lithium metal to drive dissolution of Li^+ ions in solution accompanied by naphthalene$^{\bullet-}$ radical anions. If Li_2BDC is also added to the solution, the naphthalene$^{\bullet-}$ should drive reduction of the Li_2BDC, with charge balancing maintained by insertion of Li^+ into the structure. With the CL method, there is a possibility that the same chemical or structural changes will not occur as in an electrochemical cell. Furthermore, the CL method suffers from the unquantified level of lithiation, which is possible to estimate with electrochemical data. Nevertheless, the CL method should provide a reduced phase free from additional electrode components making it a useful starting point for further analysis such as by Solid-state NMR and XRD.

In the previous chapter, six organic anode materials were characterised and studied using NMR crystallography. To expand on that work, in this chapter two of those six systems, Li_2BDC and Li_2NDC, are presented as case studies, where the CL method has been used to yield charged phases of $Li_{2+x}BDC$ and $Li_{2+x}NDC$ that can be studied using Solid-state NMR and XRD.

4.2 Experimental Details

4.2.1 Synthetic Details

Li_2BDC and Li_2NDC were reduced using a CL method adapted from Choi *et al*. under an argon atmosphere.[20] Some methodological optimisations were carried out and are discussed in the results (Section 4.3.1). Only the optimised method will be reported in this section.

Firstly, the radical solution is prepared by dissolving 0.5 g (4 mmol) of naphthalene in tetrahydrofuran (THF) (1.5 mL). To this solution 30 mg (4 mmol) of lithium metal chips were

added and the solution stirred for one hour. In a separate vial, approximately 50 mg of pristine anode material (Li_2BDC or Li_2NDC) is covered with a fibre-glass separator punched to fit snugly inside the vial. 0.5 mL of the radical solution is then dropped onto the separator. The vial is then sealed and left for 48 hours.

When the reaction is completed, the excess solution is removed with care taken not to remove sample. The sample is then washed twice by adding 1 mL of THF, lightly agitated, allowed to settle, then carefully removed. The wet powder is then left to dry *in vacuo* for two hours, before being collected in a clean vial. Synthesis procedures are carried out in triplicate and combined to ensure enough sample is produced for further analysis.

4.2.2 Solid-State NMR Details

Solid-state NMR experiments were performed on Bruker Avance III HD spectrometers operating at magnetic field strengths of 9.4 and 16.4 T. ^{13}C NMR spectra are referenced relative to tetramethylsilane using the methyl resonance of *L*−alanine at 20.5 ppm as a secondary reference. ^{7}Li NMR spectra are referenced relative to 1 M $LiCl_{(aq)}$ using solid LiCl at –1.2 ppm as a secondary reference. Full NMR details are given in the relevant figure captions but are summarised below.

^{13}C NMR spectra were recorded at an MAS rate of between 12.5 kHz and 16 kHz using cross polarisation (CP) to transfer magnetisation from ^{1}H with a contact time of between 1 and 5 ms. The CP pulse power was ramped linearly from 70% to 100%. ^{1}H heteronuclear decoupling using two-pulse phase modulation (TPPM)[22] with a pulse length of 4.8 μs and a radiofrequency field strength of 100 kHz was applied during acquisition. Spectra are the sum of between 248 and 2,040 transients separated by a recycle interval of between 10 and 60 s. ^{1}H–^{13}C heteronuclear correlation experiments were performed at an MAS rate of 11,363 Hz and are the result of 168 transients for each of 128 t_1 rows, separated by a recycle interval of 3 s.

^{7}Li MAS NMR spectra were recorded at an MAS rate of 5 or 25 kHz. Static spectra were recorded using a solid-echo (90°–τ–90°–τ–acquire) pulse sequence with a 16-step phase cycle. Spectra are the sum of 64 or 27,000 transients separated by a recycle interval of 3 s.

Variable temperature experiments were conducted with temperature sensors calibrated using $Pb(NO_3)_2$ as discussed in Chapter 2 Appendix 2.1.[23]

4.2.3 Computational Details

First-principles calculations of theoretical NMR parameters were carried out using the CASTEP[24] code including the gauge-including projector augmented wave (GIPAW) algorithm,[25] which allows the reconstruction of the all-electron wave function in the presence of a magnetic field. The CASTEP calculations employed the revised-Perdew-Burke-Ernzerhof

(rPBE) *meta*-generalised gradient approximation (*meta*-GGA) exchange-correlation (XC) functional,[26, 27] and core valence interactions were described by ultrasoft pseudopotentials.[28] Prior to the calculation of NMR parameters, structures were geometry optimised according to the Method E described in Chapter 3, Section 3.6.1, where no geometric constraints are placed on the unit cell and the DFT-D3 semi-empirical dispersion correction (SEDC) scheme is applied.[29, 30]

Geometry optimisations and NMR calculations were carried out using a planewave energy cut off, E_{cut}, of 50 Ry and a *k*-point spacing of 0.05 2π Å^{-1}. The calculations generate the absolute shielding tensor (σ) in the crystal frame. Diagonalisation of the symmetric part of σ yields the three principal components, σ_{XX}, σ_{YY} and σ_{ZZ}. The isotropic shielding, σ_{iso}, is given by (1/3)Tr[σ]. The isotropic chemical shift, δ_{iso}, is given by $\sigma_{ref} - \sigma_{iso}$, where σ_{ref} is a reference shielding determined by comparison of experimental chemical shifts over the complete range of structures. The quadrupolar coupling constant, $C_Q = eQV_{ZZ}/h$ and asymmetry parameter, $\eta_Q = (V_{XX} - V_{YY})/V_{ZZ}$ are obtained directly from the principal components of the electric field gradient tensor, which are ordered such that $|V_{ZZ}| \geq |V_{YY}| \geq |V_{XX}|$. Q is the nuclear quadrupole moment, where a value of –40.1 mb was used for ^{7}Li.[31] In addition to the magnitude, the calculations also generate the sign of C_Q. However, the sign of C_Q cannot be determined from the experimental data presented in this work; therefore, when comparing calculated and experimental quadrupolar couplings, only the magnitude of the calculated C_Q is considered.

4.2.4 Crystallography Details

Polycrystalline materials were analysed using powder XRD. Samples were analysed with a Rigaku SmartLab diffractometer equipped with a D/teX-ULTRA 250 High-Speed Position-Sensitive Detector system and a Ge(220)x2 2-bounce monochromator using CuKα_1 radiation (λ = 1.54059 Å) within a 2θ range of 5°−55° (step size of 0.01°).

4.3 Results

4.3.1 Development and Refinement of the Chemical Lithiation Procedure

The refined CL method used in this work was optimised over several attempts. Initially, the radical solution was made up of naphthalene powder, lithium metal and diglyme as the solvent. Diglyme was chosen for its stability within the voltage ranges of this CL procedure. The solution was prepared by firstly dissolving the naphthalene powder in diglyme which resulted in a clear and colourless solution. Li metal chips were then added to the solution, which dissolved as the solution turned a clear dark green, consistent with the presence of naphthalene$^{\bullet-}$ radical anion species. To this solution, the pristine material was added, where Li_2BDC results in the solution becoming a dark red-brown suspension, while Li_2NDC results in a dark green

suspension. The pristine material had been hand ground for 10 minutes to increase surface area and encourage lithiation. Ball-milling was considered for the grinding of the powder but risked disrupting the crystalline ordering of the pristine material. The reaction was then left overnight. Once the reaction had completed, the radical solution was to be removed using needles. It was observed that the needle used to extract the radical solution became clogged with sample, and only a small sample volume remained and was insufficient for further analysis.

To improve sample recovery, two steps were taken. Firstly, the powder was not ground into a very fine powder, instead left as made by the initial synthesis. Secondly, a microfiber glass separator was introduced into the reaction vial to provide a barrier between the sample and the bulk solution to be extracted. The separators were punched to fit snugly inside the reaction vial. In this methodology, the sample material was placed in the bottom of the vial first, followed by the separator, with care taken not to disturb the layer of sample. The radical solution was then added carefully on top of the separator. This time, the reaction was allowed to proceed for 48 hours. Recovery of sufficient sample was possible using this method and this experimental set up was used for all further experiments.

In the recovered sample, a colour change was observed. Pristine Li_2BDC is a white powder but following the CL procedure, the powder undergoes a colour change to a dark red-brown powder. Similarly, Li_2NDC is a white powder but undergoes a colour change to a grey-green powder. These colour changes indicate the organic linkers undergo electronic change such that they absorb the complimentary wavelengths of light, *e.g.*, the red-brown colour of the Li_2BDC product indicates an absorbance in the blue to violet regions of the visible light spectrum from 400 – 490 nm, and thus the complimentary colour of red-brown is observed. When the samples were exposed to air, a gradual change back to the white colour of the pristine phase was observed over several days, despite no changes in colour observed over three months whilst stored in inert atmosphere. Figure 4.3 shows photographs of this colour change taking place over the course of one week, where the powder is dark red-brown when the sample is first exposed to air. This colour gradually fades with the powder returning to white within one week. This colour change is indicative of air-sensitivity and a reversible redox process occurring in the sample.

In attempt to improve the CL procedure further, investigations into different solvents were carried out. Diglyme is a strongly solvating solvent and may hinder the lithium intercalation process. Choi *et al*. used tetrahydropyran (THP) and THF to chemically prelithiate graphite, as these are weaker coordinating solvents than diglyme.[20, 32] Due to logistical

challenges of procuring anhydrous THP with an inert headspace, THF was used in this work. THF is a slightly stronger coordinating solvent than THP but weaker than diglyme.

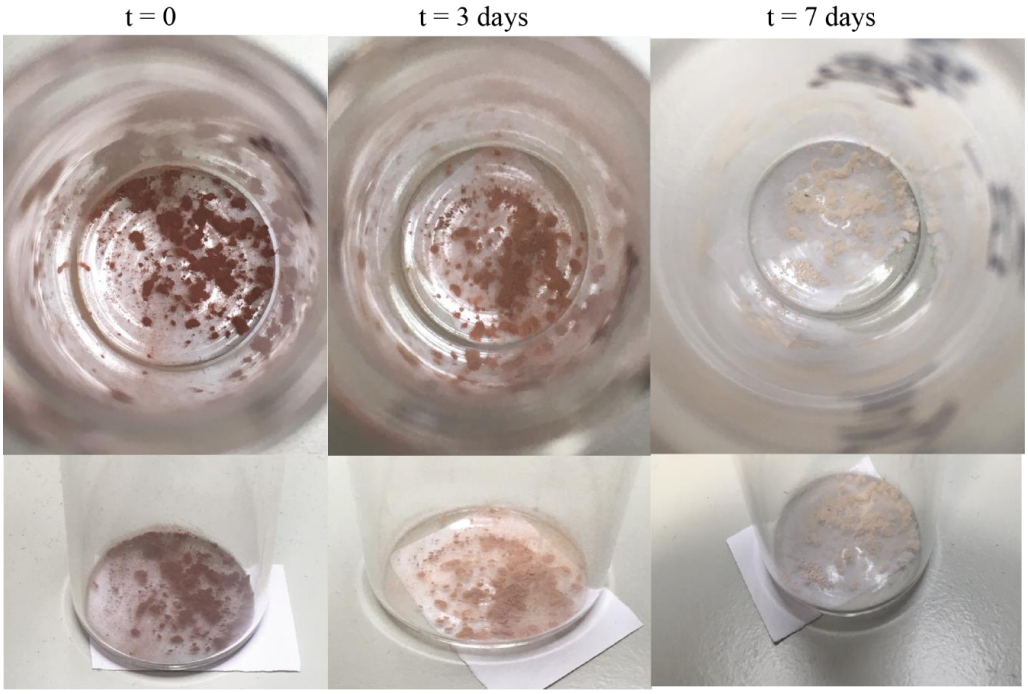

Figure 4.3 Photographs showing the colour change of the product of CL of Li_2BDC after exposure to air over the course of one week.

4.3.2 X-ray Crystallography

To obtain information of the long-range ordering of the reduced phases, XRD measurements were completed. Due to the air-sensitivity of the chemically reduced phases, PXRD analyses were carried out with the sample inside of a borosilicate capillary tube capped with a small amount of vacuum grease. The capillary tubes were packed and sealed inside the glovebox where the CL was carried out. When the capillary tubes were brought into atmospheric conditions, a colour change still occurred, but at a much slower rate (several weeks) providing sufficient time for PXRD analysis. When acquiring data of samples in a capillary tube, additional baseline is observed at low angles of 2θ, which can completely obscure some low intensity reflections at low angles that might be present in the PXRD pattern. Furthermore, capillary tubes can also give poorer signal to noise compared to a flat plate, further obscuring low intensity reflections. The slowest possible scan rate (0.1°/minute) and step size (0.0004°) were used to ensure the best possible signal acquisition. Despite the limitations of using capillary tubes, strong reflections are still visible above the baseline and can be compared with the powder patterns of the pristine phases to assess if the materials undergo structural change during the lithiation procedure.

Figure 4.4 shows a comparison of experimental PXRD powder patterns of chemically lithiated $Li_{2+x}BDC$ reduced in diglyme (Figure 4.4a), chemically lithiated $Li_{2+x}BDC$ reduced in THF (Figure 4.4b) and for comparison, pristine-Li_2BDC (Figure 4.4c). Due to the use of borosilicate capillary tubes to keep samples in an inert atmosphere, both CL products have strong baseline contributions from the capillary tube. CL in diglyme results in a powder pattern with characteristic reflections at 10°, 20°, 23°, 25°, 30°, 41° and 43°. Comparing this with the powder pattern of the pristine phase shows a strong similarity with the same characteristic reflections. From this PXRD data, it is unclear if the CL method has been successful. This suggests that despite the redox potential of the Li-naphthalene system being greater than that of Li_2BDC, lithium ions have not inserted into the structure. A possible reason for this is the strongly coordinating behaviour of the diglyme solvent due to the two ether groups which coordinate to metal centres. Choi. *et al*. have shown that chemical pre-lithiation of graphite is much more effective when a weakly coordinating solvent, such as furans, are used.[20] To this end, the CL procedure was repeated using THF as the solvent. CL in THF results in a distinctly different powder pattern to both the diglyme reduced and pristine phase suggesting structural changes have occurred with characteristic reflections at 10°, 12°, 20°, 21°, 24°, 26°, 28°, 31° and 38°. This agrees with the powder pattern of electrochemically lithiated sample reported by Armand *et al*.[1] While the powder pattern in that work is rather broad, characteristic reflections are observed at 21°, 26°, 28° and 31° which are all present in the powder pattern in the current work. The difference between the two CL products indicates that THF is a more appropriate choice of solvent for the CL method.

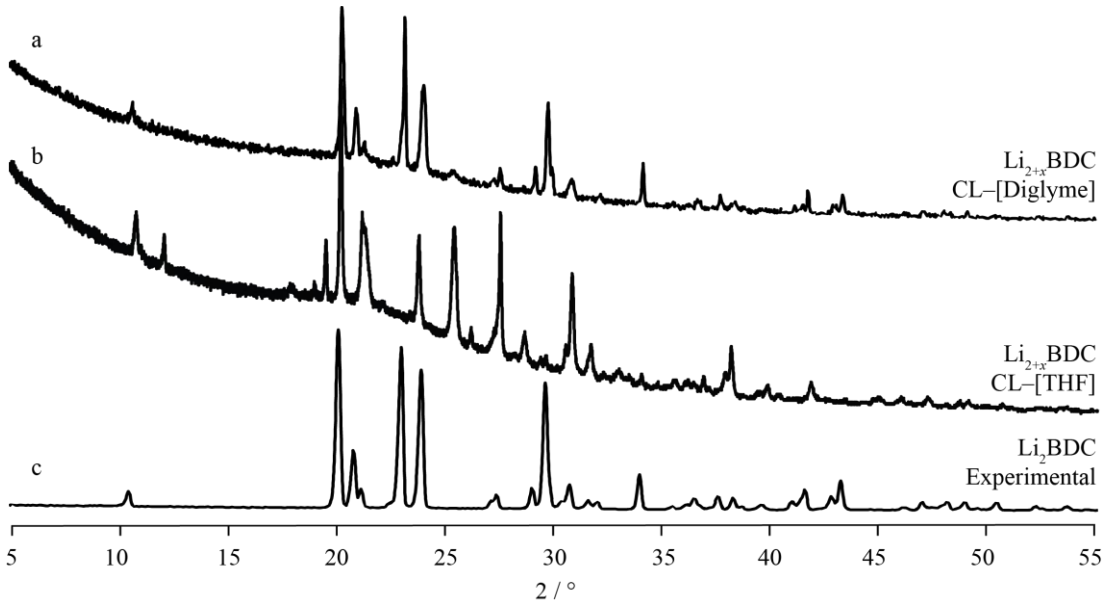

Figure 4.4 Experimental PXRD patterns of Li_2BDC and $Li_{2+x}BDC$ CL in both diglyme and THF as solvent.

Based on the results for Li_2BDC, THF was used as the solvent for subsequent lithiation procedures. Figure 4.5 shows a comparison of powder patterns for chemically lithiated $Li_{2+x}NDC$ in THF (Figure 4.5a) and pristine Li_2NDC (Figure 4.5b). Here, a clear difference between the two patterns is observed. Characteristic reflections in the PXRD pattern of the CL product are observed at 17°, 22°, 24°, 26° and 30° while characteristic reflections in the powder pattern of the pristine material are observed at 19°, 23°, 24°, 29° and 35°. Both CL products feature broadened reflections than those observed in the PXRD patterns of the pristine phases. This suggests these phases are slightly less ordered than the pristine materials, which is expected as Armand *et al*. also observed some sample degradation, but they do remain crystalline. This enables further attempts to understand the structures more thoroughly. However, for PXRD, the absence of a structural model makes it difficult to gain further insight into the structure of the chemically lithiated phases, and thus further techniques such as NMR spectroscopy can be applied to attempt to learn more about these phases.

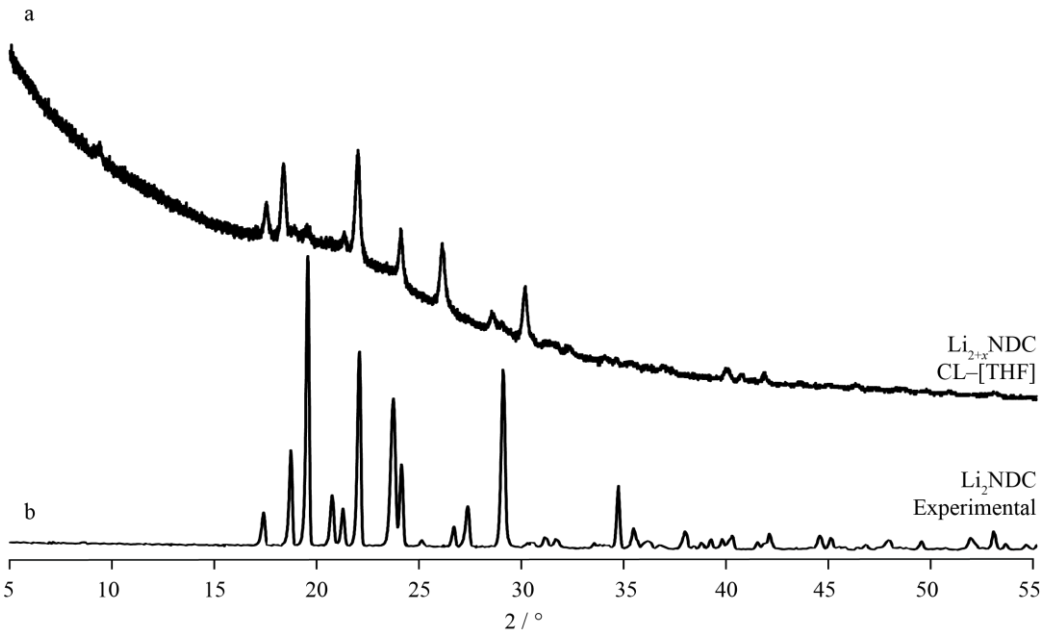

Figure 4.5 Experimental PXRD patterns of Li_2NDC and $Li_{2+x}NDC$.

4.4 ^{13}C Solid-State NMR Spectroscopy

To obtain further structural information about the lithiated phases, ^{13}C CPMAS NMR experiments were performed on both the pristine Li_2BDC and $Li_{2+x}BDC$ reduced by CL in both diglyme and THF and are shown in Figure 4.6. Comparison of the pristine spectra to that of the chemically lithiated materials reveals a significant change between pristine and chemically lithiated materials. Figure 4.6a shows a ^{13}C CPMAS NMR spectrum of the pristine phase, showing the characteristic carboxylate resonance at 177.7 ppm, and the three aromatic resonances between 140 ppm and 130 ppm. Figure 4.6b and Figure 4.6c show spectra of

chemically lithiated phases in diglyme and THF respectively. The sample chemically lithiated in diglyme shares strong similarities with the spectrum of the pristine phase, where the resonances from the pristine phase are present with additional low intensity resonances at 165 ppm, 155 ppm, 110 ppm, 93 ppm and 90 ppm. The new resonances suggest a small quantity of a new phase is present in the sample and new chemical environments are formed. However, the observation of the new phase present in the spectra highlights the high sensitivity of ^{13}C Solid-state NMR experiments to the local structural changes occurring during CL. Where PXRD suggested little or no structural change with CL in diglyme, ^{13}C Solid-state NMR was able to observe small quantities of the new phase formed. In the spectrum of the sample reduced in THF, intense resonances appear at the same chemical shifts as the low intensity resonances in the spectrum of the sample reduced in diglyme. For the most part, these new strong resonances are sharp except for the broad resonance at 115 ppm. This suggests that the same phase is produced by both CL methods, but in a greater yield when reduced in THF. This is consistent to the results of PXRD analysis that showed that a new phase was only observed when reduced in THF. Furthermore, low intensity resonances appear at 177.4 ppm and 136.6 ppm arising from a small quantity of pristine phase remaining in the sample. Resonances arising from the chemically lithiated products in the samples mostly appear at significantly different chemical shifts to resonances arising from the pristine phase. Firstly, the carboxylate resonance, which appears at 177 ppm in the pristine phase, appears as two resonances at 165 ppm and 155 ppm. This shift to lower chemical shift is consistent with a greater electron density near to the carbon atoms that is expected with additional lithium ions inserted into the structure. Secondly, resonances arising from the aromatic ring between 136 and 130 ppm in the pristine phase, appear between 115 and 90 ppm. Finally, the number of resonances increases from four in the pristine phase to six in the chemically lithiated phases, if it is assumed that the broadened resonance at 115 ppm is made up of two resonances with very similar chemical shift. This change suggests that the two phases have differing symmetry, where the pristine phase has an inversion centre at the centre of the aromatic linker, the reduced phase could have a plane of reflection along the length of the organic linker, giving a total of six chemically distinct carbon sites.

Figure 4.6d shows a spectrum of a later repetition of the THF reduction method on a different sample, where the pristine phase is observed in much stronger intensity, almost equal to that of the reduced phase. The reduction procedure was carried out according to the same procedure and therefore the reasons for the discrepancies are unclear but could indicate that the CL method is not completely reproducible, and care should be taken to ensure conditions are the same.

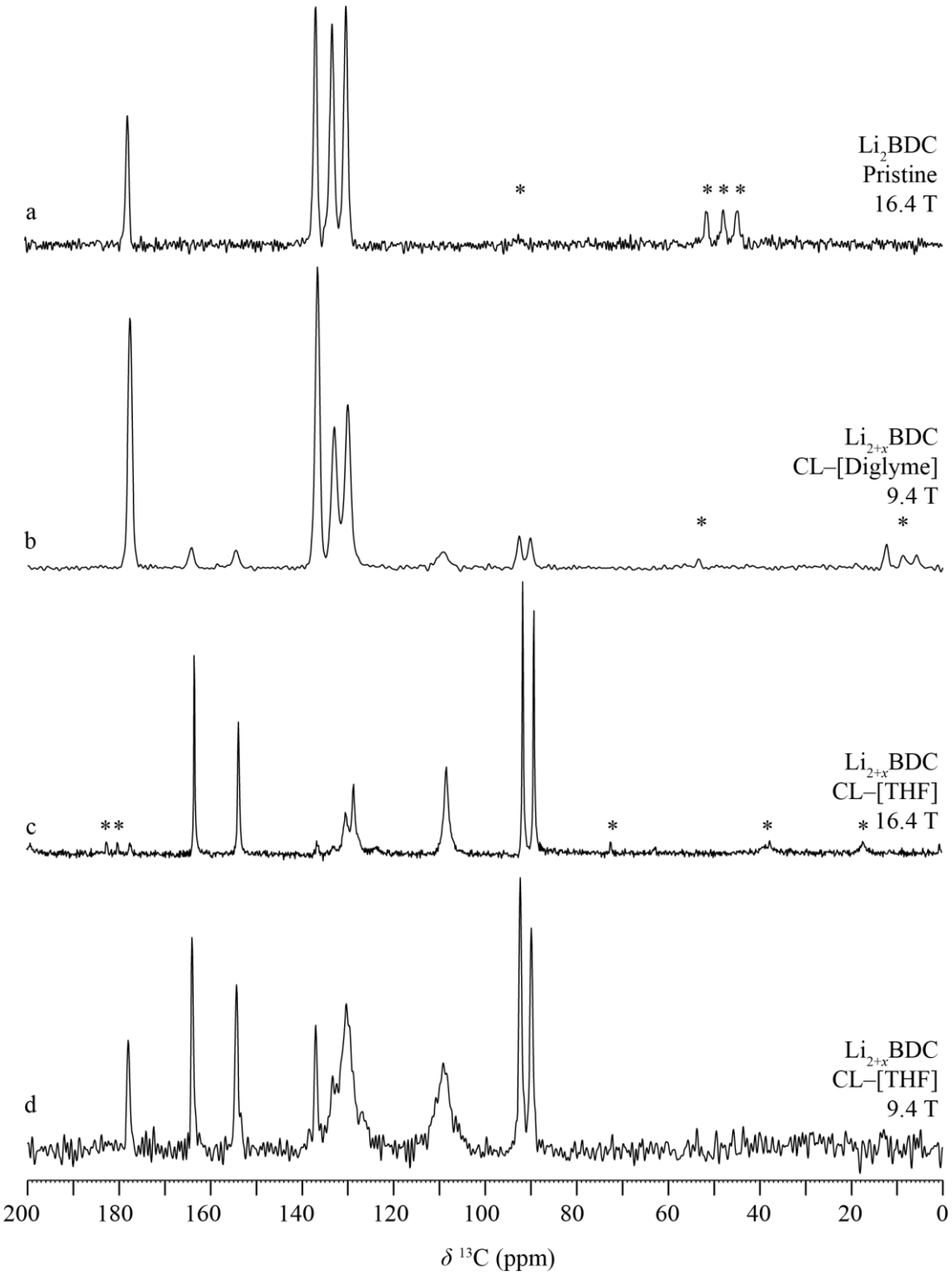

Figure 4.6 Comparison of ^{13}C CPMAS spectra of pristine-Li_2BDC and $Li_{2+x}BDC$ gained from different reduction methods. (c) and (d) are different samples made by the same procedure. Spectra collected at various MAS rates (a) = 15 kHz, (b) and (d) = 16 kHz, (c) = 12.5 kHz. Contact times: (a) = 1 ms, (b) = 3 ms (c) and (d) = 5 ms. Transients collected: (a) = 240, (b) = 2,048, (c) = 232, (d) = 512. Recycle intervals: (a) and (c) = 60 s, (b) =30 s, (d) = 10 s. * = Spinning side band (SSB).

Figure 4.7 shows a spectrum of an electrochemically reduced sample in which the pristine phase is still clearly observed alongside the new resonances observed in spectra of chemically lithiated samples. This confirms that the samples reduced by the CL method are consistent in structure to those reduced electrochemically, despite the low conversion of the

electrochemical cycling method. The electrochemically reduced sample was extracted from a coin cell, discharged to 2.6 V *vs*. Li^+/Li^0, data was collected and prepared by Professor John Griffin (unpublished work).

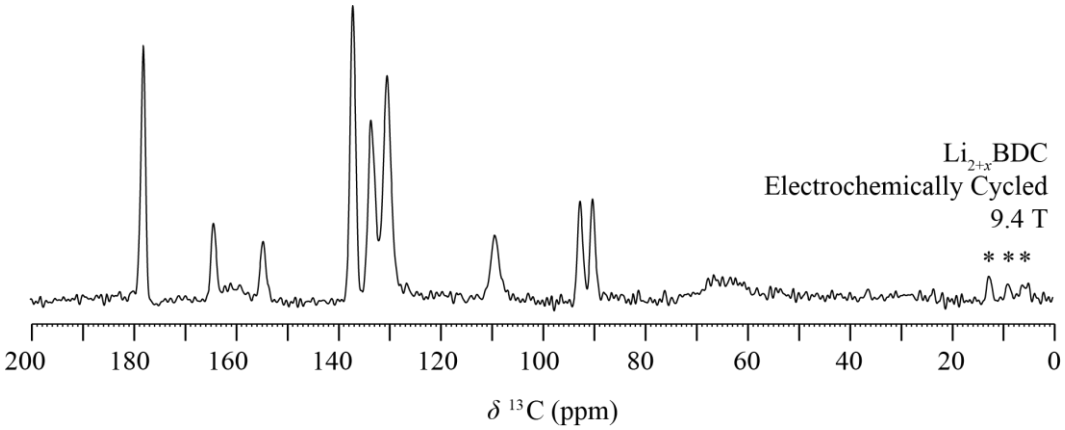

Figure 4.7 ^{13}C CPMAS spectrum of $Li_{2+x}BDC$ gained from electrochemical cycling. Spectrum is the result of 1,144 transients separated by recycle interval of 60 s, with magnetisation transferred with a contact time of 3 ms. MAS = 12.5 kHz. * = SSB.

The majority of resonances in the carbon spectra of the lithiated phases are sharp, which suggests the samples are locally ordered. The sample reduced in diglyme has resonances that are slightly broader than those of the THF samples, suggesting the crystallinity is slightly increased in samples reduced in THF. However, in the spectra of the THF-reduced phases, particularly Figure 4.6d, the resonances at 130 and 110 ppm are rather broad. This could be the result of disorder or dynamics in the structure. It is possible that this broadening arises in the aromatic region due to dynamics such as rotation of the organic linker. Chemical exchange can occur between inequivalent chemical sites and the frequency at which this occurs is directly related to temperature. If the temperature was sufficiently low that the exchange is either slow or halted, then inequivalent sites will have different chemical shifts. As temperature increases, and so does the rate of chemical exchange, motional broadening occurs where the peak widths increase. The increased temperature would lead to faster relaxation, and therefore a shorter free induction decay (FID), directly leading to the increase in peak width. As temperature continues to rise, the multiple resonances for the chemically inequivalent sites will coalesce into a single broad resonance. If temperature is increased further still, and therefore so too does the rate of chemical exchange, then motional narrowing occurs where the single resonance then gradually narrows with increasing temperature. Since the structure of the pristine phase is not porous, when additional lithium ions are inserted into the structure it is anticipated that the existing framework would require some distortion or rearrangement to be able to accept additional lithium ions. This distortion could leave sufficient space between the organic layers for the aromatic linkers to rotate. Inspection of the pristine crystal structures suggests that rotation of the organic linkers is not possible, and this is in agreement with the sharp resonances observed in the NMR

spectrum. To assess if dynamics occurred in the reduced phase, variable temperature (VT) CPMAS experiments were completed, where at high temperatures the rotation would be expected to be quicker and result in broader resonances. Conversely, at low temperatures, the rotation would slow down and result in sharper resonances. Figure 4.8 shows ^{13}C CPMAS spectra collected at three different temperatures; 262 K, 298 K and 315 K. Firstly, the intensity of the peaks relating to the pristine phase are more intense, this is possibly a result of the sample being stored inside of the NMR rotor for approximately four weeks, outside of an inert atmosphere prior to the experiment. Despite the fact that the NMR rotor was packed under an inert atmosphere, some sample degradation could occur should the NMR rotor not be sufficiently air-tight. Secondly, no change in the width in any of the resonances is observed, which suggests that dynamics of the organic linker is not the cause of the broadened resonances. However, it is possible that the temperature range studied may not be sufficient to observe any significant change in the rate of dynamics and such dynamics could still be a factor over a larger temperature range.

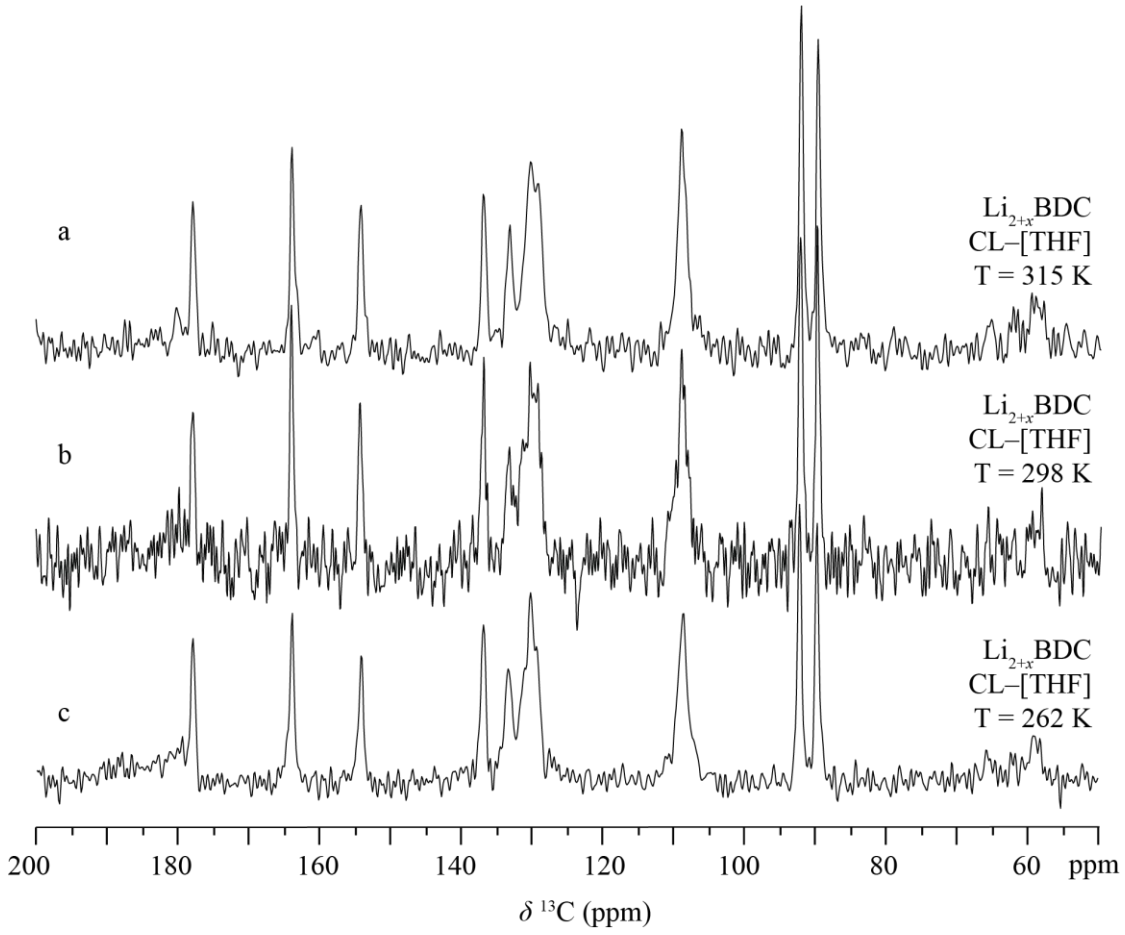

Figure 4.8 ^{13}C CPMAS spectra of $Li_{2+x}BDC$ recorded at three temperatures. All spectra collected at 12.5 kHz MAS rate, utilising a contact time of 5 ms. (b) is the result of 400 transients, while (a) and (c) are the result of 800 transients, all separated by a recycle interval of 10 s. Spectra recorded at a field strength of 16.4 T.

$^{1}H–^{13}C$ heteronuclear correlation (HETCOR) experiments can give valuable information for assignment of ^{13}C spectra by correlating carbon resonance with nearby proton resonances. The HETCOR experiment utilises a short contact pulse, during which magnetisation is transferred through space from the protons to carbons. The short contact pulse selects for carbons that are in close proximity to a proton, such as the tertiary carbon atoms on the BDC linker, while reducing signal from carbon atoms that are further in space from a proton such as the quaternary carbons in the organic linker. Typically these contact pulses are around 50 – 200 μs to select for one-bond proximities. Figure 4.9 shows a correlation of the carbon resonances at 110 ppm and 130 ppm with proton resonances at approximately 7 ppm, while the carbon resonances at 90 ppm, 93 ppm, 133 ppm and 139 ppm are correlated with a proton resonance at 7.5 ppm. No correlations are observed for the carbon resonances at 165 ppm or 155 ppm from the two crystallographically distinct carboxylate carbons. The low intensity correlations observed at 90 ppm and 93 ppm suggests these carbons are also further than one

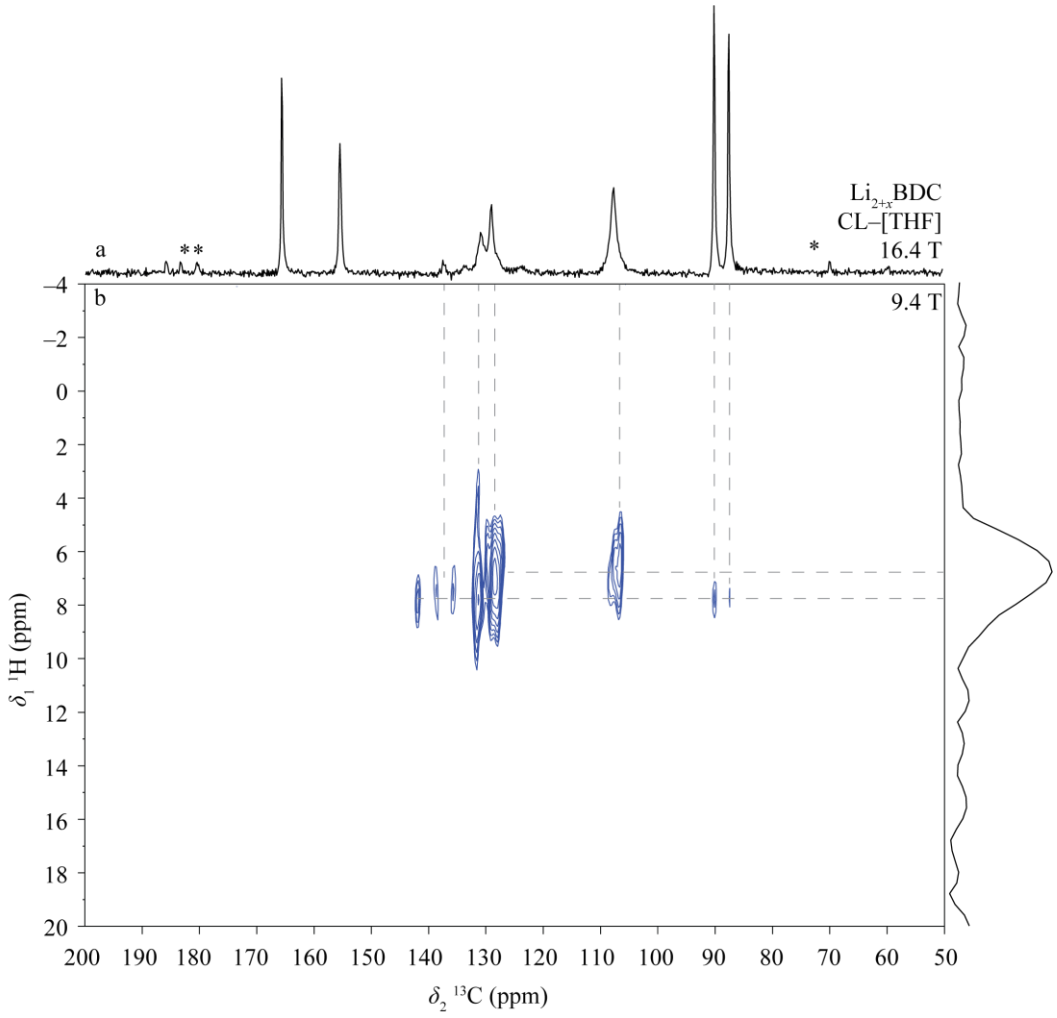

Figure 4.9 $^{1}H–^{13}C$ HETCOR NMR spectrum of $Li_{2+x}BDC$ (b). A ^{13}C CPMAS spectrum is shown above (a), experimental details are as described in Figure 4.6c. HETCOR spectrum collected at 9.4 T with an MAS rate of 11,363 Hz. The spectrum is the sum of 168 transients of each of 128 t_1 rows, separated by a recycle interval of 3 s. Grey dashed lines are visual aid for interpretation.

bond from a protonated carbon and thus are associated with the quaternary carbon atom directly bonded to the carboxylate carbon. Therefore, the low intensity correlation at 140 ppm is likely due to a tertiary aromatic carbon from the pristine phase since all quaternary carbons would otherwise be accounted for.

Figure 4.10 shows ^{13}C CPMAS NMR spectra for pristine Li_2NDC and for chemically lithiated $Li_{2+x}NDC$. In the spectrum of the pristine phase, a carboxylate resonance is observed at 180 ppm, with an unresolved aromatic region consisting of at least four resonances between 140 ppm and 125 ppm. Comparing the spectrum of the reduced phase suggests that a near complete lithiation has been achieved with the CL method in THF. A very low intensity carboxylate resonance can be seen at 179 ppm, and while aromatic resonances are observed in a similar chemical shift range, there are only three visible resonances that are observed in a smaller chemical shift range, from 138 ppm to 130 ppm. In the spectrum of the reduced phase, the carboxylate resonance is a single resonance at 159 ppm, which suggests the symmetry of the $Li_{2+x}NDC$ is similar to that of the pristine phase which is in direct contradiction to the case of Li_2BDC. However, some similarities do exist between the two anode materials, such as broadened resonances in the $Li_{2+x}BDC$ spectrum (Figure 4.6b), which are similar to those

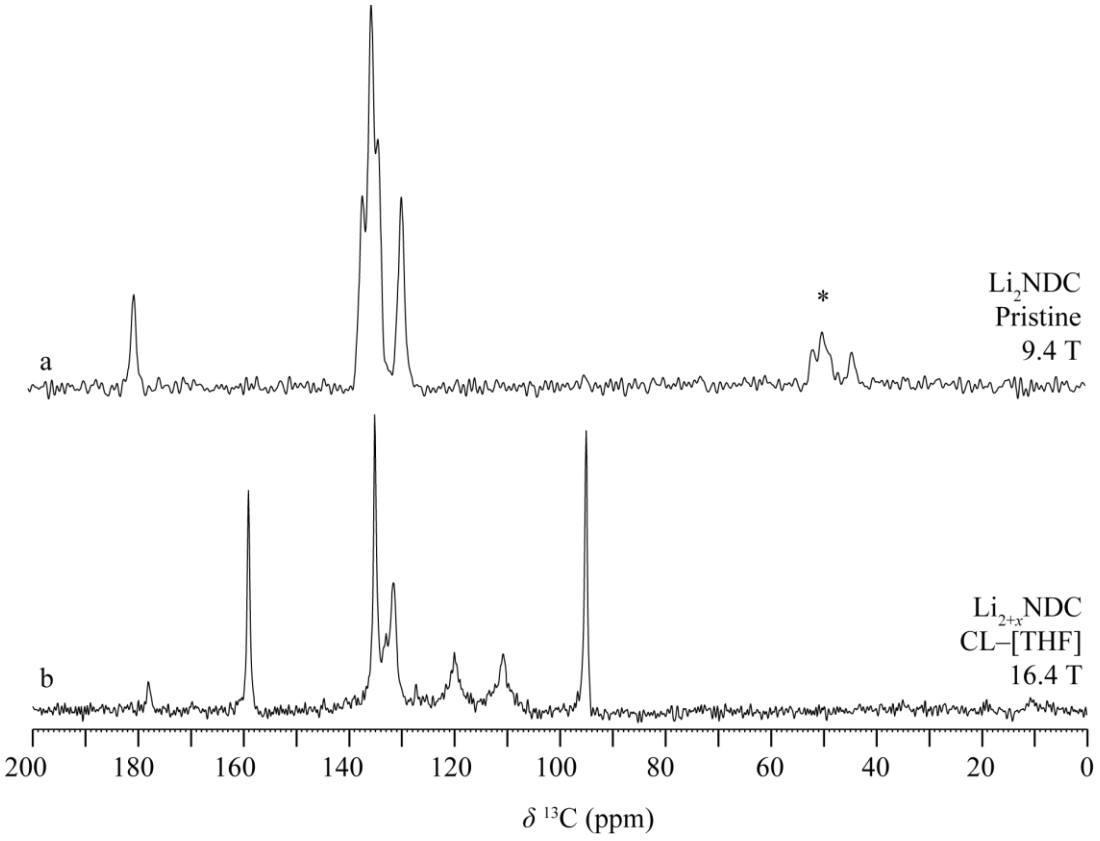

Figure 4.10 ^{13}C CPMAS NMR spectra of Li_2NDC and $Li_{2+x}NDC$. * = SSB. Spectra are collected at MAS rates of (a) = 15 kHz and (b) = 16 kHz, utilising a contact time of (a) 1 = ms and (b) = 5 ms. (a) is the sum of 960 transients separated by a recycle interval of 60 s, while (b) is the result of 400 transients separated by a recycle interval of 10 s.

present in the $Li_{2+x}NDC$ spectrum (Figure 4.10b) at 120 ppm and 111 ppm. The hypothesis that this could be a result of dynamics in the structure, such as the NDC linker rotating about the C−C bond between the carboxylate carbon and the quaternary carbon at the ends of the linker was investigated with VT experiments.

VT CPMAS experiments at three different temperatures, 262 K, 298 K and 315 K, were completed on the reduced $Li_{2+x}NDC$ phase, shown in Figure 4.11. Similarly to $Li_{2+x}BDC$, no change in peak widths were observed within this temperature range. While it is possible that dynamics could still be present, these observations suggest dynamics do not contribute to line width variations within this temperature range.

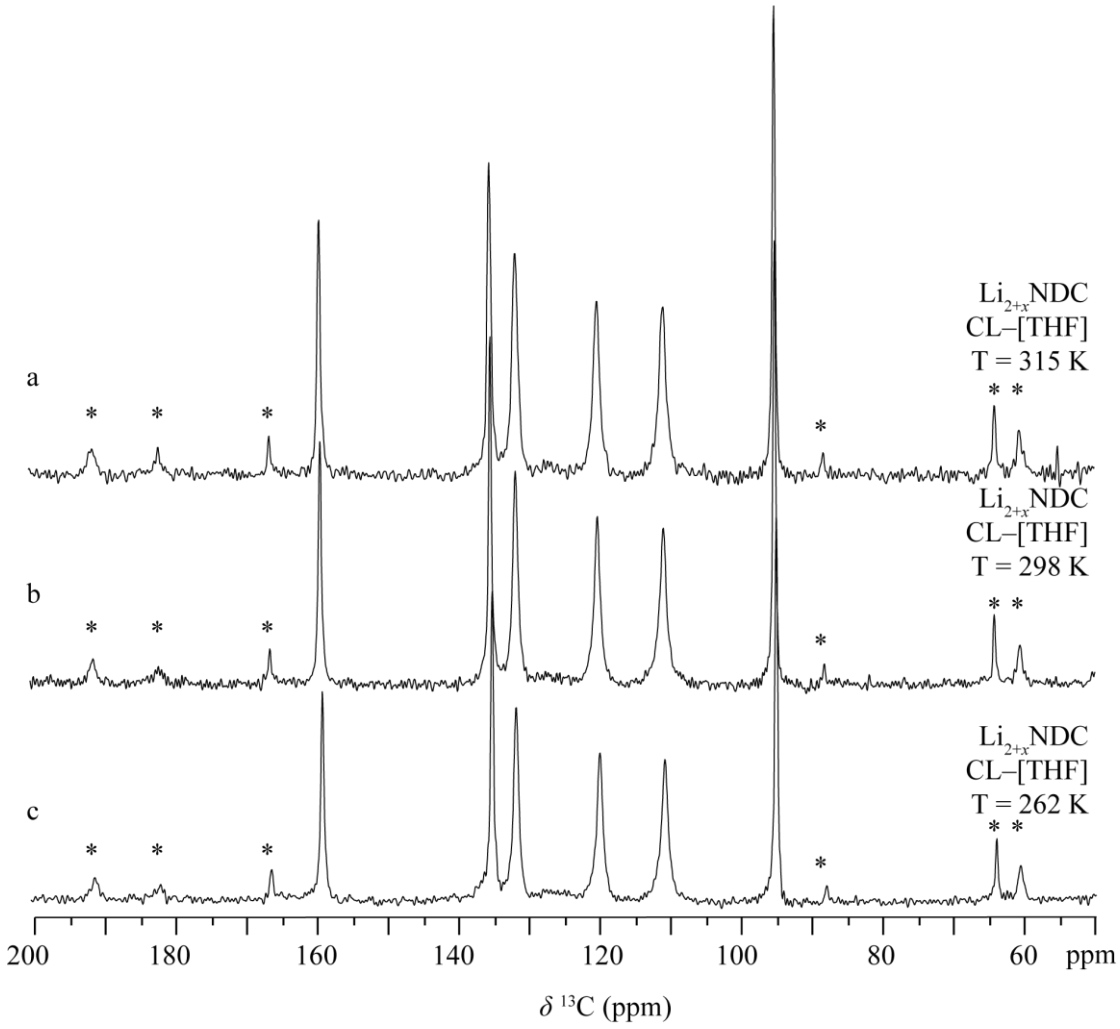

Figure 4.11 ^{13}C CPMAS NMR spectra of $Li_{2+x}NDC$ recorded at three temperatures. * = SSB. All spectra collected at 12.5 kHz MAS rate, are the sum of 400 transients separated with a recycle interval of 10 s. Magnetisation was transferred with a contact time of 5 ms. Spectra recorded at 16.4 T.

A $^{1}H–^{13}C$ HETCOR experiment reveals strong correlations between a carbon resonance at 111 ppm with a proton resonance at 6 ppm, and between carbon resonances at 120 ppm and 130 ppm with a proton resonance at 7.7 ppm (Figure 4.12). Therefore, these resonances are

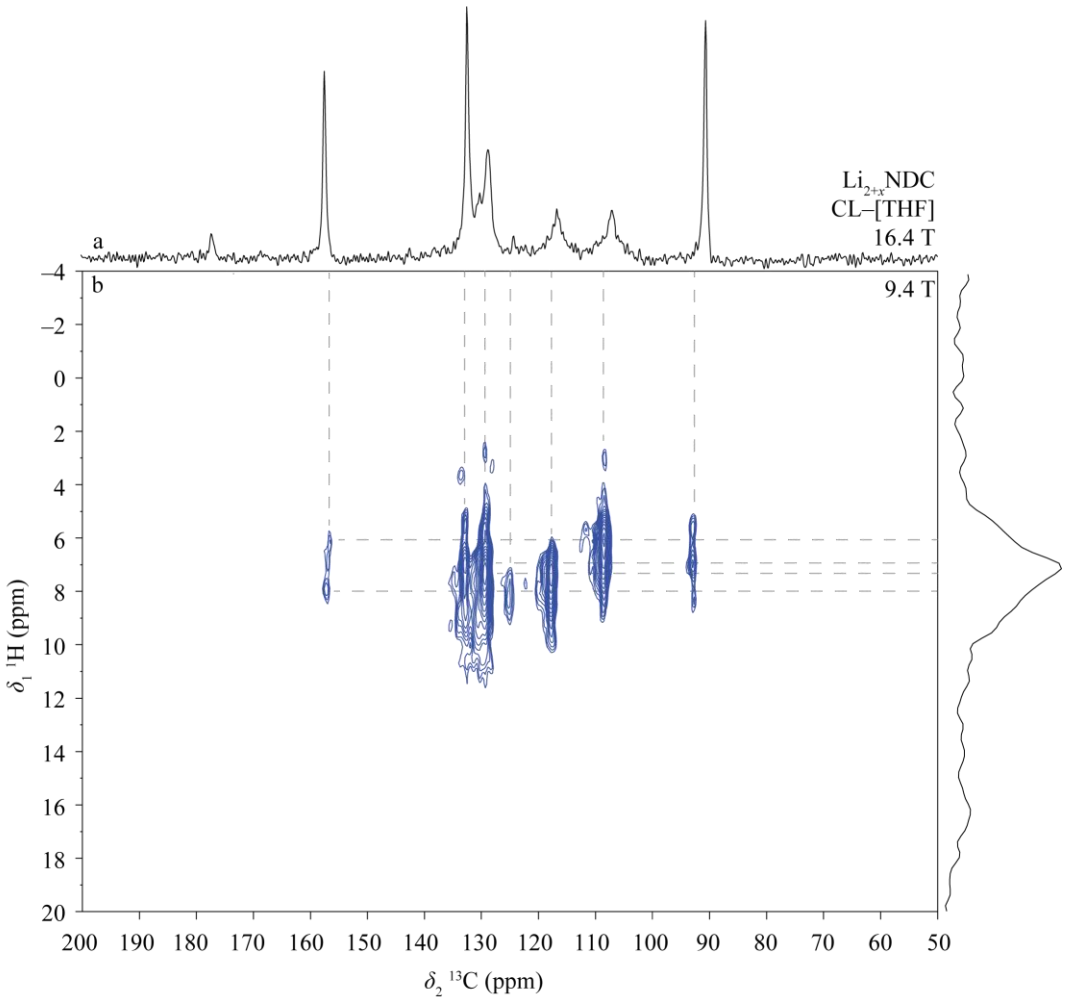

Figure 4.12 $^{1}H-^{13}C$ HETCOR NMR spectrum of $Li_{2+x}NDC$ (b). A ^{13}C CPMAS spectrum is shown above (a), experimental details are as described in Figure 4.10b. HETCOR spectrum collected at 9.4 T with an MAS rate of 11,363 Hz. The spectrum is the sum of 168 transients of each of 128 t_1 rows, separated by a recycle interval of 3 s. Dotted lines are visual aid for interpretation.

highly likely to be the result of the tertiary carbons of the NDC linker. As the symmetry between pristine and reduced phase is seemingly unaffected, observation of three tertiary resonances is expected. Furthermore, there are weaker correlations between carbon resonances at 92 ppm, 125 ppm, and 133 ppm with proton resonances at 7.5 ppm, 8 ppm, and 7.5 ppm, respectively. These correlations likely arise from the three quaternary carbons of the NDC linker which have a longer distance between the carbon atom and the nearest hydrogen atom. The carbon resonance at 159 ppm is weakly correlated with protons resonances at 6 ppm and 8 ppm suggesting that while still relatively far removed from a proton, it has equal proximity with two distinct proton sites, and is attributed to the carboxylate carbon.

4.5 ^{7}Li Solid-State NMR Spectroscopy

To directly probe the positions of lithium ions in the structures of the reduced phases, ^{7}Li NMR experiments were performed. Figure 4.13 shows fast-spinning (25 kHz), slow spinning (5 kHz) and static ^{7}Li experiments of both reduced anode materials. Fits to the static quadrupolar lineshapes, shown in red, were generated using the TopSpin software and the quadrupolar parameters (C_Q and η_Q) extracted for each experiment. Fits with $\eta_Q = 0$ and $\eta_Q = 1$ are shown for illustration above the static spectra in orange. While it is known that the pristine materials have one crystallographic lithium site each, it remains unclear how many crystallographic lithium sites the reduced phases have. As such, fits to the lineshapes are not expected to give accurate quadrupolar parameters, but rather provide a qualitative comparison

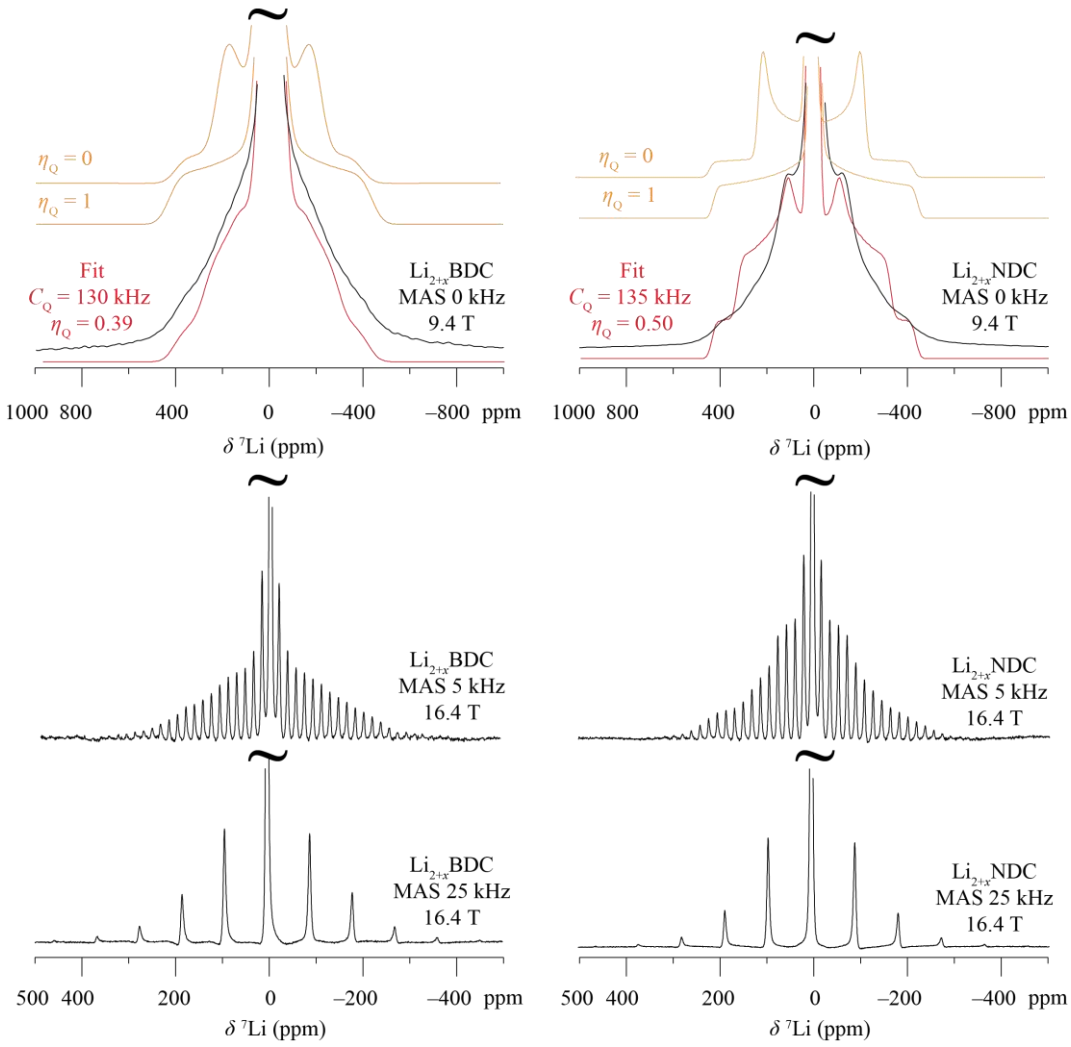

Figure 4.13 Experimental ^{7}Li NMR spectra of $Li_{2+x}BDC$ and $Li_{2+x}NDC$. MAS experiments of two different MAS rates (5 kHz and 25 kHz) were completed at a field strength of 16.4 T, while static experiments were completed at 9.4 T. MAS experiments are the sum of 64 transients, while static spectra are the sum of 27,000 transients all separated by a recycle interval of 3 s. Fits to the static quadrupolar lineshapes are shown in red, while fits with $\eta_Q = 0$ and $\eta_Q = 1$ are shown for illustration in orange.

against the quadrupolar lineshapes of the pristine materials and assess how the quadrupolar parameters change following lithiation. Inspection of the MAS lineshapes for the reduced phases does not clearly show multiple lithium sites are present. As ^{7}Li typically has a small chemical shift range of ± 1 ppm, the broadened lineshapes are likely to mask the small differences in chemical shift that would be expected for multiple lithium sites and therefore no information on the number of lithium sites can be elucidated. Experimental quadrupolar parameters for the pristine materials are given in Table 4.1.

Table 4.1 Tabulation of quadrupolar parameters of pristine and reduced anode materials

Compound	δ (ppm)	$\lvert C_Q \rvert$ / kHz	η_Q
Li_2BDC	0.0 ± 0.3	71 ± 2	0.5 ± 0.1
Li_2NDC	–0.2 ± 0.1	74 ± 5	0.6 ± 0.1
Li_{2+x}BDC	1.1 ± 0.2	130 ± 3	0.39 ± 0.1
Li_{2+x}NDC	0.7 ± 0.2	135 ± 3	0.50 ± 0.1

In the experimental spectra of the reduced materials, a systematic increase of C_Q is observed when compared with the pristine phases. For Li_{2+x}BDC, the C_Q is approximately 130 kHz, while in Li_{2+x}NDC it is approximately 135 kHz compared to 71 kHz and 74 kHz in the respective pristine phases. Firstly, the observation of a change in C_Q is consistent with a change in lithium environment as a result of the CL procedure. Secondly, an increase in C_Q suggests a less symmetric lithium site. For example, in the pristine material, the singular lithium site is in a slightly distorted LiO_4 tetrahedron, while in the reduced phases insertion of additional lithium ions is likely to cause increased distortions as the framework responds. Furthermore, if the additional lithium ions are located on the interface between the lithium-oxygen layer and organic layers, the electric field gradient (EFG) would be highly asymmetric as either side of the interface would have a significantly different electron density.

4.6 Electron Paramagnetic Resonance Spectroscopy

Electron paramagnetic resonance (EPR) spectroscopy has been used to assess if paramagnetic species, such as lithium ions, are present in the pristine and charged conjugated organic dicarboxylates. All EPR experiments were completed at room temperature on an X-band 9.8 GHz Bruker EMXplus and were performed by Chris Cook (Lancaster University). No EPR signal was observed for either of the pristine materials, confirming that no paramagnetic species are present in either sample, which is consistent with the observations of Armand *et al.*[1] However, in the lithiated materials (Li_{2+x}BDC and Li_{2+x}NDC) strong EPR signals are observed, shown in Figure 4.14. This observation is also consistent with the previous work, but with the additional knowledge that the signal does not come from conductive carbons in an electrochemical cell, but rather the sample itself. Li_{2+x}BDC has a strong signal that appears to be

isotropic (g = 2.020) with unresolved hyperfine splitting. On account of the lack of strong hyperfine splitting and the value of the g-factor, the signal is likely to be a result of a carbon-centred radical. $Li_{2+x}NDC$ also has a strong signal (g = 2.022) which also suggests a carbon-centred radical. These observations suggest that when lithium ions enter the structure, the single unpaired electron is donated to the organic backbone. The proposed reaction mechanism that accompanies reduction with two lithium ions inserted per formula unit would have no unpaired electrons, and thus, no EPR signal. If the stoichiometry of reduction is less than two lithium ions per formula unit (*i.e.* $1 < x < 2$) then some of the organic linkers must have just one lithium ion per formula unit, giving some unpaired electron density in these regions. The NMR results shown in Section 4.4 suggest the CL products are closed shell structures as no broadening or shifting of resonances is observed. However, EPR suggests that some regions of partially reduced are not observed by NMR.

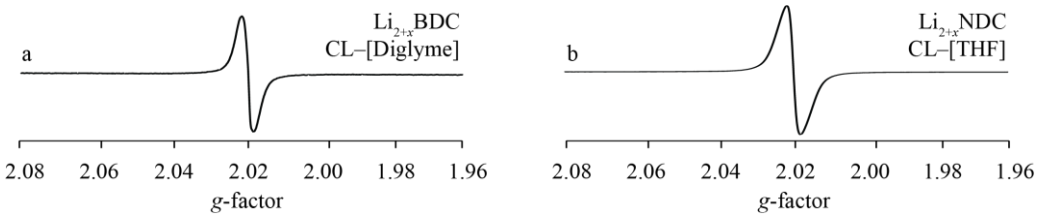

Figure 4.14 EPR spectra of chemically lithiated materials.

4.7 Density Functional Theory

The aim of this work is provide insights into the location of the additional lithium ions in the lithiated phases of conjugated dicarboxylate materials used as organic anode materials. Experimental data have given some insights but does not directly lead to structural characterisation. As shown in the previous chapter, density functional theory (DFT) can provide a link between the structure and experimental data.

As discussed in the previous chapter, a robust methodology for the calculation of NMR observables using DFT has been refined on the pristine phases of both lithium and sodium based organic anode materials. This refined methodology employs the rPBE XC functional, and the Grimme-D3 dispersion correction scheme.[26, 27, 30] With this methodology now optimised using the pristine phases it is now applied to the study of the reduced phases.

The primary challenge in the study of the reduced phases by DFT arises from the lack of published structural data. While the products of CL circumvent the issues associated with electrochemically reduced samples, it remains a significant challenge to produce a single crystal for single crystal XRD analysis. As previously discussed in Section 4.3.1, CL products are

air-sensitive, which requires PXRD data to be acquired while the sample is in a capillary tube. This makes refinement a challenge due to the increased baseline and reduced signal to noise.

4.7.1 *Ab-Initio* Random Structure Searching of $Li_{2+x}BDC$

Computationally generated structures of the reduced phases can be used to provide some insights into the structures where experimental structures are not available. *Ab-initio* random structure searching (AIRSS), performed by Professor Andrew Morris (University of Birmingham), generated theoretical structures of Li_4BDC. Generally, the starting point for the AIRSS method would be a unit cell with a random distribution of all of the atoms in the unit cell. This methodology would not be appropriate in this case, as the repeating layered structure would be too complex to be simulated by the AIRSS method. Therefore, since the pristine structures are the starting point for experimental lithiation processes, the assumption is made that the pristine structure is an appropriate starting point for AIRSS. A further assumption is made that the structure incorporates two lithium ions giving a stoichiometry of Li_4BDC, as such two lithium ions were added at random into the existing unit cell of the pristine materials. However, if the structures undergo large structural changes then the reduced structures may be unobtainable by the AIRSS approach as it does not model reaction mechanisms, only structural geometries based on the local forces on atoms. The output structures are those in energetic minima, with the electronic structure used to assess the structures viability. From AIRSS, the nine lowest energy structures were selected for further analysis.

The set of nine structures were then geometry optimised using the refined method detailed above in Section 4.7 and in the previous chapter. The nine structures can be ranked according to their single-point energy (SPE), which is calculated during the electronic energy minimisation calculation, this gives insight into which structures are most energetically favourable (Table 4.2).

Table 4.2 Ranked tabulation of the single-point energies (SPE) of the nine Li_4BDC structures generated by AIRSS.

Structure	SPE (eV)	SPE *vs.* 55 (eV)
55	−7801.19	0
54	−7801.03	+ 0.16
65	−7800.89	+ 0.30
10	−7800.83	+ 0.36
58	−7800.82	+ 0.37
17	−7800.74	+ 0.46
11	−7800.68	+ 0.51
08	−7800.40	+ 0.80
35	−7800.02	+ 1.18

Figure 4.15 shows the crystal structure of the nine geometry-optimised structures ranked according to the structures SPE, as well as a crystal structure of the pristine Li_2BDC. While the structures retain the repeating layers present in the pristine structure, a wide range of different geometries and bonding environments are observed. Interestingly, all of the structures undergo a unit cell volume contraction during the process of AIRSS and DFT geometry optimisation as shown in Figure 4.16. Structure **10** is perhaps the most visibly different structure, where the β-angle of the rhombohedral unit cell ($\beta = 111°$) is significantly larger than any of the other structures ($81.2° < \beta > 96.1°$). This accompanies a large reduction in the distance of the *a* dimension (−32.4%), a large increase in the length of the *c* dimension (+16.2%) and the second largest reduction in total unit cell volume (−13.1%). This causes the organic stacking in this structure to be significantly different to any other structure. Structure **35** has the largest reduction in unit cell volume (−17.3%) and is also the structure with the highest SPE. The lowest energy structures, **55**, **54** and **65** have relatively small unit cell contractions of −6.7%, −6.7% and −5.9%, respectively, while structure **08** has the smallest unit cell change of −5.1%.

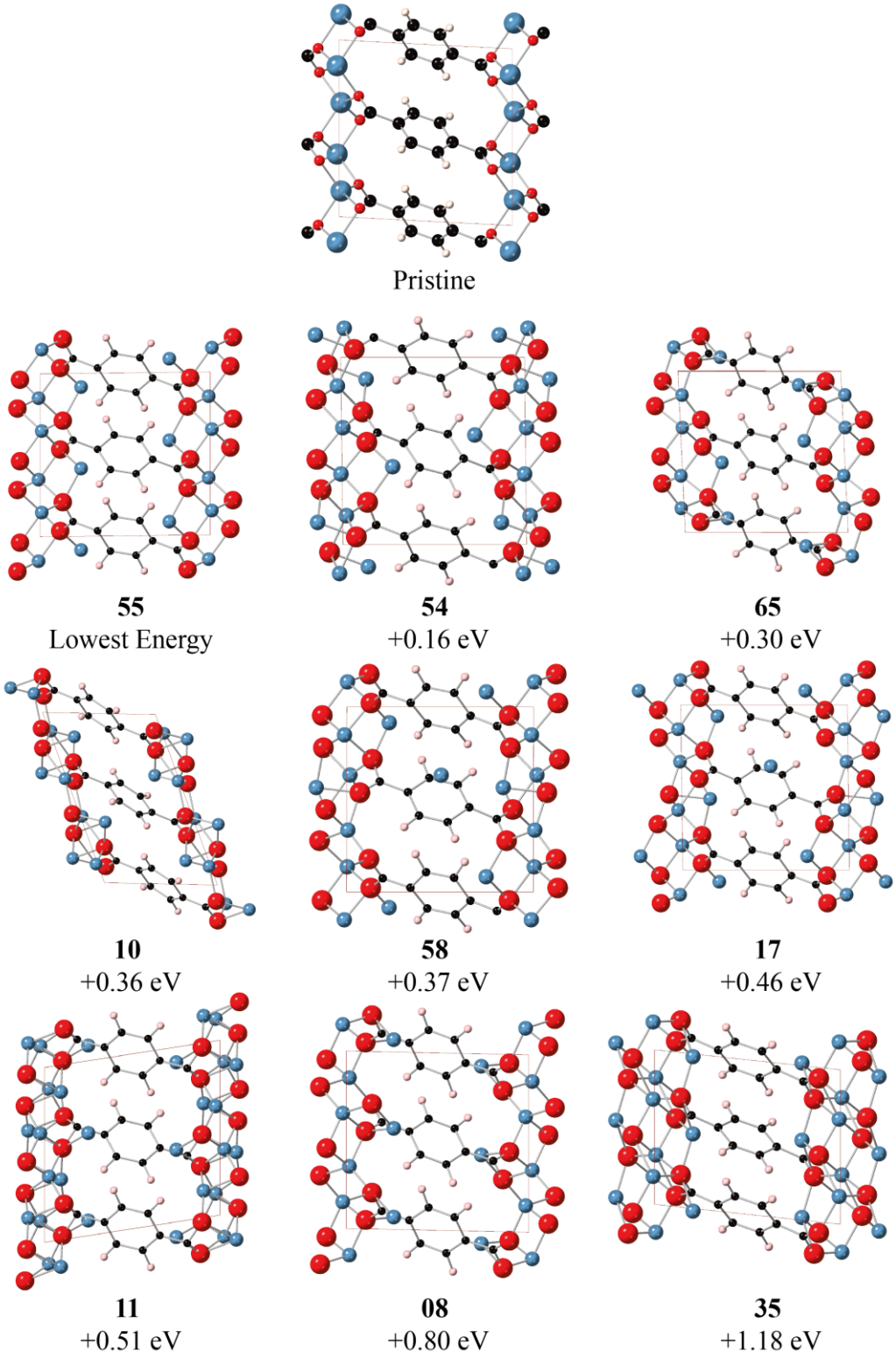

Figure 4.15 Schematics of geometry optimised pristine and Li_4BDC structures generated by AIRSS ranked according to the SPE.

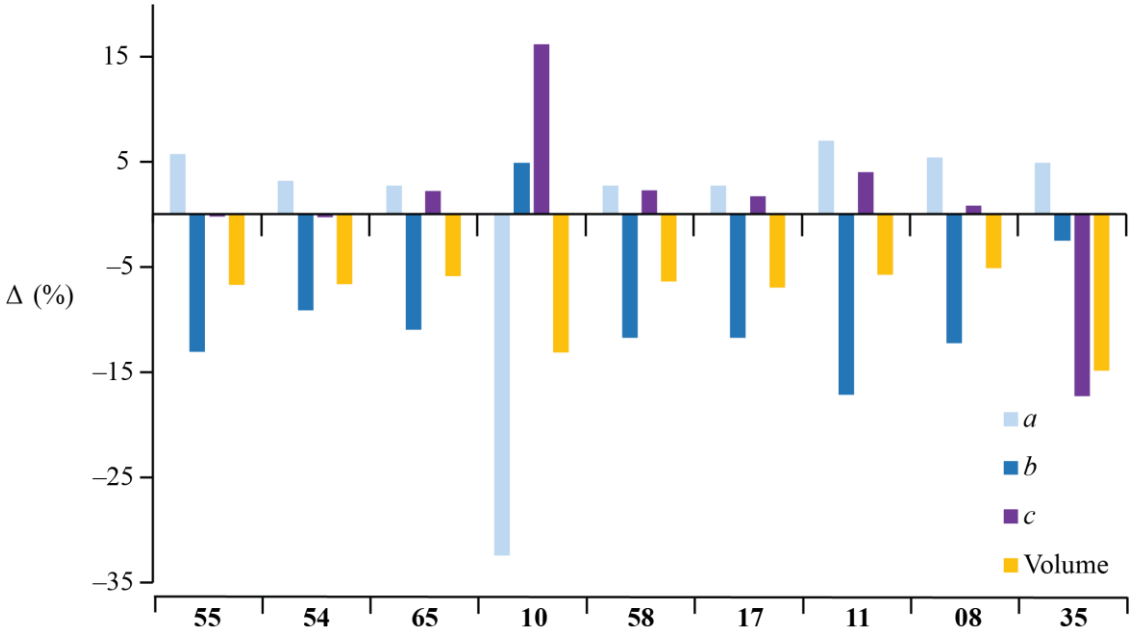

Figure 4.16 Percentage change in unit cell parameters (*a*, *b*, *c* and total unit cell volume) of each of the nine AIRSS structures as a result of the geometry optimisation procedure when compared to the unit cell parameters of the pristine Li_2BDC unit cell.

Inspection of the geometry of the additional lithium ions that are added to the structure shows that additional lithium ions tend to be located within or in close proximity to the existing lithium-oxygen layer. Figure 4.17 shows the nine geometry-optimised structures but with the bonding arrangements of the additional lithium ions highlighted for clarity. The geometry optimisation procedure has located four approximate locations in the structure where additional lithium ions can exist, which reoccur throughout the structure set. Three of these sites are located near to the lithium-oxygen layer, the first highlighted in *brown*, occupies the interstitial void space between the lithium-oxygen layer and organic layers. The second, highlighted in *green* is similar to the first, in that it is also within the interstitial site, but is located much closer (almost in plane) to the lithium-oxygen layer. The third, highlighted in *red*, is where the lithium ion is aligned with the carboxylate-aromatic carbon bond but in between the organic linker layers. The fourth and final site is the exception, highlighted in *yellow*, in that the lithium ion is located in between the aromatic systems of the organic linker rather than the lithium-oxygen layer, and is reminiscent of the intercalation of lithium in graphite. The site highlighted in *yellow* only occurs in two structures **58** and **17**, where in both cases is paired with a *green* labelled site on the same linker with this linker then sandwiched between layers of *brown* labelled sites. These two structures are the fifth and sixth lowest in energy, as such this suggests that this bonding orientation is energetically less favourable than other geometries.

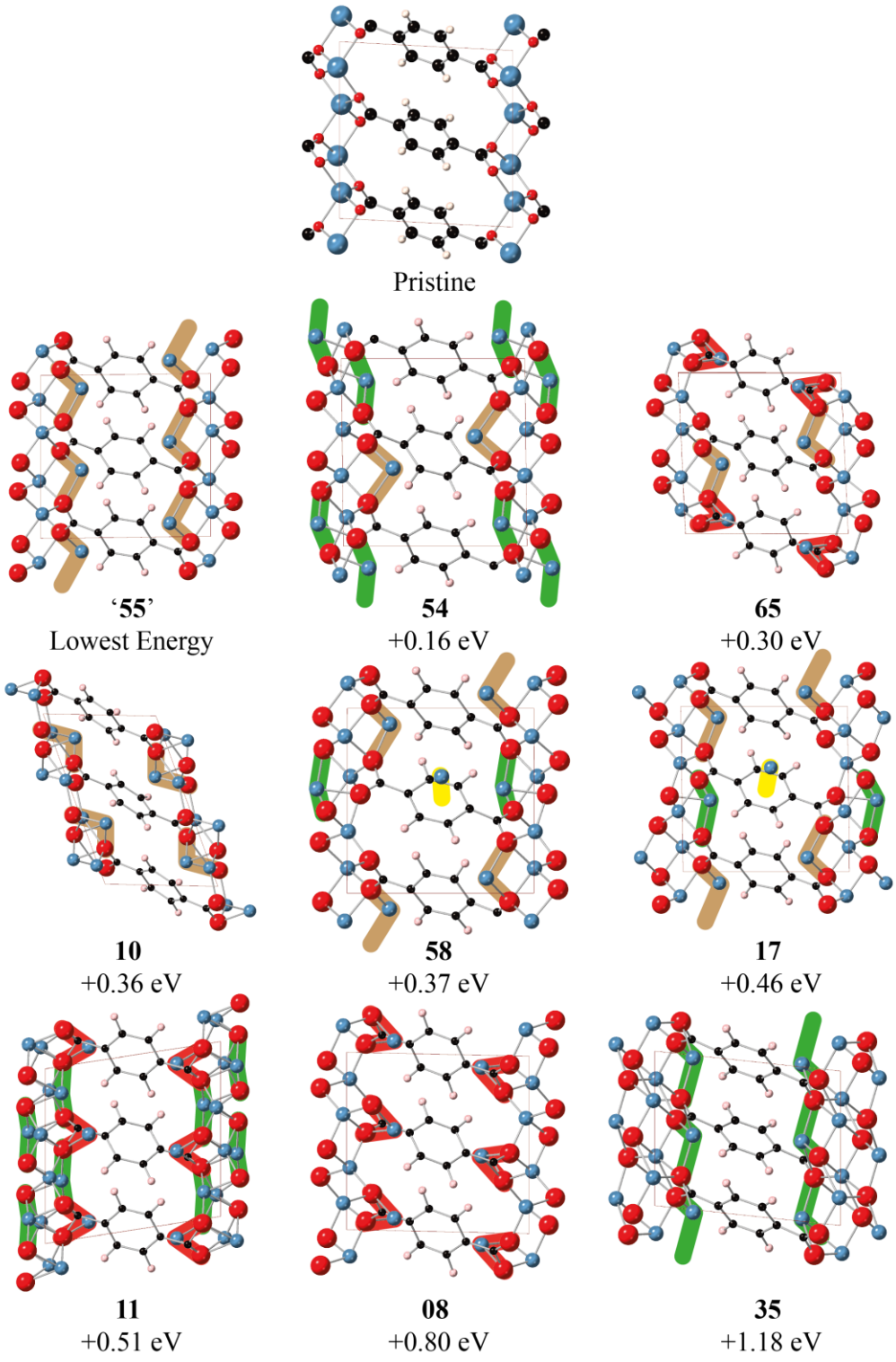

Figure 4.17 Schematics of geometry optimised pristine and Li_4BDC structures generated by AIRSS ranked according to the SPE. Bonding geometries that reoccur through the set are highlighted in different colours. Brown = interstitial site near to the aromatic ring; Green = interstitial site near to the interface of the organic and lithium-oxygen layer; Red = interstitial site, aligned with the acid-aromatic carbon carbon bond and Yellow = intercalation between ring systems.

Figure 4.18 and Figure 4.19 compare the simulated PXRD powder patterns of all the Li_4BDC AIRSS structures against the experimental powder pattern of $Li_{2+x}BDC$. Significant differences are observed which suggests the AIRSS structures remain of a different structure to that of the experimental charged phase. The differences are not consistent with a change in just unit cell parameters that would arise from temperature effects, where AIRSS structures are geometry optimised at 0 K and experimental powder pattern collected at ambient temperature. A change in unit cell parameters would result in a similar powder pattern where the reflections appear at a slightly different angle of 2θ where the entire pattern would have to be scaled along the 2θ axis in order to give good agreement. As none of the powder patterns have reasonable agreement, none of the AIRSS structures provide a reasonable starting point for Rietveld refinement.

Figure 4.20 shows the experimental ^{13}C CPMAS spectrum of $Li_{2+x}BDC$ compared against simulated ^{13}C CPMAS spectra for each of the nine AIRSS structures. Simulated spectra are simulated using SIMPSON and visualised with GSim. None of the simulated spectra give good agreement to the experimental spectrum. All nine structures have predicted resonances in the region of between 165 ppm and 155 ppm, which corresponds to the two carboxylate group resonances of the experimental spectrum. However, in four spectra, only one resonance is observed in this range, and in a further two spectra there is three resonances in this region. Thus, only three remaining structures have two resonances in this region, in agreement with the experimental spectrum. Despite this, in all structures the matching of chemical shift to experiment is poor. Of these three structures, **54** provides the closest agreement with a pair of resonances roughly centred around 60 ppm, as observed in the experimental spectrum, but are only separated by approximately 6 ppm instead of the 10 ppm separation observed in the experimental spectrum. It is also noteworthy that the two structures with three resonances are the two structures with the *yellow* intercalated bonding motif. In the region of 92 ppm to 89 ppm, two intense resonances are observed experimentally. Of the simulated spectra, four structures have only one resonance, with this resonance appearing approximately 7 ppm higher in chemical shift in the spectrum for structure **35**. Three resonances are observed in two further spectra relating to those with the *yellow* intercalated bond motif, with only three spectra remaining where two resonances are correctly predicted. These three structures are the same three structures which predicted two resonances in the carboxylate region, **54**, **65** and **11**, which interestingly does not include the lowest energy structure **55**. Four structures predict resonances near 108 ppm where in the experimental spectrum a single broadened resonance is observed. **10**, **08** and **35** predict single resonances near to 108 ppm, while **17** predicts two resonances either side of 108 ppm. Interestingly, none the three structures that have matched the multiplicity of resonances in the experimental spectrum previously have resonances in this region. Finally, for

the aromatic region between 140 ppm and 125 ppm, the experimental spectrum has one very low intensity resonance and two overlapping broadened resonances. All nine structures predict resonances near to this region, however none of the structures predict three resonances where in most cases more resonances are predicted. Furthermore, most of the resonances predicted near to this region have slightly underestimated chemical shifts and appear across the range 130 ppm to 110 ppm. With such a range in the number of predicted resonances across the structure set, it is noteworthy that the structures that predict fewer resonances (**55**, **10**, **08** and **35**) are all structures that exhibit only one bonding motif as shown in Figure 4.17. The two structures that predict many more resonances than the experimental spectrum are the two that exhibit three bonding motifs (**58** and **17**). Finally the structures that predict a similar number of resonances to the experiment are those with just two bonding motifs exhibited in the structure (**54**, **65** and **11**).

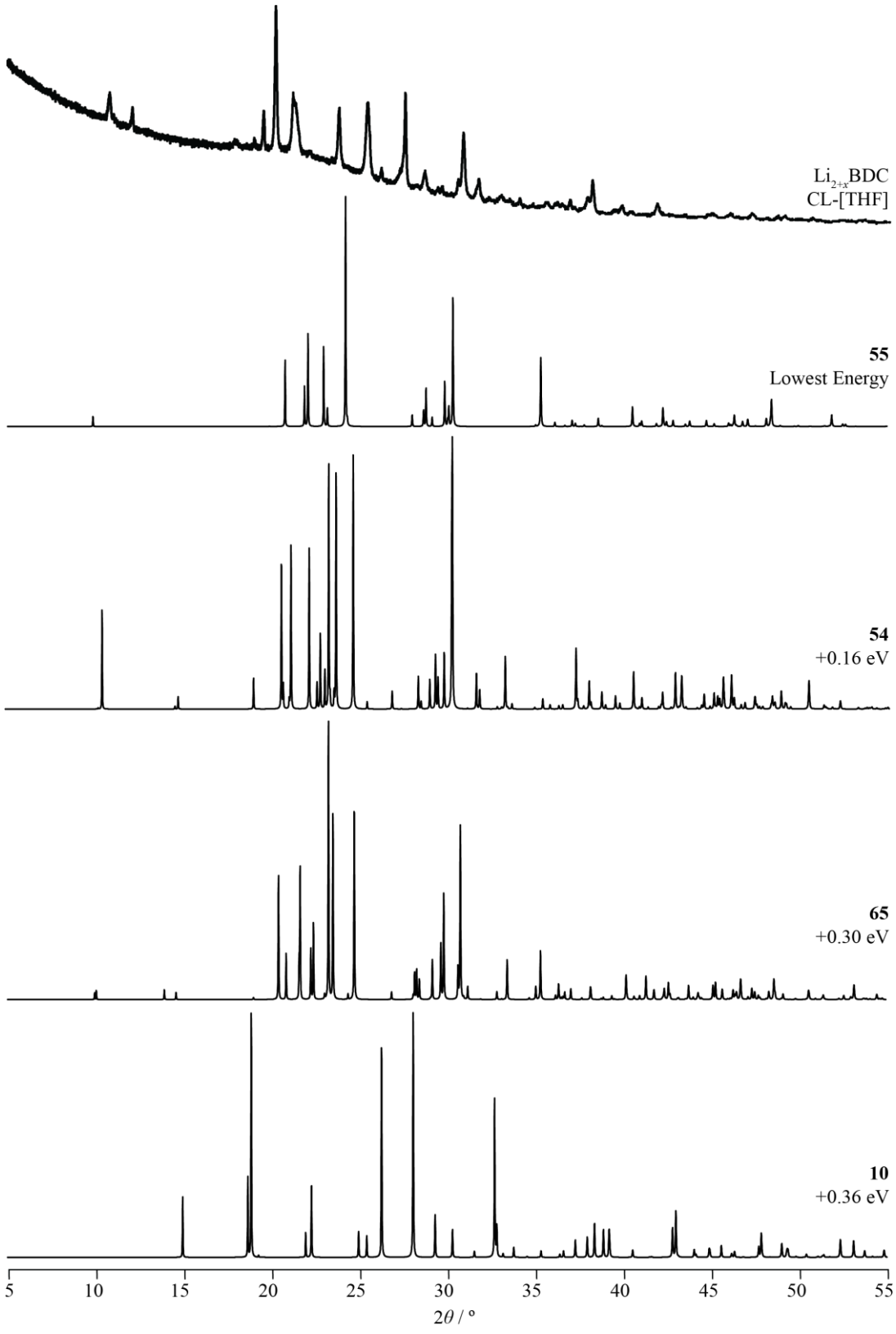

Figure 4.18 Experimental PXRD powder pattern of $Li_{2+x}BDC$ and simulated PXRD powder patterns of the AIRSS-generated structures ranked according to SPE.

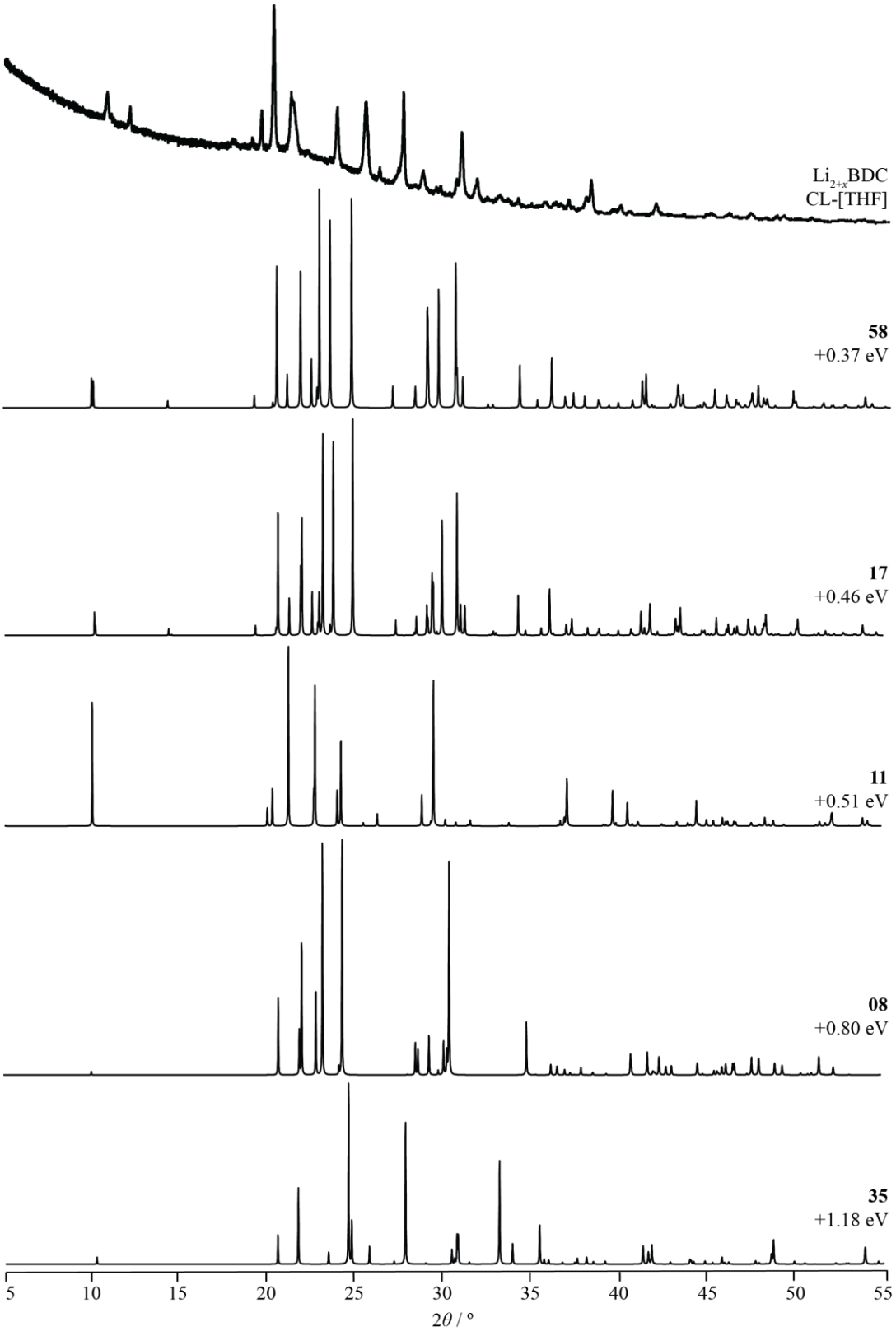

Figure 4.19 Continuation of Figure 4.18.

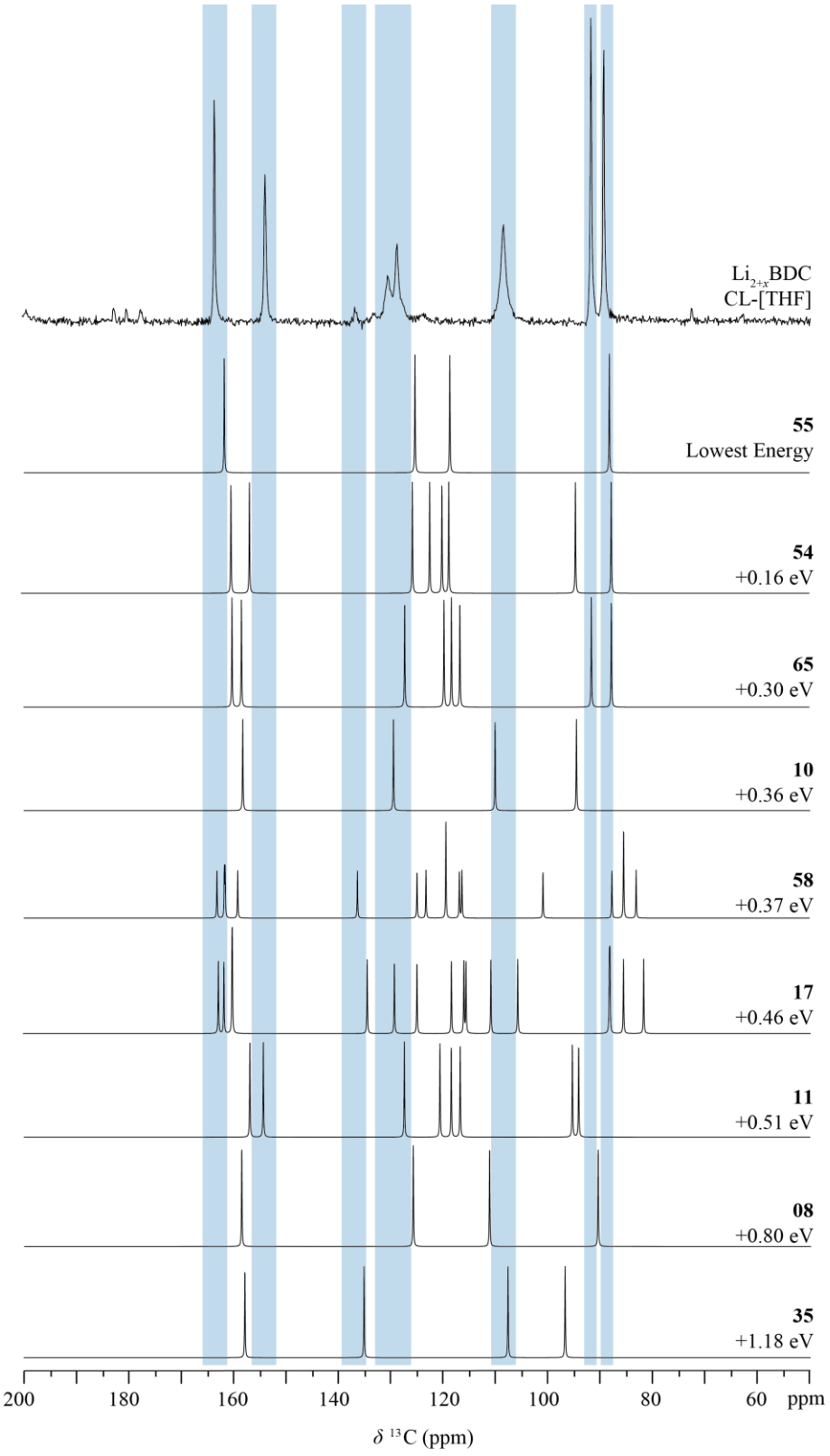

Figure 4.20 Comparison of the experimental ^{13}C CPMAS spectrum of $Li_{2+x}BDC$ with simulated CPMAS spectra of the nine AIRSS Li_4BDC structures ranked according to SPE. Blue bars are to aid visual comparison with the experimental spectrum. Spectra generated using SIMPSON and visualised in GSim.

The Li_4BDC AIRSS structures have varying numbers of crystallographic lithium sites defined by the symmetry of the structure, where the lowest energy structure, **55**, has two lithium sites, while the next lowest energy structure, **54**, has four lithium sites. In total, four structures have two lithium sites (**55**, **10**, **08** and **35**), three structures have four lithium sites (**54**, **65** and **11**) and finally two structures have eight lithium sites (**58** and **17**). The number of lithium sites can be related to the number of bonding motifs and the number of resonances in the predicted carbon spectra making three distinct subsets of structures within the nine generated structures. Figure 4.21 shows simulated ^7Li spectra for the nine AIRSS structures and are compared against the experimental quadrupolar lineshape of $Li_{2+x}BDC$. In all cases, the simulated lineshapes of the nine AIRSS structures are wider than that of the experimental lineshape, which suggests that the experimentally observed C_Q of approximately 130 kHz is overestimated across the entire structure set.

The lowest energy Li_4BDC structure, **55,** has a site of low C_Q (Li-1) and a site of high C_Q (Li-2). Full quadrupolar parameters for the lithium sites can be found in Table 4.3. The Li-1 site is in good agreement with the quadrupolar parameters observed for the pristine phase, while the Li-2 site significantly overestimates the experimental C_Q observed (130 kHz). The second lowest energy structure, **54**, has four lithium sites each with distinctly different quadrupolar character, tabulated in Table 4.4. None of these sites appear to agree with the lithium site in the pristine material, while the Li-3 site gives good agreement to the experimental C_Q of $Li_{2+x}BDC$. The Li-1 has the smallest C_Q, and thus is the closest match to the pristine material, but is still significantly smaller than the 71 kHz observed experimentally. **65** is similar in quadrupolar character to **54** and has four lithium sites with C_Q values ranging from 124 – 291 kHz and η_Q values ranging from 0.41 to 0.70. The next lowest energy structure, **10**, has two lithium sites in similarity to **55**, where both sites have high C_Q values of 208 – 233 kHz, and low η_Q values of 0.19 – 0.35. The lowest energy structure with eight lithium sites is **58**. Full quadrupolar parameters for the eight lithium sites can be found in Table 4.5. The eight sites can be roughly paired into four pairs with similar C_Q values. A pair of high C_Q sites (Li-5 and Li-8) have notably higher chemical shifts, while a pair of low C_Q sites (Li-4 and Li-6) have notably high η_Q values. The four remaining sites have moderate C_Q values between 101 – 168 kHz. A full tabulation of all predicted lithium quadrupolar parameters for all nine structures can be found in Appendix 4.1.

Table 4.3 Tabulation of quadrupolar parameters of the two crystallographic lithium sites in the Li_4BDC structure **55** generated by AIRSS.

55-Site	δ (ppm)	$\lvert C_Q \rvert$ / kHz	η_Q
Li-1	−0.07	83	0.83
Li-2	0.9	229	0.24

Table 4.4 Tabulation of quadrupolar parameters of the four crystallographic lithium sites in the Li_4BDC structure **54** generated by AIRSS.

54-Site	δ (ppm)	$\lvert C_Q \rvert$ / kHz	η_Q
Li-1	0.07	40	0.85
Li-2	−0.44	338	0.18
Li-3	0.19	142	0.56
Li-4	1.59	204	0.41

Table 4.5 Tabulation of quadrupolar parameters of the eight crystallographic lithium sites in the Li_4BDC structure **58** generated by AIRSS.

58-Site	δ (ppm)	$\lvert C_Q \rvert$ / kHz	η_Q
Li-1	−0.48	104	0.93
Li-2	−0.08	135	0.62
Li-3	−0.01	101	0.58
Li-4	−0.35	68	0.92
Li-5	1.77	257	0.48
Li-6	−0.31	84	0.79
Li-7	0.56	168	0.26
Li-8	1.17	368	0.09

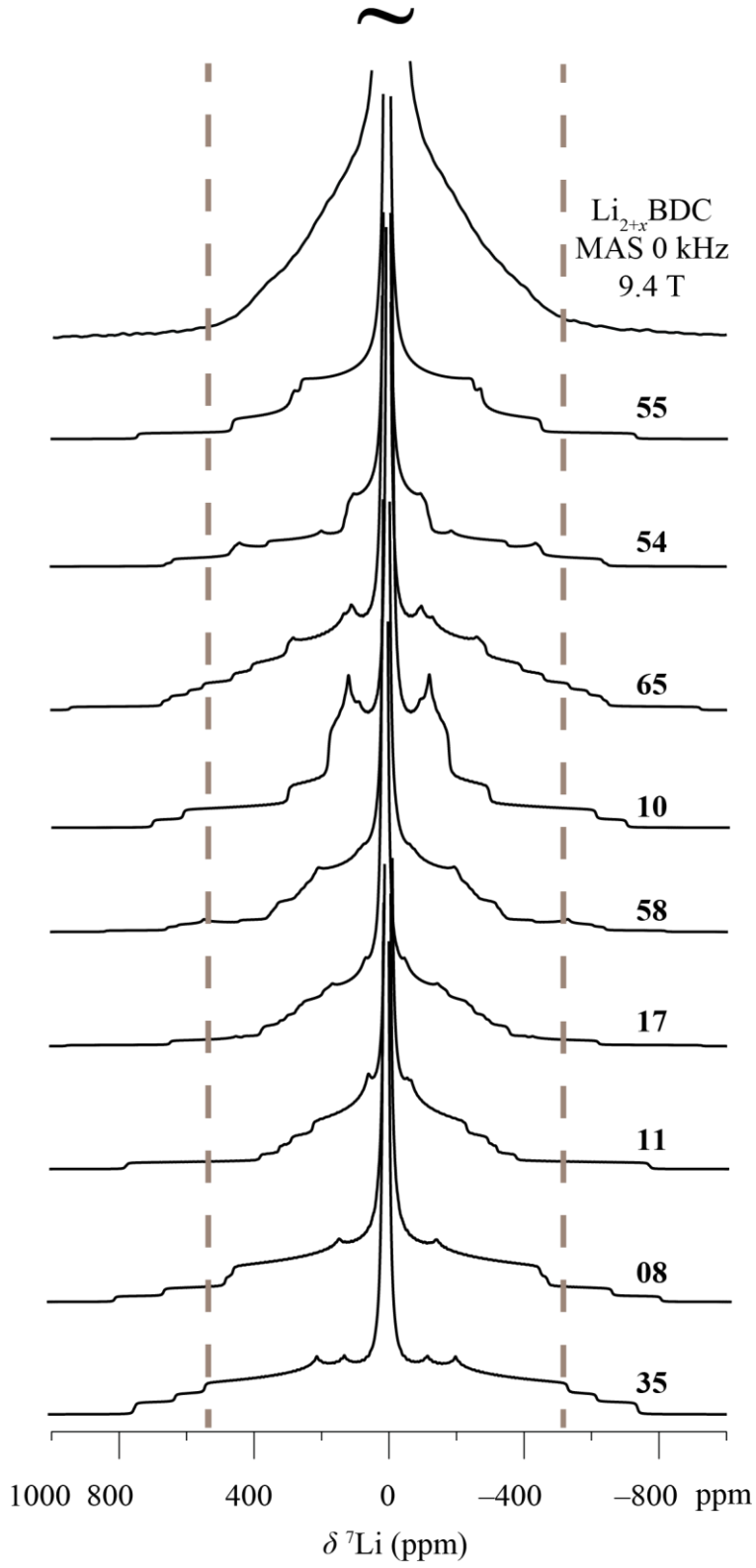

Figure 4.21 Experimental ^{7}Li quadrupolar lineshapes of $Li_{2+x}BDC$ and simulated ^{7}Li quadrupolar lineshapes of the nine AIRSS structures (shown descending with increasing SPE). Grey dashed lines are to aid visualisation and comparison of the relative C_Q of the lineshapes. Simulated sapectra generated using SIMPSON and visualised in GSim.

4.7.2 Computationally Generated $Li_{2+x}NDC$ Structures

Four Li_4NDC structures were generated computationally using an alternative approach and are labelled **A**-**D**. For Li_2BDC, AIRSS revealed that additional lithium ions are likely to locate closer to the interface of the organic and lithium-oxygen layers. As such, two lithium ions were manually added into this region of the pristine phase structure using the CrystalMaker program, yielding structures with stoichiometry Li_4NDC. The four structures then underwent an electronic energy minimisation calculation to yield SPE values and a geometry optimised structure. It is notable one of the structures, **B**, failed to converge to an energetic minimum within 200 self-consistent field (SCF) cycles, and as such the structure is deemed to have a geometry that is particularly energetically unfavourable and is henceforth ignored.

Of the three remaining structures, an energetic minimum was observed with structure **A**, with relatively large increases for **D** and **C**. Full tabulation of calculated SPE's given in Table 4.6. A visual inspection of the structures showed that the best guess structure, **A**, optimised to a geometry that is very similar to one of the higher energy structures, **D**. Despite the very similar geometries, **D** has a significantly higher SPE (+0.23 eV) respective to **A**. The remaining structure, **C**, has a distinctly different geometry and is the highest energy structure.

Table 4.6 Ranked tabulation of the single-point energies of the four Li_4NDC structures generated computationally.

Structure	SPE (eV)	SPE *vs.* 'A' (eV)
A	−9122.61	0
D	−9122.38	+ 0.23
C	−9121.70	+ 0.91
B	N/A	N/A

Simulated PXRD powder patterns of Li_4NDC show significant differences to that of the experimentally reduced phase, $Li_{2+x}NDC$, and as such the computationally generated structures are of significantly different structure to the experimental phase. Key distinctions include the strong reflections at 17° and 22° that do not appear in the simulated patterns, while all simulated patterns feature a strong reflection at approximately 32° which is absent in the experimental pattern. Furthermore, despite a strong resemblance, key distinctions can be drawn between the simulated patterns of **A** and **D**, in particular additional reflections present in the pattern of **A** at approximately 27° and 28° while some other reflections appear to have shifted relative to each other at approximately 25° and 35°. These small differences confirm the structures of **A** and **D**, while similar, are indeed distinct.

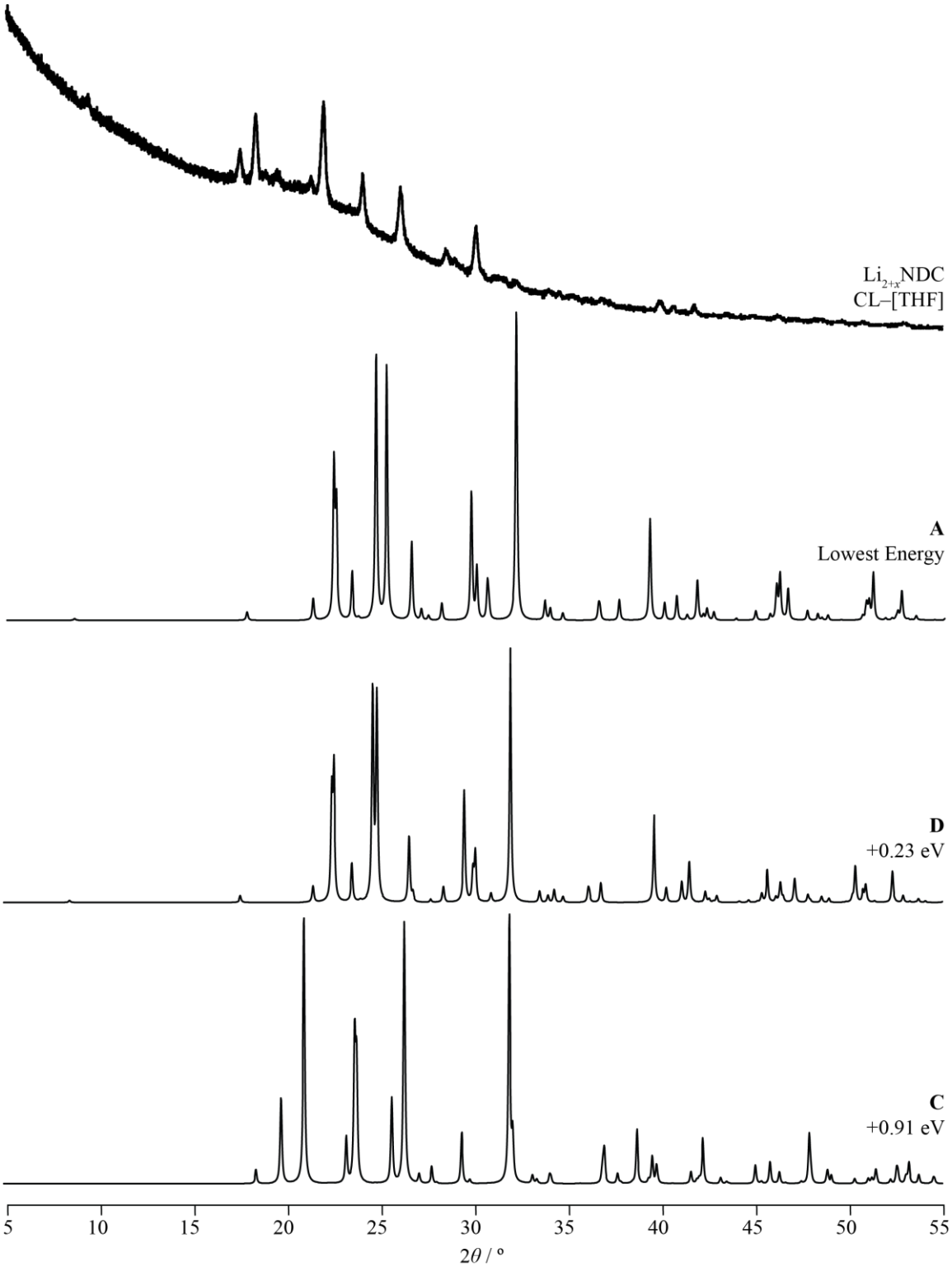

Figure 4.22 Experimental PXRD powder pattern of $Li_{2+x}NDC$ and simulated PXRD powder patterns of the three computationally generated Li_4NDC structures that were successfully geometry optimised. Ranked according to SPE.

Figure 4.23 shows a comparison of simulated ^{13}C CPMAS NMR spectra of Li_4NDC against the experimental spectrum of $Li_{2+x}NDC$. None of the three simulated spectra perfectly match with the experimental spectrum. The spectra for **A** and **D** show a similarity to the experimental spectrum, with resonances appearing approximately 5 ppm higher, except for the resonance at approximately 95 ppm which appears approximately 2 ppm lower. The six predicted carbon resonances is slightly less than the eight resonances predicted in the experimental spectrum. Notably, the carboxylate resonances at 179 ppm is absent in the simulated spectra, confirming that this resonance should not be present in a pure sample of $Li_{2+x}NDC$. Furthermore, only two resonances are predicted in the organic region around 140 – 135 ppm, which in the experimental spectrum there are two strong resonances with another low intensity resonance in between. This is further evidence that the sample of the experimental spectrum had residual pristine phase present.

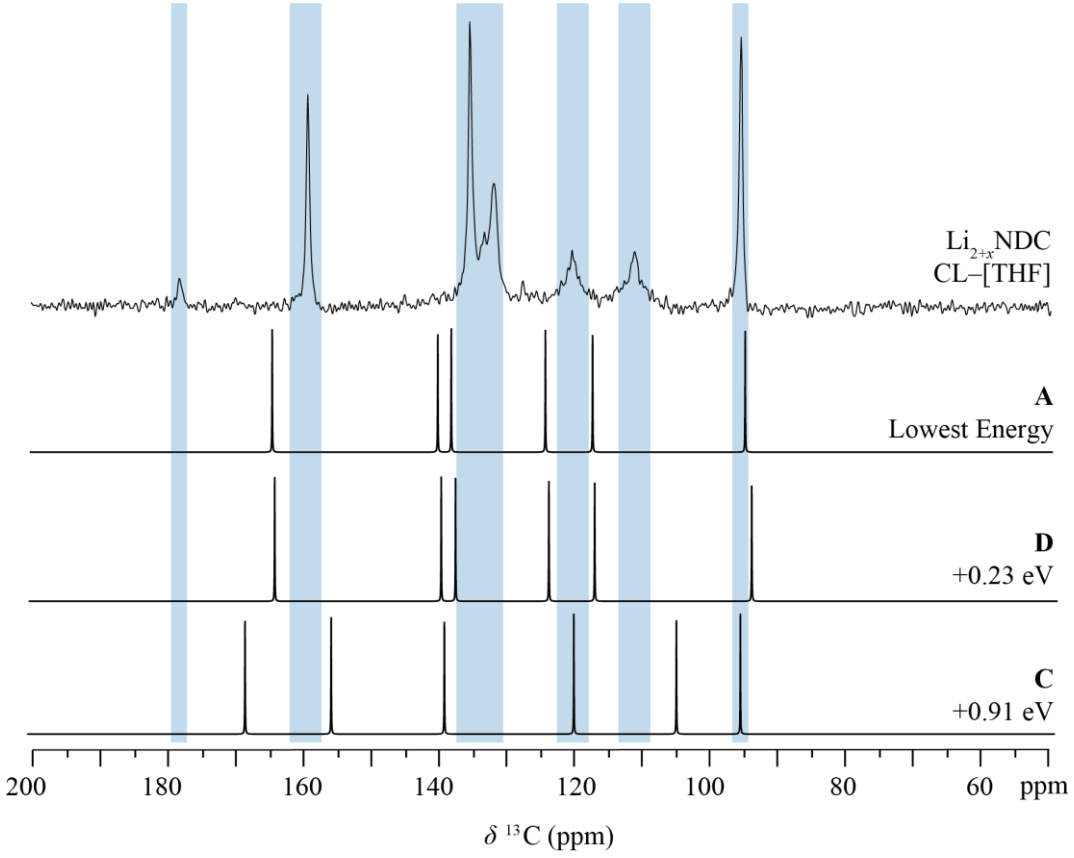

Figure 4.23 Experimental ^{13}C CPMAS spectrum of $Li_{2+x}NDC$ and simulated ^{13}C CPMAS spectra of the three computationally generated Li_4NDC structures that were successfully geometry optimised. Ranked according to SPE. Blue bars are to aid visibility for comparison with experimental spectrum. Simulated spectra generated using SIMPSON and visualised in GSim.

In each of the computationally generated structures of Li_4NDC there are two crystallographic lithium sites. Calculated quadrupolar parameters are tabulated in Table 4.7, while simulated lineshapes are shown in Figure 4.24. The two lowest energy structure, **A** and **D**, have a low C_Q site A-1 and D-1, respectively, and a high C_Q site A-2 and D-2, respectively. The

high and low C_Q sites in **A** and **D** are in good agreement with each other. The highest energy structure, **C**, has two sites both with moderate C_Q values that do not agree with either of **A** or **D**. Experimental ^{7}Li MAS NMR does not show multiple sites due to second-order quadrupolar broadening, however the chemical shift range is sufficiently small that a second site would likely exist within the broadened peaks and be invisible. In this instance, a fit to the experimental static lineshape would not be expected to give accurate quadrupolar parameters for a given lithium site, but can provide insight into the trend of C_Q experimentally. The fit gives C_Q = 160 kHz and η_Q = 0.38, interestingly, this is most similar to the C-2 site, although the chemical shift is significantly underestimated compared to the experimental shift of 0 ppm.

Table 4.7 Tabulation of quadrupolar parameters of the two crystallographic lithium sites in the three Li_4NDC structures generated computationally.

Site	δ (ppm)	$\lvert C_Q \rvert$ / kHz	η_Q
A-1	–0.69	79	0.48
A-2	0.07	259	0.17
C-1	–1.89	133	0.80
C-2	–2.70	175	0.30
D-1	–0.55	82	0.30
D-2	0.19	266	0.32

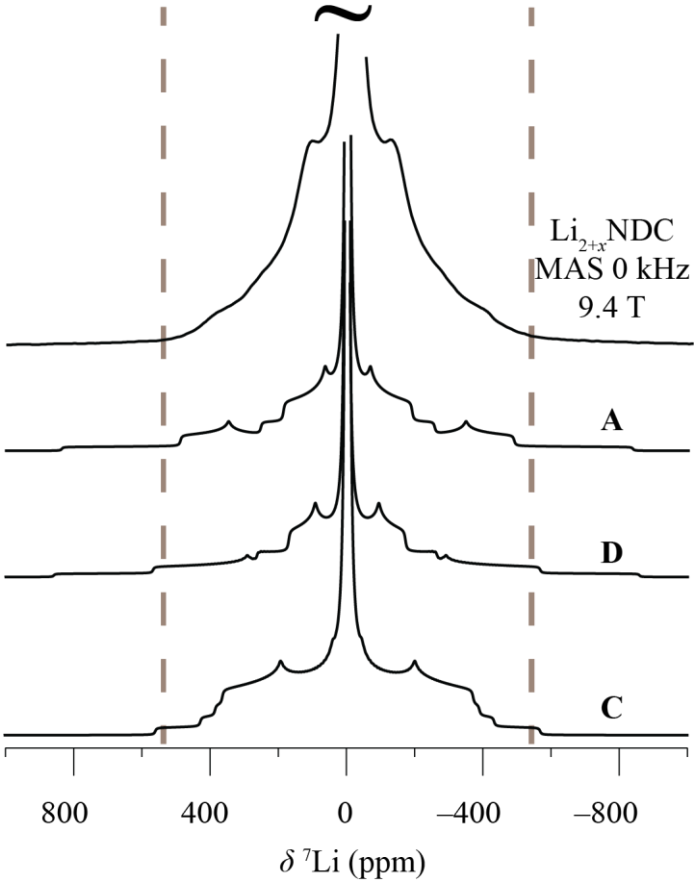

Figure 4.24 Experimental ^{7}Li spectrum of $Li_{2+x}NDC$ and simulated ^{7}Li spectra of the three computationally generated Li_4NDC structures that were successfully geometry optimised. Grey dashed lines are to aid visualisation and comparison of the relative C_Q of the lineshapes. Simulated spectra generated using SIMPSON and visualised in GSim.

4.8 Conclusions

In this chapter the structure of the reduced phase of Li_2BDC and Li_2NDC has been investigated using an adapted chemical lithiation method. The CL method has been demonstrated to yield reduced phases, Li_{2+x}BDC and Li_{2+x}NDC, in sufficient yields for further analysis. Optimisation of the CL method showed that the method produces greater yields of reduced phases when the solvent used was weakly coordinating such as THF. PXRD analysis of these phases shows that the structures are significantly different to those of the pristine materials and are in broad agreement with previous literature. ^{13}C CPMAS NMR spectroscopy showed that, independent of solvent choice, the reduced phase could be observed, albeit in much greater yield in THF. Five new ^{13}C resonances appear in the spectrum, with potential for an additional resonance to be obscured, signifying a distinct change in symmetry and structure in the reduced phases. Furthermore, ^{13}C CPMAS NMR shows that the products of CL can be expected to be of similar structure to electrochemically reduced phases gained *via* electrochemical cycling. ^{7}Li NMR spectroscopy shows that in both materials, the quadrupolar character is significantly different, and in particular large increases in the quadrupolar coupling constant are consistent with lithium ions occupying interstitial sites within the structure, with a significantly anisotropic electric field gradient. EPR spectroscopy shows isotropic resonances for CL products arising from unpaired electrons within the structures, and therefore it is possible that the structures contain regions with different degrees of lithiation. Structural prediction methods were used to gain candidate structures for the reduced phase, including *ab-initio* random structure searching (AIRSS). A suite of candidate structures were found, and subsequently used in the prediction of NMR observables. Comparison of experimental and simulated ^{13}C CPMAS NMR of the nine Li_{2+x}BDC structures shows that while a broad agreement in symmetry and chemical shifts can be seen in some of the structures, no perfect match is found and thus are not in agreement with the true structure gained from CL. A wide range of ^{7}Li quadrupolar parameters are predicted across the AIRSS structure set with some lithium sites that are in agreement with the experimental data, though the experimental data is expected to be a combination of multiple sites that cannot easily be separated. For Li_{2+x}NDC, four structures were found. Two of the structures have visibly similar geometries despite significantly different single point energies. Similarly to Li_{2+x}BDC however, a broad agreement of experimental and simulated ^{13}C CPMAS NMR spectra is observed with good agreement in symmetry and reasonable agreement in chemical shifts, though no exact match is observed. While these results point to a similarity between the simulated and true structures, the simulated structures still do not quite capture the true geometry of the reduced phase.

4.9 References

1. M. Armand, S. Grugeon, H. Vezin, S. Laruelle, P. Ribiere, P. Poizot and J. M. Tarascon, Nat Mater, 2009, 8, 120-125.
2. C. P. Grey and J. M. Tarascon, Nat Mater, 2016, 16, 45-56.
3. K. Bechgaard and V. D. Parker, J. Am. Chem. Soc., 1972, 94, 4749-4750.
4. W. Walker, S. Grugeon, H. Vezin, S. Laruelle, M. Armand, J. M. Tarascon and F. Wudl, Electrochemistry Communications, 2010, 12, 1348-1351.
5. L. Zhao, J. Zhao, Y.-S. Hu, H. Li, Z. Zhou, M. Armand and L. Chen, Advanced Energy Materials, 2012, 2, 962-965.
6. A. Abouimrane, W. Weng, H. Eltayeb, Y. Cui, J. Niklas, O. Poluektov and K. Amine, Energy & Environmental Science, 2012, 5.
7. K. Lei, F. Li, C. Mu, J. Wang, Q. Zhao, C. Chen and J. Chen, Energy & Environmental Science, 2017, 10, 552-557.
8. L. Wang, C. Mou, B. Wu, J. Xue and J. Li, Electrochimica Acta, 2016, 196, 118-124.
9. Y. Park, D. S. Shin, S. H. Woo, N. S. Choi, K. H. Shin, S. M. Oh, K. T. Lee and S. Y. Hong, Adv Mater, 2012, 24, 3562-3567.
10. A. Tripathi, Y. Chen, H. Padhy, S. Manzhos and P. Balaya, Energy Technology, 2019, 7.
11. S. Lee, J. E. Kwon, J. Hong, S. Y. Park and K. Kang, Journal of Materials Chemistry A, 2019, 7, 11438-11443.
12. C. Luo, J. J. Shea and J. Huang, Journal of Power Sources, 2020, 453.
13. R. Mikita, N. Ogihara, N. Takahashi, S. Kosaka and N. Isomura, Chemistry of Materials, 2020, 32, 3396-3404.
14. Y. Wang, Y. Deng, Q. Qu, X. Zheng, J. Zhang, G. Liu, V. S. Battaglia and H. Zheng, ACS Energy Letters, 2017, 2, 2140-2148.
15. X. Han, C. Chang, L. Yuan, T. Sun and J. Sun, Advanced Materials, 2007, 19, 1616-1621.

16. X. Han, G. Qing, J. Sun and T. Sun, Angew Chem Int Ed Engl, 2012, 51, 5147-5151.
17. L. Fédèle, F. Sauvage and M. Bécuwe, J. Mater. Chem. A, 2014, 2, 18225-18228.
18. L. Fédèle, F. Sauvage, S. Gottis, C. Davoisne, E. Salager, J.-N. Chotard and M. Becuwe, Chemistry of Materials, 2017, 29, 546-554.
19. A. Choi, Y. K. Kim, T. K. Kim, M.-S. Kwon, K. T. Lee and H. R. Moon, J. Mater. Chem. A, 2014, 2, 14986-14993.
20. J. Choi, H. Jeong, J. Jang, A. R. Jeon, I. Kang, M. Kwon, J. Hong and M. Lee, J Am Chem Soc, 2021, 143, 9169-9176.
21. F. Holtstiege, P. Bärmann, R. Nölle, M. Winter and T. Placke, Batteries, 2018, 4.
22. A. E. Bennett, C. M. Rienstra and M. Auger, J. Chem. Phys., 1995, 103, 6951.
23. A. Bielecki and D. P. Burum, J Magn Reson, 1995, 116, 215-220.
24. M. D. Segall, P. J. D. Lindan, M. J. Probert, C. J. Pickard, P. J. Hasnip, S. J. Clark and M. C. Payne, J Phys Condens Matter, 2002, 14, 2717-2744.
25. C. J. Pickard and F. Mauri, Physical Review B, 2001, 63.
26. J. P. Perdew, K. Burke and M. Ernzerhof, Phys Rev Lett, 1996, 77, 3865-3868.
27. B. Hammer, L. B. Hansen and J. K. Nørskov, Physical Review B, 1999, 59, 7413-7421.
28. J. R. Yates, C. J. Pickard and F. Mauri, Physical Review B, 2007, 76.
29. S. Grimme, J Comput Chem, 2006, 27, 1787-1799.
30. S. Grimme, J. Antony, S. Ehrlich and H. Krieg, J Chem Phys, 2010, 132, 154104.
31. P. Pyykkö, Molecular Physics, 2008, 106, 1965-1974.
32. G. W. Canters and E. De Boer, Molecular Physics, 1972, 26, 1185-1198.

Appendix 4.1 – AIRSS-Predicted Li_4BDC ^7Li NMR Quadrupolar Parameters

Table 4.A8 Tabulation of quadrupolar parameters of the two crystallographic lithium sites in the Li_4BDC structure **55** generated by AIRSS.

55-Site	δ (ppm)	$\lvert C_Q \rvert$ / kHz	η_Q
Li-1	−0.07	83	0.83
Li-2	0.9	229	0.24

Table 4.A9 Tabulation of quadrupolar parameters of the four crystallographic lithium sites in the Li_4BDC structure **54** generated by AIRSS.

54-Site	δ (ppm)	$\lvert C_Q \rvert$ / kHz	η_Q
Li-1	0.07	40	0.85
Li-2	−0.44	338	0.18
Li-3	0.19	142	0.56
Li-4	1.59	204	0.41

Table 4.A10 Tabulation of quadrupolar parameters of the four crystallographic lithium sites in the Li_4BDC structure **65** generated by AIRSS.

65-Site	δ (ppm)	$\lvert C_Q \rvert$ / kHz	η_Q
Li-1	−0.47	124	0.48
Li-2	−0.01	199	0.70
Li-3	1.94	291	0.41
Li-4	−3.42	185	0.56

Table 4.A11 Tabulation of quadrupolar parameters of the two crystallographic lithium sites in the Li_4BDC structure **10** generated by AIRSS.

10-Site	δ (ppm)	$\lvert C_Q \rvert$ / kHz	η_Q
Li-1	0.49	209	0.35
Li-2	−0.10	233	0.19

Table 4.A12 Tabulation of quadrupolar parameters of the eight crystallographic lithium sites in the Li_4BDC structure **58** generated by AIRSS.

58-Site	δ (ppm)	$\lvert C_Q \rvert$ / kHz	η_Q
Li-1	−0.48	104	0.93
Li-2	−0.08	135	0.62
Li-3	−0.01	101	0.58
Li-4	−0.35	68	0.92
Li-5	1.77	257	0.48
Li-6	−0.31	84	0.79
Li-7	0.56	168	0.26
Li-8	1.17	368	0.09

Table 4.A13 Tabulation of quadrupolar parameters of the eight crystallographic lithium sites in the Li_4BDC structure **17** generated by AIRSS.

17-Site	δ (ppm)	$\lvert C_Q \rvert$ / kHz	η_Q
Li-1	0.14	115	0.69
Li-2	−0.46	113	0.64
Li-3	−0.10	76	0.52
Li-4	−0.08	115	1.00
Li-5	1.71	293	0.35
Li-6	0.23	131	0.26
Li-7	1.31	335	0.18
Li-8	−0.49	91	0.77

Table 4.A14 Tabulation of quadrupolar parameters of the four crystallographic lithium sites in the Li_4BDC structure **11** generated by AIRSS.

11-Site	δ (ppm)	$\lvert C_Q \rvert$ / kHz	η_Q
Li-1	−0.03	159	0.83
Li-2	1.38	211	0.50
Li-3	−0.54	197	0.24
Li-4	−0.60	110	0.33

Table 4.A15 Tabulation of quadrupolar parameters of the two crystallographic lithium sites in the Li_4BDC structure **08** generated by AIRSS.

08-Site	δ (ppm)	$\lvert C_Q \rvert$ / kHz	η_Q
Li-1	−0.56	147	0.90
Li-2	−2.68	250	0.65

Table 4.A16 Tabulation of quadrupolar parameters of the two crystallographic lithium sites in the Li_4BDC structure **35** generated by AIRSS.

35-Site	δ **(ppm)**	$\lvert C_Q \rvert$ **/ kHz**	η_Q
Li-1	0.12	231	0.67
Li-2	−0.77	230	0.45

Chapter 5

A Structural Investigation of Phenazine Chloranilic Acid – an Organic Ferroelectric Material

5.1 Introduction

Issues surrounding sustainability have come to the forefront in the design of many technologies and are not exclusive to the battery industry. While the prevalence of the battery is well understood, the ever-increasing digital transformation of society brings about a ubiquity in all aspects of electronics, including but not limited to optical displays and data storage. These other electrical components, like battery materials, often contain rare, expensive, toxic or environmentally harmful components. A concerted shift towards all-organic electronics featuring only abundant, cheap and versatile molecules would increase sustainability throughout electronics. A key example here is the current ferroelectric materials used in ferroelectric random-access memory (RAM) (FeRAM). Most ferroelectric materials used in electronics are perovskite transition metal oxides *e.g.*, barium titanate ($BaTiO_3$, BTO) and lead zirconate titanate ($PbZr_{1-x}Ti_xO_3$, PZT). In this class of materials, transition metals are present in high stoichiometric quantities, with which their extraction is associated with high energetic, economic and environmental costs. An alternative solution that has recently been the subject of significant interest towards the application of organic data storage is organic ferroelectric materials. While ferroelectricity is not a recently discovered phenomenon, first observed in Rochelle salt in 1920, organic ferroelectric materials are not widespread.[6] A vinylidene fluoride copolymer was an early commercial use of ferroelectricity as a transducer in loudspeakers.[7] However, low molecular mass alternatives are exceptionally few.[8]

Materials can become polarised through mechanical stress, exposure to an electric field or changes in temperature. This polarisation leads to properties such ferroelectricity and paraelectricity. Ferroelectricity is the property of a material to undergo spontaneous electric polarisation, reaching a stable polarised state that can be reversed by inversion of an external

electric field, called a coercive field. Comparatively, a paraelectric material cannot retain polarisation outside of an applied electric field. The ability of such materials to be stable in multiple electric states is the source of the potential for application in FeRAM. Ferroelectric materials have a unique Curie temperature (T_C) at which the transition between paraelectric and ferroelectric phases occur usually resulting in some level of structural change. The structural changes that occur in ferroelectric materials differ by structure. For example, in $NaNO_2$, the dipolar nature of the structure generates spontaneous polarisation, with reorientation of the polar molecules generating the ferroelectricity. An alternative mechanism, observed in BTO, sees a relative displacement of ions creating a spontaneous polarisation.[9] PZT also exhibits this displacive mechanism and is one of the most commonly used ferroelectric materials.[10] The PZT structure consists of a cubic cell with a central titanium or zirconium atom, an oxygen octahedron at the centre of the faces, with lead atoms at each vertex. PZT has a T_C of approximately 623.15 K, where above this the unit cell is cubic, and below the unit cell elongates in one dimension resulting in a cuboidal unit cell and a further displacement of the central metal atom. One final example of structural change in ferroelectric materials is the dynamic rearrangement of hydrogen-bonded protons, as in KH_2PO_4.[11] Here, a proton hydrogen-bonded between two molecules switches position and triggers the electric polarisation. It should be noted that these mechanisms may not exist in exclusivity nor be an exhaustive list. Organic ferroelectric materials present a more sustainable alternative to transition metal-based ferroelectrics, though they are currently less widespread. While the first reported example of ferroelectricity in an organic molecule was glycine salts in the 1950s, ferroelectricity was observed in thiourea (CH_4N_2S) shortly thereafter. With significant research interest in the following decades, multicomponent charge-transfer (CT) complexes have emerged as the most promising with near room temperature ferroelectricity observed. New organic ferroelectric materials with improved ferroelectric properties have been successfully designed with the displacive and proton-transfer mechanisms. These CT structures utilise either a proton- or electron-transfer from a donor (D) to an acceptor (A) molecule. An early example includes tetrathiafulvalene complexes with a *p*-haloanil.[12, 13] Notably these structures are non-polar and planar with the planarity lost at lower temperatures along with a reduction in symmetry.[14]

In 2005, Horiuchi *et al*., demonstrated the ferroelectricity of phenazine chloranilic acid (P-CA) alongside the brominated analogue phenazine bromanilic acid (P-BA).[15] P-CA and P-BA are non-polar conjugated charge transfer co-crystals featuring planar units, in which charge transfer is achieved through displacement of a proton. P-CA has the added advantage of being lightweight due to the molecular mass difference of chlorine and bromine. P-CA and P-BA are made *via* a simple co-crystallisation synthetic route which provides a much more

energy efficient route to ferroelectric materials than the high temperatures required for ceramic ferroelectrics such as PZT. Furthermore, the use of abundant atoms with organic tuneability and lack of rare or toxic metals (*e.g.*, lead) provides another benefit. Structurally these cocrystals have the space group $P2_1/n$ at room temperature and feature π-stacks of both phenazine and the haloanilic acid (HA). This is shown in Figure 5.1, which shows the crystal structure for P-CA collected at 298 K, a full discussion of the reported crystal structures for P-CA is given below. In the structure, both the D (HA) and A (phenazine) units are located on inversion centres, with two identical units of each in the unit cell. Infrared spectroscopy (IR) data indicates a strong hydrogen bond is present and is of the form O−H···N with no evidence of proton displacement observed.[15] The O···N bond length is 2.724 Å, O−H = 0.727 Å and H···N = 2.184 Å. However, the most significant property of these materials is that they display near room temperature ferroelectric behaviour, where the temperature can be increased further with increases in hydrostatic pressure or deuteration. The mechanism of how this room temperature ferroelectricity is achieved has been the subject of significant interest, and though many have studied the structural changes with diffraction, a local probe such as NMR spectroscopy could provide further insight into the microscopic origin of the ferroelectricity.

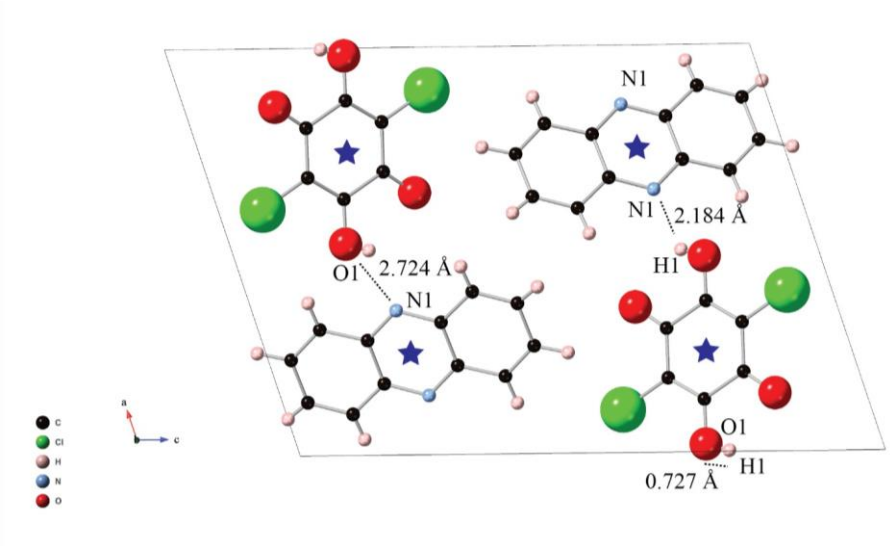

Figure 5.1 Unit cell of P-CA (CCDC deposition code: MAMPUM01). Blue stars indicate localised inversion centres within each molecule. Select bond lengths and atom labels shown. T = 298 K.

At room temperature under ambient pressure, both P-CA and P-BA are in the paraelectric phase (PE-I). Horiuchi *et al.*, found the T_C of P-CA and P-BA to be 253 K and 138 K, respectively.[1, 15] The much lower T_C and heavier molecular mass makes P-BA more difficult to study where such low temperatures are prohibitive, and less attractive for applications where lightweight components are usually preferred – as such, only P-CA is examined in this chapter. As mentioned previously, the T_C can be increased with deuteration. In P-CA, deuteration yielding deuterated P-CA (d-P-CA) elevates T_C by up to 51 K

(thus, T_C = 304 K), dependent on the degree of deuteration. The significant isotope dependence indicates the importance of the hydrogen bond for the phase transition and is due to the elongation of the O−H bond and shortening of the H···N hydrogen bond. Below T_C, P-CA becomes ferroelectric and is in the FE-I phase. Further lower temperature transitions were observed in 2006 by Saito *et al*. using heat capacity measurements, and shortly after by Gotoh *et al*. using nuclear quadrupole resonance (NQR).[2, 16] These lower temperature transitions were observed at 146 K (to FE-IC) and 136 K (to FE-II), respectively. A list of the known phases can be found in Table 5.1, with a full review of each phase below.

Table 5.1 A list of all known phases of P-CA and d-P-CA with the associated temperature range.

Phase	P-CA Temperature Range (K)	d-P-CA Temperature Range (K)
PE-I	> 253	> 304
FE-I	252 – 148	303 – 199
FE-IC	147 – 137	198 – 188
FE-II	< 136	< 187

Three crystal structures of the paraelectric phase (PE-I) have been determined, two by Horiuchi *et al*.,[1] and another later by Kumai *et al*.[3] The first (CCDC deposition code: MAMPUM) is a deuterated structure collected at 305 K by synchrotron XRD, where the protons of the chloranilic acid (CA) units are replaced by deuterium atoms.[1] The second, MAMPUM01, is a protonated analogue collected at 298 K also by synchrotron XRD.[1] The third PE-I phase structure, MAMPUM04, was collected at 300 K, using neutron diffraction (ND).[3] In the deuterated MAMPUM structure, the O···N distance is 2.732 Å, slightly longer than the O···N distance of 2.72 Å in the MAMPUM01 structure.

Below the first phase transition temperature, $T_{C,I}$ (253 K), and above $T_{C,IC}$ (147 K), P-CA exists in the FE-I phase. Two crystal structures have been deposited, both in 2007 from different groups but in good agreement with each other. The first, MAMPUM02, was collected at 170 K, *via* single-crystal XRD (scXRD) by Gotoh *et al*.[2] It is noteworthy that in some communications, including the aforementioned, a different nomenclature for these phases has been used where FE-I is also known as Phase II, while PE-I is known as Phase I. In this work, the PE / FE notation will be used including when referring to works that use the alternative notation which will be translated accordingly. The second deposited structure, MAMPUM05, was deposited by Kumai *et al*. and collected at 160 K by ND.[3] The most notable change to the structure from that of the PE-I phase is the reduction in symmetry, with the FE-I phase having the space group $P2_1$. The individual molecular units no longer sit atop local inversion centres, instead a single inversion centre is present at the centre of the unit cell, thus each molecule in the unit cell is the identical mirror image of its nearest neighbour (Figure 5.2). All atoms within each molecule are crystallographically distinct, resulting in double the number of distinct sites, compared with the PE-I phase. The reason for the reduced symmetry is the slight elongation of

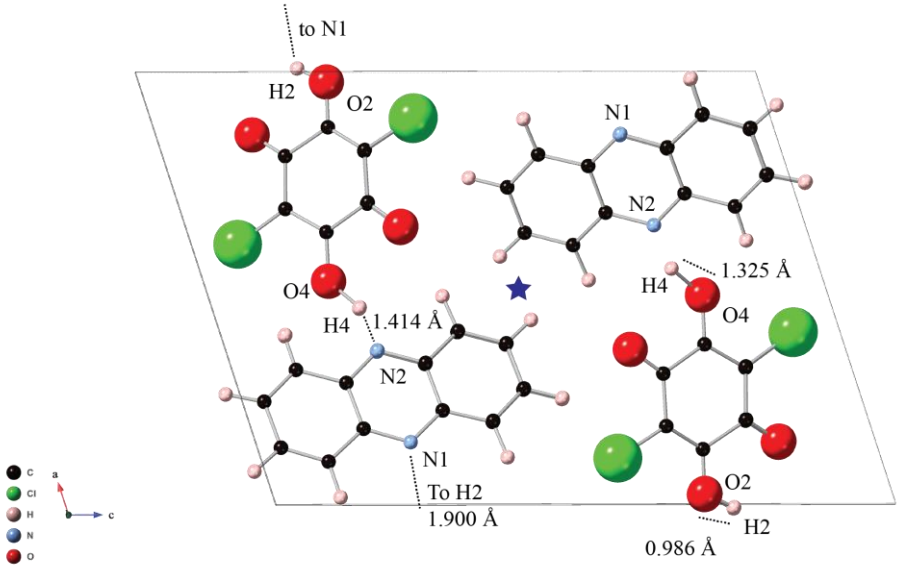

Figure 5.2 Unit cell of P-CA (CCDC deposition code: MAMPUM05). Blue star indicates inversion centre. Select bond lengths and atom labels shown. T = 160 K.

O–H distance, where the proton begins to displace towards the phenazine molecule, demonstrated by the large thermal ellipsoid observed by ND.[3] This proton displacement leads to significant changes in the proton geometry. In the PE-I structure MAMPUM01, the O−H bond length is 0.727 Å, whereas in the FE-I structure MAMPUM05, this O−H bond length is elongated to 0.986 Å, and since the two C−OH groups on the CA are no longer identical, the other O−H bond length is even longer at 1.325 Å. Furthermore, in MAMPUM01, the proton is located 13° outside of the plane of the aromatic ring, whereas in MAMPUM05, the proton of the longer O−H bond is 14° outside the plane of the aromatic ring, while the proton of the shorter O−H bond is only 4° outside the plane.

Below $T_{C,IC}$ (147 K) and above $T_{C,II}$ (137 K), P-CA exists in the FE-IC phase. Only one structure, MAMPUM07, has been deposited in the literature for this phase, by Noohinejad *et al.* in 2015.[4] The structure is incommensurately modulated and was found to have superspace group $P2_1(½\ \sigma_2\ ½)0$ where $\sigma_2 = 0.5139$. Incommensurate structures feature a modulation of some aspect of the structure across an irrational multiple of a unit cell length and as such cannot be defined by a supercell. The authors suggest that in P-CA, the modulation affects the proton position of the CA, such that every other CA molecule features one proton transferred hydrogen bond (N−H···O) hydrogen bond and one non-proton transferred hydrogen bond (O−H···N). The remaining half of the CA molecules feature no proton transferred hydrogen bonds. In the CA molecules where proton transfer is not observed, the O−H bond distance is elongated but still appears covalent, while the N···H bond distance is shortened, but is still greater than 1.03 Å, the length of a covalent N−H bond.

Below $T_{C,II}$ (137 K), a lock-in transition occurs to give the FE-II phase, which is a twofold superstructure. Two structures have been deposited in the literature. The first, MAMPUM03, was deposited by Gotoh *et al*. in 2007, and was collected using scXRD at 97 K.[2] The second, MAMPUM06, was deposited by Noohinejad *et al*. in 2014 and was collected at 100 K using synchrotron XRD.[5] The two reports are in contradiction, with the former suggesting the structure has $P2_1$ symmetry, and thus an inversion centre in the cell, and salt formation with a proton transfer onto the phenazine as depicted in schematic form in Figure 5.3 and in the crystal structure in Figure 5.4.[2] The latter suggests the structure is a commensurately modulated twofold superstructure with superspace group $P2_1(½\ \sigma_2\ ½)0$ where $\sigma_2 = ½$.[5] Thus a single unit cell has reduced symmetry compared to the FE-I phase, with the triclinic space group

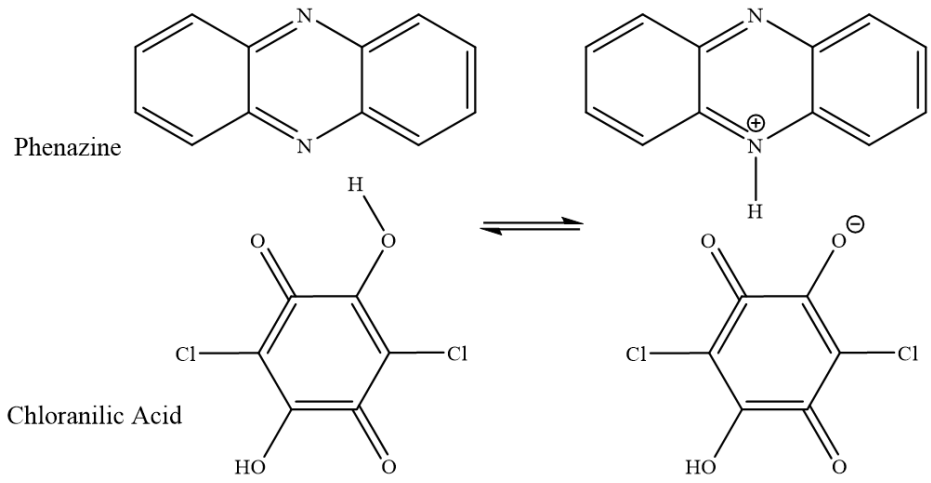

Figure 5.3 Simplified schematic of proton transfer mechanism in P-CA.

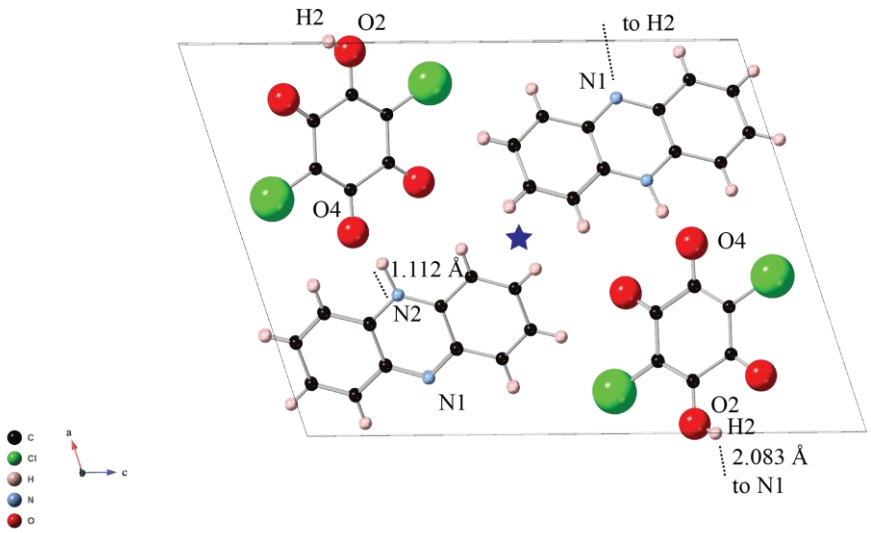

Figure 5.4 Unit cell of P-CA (CCDC deposition code: MAMPUM03). Select bond lengths and atom labels shown. T = 97 K.

P_1. Noohinejad *et al*. found that only one in every four hydrogen bonds resulted in a proton transition, as first proposed by Kumai *et al.* in 2012, directly contradicting the one-in-two proton transfer proposed by Gotoh *et al.*[2, 5, 17] Assessment of the intensity of the C−O^- band observed with IR at low temperatures showed that the ionicity of P-CA increases with decreasing temperature towards $T_{C,IC}$, and results in neutral (N) and ionic (I) pairs. A full tabulation of all the deposited structures along with the phase, collection method and temperature and literature source can be found in Table 5.2, while a full tabulation of the hydrogen bonding environments of each structure can be found in Table 5.3**.**

Table 5.2 Tabulation of all literature deposited structures of P-CA.[1-5]

CCDC Code	Phase	Collection Method	Collection Temperature (K)	Source
MAMPUM	PE-I	Synchrotron XRD	305	[11]
MAMPUM01	PE-I	Synchrotron XRD	298	[11]
MAMPUM02	FE-I	scXRD	170	[13]
MAMPUM03	FE-II	scXRD	97	[13]
MAMPUM04	PE-I	ND	300	[14]
MAMPUM05	FE-I	ND	160	[14]
MAMPUM06	FE-II	Synchrotron XRD	100	[16]
MAMPUM07	FE-IC	Synchrotron XRD	139	[15]

Table 5.3 Tabulation of hydrogen bond geometries of all deposited P-CA structures from the literature. In structures with $P2_1/n$ space group, only one environment is given as all hydrogen bonds are equivalent.

CCDC Code	O–H (Å)	N···H (Å)	O–H (Å)	N···H (Å)
MAMPUM	0.817	2.071	–	–
MAMPUM01	0.727	2.184	–	–
MAMPUM02	1.028	1.658	0.729	2.145
MAMPUM03	1.572	1.112	0.793	2.083
MAMPUM04	0.953	1.873	–	–
MAMPUM05	1.325	1.414	0.986	1.900
MAMPUM06	0.824	2.015	1.264	1.450
MAMPUM07	0.908	1.943	1.435	1.320

In this chapter, the structure of P-CA has been studied using Solid-state NMR spectroscopy to gain local information on the exact nature of the proton transfer mechanism, in combination with density functional theory (DFT) calculations to aid in assignment and structural investigation. Variable temperature (VT) NMR experiments have been used to investigate the structural changes with respect to temperature.

5.2 Experimental Details

5.2.1 Synthetic Details

P-CA was synthesised using a methodology adapted from Gotoh *et al*. and Noohinejad *et al*.[2, 5] First, phenazine (0.901 g, 5 mmol) was dissolved in methanol (100 mL) under heating to 40 °C. Separately, CA (1.045 g, 5 mmol) was dissolved in methanol (100 mL)

under heating to 40 °C. Once dissolved, the two solutions were mixed under stirring for 30 minutes. The resulting solution was then filtered and washed three times with methanol.

d-P-CA was synthesised following the same methodology but at 1/10 scale and using deuterated methanol (CH_3OD). First, phenazine (0.0901 g, 0.5 mmol) was dissolved in methanol (10 mL) under heating to 40 °C. Separately, CA (0.105 g, 0.5 mmol) was dissolved in deuterated methanol (10 mL) under heating to 40 °C. Once dissolved, the two solutions were mixed, and five drops of deuterated water (D_2O) was added. The solution was then left to stir for 30 minutes, before being filtered and washed three times with deuterated methanol.

5.2.2 Solid-State NMR Details

Solid-state NMR experiments were performed on Bruker Avance III HD spectrometers operating at magnetic field strengths of 9.4 T and 16.4 T. ^{13}C NMR spectra are referenced relative to tetramethylsilane using the methyl resonance of *L*−alanine at 20.5 ppm as a secondary reference. ^{1}H spectra are referenced relative to *L*−alanine using the carboxylate acid resonance at 8.5 ppm. ^{2}H spectra are referenced relative to d4-malonic acid using the hydroxyl resonance at 13 ppm. Full NMR details are given in the relevant figure captions but are summarised below. Temperature sensors for VT NMR experiments were calibrated using $Pb(NO_3)_2$ as discussed in Chapter 2 Appendix 2.1.[18]

^{13}C NMR spectra were recorded at a field strength of 9.4 T. ^{13}C NMR spectra were recorded at a magic-angle spinning (MAS) rate of 12.5 kHz using cross polarisation (CP) to transfer magnetisation from ^{1}H with a contact time of 1 – 5 ms. The CP pulse power was ramped linearly from 70% to 100%. ^{1}H heteronuclear decoupling using two-pulse phase modulation (TPPM)[19] with a pulse length of 4.8 μs and a radiofrequency field strength of 100 kHz was applied during acquisition. Spectra are the sum of between 128 and 1,744 transients separated by a recycle interval of 30 s. A dynamic nuclear polarisation (DNP) experiment was completed at the DNP MAS Facility at the University of Nottingham, all relevant details are given in Section 5.4.

^{1}H NMR spectra were recorded at a field strength of 16.4 T. ^{1}H MAS NMR spectra were recorded at an MAS rate of 15 kHz. Spectra are the sum of 16 transients separated by a recycle interval of 1 s.

^{2}H MAS NMR spectra were recorded at a field strength of 16.4 T using an MAS rate of 15 kHz. MAS spectra are the sum of 240 transients separated by a recycle interval of 5 s. A static spectrum was recorded using a solid echo (90°-τ-90°-τ-acquire) pulse sequence with a 16-step phase cycle. The static spectrum is the sum of 49,264 transients separated by a recycle interval of 5 s.

5.2.3 Computational Details

First-principles calculations of theoretical NMR parameters were carried out using the CASTEP[20] code including the gauge-including projector augmented wave (GIPAW) algorithm,[21] which allows the reconstruction of the all-electron wave function in the presence of a magnetic field. The CASTEP calculations employed the revised-Perdew-Burke-Ernzerhof (rPBE) *meta*-generalised gradient approximation (*meta*-GGA) exchange-correlation (XC) functional,[22, 23] and core valence interactions were described by ultrasoft pseudopotentials.[24] Prior to the calculation of NMR parameters, structures were geometry optimised according to Method E described in Chapter 3 Section 3.6.1, where no geometric constraints are placed on the unit cell and the DFT-D3 semi-empirical dispersion correction (SEDC) scheme is applied.[25, 26]

Geometry optimisations and NMR calculations were carried out using a planewave energy cut off of 50 Ry and a *k*-point spacing of 0.05 2π Å^{-1}. The calculations generate the absolute shielding tensor (σ) in the crystal frame. Diagonalisation of the symmetric part of σ yields the three principal components, σ_{XX}, σ_{YY} and σ_{ZZ}. The isotropic shielding, σ_{iso}, is given by (1/3)Tr[σ]. The isotropic chemical shift, δ_{iso}, is given by $\sigma_{ref} - \sigma_{iso}$, where σ_{ref} is a reference shielding determined by comparison of experimental chemical shifts over the complete range of structures. The quadrupolar coupling constant, $C_Q = eQV_{ZZ}/h$ and asymmetry parameter, $\eta_Q = (V_{XX} - V_{YY})/V_{ZZ}$ are obtained directly from the principal components of the electric field gradient tensor, which are ordered such that $|V_{ZZ}| \geq |V_{YY}| \geq |V_{XX}|$. Q is the nuclear quadruple moment, where a value of 2.86 mb was used for ^{2}H.[27] In addition to the magnitude, the calculations also generate the sign of C_Q. However, the sign of C_Q cannot be determined from the experimental data presented in this work; therefore, when comparing calculated and experimental quadrupolar couplings, only the magnitude of the calculated C_Q is considered.

5.2.4 Crystallography Details

Polycrystalline materials were analysed using powder XRD (PXRD). Samples were analysed at ambient temperature with a Rigaku SmartLab diffractometer equipped with a D/teX-ULTRA 250 High-Speed Position-Sensitive Detector system and a Ge(220)x2 2-bounce monochromator using CuKα_1 radiation (λ = 1.54059 Å) within a 2θ range of 5°−50° (step size of 0.01°).

5.3 Results

5.3.1 X-ray Crystallography

Figure 5.5 shows a comparison between PXRD patterns of P-CA obtained from experiment (Figure 5.5a) and simulated from PE-I structures, (Figure 5.5b-d). Very good agreement is observed between experiment and the simulated patterns with characteristic reflections at 7°, 11°, 15°, 16° and 26°. Notably, the pattern of MAMPUM04 features a shifting of some reflections to a slightly higher 2θ angle. The reflections between 26° and 36° appear approximately 1°−2° higher than in the other patterns. While no significant difference is observed between the unit cell parameters of these three structures, MAMPUM04 features a slightly different O−H···N environment which could be the cause of the shift in reflections. In MAMPUM04, the C−O−H angle is 8° greater than in the other two structures, while the O−H bond length is slightly elongated by approximately 0.14 Å. Comparison of the PXRD patterns of all published crystal structures is given in Figure 5.A26 of Appendix 5.1. The simulated PXRD patterns of all the structures are almost identical with only minor differences in peak widths. This observation is consistent with only minor variations in the geometries of heavy atoms in the unit cells. Between different phases the major structural difference is the position of the proton of the CA, which due to the low scattering factor of protons produces only minor differences in the PXRD patterns.

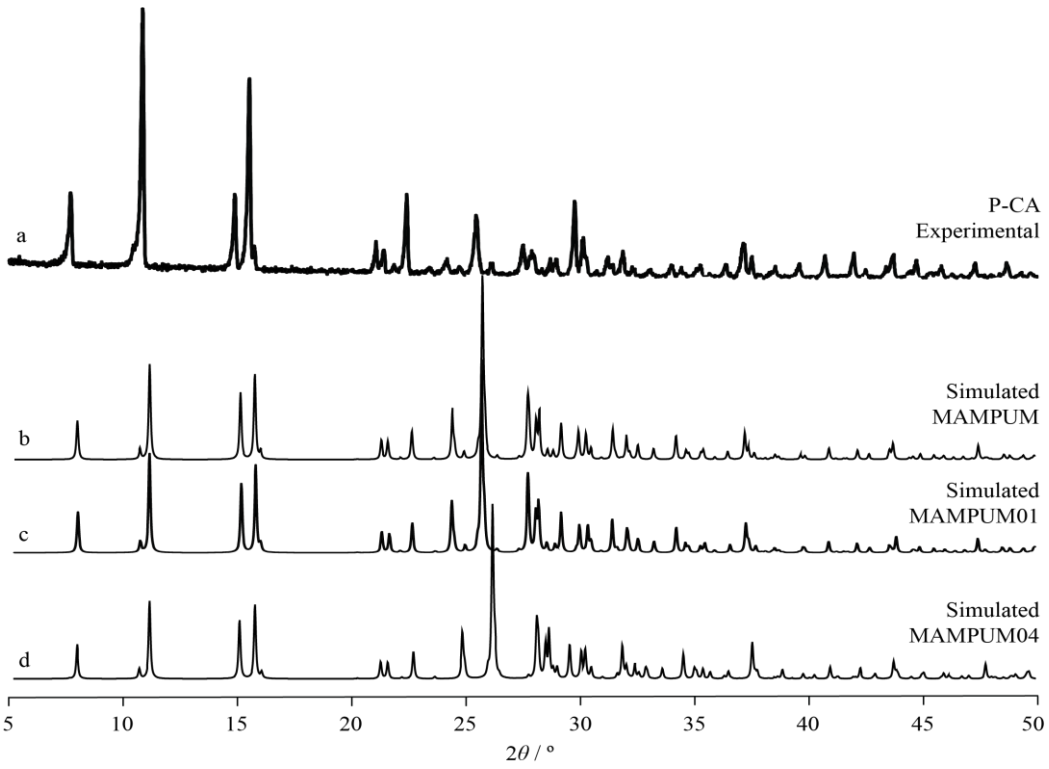

Figure 5.5 PXRD patterns of P-CA (a) experimental diffraction pattern collected at ambient temperature and (b-d) simulated diffraction patterns of the three PE-I structures MAMPUM, MAPUM01 and MAMPUM04.

5.4 ^{13}C Solid-State NMR Spectroscopy

^{13}C CPMAS NMR spectra of P-CA and deuterated P-CA collected at ambient temperature (≈ 298 K) are shown in Figure 5.6. In the spectrum of P-CA, Figure 5.6a, a total of nine resonances are observed, which is consistent with the nine crystallographically distinct carbons in the crystal structure. The crystal structure suggests that nine resonances should be expected, comprised of three from the CA molecule and the remaining six from the phenazine molecule. However, this is not what is observed experimentally. The five broadened intense resonances at 139.1 ppm, 134.0 ppm, 132.3 ppm, 129.7 ppm and 123.3 ppm can be attributed to the aromatic carbons of the phenazine molecule. The other four, less intense and broader resonances are from the CA. The two resonances at higher chemical shift, those at 175.7 ppm and 158.7 ppm are from the carbonyl and alcohol carbons respectively, while both of the low chemical shift resonances at 113.7 ppm and 108.6 ppm are from the chloro-substituted carbon. The single crystallographically distinct chloro-substituted carbon is observed as two resonances. This splitting of resonances arises due to the second-order quadrupolar-dipolar interaction where the dipolar coupling of an I = ½ nucleus (*i.e.* ^{13}C) to a quadrupolar nucleus with a large quadrupole moment (*i.e.* $^{35/37}$Cl) can lead to the transferral of second-order quadrupolar effects to the I = ½ nucleus.[28, 29] Thus, four resonances are observed from the CA molecule, and five

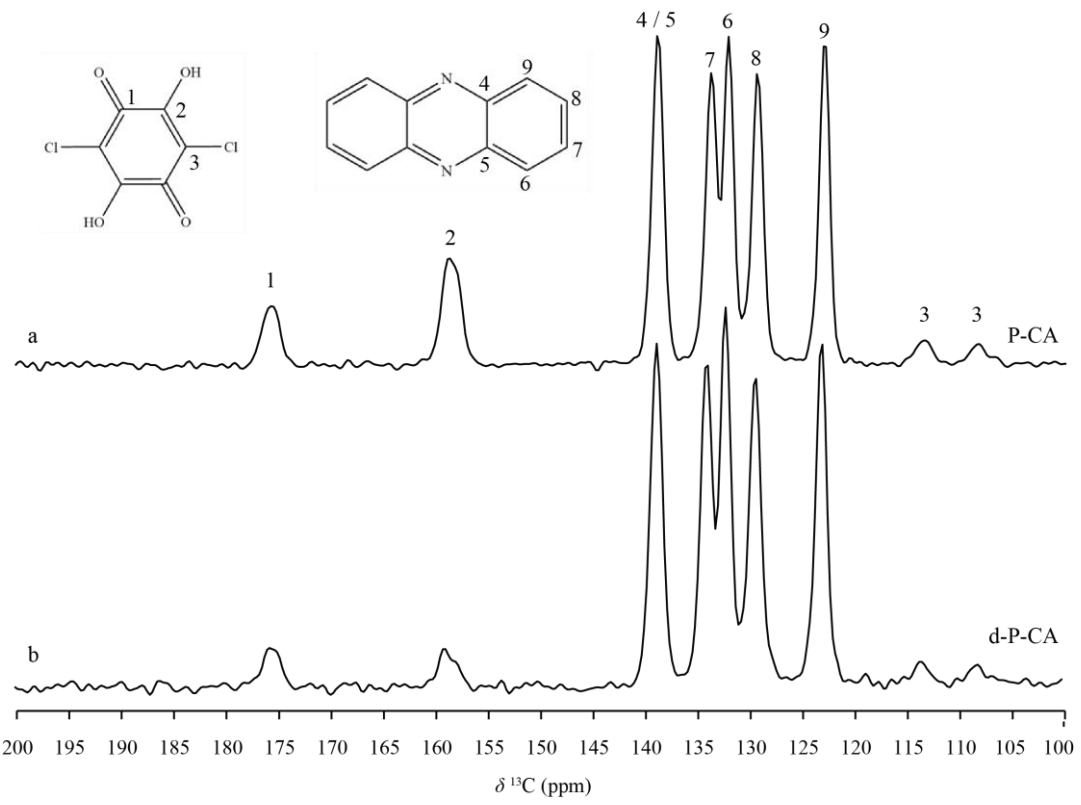

Figure 5.6 ^{13}C CPMAS NMR spectra of P-CA (a) and d-P-CA (b) collected at 9.4 T. Samples were spun at an MAS rate of 12.5 kHz. A contact pulse of 1 ms was applied. Spectra are the sum of 1,744 transients separated by a recycle interval of 30 s.

from the phenazine molecule, which suggests one phenazine resonance is not resolved due to the observed broadening. In the spectrum of d-P-CA, Figure 5.6b, the intensity of resonances from the CA molecule are slightly reduced. This arises due to the use of the CP experiment, where magnetisation is transferred from ^{1}H to ^{13}C atoms in the sample. Since in this sample the ^{1}H atoms of the CA are replaced by ^{2}H atoms, magnetisation is not transferred from any atoms on the CA molecules. Instead, magnetisation can still be transferred, but across longer distances with longer CP match durations from the protons of the nearby phenazine molecules; however, this distance reduces the intensity at which these resonances appear.

To investigate the progression of the PE-I to FE-I phase transition, variable temperature NMR experiments were completed, as shown in Figure 5.7 and Figure 5.8. For these experiments the d-P-CA sample was studied, as the higher T_C enables a wider temperature range around T_C to be probed. The experiments shown in Figure 5.7 were a preliminary study completed without a recent calibration of the temperature sensors, and thus the reported temperatures are as read from the detector and are not calibrated. Figure 5.8 consists of a second collection of this data following a temperature calibration, with the reported temperatures calculated from a $Pb(NO_3)_2$ calibration, discussed in detail in Chapter 2.[18] In Figure 5.7, a better resolution is observed in all spectra, as a result of the longer recycle interval used compared with the spectra shown in Figure 5.8. Time constraints arising from limited instrument availability dictated that shorter experiments were required to fully cover the temperature range chosen. Therefore, a shorter recycle interval was used, decreasing resolution overall, however, sufficient resolution is still obtained to make similar observations in both figures.

In Figure 5.7, the spectra collected at higher temperatures (Figure 5.7a-d) are consistent with the ambient temperature spectrum shown in Figure 5.6b. In the lower temperature spectra (Figure 5.7e-i), a splitting of resonances is observed. In Figure 5.7e, this splitting appears as a broadening, whereas at temperatures below this, resolution improves to show clear splitting of the resonances. The splitting of resonances is consistent with a transition of P-CA from the PE-I phase to the FE-I phase, where due to the reduction in symmetry two environments with very similar chemical shift are expected. Where in the PE-I phase, the CA molecule has three crystallographically distinct carbons, in the FE-I phase there are six crystallographically distinct carbons due to this change in symmetry. In Figure 5.7e, resonances of the carbonyl carbon appear at 176.4 ppm and 174.2 ppm (2.2 ppm apart), while in Figure 5.7h those resonances appear at 176.7 ppm and 173.9 ppm (2.8 ppm apart). This suggests that the phase transition is not as simple as an instantaneous switch from one phase to another. For example, at temperatures near to T_C, there is likely to be a mix of both phases such that the resolution of either phase is convoluted. Further evidence of this is observed for the phenazine resonances centred at 139 ppm and 123 ppm of which resolution improves with decreasing temperature.

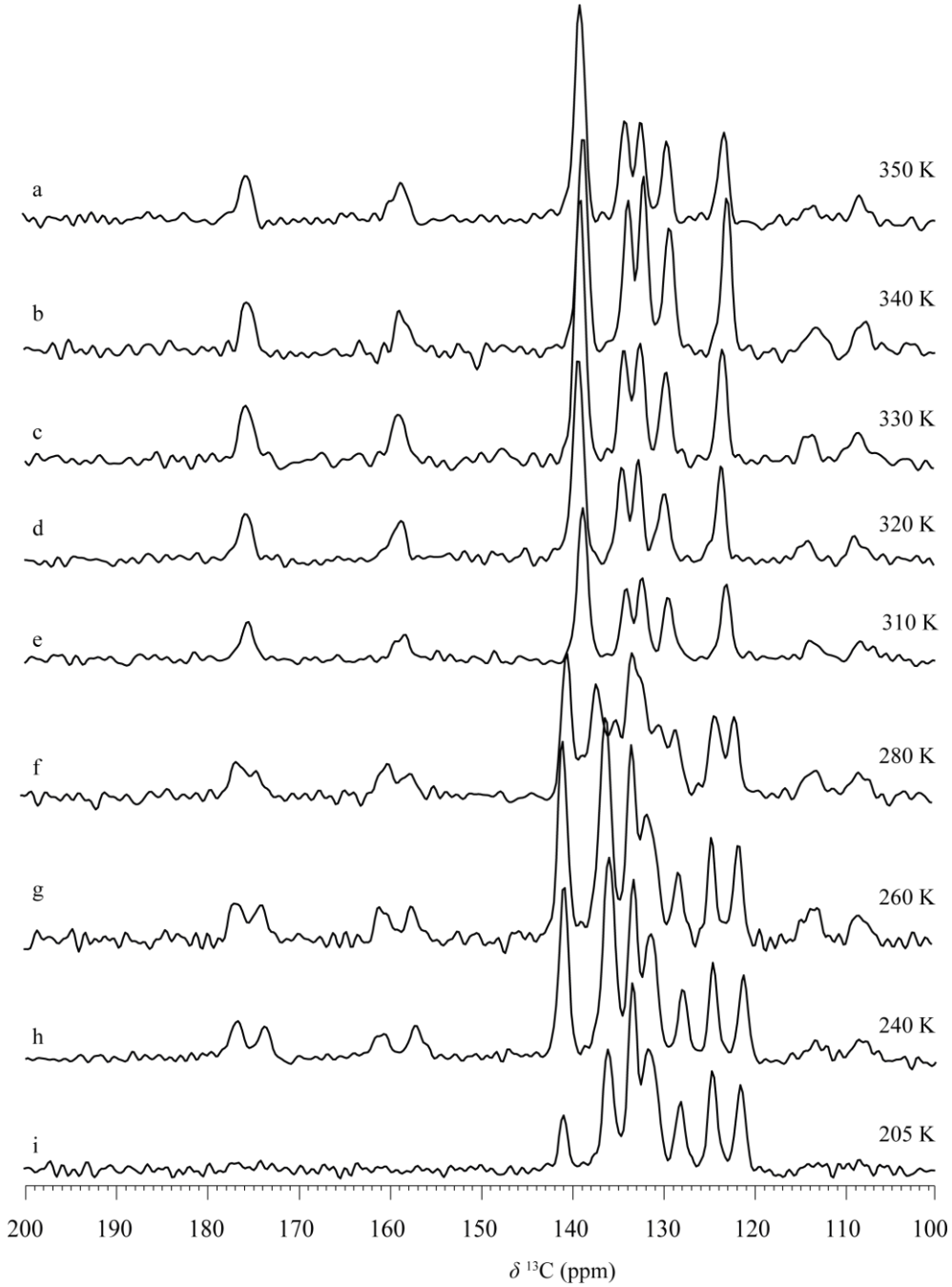

Figure 5.7 ^{13}C CPMAS NMR experiments of d-P-CA collected at variable temperatures. Spectra are collected at 9.4 T with an MAS rate of 12.5 kHz and are the sum of 128 transients (a-g) separated by a recycle interval of 30s. (h) is the sum of 256 transients. (i) is the sum of 336 transients. Magnetisation is transferred with a contact time of 5 ms. Reported temperatures are not calibrated instead are as read from the detector.

This broadening near to T_C could be a result of a gradual movement of the charge transfer proton, which would lead to a range of possible hydrogen bond geometries with small differences in the structure. This may not be the only source of broadening, however, as temperature inhomogeneity of the sample may be another potential cause.

In the lowest temperature spectra (Figure 5.7h-i), the resonances associated with the CA molecule appear to initially lose some intensity (Figure 5.7h, resonances centred at 175 ppm,

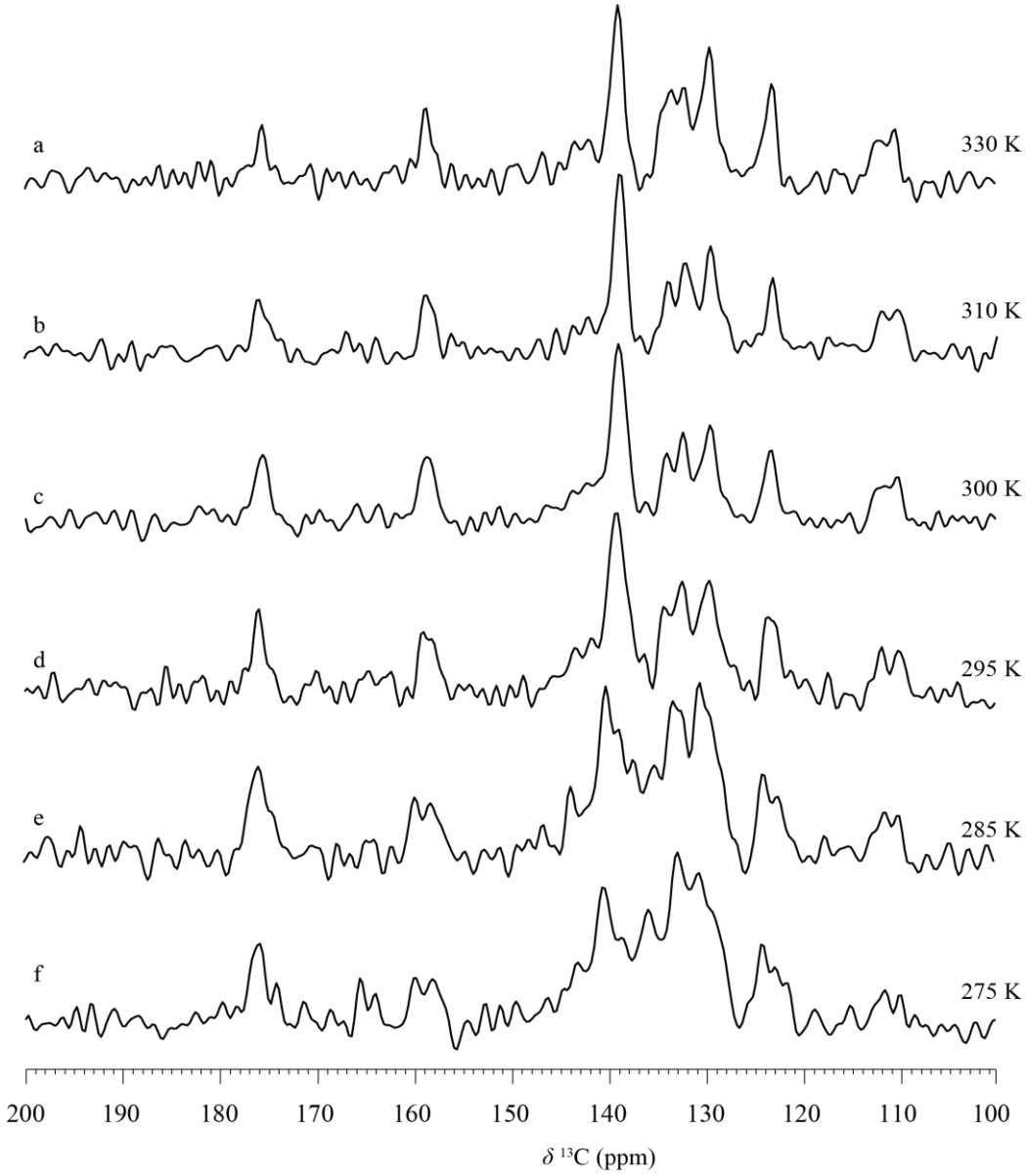

Figure 5.8 ^{13}C CPMAS NMR experiments of d-P-CA collected at variable temperatures. Spectra are collected at 16.4 T with an MAS rate of 15 kHz and are the sum of 256 transients separated by a recycle interval of 10s. Magnetisation is transferred with a contact time of 5 ms.

159 ppm, 115 ppm and 109 ppm), while those from the phenazine remain unchanged. While in Figure 5.7i, the resonances from the CA molecule are no longer visible. There is also a reduction of intensity in the resonance at 141 ppm arising from the quaternary carbon of the phenazine. It is unlikely these observations are the result of a phase transition as the T_C of phase transitions has been well established in the literature. While the temperature of the sample in the NMR rotor is inhomogeneous, another phase transition would not be expected until approximately 199 K. Inhomogeneity of sample temperature in VT experiments is caused by multiple aspects of the experimental set up. Frictional heating of the sample occurs when spinning at high frequencies, in this case where an MAS rates of 12.5 kHz and 15 kHz have been used. The $Pb(NO_3)$ temperature calibration suggests this frictional heating results in an

increase in sample temperature > 10 K. This is further complicated with ambient temperature bearing and drive gas streams used to conduct the MAS experiment and further still with the cryogenic cooling gas applied. Additionally, the reduced intensity of the CA resonances is unlikely to result from disorder, as this would result in a broadening of all resonances in the spectrum instead of just those carbons not in proximity of a proton. Thus, it is possible that the reduced intensity of these resonances is due to a change in either the carbon or proton $T_{1\rho}$. In rigid solids, $T_{1\rho}$ can be of the order of tens of milliseconds, and can be extended further at lower temperatures, such that the efficiency of magnetisation transfer is increased, and thus greater intensity is observed in carbons at short distances from protons. Oppositely, the intensity of resonances from distant interactions decreases.

As noted previously, similar observations can be made from Figure 5.8, to those already discussed for Figure 5.7. The broadening, or splitting at lower temperatures, is most easily observed for the C−OH group resonance centred at approximately 159 ppm. This resonance is broadened in the spectrum collected at 295 K, and splits into two resonances in the spectra below 295 K. Significant changes are observed in the aromatic region as temperature is decreased. As the phase transition is passed, the number of crystallographic carbons doubles, resulting in double the number of resonances expected to appear in the same chemical shift range. This, alongside the already poor signal to noise ratio, results in particularly poor resolution in this region. The observation of splitting occurs at a slightly lower temperature than the reported T_C of d-P-CA at 304 K. This is likely due the sample temperature inhomogeneity in the NMR rotor.

To aid visualisation, the chemical shifts of the carbonyl and C−OH resonances are plotted as a function of temperature in Figure 5.9, based on the spectra shown in Figure 5.8. At temperatures of 295 K and below, the C−OH resonance splits into two resonances centred at approximately 158 ppm. At 275 K, slightly improved resolution between the two peaks suggest that the resonances may continue to diverge with reduced temperature, and potentially indicating the structures could continually and gradually change geometry throughout the stable phase windows. However, more experiments at lower temperatures would be required to provide more insight. The split resonances remain centred at a chemical shift consistent with the single resonances in the higher temperature spectra. It is reasonable to assume that with the change in symmetry and a slight elongation of the O−H bond in the FE-I phase, the ^{13}C chemical shift would be slightly shifted to lower chemical shift as a result of the change in shielding from the oxygen atom. This could in turn encourage the opposite hydroxyl group to react oppositely, with a shorter O−H bond and less electron density on the oxygen atom, and thus a carbon resonance at slightly higher chemical shift resulting from deshielding. However,

no evidence has been reported to date of a shortening of the O−H bond in response to a reduced temperature phase transition.

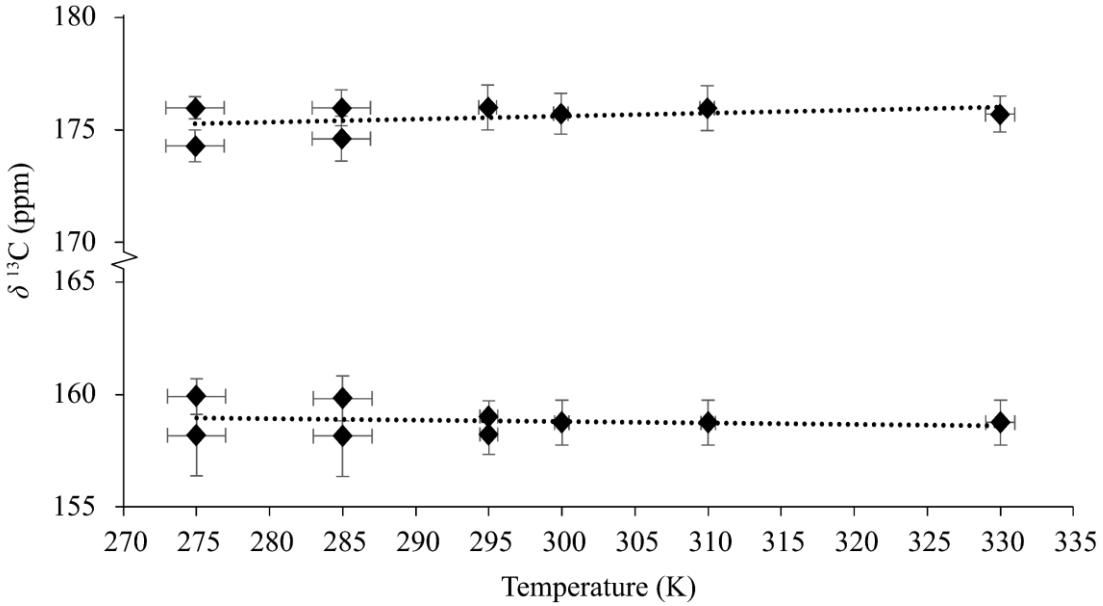

Figure 5.9 ^{13}C chemical shift of carbonyl and C−OH resonances from the variable temperature CPMAS NMR spectra of d-P-CA shown in Figure 5.8 plotted as a function of temperature. Horizontal error bars show uncertainty in temperature calibration arising from difference between sensors, vertical error bars are peak width at half maximum.

Study of the FE-II phase is challenging as reaching the low temperatures required is not straightforward. However, a preliminary experiment was attempted at the DNP MAS Facility at the University of Nottingham. The ^{13}C CPMAS NMR experiment was completed on d-P-CA at 97 K by Dr Abby Haworth (formerly Lancaster University, presently University of Liverpool). Recalling that $T_{C,II}$ of d-P-CA = 187 K, thus 97 K should be sufficiently low in temperature to give confidence that the FE-II phase is present in the sample. Figure 5.10 shows four intense but

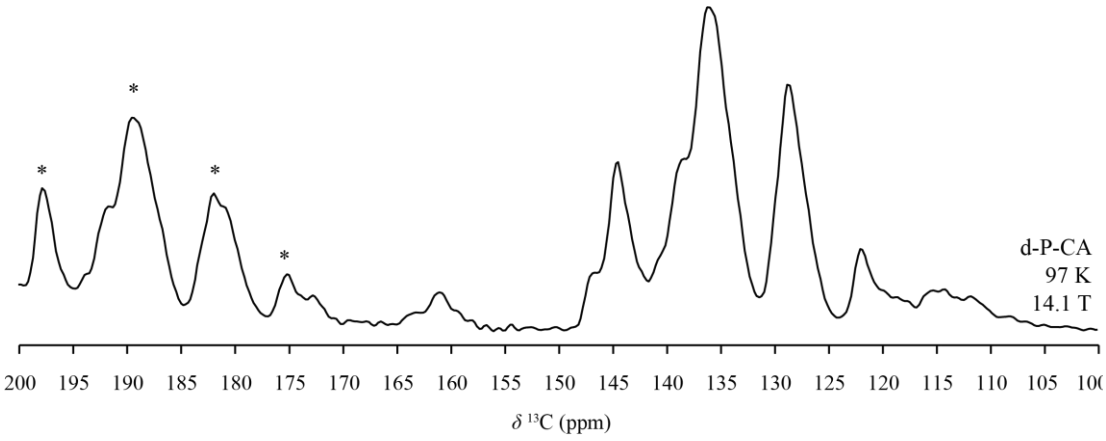

Figure 5.10 ^{13}C CPMAS DNP NMR of d-P-CA collected at 97 K. The spectrum was collected by Dr Abby Haworth at a field strength of 14.1 T at the Nottingham DNP MAS Facility at the University of Nottingham, May 2022. Sample was spun in a 3.2 mm sapphire rotor at an MAS rate of 8 kHz. A contact time of 5 ms was used to transfer magnetisation, and the spectrum is the sum of 8 transients separated by a recycle interval of 120 s. * = SSB. Spectral width shown was chosen for consistency with Figure 5.6.

broad resonances between 145 ppm and 123 ppm, a weak and broad resonance at 162 ppm and an additional broadened resonance from 115 ppm to 110 ppm. An additional low intensity shoulder on the low frequency side of the SSB at 175 ppm is present of which there are no stronger resonances observed at a frequency difference matching that of the MAS rate, thus is likely to be an isotropic resonance (δ = 173 ppm). The broad resonance at 162 ppm has shoulders on both sides of the isotropic resonance, which could indicate a complex ordering with subtly different local environments. Broadened resonances could be expected for the FE-IC phase, where the incommensurate modulation, comparable to disorder would result in broadening. However, 97 K is significantly below the expected temperature range for the FE-IC phase (188 K – 198 K) and as such the broadening could indicate that the ordering in the FE-II phase may be more complex with multiple crystallographically distinct molecules in different environments. Multiple spinning sidebands (SSB) are present in the spectra due to the low MAS rate used to reduce the effects of rotational heating. Therefore, a total of seven distinct resonances are observed, significantly less than the 18 expected resonances of the FE-I phase, and the nine observed resonances of the PE-I phase. The lack of apparent doubling of the peaks as observed in the FE-I phase could suggest this sample did not undergo the phase transitions and is locked in the PE-I phase as the cooling method in DNP experiments is much more rapid and involves placing samples into a precooled probe. This rapid cooling may effectively freeze the samples and restrict proton motion. Alternatively, despite the previously reported superspace groups indications, the carbon environments in the FE-II phase are sufficiently similar to not produce a splitting.

5.5 ^{1}H Solid-State NMR Spectroscopy

To directly probe the changes to the proton environment, variable temperature ^{1}H NMR experiments of P-CA were performed and are shown in Figure 5.11. The figure shows nine spectra collected across a temperature range of 250 K to 330 K, with the temperature of the sample calculated through calibration using $Pb(NO_3)_2$.[18] In all spectra, a significant background is observed from the stator in the probe, resulting in a broad hump from approximately –30 ppm to approximately 20 ppm. In the spectra of experiments completed at 267.5 K and above, the proton of the hydroxyl group of the CA molecule results in a single resonance at approximately 13.2 ppm. At 265 K, in Figure 5.11f, this resonance is broadened which suggests there is a range of proton environments present at this temperature. Below 262.5 K, the resonance is split into two resonances centred at approximately 13.2 ppm. The resonances arising from protons associated with the phenazine molecule also differ with varying temperature. At low temperatures, up to 270 K, the resonance appears as a single broad resonance between 7.3 ppm and 7.5 ppm, but covering a chemical shift range of approximately 7 ppm. In the spectra collected at 290 K and above, an additional sharper resonance is observed at approximately

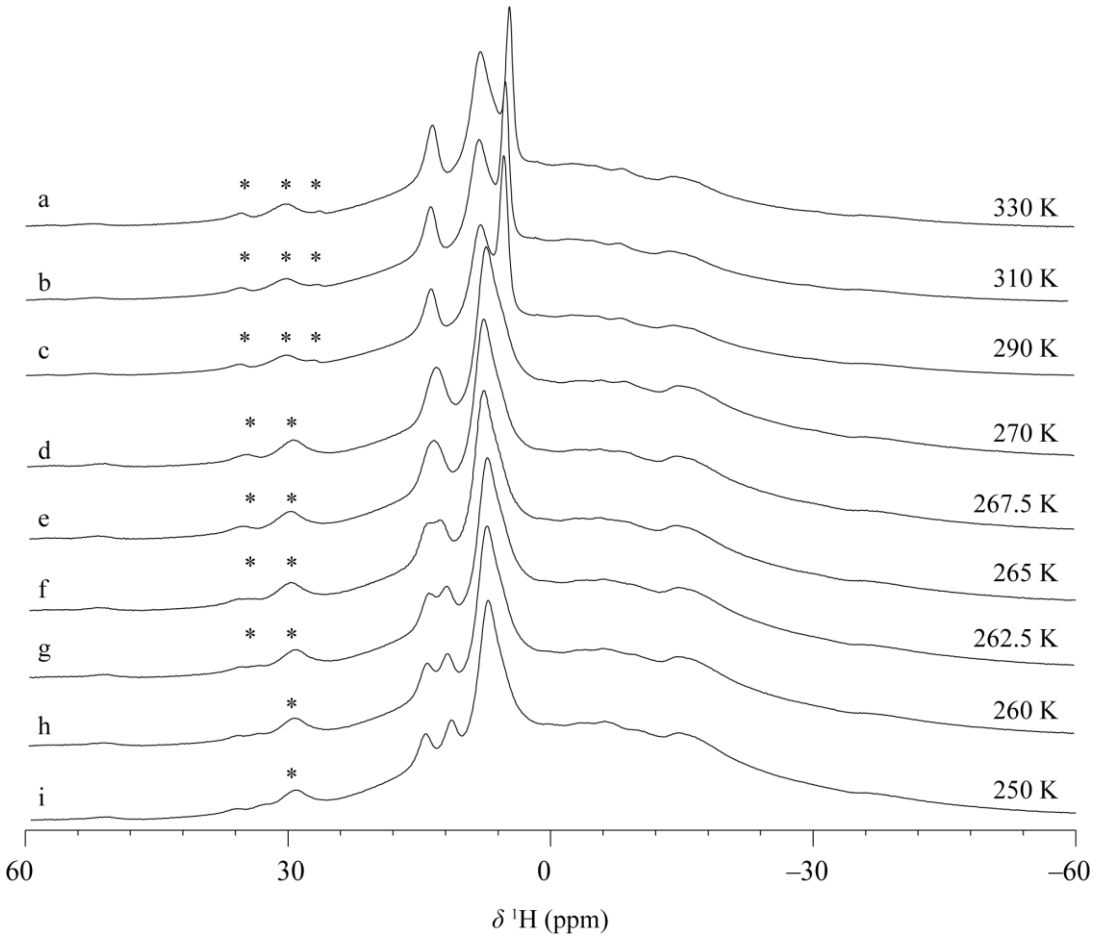

Figure 5.11 ^{1}H MAS NMR experiments of P-CA collected at variable temperatures. Spectra are collected at 16.4 T with an MAS rate of 15 kHz. Spectra are the sum of 16 transients separated by a recycle interval of 1 s. * = SSB

4.5 ppm, in addition to the broad resonance at approximately 7.5 ppm and the well resolved resonance at approximately 13.2 ppm. It appears that the splitting of the high frequency resonance and the disappearance of the low frequency resonance happens concurrently, indicating that both are the result of a structural change in the sample.

To aid visibility of the gradual changes in the hydroxyl proton environment, the ^{1}H chemical shift has been plotted as a function of temperature in Figure 5.12. The graph highlights the gradual separation of the split resonances with decreasing temperature below 262.5 K. It is possible that the separation between these resonances continues to grow with decrease in temperature, however more experiments would be required to test this, which were not possible here due to constraints to accessible temperature range.

The observations made from ^{1}H NMR experiments are consistent with a reduction in the symmetry of the unit cell, such that the number of crystallographic protons is doubled at the phase transition temperature, $T_{C,I}$. The number of crystallographic protons associated with the CA molecule doubles from one to two, which is consistent with the observation of a splitting of

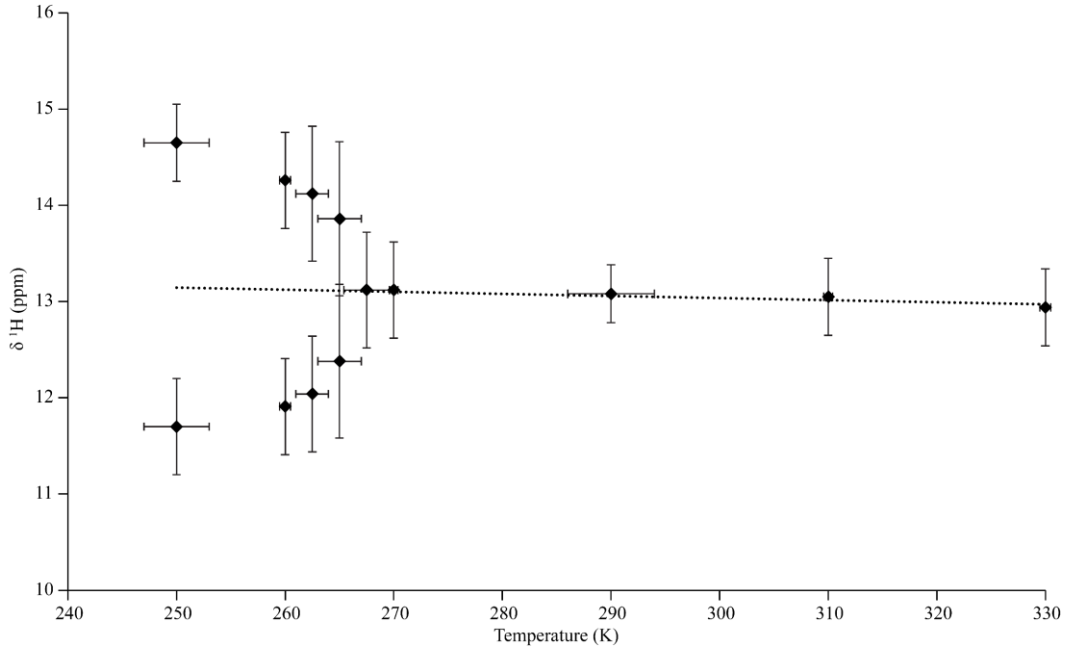

Figure 5.12 ^{1}H chemical shift of the hydroxyl proton resonance of the CA molecule from the variable temperature MAS NMR spectra shown in Figure 5.11, plotted as a function of temperature. Horizontal error bars show uncertainty in temperature calibration arising from difference between sensors, vertical error bars are peak width at half maximum.

the high frequency resonance. The number of crystallographic protons associated with the phenazine doubles from four to eight, consistent with the observation of a reduction in intensity of the low frequency resonance into a continuum of intensity spanning across a chemical shift range from 2 ppm to 9 ppm. While the highest reported phase transition temperature of P-CA is 253 K, observations in agreement with a phase transition are herein observed at the slightly higher temperature of approximately 265 K. The observations reported here suggest that the phase transition is more complex than an instantaneous switch from the PE-I phase to the FE-I phase, instead there may be a mixture of both phases present, or the phase transition may occur gradually. Furthermore, the temperatures of the NMR experiments here are calculated based on a $Pb(NO_3)_2$ calibration which could be a significant source of error. Further attempts to gain information on these phase transitions with ^{1}H NMR could utilise the DUMBO pulse sequence (decoupling using mind-boggling optimisation). DUMBO experiments provide enhanced resolution, however, as chemical shifts are scaled it is difficult to collect unambiguous measurements. Furthermore, the DUMBO pulse sequence requires avoidance of certain MAS rates that interfere with the pulse sequence, as such an MAS rate of 9,671 Hz is typically used. Therefore, to use this method another temperature calibration would be required due to the differences in frictional heating between the respective MAS rates used herein, and in a DUMBO experiment.

5.6 ^{2}H Solid-State NMR Spectroscopy

To further investigate the changing environments of the charge transfer proton with respect to temperature, deuterium Solid-state NMR experiments were carried out on d-P-CA samples. Deuterium is a spin I = 1 nucleus and as such, NMR spectra will feature quadrupolar lineshapes which can be analysed to gain information about the deuterium environment. A static ^{2}H spectrum collected at ambient temperature is shown in Figure 5.13. The spectrum features a broadened quadrupolar lineshape, where a fit to the lineshape reveals a C_Q of approximately 150 kHz with an η_Q of approximately 0.1, though the less pronounced horns may suggest the presence of dynamic disorder of the deuteron at ambient temperature. This is comparable to, but slightly lower than, that previously observed in a study of brucite, a hydrous magnesium silicate where C_Q values of roughly 230 kHz were observed in similar hydroxyl environments.[30] Furthermore, a strong resonance is observed at 5.5 ppm, consistent with a small amount of D_2O, suggesting the sample was not completely dry. This D_2O resonance is commonly observed in deuterated samples and appears as a single intense resonance due to molecular tumbling averaging the orientation dependence of the quadrupolar interaction, despite no MAS being used in this experiment. Despite the apparent intensity, the integrated intensity is small compared to the rest of the lineshape. Furthermore, this resonance does not appear in the fit to the lineshape as it is not a part of the quadrupolar lineshape.

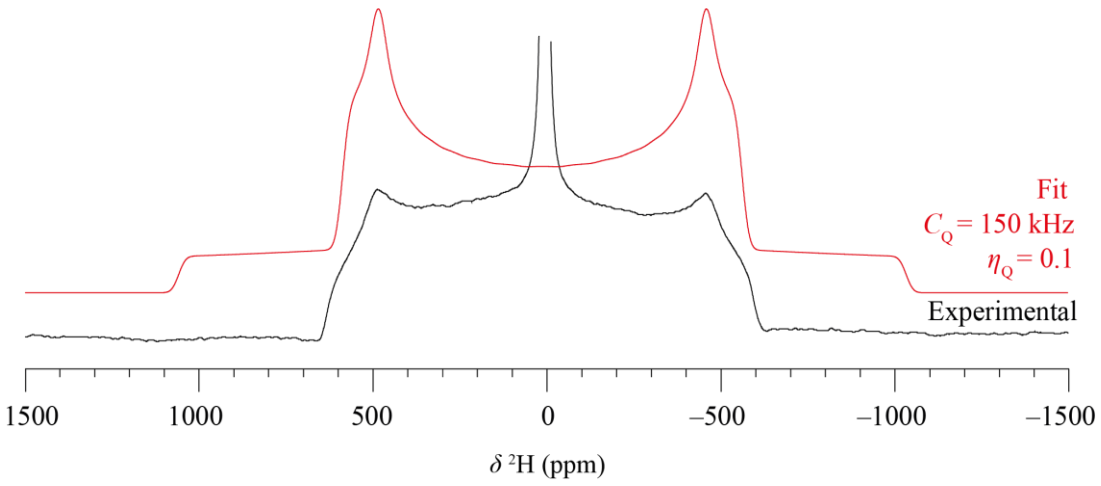

Figure 5.13 Static ^{2}H NMR experimental spectrum (black) with fit to the quadrupolar lineshape (red). Experimental spectrum collected at a field of 16.4 T, utilising a solid-echo pulse sequence. The spectrum is the sum of 49,264 transients separated by a recycle interval of 5 s.

To directly probe the system at different temperatures, VT MAS NMR experiments were completed and are shown in Figure 5.14. Only the central transition is shown, while a large manifold of spinning sidebands trace out the quadrupolar lineshape. Static VT measurements were not possible due to limited instrument availability and the long experimental time required to obtain the powder lineshape. Long low temperature experiments

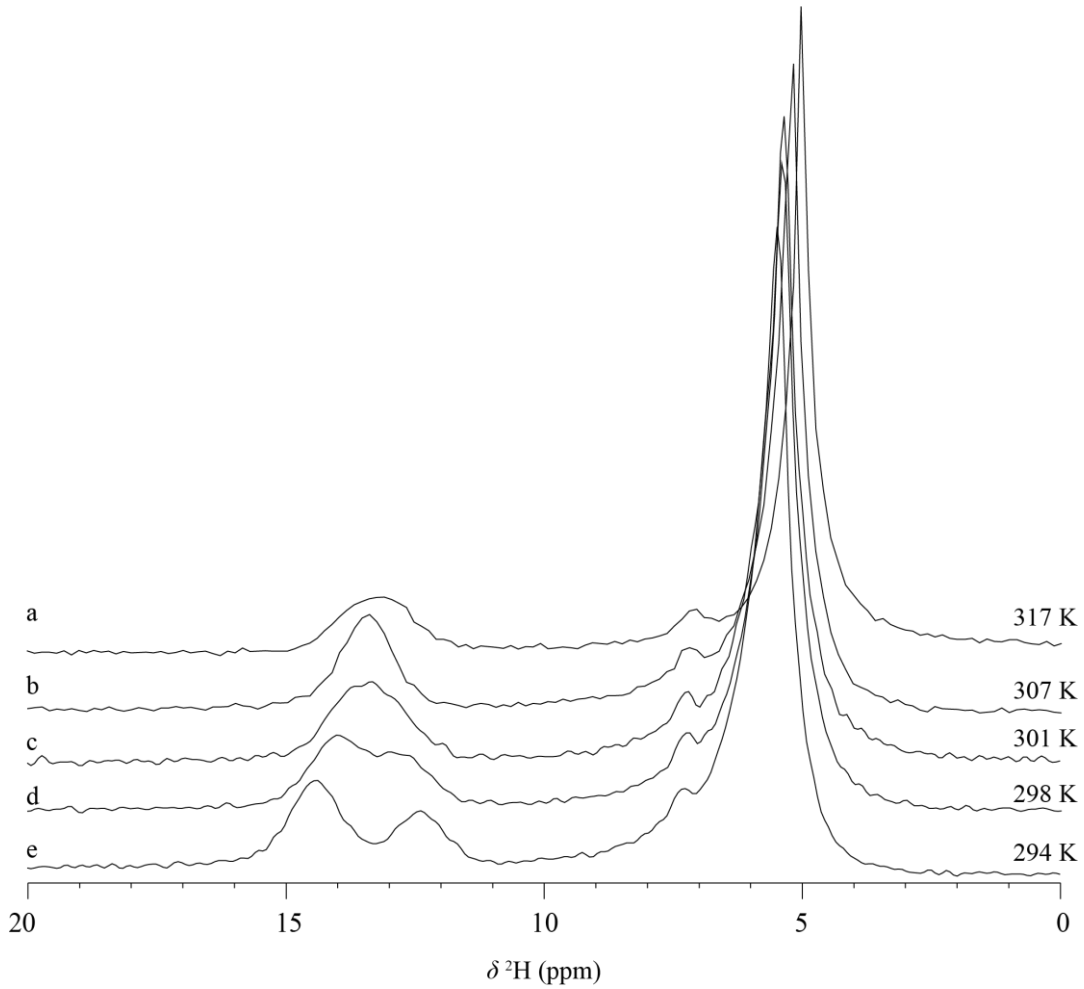

Figure 5.14 ^{2}H MAS NMR of d-P-CA collected at a range of temperatures. Spectra are collected at a field strength of 16.4 T using an MAS rate of 15 kHz and are the sum of 240 transients separated by a recycle interval of 5 s.

pose significant risks to the NMR hardware such as quenching. The ^{2}H spectra show a strong resonance at 5.5 ppm arising from the residual D_2O and a further less intense resonance at 13.5 ppm from the hydroxyl group of the CA unit. Despite the appearance, the D_2O resonance arises from only a miniscule amount of residual D_2O. Since the resonance does not have spinning side bands (unlike the isotropic resonance of the hydroxyl group of P-CA at 13.5 ppm), therefore the only signal from D_2O is observed at the isotropic chemical shift and is not spread across a spinning side band manifold. As such, the relative integrated intensity of the D_2O is much smaller than the hydroxyl resonances. Inspection of the change in the hydroxyl resonance with variable temperature gives insight into the thermal behaviour of the structure. As temperature decreases below 301 K, the resonance of the hydroxyl group deuterium begins to split into two resonances, suggesting the phase transition has occurred with the break in symmetry described previously causing two inequivalent deuterium sites. At first this manifests as a broadened resonance at 298 K, but at 294 K is resolved as two distinct resonances. To aid visualisation, the response of chemical shift with respect to temperature is plotted in Figure

5.15. The chart highlights the gradual splitting of the hydroxyl resonances when near to $T_{C,I}$, with the distinct split observed at 294 K. A gradual separation of the split resonances is observed within the limited temperature range, in similarity to the observations in ^{13}C and ^{1}H experiments.

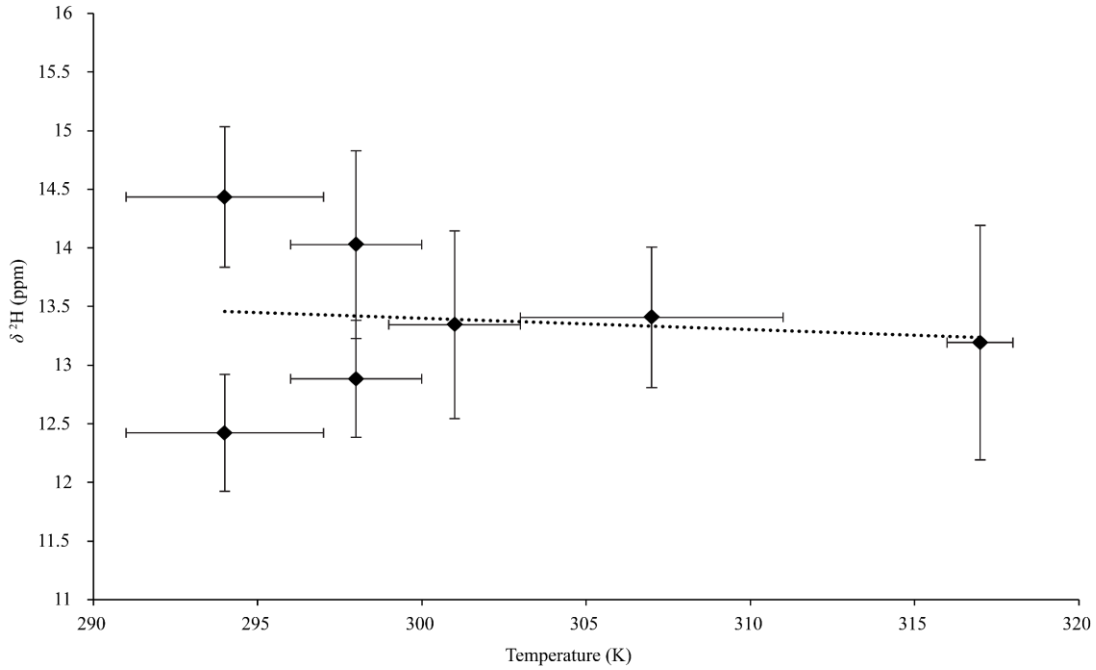

Figure 5.15 The ^{2}H chemical shift of the hydroxyl deuterium atom of the CA unit from the variable temperature MAS NMR spectra shown in Figure 5.14, plotted as a function of temperature. Horizontal error bars show uncertainty in temperature calibration arising from difference between sensors, vertical error bars are peak width at half maximum.

To further assess how the electronic environment of the charge transfer proton changes with respect to temperature, the quadrupolar parameters of deuterium were extracted at the extremities of the studied temperature range. Fits to the spinning sideband manifolds which trace out the quadrupolar powder pattern at the extremes of the temperature range studied are shown in Figure 5.16. At high temperature (317 K), the single ^{2}H site has C_Q of approximately 150 kHz and η_Q of approximately 0.18, while at low temperature (294 K) below $T_{C,I}$ there are two ^{2}H sites with C_Q of approximately 136 kHz and approximately 198 kHz and approximate η_Q values of 0.14 and 0.00, respectively. The quadrupolar parameters extracted from the high temperature spectrum are in good agreement with those extracted from the static spectrum in Figure 5.13, giving confidence to the extracted values. However, the quadrupolar parameters extracted from the low temperature spectrum are significantly different. Firstly, observation of two sites is consistent with the reduction of symmetry expected with the phase transition to FE-I. The site with C_Q of approximately 136 kHz is slightly reduced compared to the 150 kHz site observed in the high temperature PE-I phase spectrum. Thus, the deuteron has a reduced quadrupolar interaction but a higher η_Q. This is consistent with a deuteron that has slightly moved away from the oxygen atom and has a more diffuse location as has been observed by

diffraction studies.[3] This could indicate some dynamic disorder as this would result in an increased quadrupolar interaction, with elongation of C–^{2}H bond due to the increased size of the electric field gradient (EFG) tensor. The other site, with increased C_Q of approximately 198 kHz is therefore likely to be a result of a deuteron located in a stronger hydrogen bond. This is consistent with previous observations of strongly located deuterons in wadsleyite, where with no motion and a strong hydrogen bond resulted in an increased quadrupolar interactions and reduced η_Q.[31]

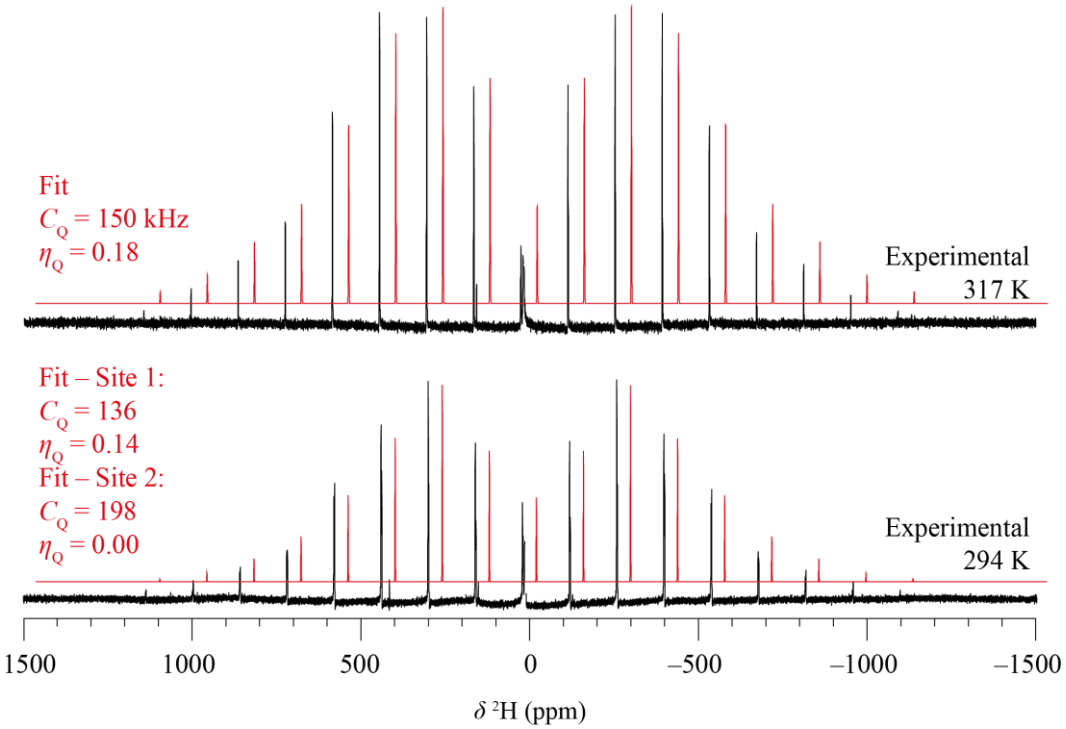

Figure 5.16 Experimental MAS ^{2}H NMR spectra (black) at the two extremes of the temperature range studied, along with fits to the spinning sideband manifold lineshape (red). The fits are offset by 25 ppm to aid visibility. Experimental details are as described in Figure 5.14.

5.7 Density Functional Theory

In attempting to gain insight into the structural changes accompanying phase transitions in P-CA, experimental data has shed some light on the nature of these transitions, however the use of DFT can supplement these investigations. As discussed in Chapter 3 and Chapter 4, a robust DFT methodology has been refined on organic anode materials. In this chapter, the same methodology is applied under the assumption that this method is appropriate as the structure of P-CA is also a supramolecular organic framework made up of small constituent molecules similar to organic anode materials. For the same reason, it is assumed that the same planewave energy cut off, E_{cut}, of 50 Ry and *k*-point spacing of 0.05 2π Å^{-1} used previously are appropriate for investigations of P-CA. It should be noted that the two modulated structures (MAMPUM06 and MAMPUM07) are not studied here as this modulation cannot be described within a unit cell

input for planewave DFT calculations. This refined methodology employs the rPBE XC functional, and the Grimme-D3 dispersion correction scheme. The command '`symmetry_generate`' has been applied, which locks the symmetry to the input space group to prevent any changes to space group and symmetry during the electronic minimisation.

Following the completion of the electronic minimisation calculation, an initial assessment of the unit cell parameters was carried out and is shown in Figure 5.17. Small reductions in total unit cell volume were expected as observed in the organic anode materials studied in the previous chapters, on account of DFT calculations carried out at 0 K, while the crystallographic data was collected at the finite temperatures listed in Table 5.2. However, for five of the six structures, small unit cell volume expansions were observed. The magnitude of volume change is less than 3% for all structures, which is roughly consistent with the magnitude of volume changes observed in Chapter 3 with organic anode materials. Furthermore, in all structures the *a* dimension decreases, whereas in all but one case, the *b* and *c* dimensions increase. This relates to a reduction along the dimension of the hydrogen bond (*a*), and elongation along the dimension of molecular stacking (*b*) and in the dimension perpendicular to the hydrogen bond (*c*). Elongation of the *b* dimension could indicate a rotation of the molecules about the *c* axis.

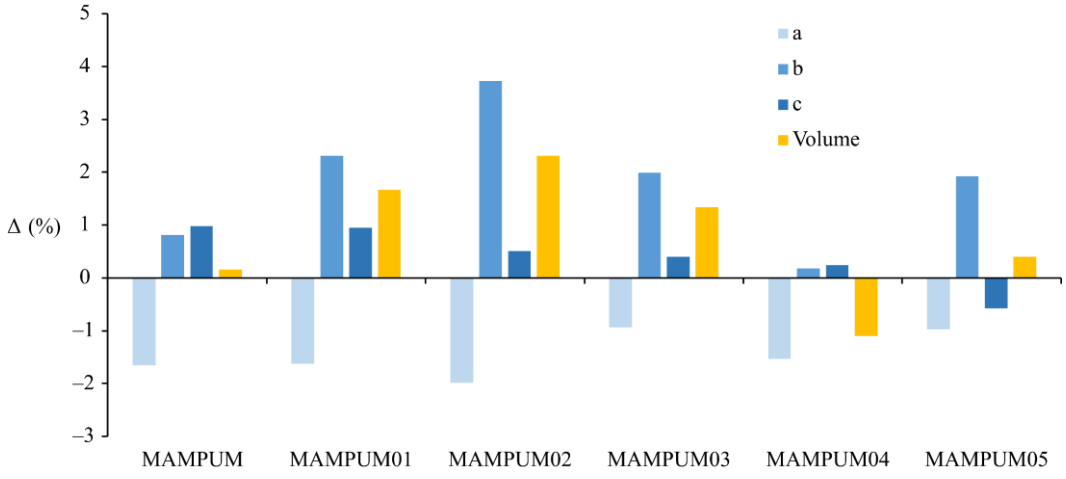

Figure 5.17 Bar chart showing the change in unit cell parameters (*a*, *b* and *c*) following DFT geometry optimisation for the deposited P-CA structures MAMPUM to MAMPUM05, as well as the change in total unit cell volume.

Prior to DFT geometry optimisation, each deposited structure of P-CA has a unique set of hydrogen bond geometries, however, inspection of these environments following DFT geometry optimisation indicates that optimised structural geometries fall into two distinct groups, and are illustrated in Figure 5.18. The first group (MAMPUM, MAMPUM01, MAMPUM04, MAMPUM02) features a proton associated with the oxygen atom of the CA molecule hydrogen bonded to the nitrogen atom of the phenazine molecule. In MAMPUM02, this bonding arrangement is retained, but due to the reduced symmetry the precise bond lengths

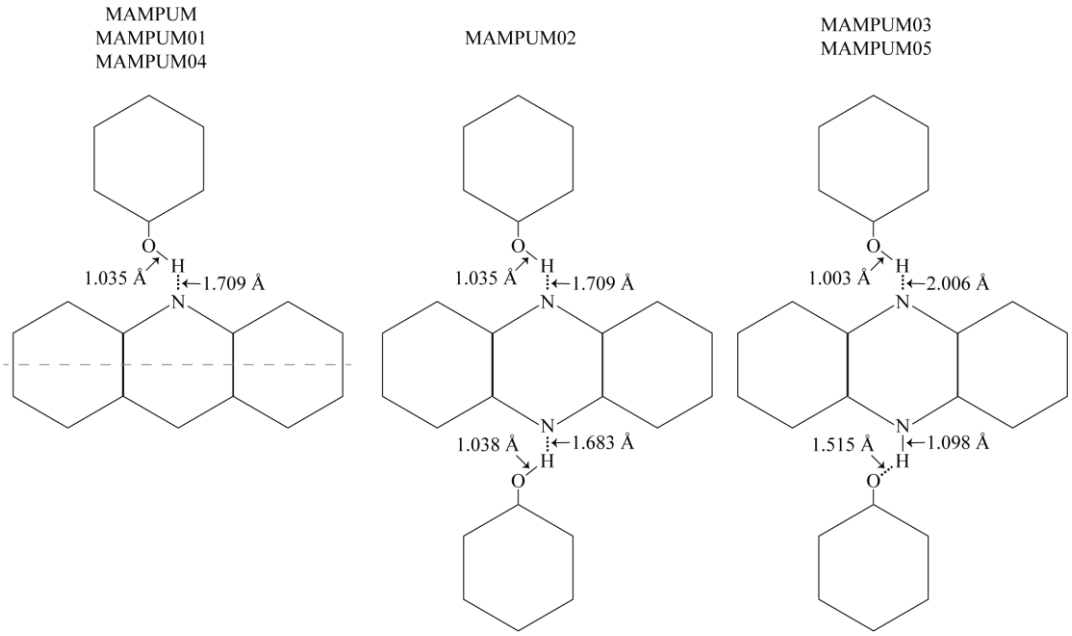

Figure 5.18 Simplified illustrations of the hydrogen bonding geometries in DFT optimised structures of P-CA. Grey dashed line signifies a plane of reflection. Variation in bond lengths between structures combined here are reported in the text.

are slightly altered on the other side of the phenazine molecule with differences of less than 0.03 Å observed. The second group consists of MAMPUM03 and MAMPUM05, where one hydrogen bond is retained in a significantly different geometry in addition to a proton transferred hydrogen bond with the proton associated with the nitrogen atom of the phenazine. This group also account for the structures with the lowest single point energies (SPE) of the structure set, approximately 0.1 eV lower in energy than those structures in the first group. Despite the observation of two distinct geometries being found by DFT geometry optimisation, no similar pattern is observed in either the optimised unit cell parameters or the SPE of the optimised structure set. Thus, DFT calculations seemingly find distinct energy minima for the hydrogen bond geometries only and not all properties of the structures. A complete tabulation of these hydrogen bond geometries can be found in Table 5.4, but a detailed discussion is given below.

Table 5.4 Tabulation of SPE and hydrogen bond geometries of all deposited P-CA structures from the literature following DFT geometry optimisation. In structures with $P2_1/n$ space group, only one environment is given as all hydrogen bonds are equivalent.

CCDC Code	SPE *vs.* MAMPUM05 (eV)	O–H (Å)	N···H (Å)	O–H (Å)	N···H (Å)
MAMPUM	+ 0.1363	1.034	1.708	–	–
MAMPUM01	+ 0.1517	1.034	1.710	–	–
MAMPUM02	+ 0.1381	1.034	1.715	1.038	1.683
MAMPUM03	+ 0.0053	1.003	2.003	1.517	1.098
MAMPUM04	+ 0.1260	1.036	1.703	–	–
MAMPUM05	Lowest energy	1.003	2.009	1.514	1.098

The first geometry has a hydrogen bond with an O–H distance of approximately 1.035 Å (± 0.001 Å) and a N···H distance of approximately 1.709 Å (± 0.006 Å) and is observed in all three PE-I structures (MAMPUM, MAMPUM01, MAMPUM04) and in one FE-I structure (MAMPUM02). Due to the reduced symmetry of MAMPUM02, another very similar hydrogen bond geometry exists; it features an O–H distance of 1.038 Å and a slightly shorter N···H distance of 1.683 Å. The distinctly different second geometry is observed in the other FE-I structure MAMPUM05, and in the FE-II structure MAMPUM03. In these structures, half of the hydrogen bonds, the O–H has an approximate distance of 1.003 Å (± 0.001 Å), with a N···H distance of approximately 2.006 Å (± 0.003 Å). The other half of the hydrogen bonds feature a lengthened O···H distance of approximately 1.515 Å (± 0.002 Å) and a shortened N–H distance of 1.098 Å (± 0.000 Å). Given the length of a covalent N–H bond (≈ 1.1 Å), and a covalent O–H bond (≈ 0.97 Å), this is consistent with proton transfer. Despite being collected at a temperature within the FE-I range, MAMPUM05 optimises to a geometry consistent with the FE-II phase, however it is noted that DFT calculations are completed at 0 K conditions which could also impact the determination of the two stable hydrogen bond geometries. Furthermore, Kumai *et al*. observed an increased thermal ellipsoid along with a slight increase in bond lengths in FE-I structure MAMPUM05,[3] which is not observed herein likely due to the 0 K conditions of the DFT calculations such that the FE-I phase is not captured. Unsurprisingly, no modulation of the hydrogen bond geometries, similar to that noted in the works by Noohinejad *et al*., is captured by the DFT calculations on account of the restriction of the calculations to a single unit cell.[4, 5]

In Figure 5.19, a correlation between the experimentally observed ^{13}C chemical shifts and the calculated chemical shielding for each of the three PE-I phase structures (MAMPUM,

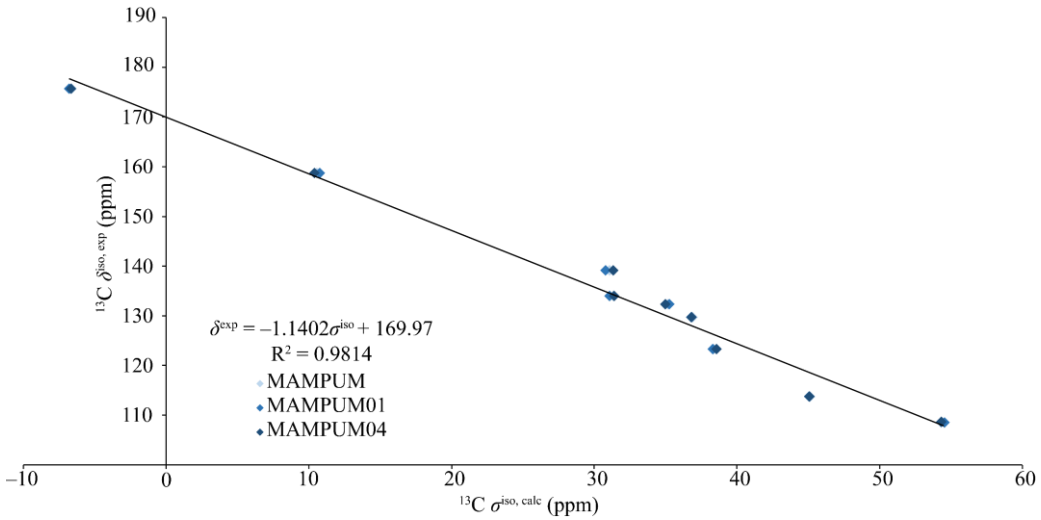

Figure 5.19 Correlation of experimental ^{13}C chemical shifts and DFT calculated chemical shielding of the three PE-I structures.

MAMPUM01 and MAMPUM04) shows a good agreement. Furthermore, the chart highlights the similarity between the three structures despite the energetic differences. Significant scatter is observed for the carbons between 150 ppm and 125 ppm, all of which are carbons in the phenazine molecule, whereas the carbons from the CA molecule are found much closer to the line of best fit. Simulated ^{13}C CPMAS spectra for the optimised P-CA structures generated with SIMPSON and visualised in GSim are shown in Figure 5.20, where some spectra with strong similarities are omitted for brevity. Since the structures optimise to one of two geometries, it is unsurprising therefore that two sets of chemical shifts are observed, one for each of the two unique optimised geometries. Simulated spectra from the three high temperature structures feature significant resemblance to the experimental spectra, with a total of nine resonances, consisting of five in the aromatic region, two at higher chemical shift and a further two at lower chemical shift. The spectrum of MAMPUM is shown, with MAMPUM01 and MAMPUM04 omitted on account of their similarity. MAMPUM02 shares a resemblance with the spectra of the three structures collected in the PE-I temperature range, however here every resonance is split into two resonances which is consistent with the reduction in symmetry of the FE-I phase. Despite this, the resonances all appear at approximately the same chemical shifts as those in the spectra of the structures collected at high temperature, further evidencing the similar geometry found by DFT calculation. Similarly, the MAMPUM05 spectrum is omitted, but a simulated spectrum of MAMPUM03 features distinctly different chemical shifts than all the other structures. Firstly, the high frequency carbonyl and C−OH resonances are split over a wider

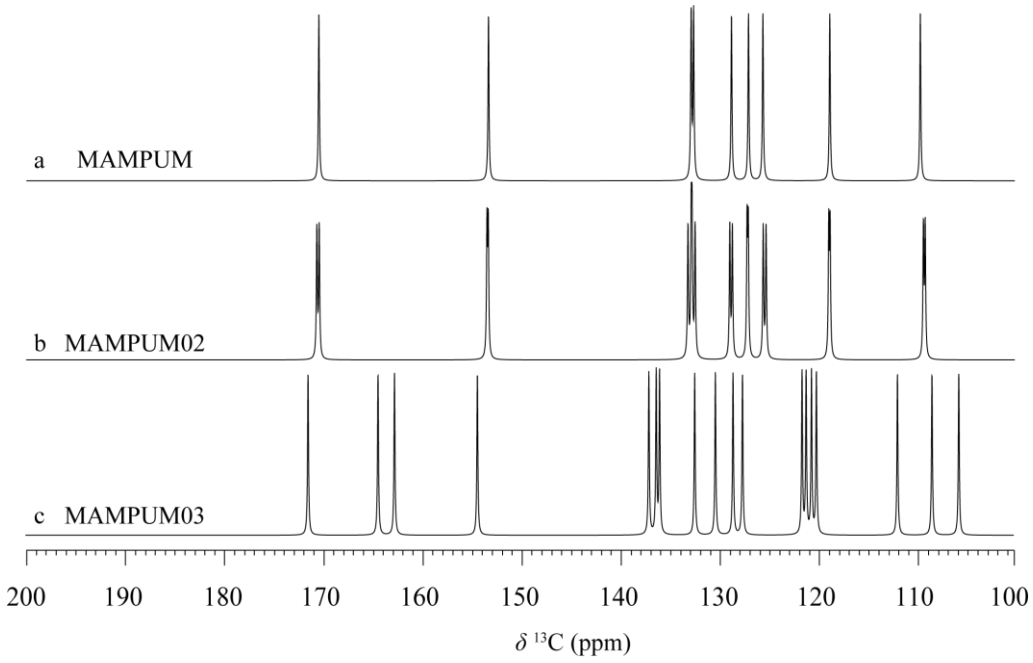

Figure 5.20 Simulated ^{13}C CPMAS spectra of three of the P-CA structures following DFT geometry optimisation. Spectra of MAMPUM01 and MAMPUM04 are omitted for brevity as they are almost identical to MAMPUM. Likewise, MAMPUM05 is almost identical to MAMPUM03 and is also omitted. Spectra generated using SIMPSON and visualised in GSim.

frequency range (approximately 8 ppm, *c.f.* approximately 0.5 ppm in PE-I temperature range structures). Secondly, the resonances at low chemical shift from the chloro-substituted carbon are predicted to split into several resonances (up to seven) covering a wider frequency range. No evidence of either of these changes have yet been observed experimentally, suggesting that no proton transfer is observed in phases that exist within the accessible temperature range of routine NMR experiments.

Experimental ^{1}H MAS NMR spectra show three broad proton resonances are observed at 12.8 ppm, 7.4 ppm and 4.2 ppm. At low temperatures, the C−OH resonance at 12.8 ppm splits into two broad resonances separated by approximately 2 ppm. In DFT calculations of the structure collected in the PE-I temperature range, the chemical shift is slightly overestimated at approximately 14.3 ppm. Phenazine protons are predicted at between 6 ppm and 7.5 ppm, giving good agreement to the 7.4 ppm resonance but overestimating the 4.2 ppm resonance. The splitting of the CA C−OH resonance is predicted in calculations of low temperature structures (MAMPUM03 and MAMPUM05) with the two resonances appearing approximately 8 ppm apart, at 10.2 ppm and 18.7 ppm in both structures, significantly wider than the 2 ppm splitting observed experimentally. Furthermore, in the low temperature structures, eight proton resonances from the phenazine molecule are predicted within the chemical shift range of 6.2 ppm and 8.1 ppm. Experimentally, a broad resonance is observed in this chemical shift range which could result from the numerous crystallographic proton environments of the phenazine molecule. In this experiment, dipolar broadening limits the possible resolution such that it would not be possible to distinguish between similar environments. These disagreements between experiment and calculation could result partially from the use of one unit cell to describe FE-II structures instead of the commensurately modulated twofold superstructure described by previous works.

Finally, considering the ^{2}H NMR spectra, significant variation is observed in the agreement of experimental quadrupolar parameters extracted from experimental spectra with calculated quadrupolar parameters for each of the optimised structures. Despite the variable agreement, the predicted values mirror experiment in that a moderate C_Q site is observed at high temperature, while two sites are observed at low temperature, one with high C_Q and one with low C_Q. Tabulation of the calculated quadrupolar parameters is given below in Table 5.5. Experimentally, a C_Q of 150 kHz is observed at 317 K, which is slightly higher than the calculated quadrupolar parameters for the PE-I phase structures of between 128 kHz and 135 kHz. Additionally, calculations slightly underestimate η_Q values to approximately 0.02 to 0.03, while experimentally an η_Q value of approximately 0.1 is observed. However, the agreement for lower temperature phases is poorer, this could be partially due to the use of a single unit cell to describe low temperature phases for DFT calculations here, where true

structures have previously been shown to be commensurately modulated twofold superstructures. Experimentally, two sites are observed with C_Q of approximately 136 kHz and 198 kHz. The low C_Q site with C_Q = 83 kHz has poor agreement to experiment, and a high C_Q site with C_Q = 199 kHz has very good agreement. Therefore, DFT underestimates the C_Q of the low C_Q site by approximately 50 kHz, while accurately predicting the C_Q of the high C_Q site. The low C_Q site in the FE-II structures is assigned to the higher chemical shift (MAMPUM03 Site 1; C_Q = 83 kHz, δ = 18.7 ppm), and is the result of the proton of the hydroxyl group where the proton is comparatively more deshielded due to the proximity to an oxygen atom. While the high C_Q site (C_Q = 199 kHz, δ = 10.2 ppm) is assigned to the charge transfer proton located 1.1 Å from the phenazine nitrogen atom. Thus, good agreement of the high C_Q site is consistent with a partial proton transfer in the experimental low temperature phases, despite other methods suggesting no such transfer occurs.

Table 5.5 Tabulation of proton quadrupolar parameters predicted by DFT calculations. In the structures with multiple sites, the sites are organised in decreasing chemical shift order, such that Site 1 has the higher chemical shift.

CCDC Code	Site	$\lvert C_Q \rvert$ / kHz	η_Q
MAMPUM	1	132	0.03
MAMPUM01	1	134	0.03
MAMPUM02	1	135	0.03
	2	128	0.02
MAMPUM03	1	83	0.28
	2	199	0.05
MAMPUM04	1	132	0.03
MAMPUM05	1	83	0.28
	2	199	0.05

5.7.1 Investigation of Supercell Structure

The structure of the FE-II phase is still not fully understood, with previous diffraction studies suggesting a commensurately modulated twofold superstructure. Thus, the structure cannot be described within the unit cell of the higher temperature phases, but rather a supercell with commensurate modulation of the proton positions. In attempt to study this phase, DFT calculations utilising supercell structures were completed. A range of candidate structures were created in the CrystalMaker software using the 1 x 1 x 1 MAMPUM01 structure as a starting point and by doubling the *a*-dimension, as shown in Figure 5.21a-c. It is helpful to consider a 1 x 1 x 1 unit cell as comprised of two proton transfer molecular pairs with one phenazine and CA in each pair and thus a 2 x 1 x 1 supercell as comprised of four molecular pairs. With the appropriate number of unit cells redefined as a single larger unit cell, the charge transfer proton

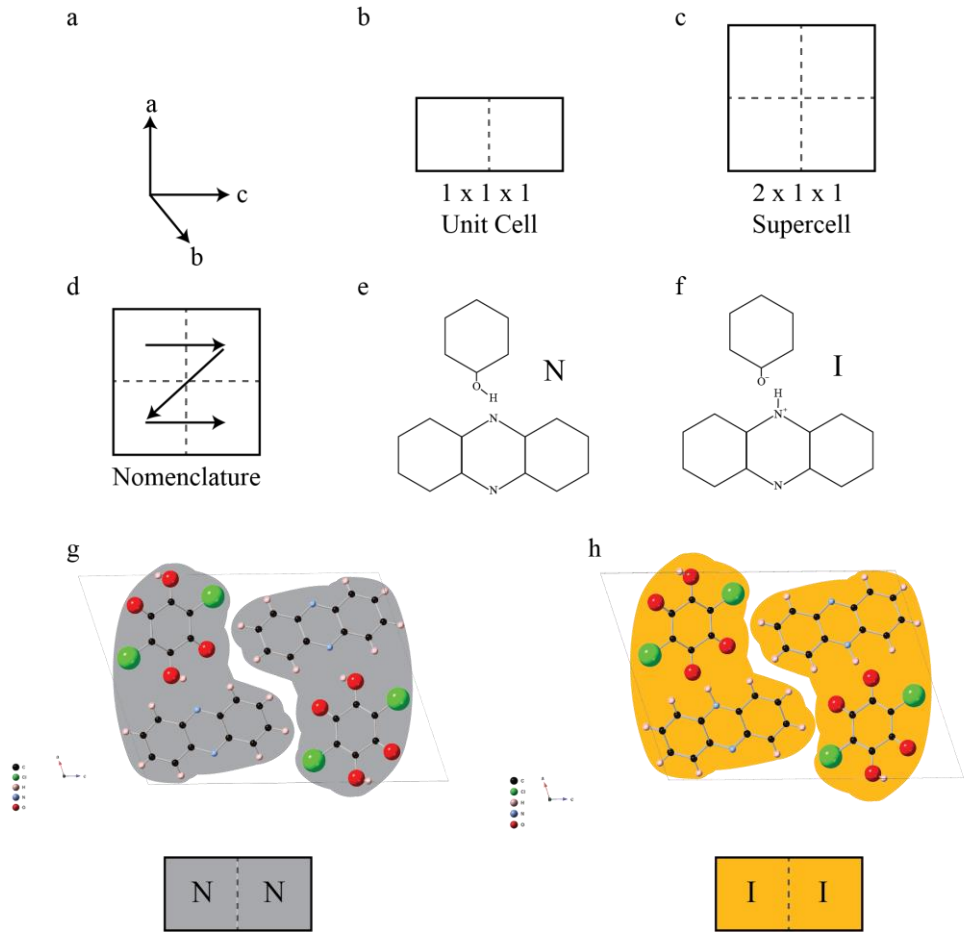

Figure 5.21 Schematic visualisation of the treatment of unit cells and nomenclature of neutral and ionic pairs. (a) axes; (b) a 1 x 1 x 1 unit cell with the unit cells defined by black solid lines and grey dashed line representing imaginary lines between molecular pairs; (c) a 2 x 1 x 1 unit cell; (d) schematic of the nomenclature used herein to refer to supercell structures; (e-f) chemical structure of neutral pair (N) and ionic pair (I); (g-h) unit cells with molecular pairs highlighted to show two pairs in one 1 x 1 x 1 unit cell, grey = neutral, orange = ionic.

was manually moved from the CA to the phenazine and located in plane with the other protons of the phenazine molecule and at the distance of a N−H covalent bond (1.1 Å). To keep consistency with the frequency of proton transfer reported in the previous work by Noohinejad *et al.*, a total of two proton transfers are required per supercell.[4, 5] This results in ionic pairs (featuring transfer of a single proton, resulting in one CA^- ion and one $phenazine^+$ ion) and neutral pairs (with no proton transfer taking place). The respective orientation of these bonding pairs was systematically varied to include all potential hydrogen bonding patterns. A total of four structures were created and are shown in Figure 5.22. Two structures contain the four molecular pairs entirely within the supercell (labelled according to their bonding pair arrangement ININ and INNI), while the remaining two feature a molecular pair overlapping with the unit cell boundary to create a staggered arrangement of bonding pairs (labelled ININI and INNIN). Notably, these 2 x 1 x 1 structures feature modulation of the hydrogen bonding in one or two dimensions, however it is possible that the modulation could occur in all three dimensions, and as such 2 x 2 x 1 supercells were created to assess if modulation in a third

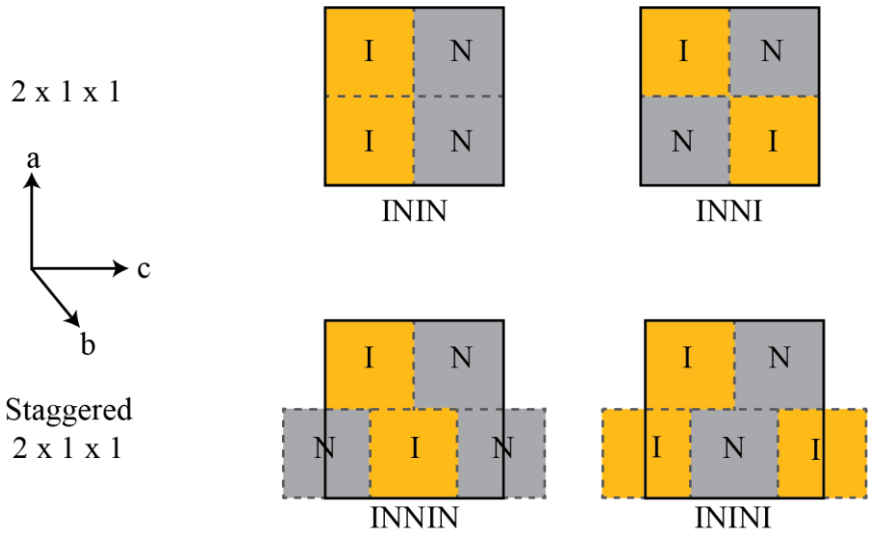

Figure 5.22 Simplified visualisation of the arrangement of ionic and neutral pairs in the manually created FE-II supercell structures. I = Ionic pair (orange background); N = Neutral pair (grey background). Unit cells are defined by black solid lines, grey dashed lines represent imaginary lines between molecular pairs.

dimension has an impact on predicted NMR parameters. Figure 5.23 shows the three 2 x 2 x 1 supercells that are required to describe all potential modulations of the proton transfer and are derived from the previously mentioned 2 x 1 x 1 supercell structures through a doubling of the *b*-dimension. To best visualise these structures, it is helpful to ignore the 'front' four bonding pairs and focus on the 'rear' four bonding pairs. The first and simplest structure is derived from the INNI structure and features periodic alternation of the neutral (N) and ionic (I) pairs in all three dimensions in a 3D checkerboard pattern such that the 'rear' four bonding pairs would be NIIN (labelled INNI-NIIN). The remaining two structures are derived from the ININ structure, where the 'rear' bonding pairs feature the remaining geometries and are NIIN (labelled

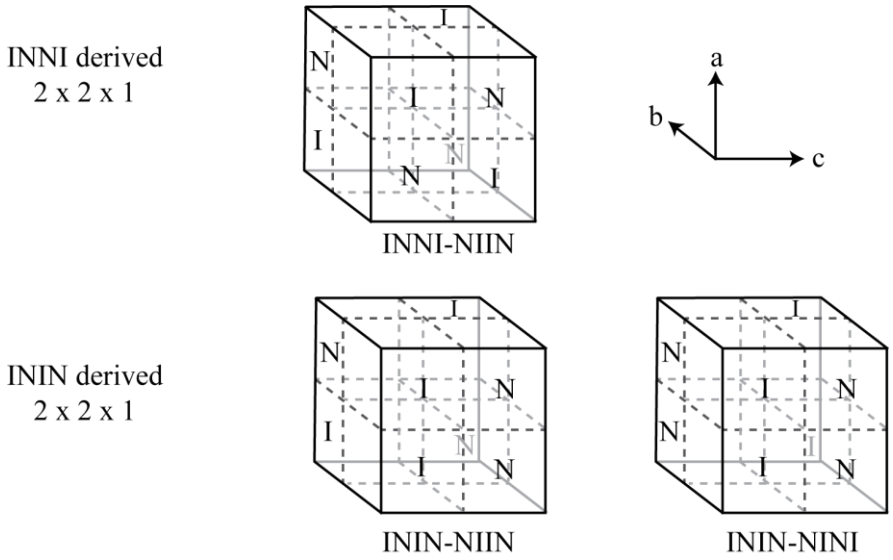

Figure 5.23 Simplified visualisation of the arrangement of ionic and neutral pairs in the manually created 2 x 2 x 1 FE-II supercell structures. I = Ionic pair; N = Neutral pair. Unit cells are defined by black solid lines, grey dashed lines represent imaginary lines between molecular pairs.

ININ-NIIN) and NINI (labelled ININ-NINI) respectively. The macrostructure of these structures can be considered as channels of alike bonding pairs. In the first structure (INNI-NIIN) no channels are present, and there exists a 3D checkerboard arrangement of bonding pairs. Whereas in the other two structures, these channels are present; ININ-NIIN features interlocking channels in both *a*- and *b*-dimensions forming a grid like macrostructure, while ININ-NINI features channels in only the *a*-dimension, such that there is a 2D checkerboard in the *bc*-plane but channels in the *ab*- and *ac*-planes. More geometries are possible here with different 'rear' bonding pair arrangements, but these result in structures that are equivalent by translation to those already described. Furthermore, alternative geometries for both 2 x 1 x 1 and 2 x 2 x 1 structures are possible with consideration of the relative orientation of the molecular units to the unit cells, however for simplicity here these are ignored.

All seven of the supercell structures were subjected to a geometry optimisation calculation as using the previously discussed refined methodology. Firstly, the two staggered 2 x 1 x 1 supercell structures (ININI and INNIN) failed to reach an energy minima within 200 self-consistent field (SCF) cycles and as such are deemed to be sufficiently unfavourable structures and are henceforth ignored. Both of the non-staggered 2 x 1 x 1 structures (INNI and ININ) optimised to an entirely ionic structure (IIII), where each hydrogen bonding molecular pair features one proton transfer to a fraction of ½ of all hydrogen bonds as was reported by Gotoh *et al*., and in contradiction to the ¼ of all hydrogen bonds reported previously by Noohinejad *et al*.[2, 4, 5] This suggests that the commensurate modulation cannot easily be captured by DFT calculations. It is interesting then, that of the three 2 x 2 x 1 supercell structures, two structures optimised without change to the input hydrogen bond arrangements (INNI-NIIN and ININ-NINI). The remaining 2 x 2 x 1 structure, ININ-NIIN, optimised to a structure with more ionic pairs than the initial input structure, with six ionic pairs and two neutral pairs arranged as INII-NIII in the optimised structure. The geometry of the optimised 2 x 2 x 1 supercell structures is illustrated in Figure 5.24. This could indicate that with a sufficiently complex structure, DFT calculations can start to describe the commensurate modulation, but the previously described 2 x 1 x 1 supercell structure is seemingly too simple.

Inspection of SPE can give some information on the energetic favourability of the structures. Previously, the SPE of the 1 x 1 x 1 unit cells were given in Table 5.4. The calculated SPE of each of supercell structures is found to be comparable to the 1 x 1 x 1 structures, with a full tabulation below in Table 5.6. Notably, the two lowest energy supercell structures are the two non-staggered 2 x 1 x 1 supercell structures (INNI and ININ), which optimised to entirely ionic structures, and are comparable in SPE with the two 1 x 1 x 1 structures with proton transferred geometries (MAMPUM03 and MAMPUM05). Furthermore, the two 2 x 2 x 1 supercell structures that did not reorganise the hydrogen bond geometries (ININ-NIIN and

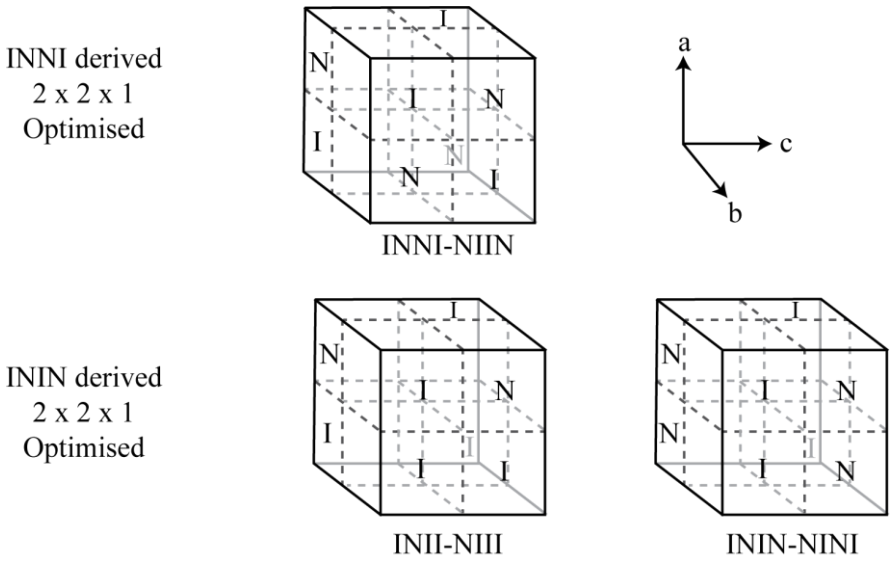

Figure 5.24 Simplified visualisation of the arrangement of ionic and neutral pairs in the optimised 2 x 2 x 1 FE-II supercell structures. I = Ionic pair; N = Neutral pair. Unit cells are defined by black solid lines, grey dashed lines represent imaginary lines between molecular pairs.

Table 5.6 Ranked tabulation of SPE of all deposited P-CA structures from the literature and modified supercell structures following DFT geometry optimisation.

Structure	SPE *vs.* ININ (eV)
ININ	Lowest energy
MAMPUM05	+ 0.0018
INNI	+ 0.0030
MAMPUM03	+ 0.0072
ININ-NIIN	+ 0.0173
INNI-NIIN	+ 0.0283
ININ-NINI	+ 0.0285
MAMPUM04	+ 0.1278
MAMPUM	+ 0.1381
MAMPUM02	+ 0.1399
MAMPUM01	+ 0.1535

INNI-NIIN) have lower SPE than the one 2 x 2 x 1 supercell structure that did rearrange hydrogen bond geometry (ININ-NINI). These three supercell structures have a significantly higher SPE than the previously mentioned ionic supercell structures, but significantly lower SPE than the remaining 1 x 1 x 1 high temperature structures that do not feature proton transfer in the optimised structures (MAMPUM04, MAMPUM, MAMPUM02 and MAMPUM01).

Comparisons can be made to the low temperature NMR spectrum previously shown in Figure 5.10, however it is difficult to draw strong conclusions due to the significant broadening observed. Nevertheless, comparison can give an overview of the approximate agreement of the experimental spectrum and simulated data. Comparison is also made to the high temperature NMR data, where good agreements are not expected due to the expected structural differences of the low temperature FE-II phase. Simulated ^{13}C spectra are shown in Figure 5.25 for each of the five supercell structures. Figure 5.25a-b show simulated spectra of the two 2 x 1 x 1

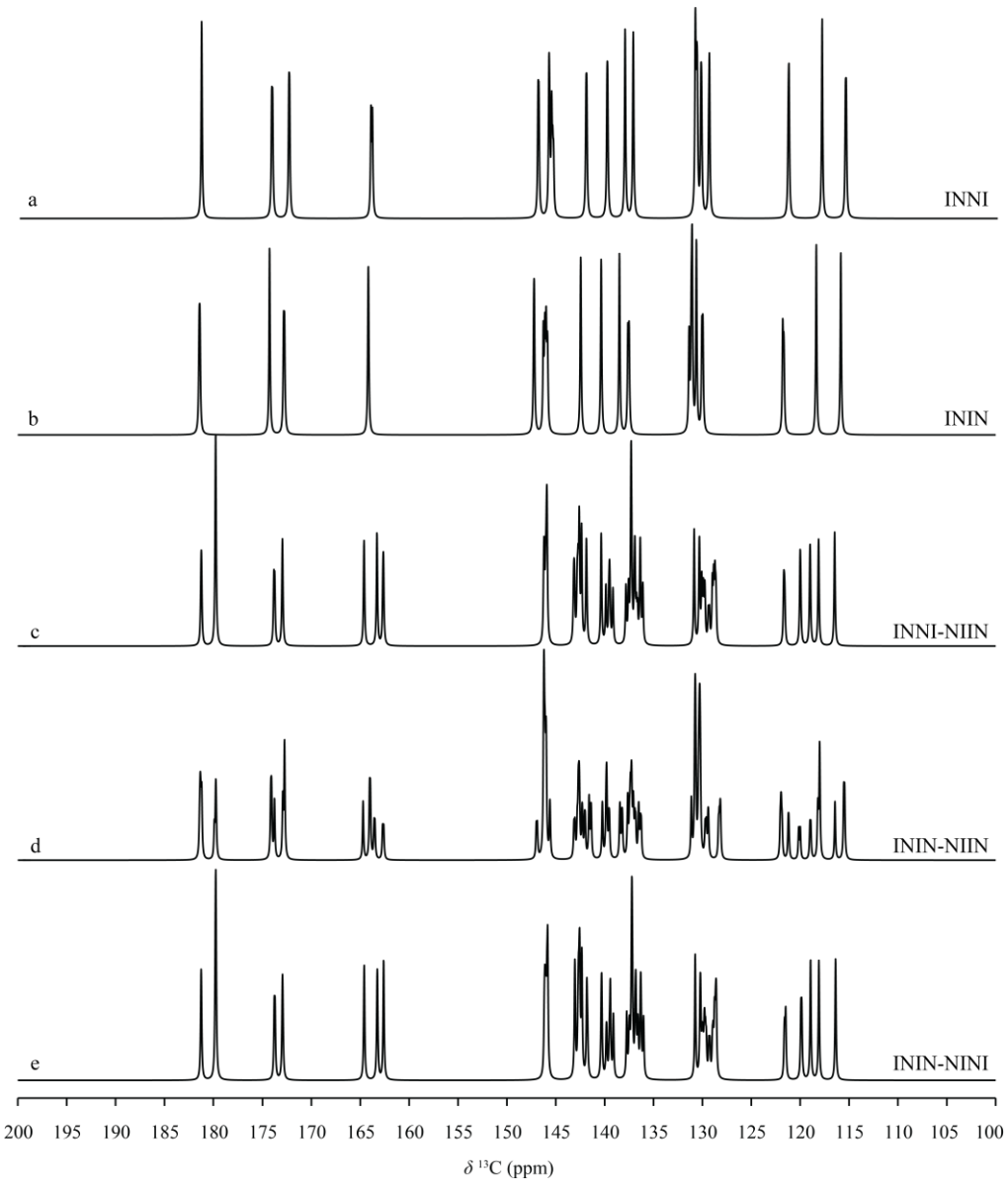

Figure 5.25 Simulated ^{13}C CPMAS spectra of the five supercell structures following DFT geometry optimisation. Spectra generated using SIMPSON and visualised in GSim.

structures (INNI and ININ) which optimise to entirely ionic structures. 72 crystallographic carbon sites are observed, double that of the 1 x 1 x 1 unit cell structures, which is a direct consequence of the formation of the supercell with space group P1. The two simulated spectra share a significant resemblance in the quantity and position of resonances, as would be expected as the two optimised structures are very similar and entirely ionic. Closer inspection of the two optimised structures reveals differences in bond lengths of < 0.01 Å, and differences in bond angles of < 0.01°. Compared to the low temperature experimental spectrum (Figure 5.10), the resonances above 165 ppm are not observed experimentally, where if present would be expected in the same region as the intense spinning sidebands. Furthermore, no resonance is expected at approximately 160 ppm, where a broad but weak resonance is observed experimentally. The resonances below 150 ppm can be roughly grouped into four groups, which would be consistent

with the four broad resonances observed in the experimental spectrum, though the approximate position of these groups is not consistent. In the high temperature experiments, a broad agreement is observed to simulated data with simulations predicitng that four distinct resonances are observed at high frequency but are slightly overestimated. Experimentally, these four resonances appear between 155 ppm and 180 ppm, while calculated chemical shifts are between 182 ppm and 164 ppm. Furthermore, a region with a significantly higher density of information exists in both experimental and simulated spectra. This region relating to the aromatic carbon atoms covers a wider frequency range in the simulated spectra, where resonances are observed between 150 ppm and 125 ppm, while experimentally these are limited to between 141 ppm and 120 ppm. Each apparent resonance in the simulated spectra is made up of multiple resonances with only tiny variations in chemical shift, *e.g*., the resonances at high frequency are made up of four different resonances, each with < 0.01 ppm difference between them. This is a partial cause of the highly convoluted spectra which arises due to the similarity of many of the carbon sites in these optimised structures. Despite the broad similarities, the overall agreement to high temperature NMR spectra is rather poor which is likely a combination of the DFT geometry optimisation giving structures with an entirely ionic structure and the difference in the phase studied by DFT (FE-II) and the VT NMR experiments (FE-I).

The 2 x 2 x 1 structures have 144 crystallographic carbon sites from the doubling of the 2 x 1 x 1 supercell (72 carbons sites). Similarly, each resonance in the simulated spectra is convoluted by eight distinct resonances within < 0.01 ppm. Two of the 2 x 2 x 1 supercell simulated spectra feature a significant resemblance to each other, these of INNI-NIIN (optimised to INNI-NIIN) and ININ-NINI (optimised to ININ-NINI). The spectrum of the other structure ININ-NIIN (optimised to INII-NIII) features a slight variation, most notably in the resonances at 148 ppm, 130 ppm and the region of resonances centred at 120 ppm. However, the agreement of all three spectra to experiment is particularly poor. Notably, the resonances at high frequency are the most obvious in their distinction to experiment. Experimentally, the resonances of the carbonyl and C−OH carbons split at low temperatures and are observed as two doublets. Here, however, many more resonances are observed. Ignoring the sub-ppm scale variations, resulting from the low symmetry of the structures, these doublets are themselves split again. This results in four doublets, with two of the doublets positioned very close together at approximately 162 ppm and 163 ppm. Further differences are apparent in the region of resonances at lower frequency, with many more resonances present across a wider frequency range. Thus, these 2 x 2 x 1 supercell structures, in similarity to the 2 x 1 x 1 structures, may describe the FE-II phase well, but as conventional VT NMR experiments are unable to study the FE-II phase this remains unclear. However, increasingly complex superstructures could lead to

broadening of NMR resonances such as those seen in the ^{13}C CPMAS NMR spectrum collected at 97 K (Figure 5.10), though agreement remains poor.

5.8 Conclusions

In this chapter, the phase transitions of P-CA have been investigated using Solid-state NMR spectroscopy and DFT calculations. VT NMR experiments were used to probe structure at various temperatures around the first phase transition at $T_{C,I}$ from PE-I to FE-I. Despite the inherent limitations of the VT NMR method, such as temperature inhomogeneity in the rotor and temperature sensor error, the phase transition in both P-CA and d-P-CA has been observed. ^{13}C and ^{1}H spectra show a gradual phase transition in P-CA as temperature reduces from 270 K to 250 K, agreeing with previous literature suggesting $T_{C,I}$ = 253 K. However, this highlights the possibility that the phase transition is not as simple as an instantaneous change in structure, but could show a more gradual and diffuse phase transition. ^{2}H spectra corroborate this finding with a gradual phase change between 317 K and 294 K, where the deuteration effect raises $T_{C,I}$ to 304 K. The change in structural symmetry from $P2_1/n$ to $P2_1$ as a result of the phase change is herein supported by observations of doubling of resonances below phase transitions, indicating a doubling in the number of crystallographically distinct atomic sites. DFT calculations have been used to accurately predict ^{13}C NMR chemical shifts for the PE-I phase. Furthermore, the agreement of experimental ^{2}H quadrupolar parameters with those calculated by DFT is shown to be good. This confirms that, should NMR parameters be calculated from an adequate structural model, comparison to experimentally observed parameters should be expected to give a very good agreement. The DFT geometry optimisations carried out herein to find a suitable FE-II structural model find two energetically favourable structures, of which neither give good agreement to experimental NMR spectra of the FE-I phase. One of the energetically favourable structures agrees with experimental observations for the PE-I phase, while the other produces a structure partially in agreement with findings in previous literature of partial proton displacement to the phenazine unit of P-CA at low temperature. It is worth noting that DFT calculations are carried out at 0 K and as such this other structure that is in partial agreement could share similarity with the FE-II phase. This FE-II phase has not been studied herein with VT NMR, as the phase transition temperature of FE-I to FE-II is too low to be reachable with conventional techniques ($T_{C,II}$ < 187 K). However, a spectrum collected at 97 K at the DNP MAS NMR Facility shows significantly broadened resonances. Supercell structures were created in attempt to mimic the commensurately modulated two-fold superstructure of the FE-II phase previously noted in the literature. Five supercell structures were required to describe all possible commensurate modulations of proton transfer. The simplest structures where the input modulation remained after DFT geometry optimisation were 2 x 2 x 1 supercells. Comparison to experiment gives poor agreement, with calculated NMR parameters indicating a significant difference should be expected to experimental spectra of the FE-I phase.

5.9 References

1. S. Horiuchi, R. Kumai and Y. Tokura, *J Am Chem Soc*, 2005, **127**, 5010-5011.
2. K. Gotoh, T. Asaji and H. Ishida, *Acta Crystallogr C*, 2007, **63**, o17-20.
3. R. Kumai, S. Horiuchi, H. Sagayama, T.-h. Arima, M. Watanabe, Y. Noda and Y. Tokura, *J Am Chem Soc*, 2007, **129**, 12920-12921.
4. L. Noohinejad, S. Mondal, S. I. Ali, S. Dey, S. van Smaalen and A. Schonleber, *Acta Crystallogr B Struct Sci Cryst Eng Mater*, 2015, **71**, 228-234.
5. L. Noohinejad, S. Mondal, A. Wölfel, S. I. Ali, A. Schönleber and S. van Smaalen, *Journal of Chemical Crystallography*, 2014, **44**, 387-393.
6. S. Horiuchi and Y. Tokura, *Nature Mater.*, 2008, **7**, 357-366.
7. T. Furukawa, *Phase Transitions*, 1989, **18**, 143-211.
8. J. Sworakowski, *Ferroelectrics*, 1992, **128**, 295-306.
9. K. Roleder, I. Jankowska-Sumara, G. E. Kugel, M. Maglione, M. D. Fontana and J. Dec, *Phase Transitions*, 1999, **71**, 287-306.
10. M. Maglione, R. Bohmer, A. Loidl and U. T. Hochli, *Phys Rev B Condens Matter*, 1989, **40**, 11441-11444.
11. S. Koval, J. Kohanoff, J. Lasave, G. Colizzi and R. L. Migoni, *Physical Review B*, 2005, **71**.
12. Y. Tokura, S. Koshihara, Y. Iwasa, H. Okamoto, T. Komatsu, T. Koda, N. Iwasawa and G. Saito, *Phys Rev Lett*, 1989, **63**, 2405-2408.
13. H. Okamoto, T. Mitani, Y. Tokura, S. Koshihara, T. Komatsu, Y. Iwasa, T. Koda and G. Saito, *Phys Rev B Condens Matter*, 1991, **43**, 8224-8232.
14. M. Le Cointe, M. H. Lemee-Cailleau, H. Cailleau, B. Toudic, L. Toupet, G. Heger, F. Moussa, P. Schweiss, K. H. Kraft and N. Karl, *Phys Rev B Condens Matter*, 1995, **51**, 3374-3386.
15. S. Horiuchi, F. Ishii, R. Kumai, Y. Okimoto, H. Tachibana, N. Nagaosa and Y. Tokura, *Nat Mater*, 2005, **4**, 163-166.

16. K. Saito, M. Amano, Y. Yamamura, T. Tojo and T. Atake, *Journal of the Physical Society of Japan*, 2006, **75**.

17. R. Kumai, S. Horiuchi, J. Fujioka and Y. Tokura, *J Am Chem Soc*, 2012, **134**, 1036-1046.

18. A. Bielecki and D. P. Burum, *J Magn Reson*, 1995, **116**, 215-220.

19. A. E. Bennett, C. M. Rienstra and M. Auger, *J. Chem. Phys.*, 1995, **103**, 6951.

20. M. D. Segall, P. J. D. Lindan, M. J. Probert, C. J. Pickard, P. J. Hasnip, S. J. Clark and M. C. Payne, *J Phys Condens Matter*, 2002, **14**, 2717-2744.

21. C. J. Pickard and F. Mauri, *Physical Review B*, 2001, **63**.

22. J. P. Perdew, K. Burke and M. Ernzerhof, *Phys Rev Lett*, 1996, **77**, 3865-3868.

23. B. Hammer, L. B. Hansen and J. K. Nørskov, *Physical Review B*, 1999, **59**, 7413-7421.

24. J. R. Yates, C. J. Pickard and F. Mauri, *Physical Review B*, 2007, **76**.

25. S. Grimme, *J Comput Chem*, 2006, **27**, 1787-1799.

26. S. Grimme, J. Antony, S. Ehrlich and H. Krieg, *J Chem Phys*, 2010, **132**, 154104.

27. P. Pyykkö, *Molecular Physics*, 2008, **106**, 1965-1974.

28. R. K. Harris and A. C. Olivieri, *Progress in Nuclear Magnetic Resonance Spectroscopy*, 1992, **24**, 435-456.

29. S. E. Ashbrook, J. McManus, M. J. Thrippleton and S. Wimperis, *Progress in Nuclear Magnetic Resonance Spectroscopy*, 2009, **55**, 160-181.

30. J. M. Griffin, A. J. Miller, A. J. Berry, S. Wimperis and S. E. Ashbrook, *Phys Chem Chem Phys*, 2010, **12**, 2989-2998.

31. R. F. Moran, D. McKay, C. J. Pickard, A. J. Berry, J. M. Griffin and S. E. Ashbrook, *Phys Chem Chem Phys*, 2016, **18**, 10173-10181.

Appendix 5.1 – Simulated PXRD of P-CA

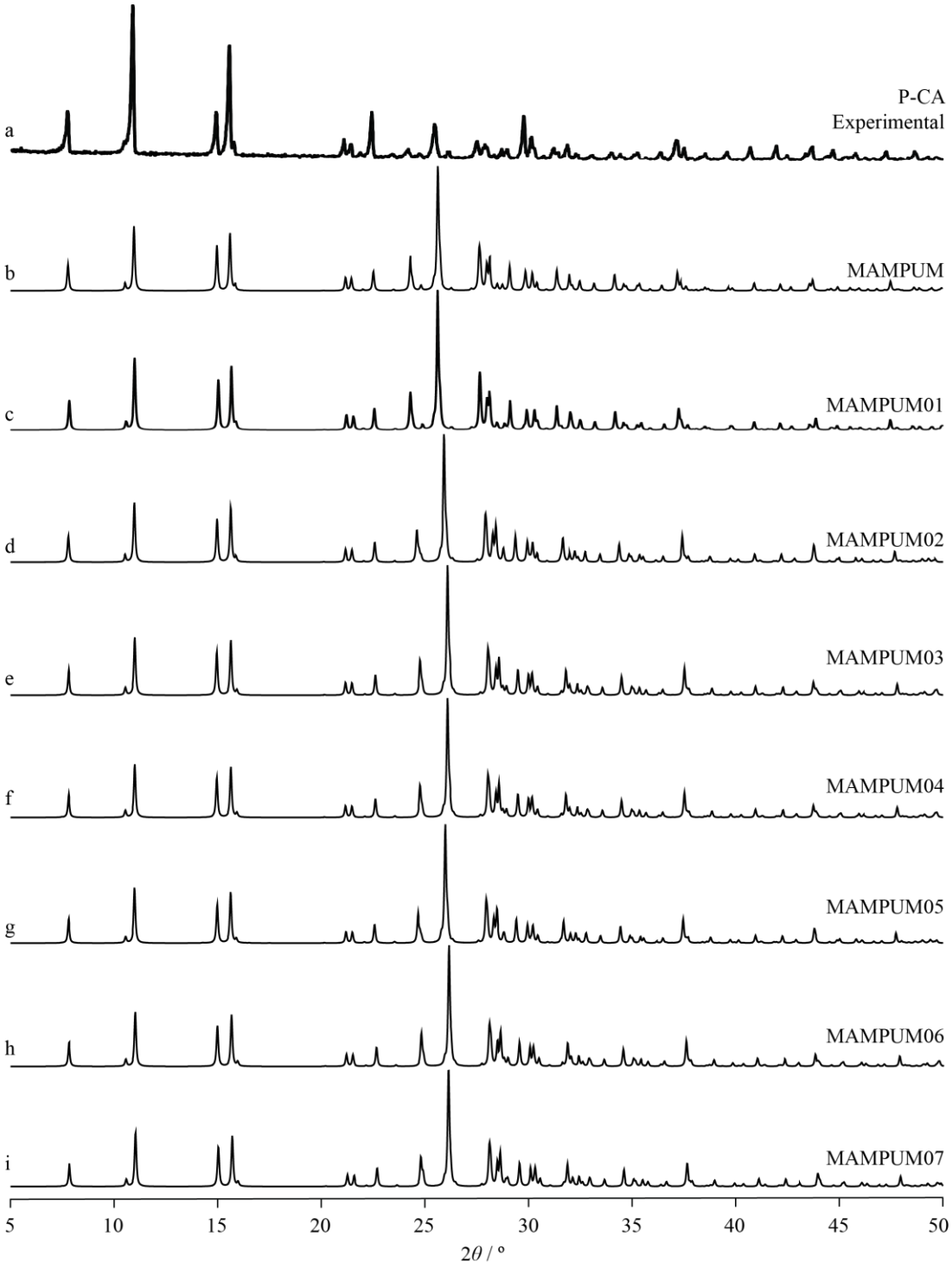

Figure 5.A26 Experimental PXRD pattern of P-CA with simulated patterns of all published crystal structures.

Chapter 6

Conclusions

The overall aim of this project was to gain a deeper understanding of organic functional materials that offer a sustainable alternative to currently used inorganic materials in some key energetic and technological applications. With a greater understanding of the structures of these materials, and the structural changes that occur during their respective functionalities, it will be possible to develop better materials with improved performance, sufficient for wider application. The industry standard inorganic materials are often associated with high energetic costs, environmental damage or ethical concerns. Therefore, in this thesis, two different classes of organic functional materials (organic anode materials and organic ferroelectric materials) have been studied. These materials undergo significant chemical and structural changes which are important for their respective applications. To study these changes, a combination of structural analysis methods have been used including multinuclear Solid-state nuclear magnetic resonance (NMR) spectroscopy, X-ray crystallography, density functional theory (DFT) calculations, electron paramagnetic resonance (EPR) spectroscopy and thermogravimetric analysis. A methodical optimisation of some of these methods, most notably DFT calculations, has been completed alongside the structural characterisations. Despite the wide array of methods used, further investigations using additional structural characterisation techniques, or more in depth theory levels would supplement the findings presented here.

In Chapter 3, a systematic structural study of model lithium- and sodium-ion battery organic anode materials by NMR crystallography has been presented. The use of diffraction structures enabled the calculation of ^{13}C, ^{7}Li and ^{23}Na NMR parameters using DFT. A variety of DFT electronic structure minimisation calculation methods were used to find the optimum methodology for organic anode materials. Comparison of the DFT calculated NMR parameters with experimentally observed parameters showed that while the optimisation method does not significantly affect the accuracy of the calculated NMR parameters, the optimisation of all atomic location is essential. Poor agreement was observed particularly for a methodology where only the proton positions were optimised, highlighting the sensitivity of the ^{23}Na quadrupolar interaction to the local chemical environment. Furthermore, weak non-bonding interactions between adjacent ligands are shown to be important in defining the structure, with large unit cell expansions observed without the use of a semi-empirical dispersion correction (SEDC) scheme.

A further investigation of the hydration behaviour of Na_2NDC and Na_2BPDC was conducted. A new hydrated phase of Na_2NDC is described for the first time and is shown to be a mixed phase with a majority dihydrate phase, with only anhydrous and tetrahydrate phases reported previously.

In Chapter 4, a chemical lithiation (CL) method was used to gain insights into the structural changes that take place in organic anode materials during battery cycling. Using Li_2BDC and Li_2NDC as case studies, the CL method is shown to successfully yield reduced phases, with the same structure as electrochemically reduced phases. The CL method is shown to produce greater yield when completed with a weakly coordinating solvent such as THF. More resonances are observed in ^{13}C NMR spectra of the reduced phases, signifying a significant change in structural symmetry, while ^{7}Li NMR experiments confirm significantly altered quadrupolar character. Structural prediction methods including *ab-initio* random structure searching (AIRSS) have been used to gain insight into these structures where there is a lack of previously reported structures from diffraction. From the candidate structures, NMR observables were calculated and compared with experimental observations giving overall agreements with some significant disparities such that no candidate structure appears to give perfect agreement. EPR spectra show isotropic resonances for the CL phases, suggesting that a level of disorder is present in the structures, with regions or domains carrying different degrees of lithiation. These results shed some light on the structure of reduced phases and add further evidence of the potential of NMR crystallography for structural elucidation of organic anode materials.

In Chapter 5, the structure and mechanism of a previously reported near room temperature organic ferroelectric material, phenazine chloranilic acid (PCA), was studied. Variable temperature (VT) NMR experiments characterised the changes in symmetry at various temperatures above and below the phase transition temperature, $T_{C,I}$. The limitations of the VT method prohibited efforts to explore a wider temperature range and characterise the structural changes that take place at lower temperature phase transitions, $T_{C,IC}$ and $T_{C,II}$. A low temperature spectrum (97 K) was collected at the Dynamic Nuclear Polarisation (DNP) NMR Facility which showed significant broadening. ^{13}C and ^{1}H spectra suggest the phase transition is not an instant sample-wide transition, instead appearing to be gradual, or that different regions of the sample transition at slightly different temperatures. However, in agreement with previous work, this gradual phase transition was observed through the reported phase transition temperature at 253 K. These findings are further evidenced in ^{2}H spectra, where accounting for the higher phase transition temperatures of deuterated structures, a gradual phase change was observed once more. NMR spectra herein further support the structural symmetry change from $P2_1/n$ in PE-I phase to $P2_1$ in FE-I phase with the observation of doubling of all resonances. DFT

calculations have once again been used to accurately predict NMR observables for all nuclei, confirming that, should an adequate structural model be used for calculation, there can be reasonable expectation of a very good agreement to experiment. DFT calculations searching for the FE-II structure reveal two energetically favourable structures, of which neither produces a good match to experimental data, which is possibly due to the temperature at which DFT calculations are carried out (0 K). In attempt to accurately model the proton transfer in the commensurately modulated FE-II structures, supercell structures were created comprised of four- or eight-unit cells. While experimental comparison is limited here, the results give insight in what could be expected should NMR experiments be carried out on the FE-II phase.

With advances to the theory of DFT calculations including exchange-correlation functionals and SEDC schemes, future work could aim to expand on the electronic structure minimisation process to continue finding optimal methodologies for small organic crystalline materials. With further optimised methods and greater confidence in DFT calculated parameters, the CL methodology could be applied to a wider variety of battery anode materials to continue to gain structural information through NMR crystallography. With enhanced structural understanding of organic anode materials, future studies could aim to apply these understandings in the design and testing of new and improved organic anode materials, with a view to application within lithium- or sodium-ion batteries. The improved NMR crystallography method could be applied once more to organic ferroelectric materials. With lower temperature NMR studies, insights into the lower temperature phase transitions could be gained, while improvements in the DFT methodology would shed more light on the complex modulated structure of the low temperature phases.

The results presented within this thesis have demonstrated the ability of NMR crystallography to gain valuable insights into structure and structural changes in crystalline organic functional materials. This combination of complimentary techniques allows a diverse range of data to be collected, probing both long-range and short-range structure.